UiT The Arctic University of Norway

Faculty of Science and Technology
Department of Physics and Technology

Waveguide–based Excitation for High–throughput Imaging

David A. Coucheron

A dissertation for the degree of Philosophiae Doctor – January 2021

Abstract

Fluorescence microscopy allows researchers to image biological samples that normally are transparent under white light illumination. Chip–based fluorescence imaging is an emerging field where the fluorophores in a sample are selectively excited at the surface of a photonic chip by the evanescent field generated outside of waveguides guiding light. Although the application of waveguide–based excitation is new in imaging, the idea has been used in bio–sensing for decades. Now, however, even super–resolution optical microscopy is possible, as waveguides have been designed which can provide a sufficiently high excitation intensity. The aim of this thesis is to explore how waveguide–based excitation can benefit super–resolution optical microscopy, as well as investigate other imaging and spectroscopic applications which can benefit from the same platform.

For all imaging and spectroscopic applications, a background signal can be detrimental to the results. Most components used in common applications, such as the sample holder, have been optimised to have minimal background. Waveguides, on the other hand, may not have gone through the same optimisation for imaging applications. The first part of this thesis is thus an experimental evaluation of the background signal from two common waveguide platforms, silicon nitride (Si_3N_4) and tantalum pentoxide (Ta_2O_5), to evaluate their potential use for imaging and sensing applications within the visible spectrum of light. It is shown that both platforms perform approximately equally well at 640 nm excitation, but at shorter wavelengths Si_3N_4 has an increasing fluorescent background. A thorough analysis of the background from Ta_2O_5 at 532 nm excitation is also performed, showing that the background is a Raman signal from the Ta_2O_5 material. We show that the increasing background for Si_3N_4 at shorter wavelength reduces the localisation precision, and thus the resolution of *direct* stochastic optical reconstruction microscopy. Using the results from the background measurement, chip–based resonance Raman spectroscopy of haemoglobin with 532 nm excitation using a Ta_2O_5 platform was performed.

Direct stochastic optical reconstruction microscopy is a popular super–resolution optical microscopy technique due to its ease of use and extremely high res-

olution. To reduce out–of–focus light in order to increase the contrast and resolution, total internal reflection fluorescence excitation is often preferred to epi–illumination. This is commonly generated through specialised lenses which have a small field–of–view, thus limiting the throughput. In this thesis, I show how using photonic integrated circuits for excitation can enable imaging of unprecedentedly large areas for nanoscopy. The chip–based nanoscope exchanges the excitation pathway and sample holder of a traditional microscope for an integrated photonic chip. The sample is placed directly on top of the photonic chip and illuminated by the surface evanescent field present on top of waveguides. The photonic chip is then combined with a simple microscope to enable total internal reflection fluorescence imaging. This thesis exhibits both diffraction–limited and super–resolution imaging with the chip–based system, including a super–resolved 500 μm × 500 μm image of liver sinusoidal endothelial cells. A typical total internal reflection fluorescence microscopes has a field–of–view of 50 μm × 50 μm , meaning that the chip–based system provides approximately 100x the imaging area of the free–space equivalent. Furthermore, a modified system was developed to combine the super–resolution imaging of chip–based *direct* stochastic optical reconstruction microscopy with quantitative phase imaging for three–dimensional morphological imaging, instead of the two–dimensional imaging typically found with total internal reflection fluorescence microscopy. The combined system achieved a spatial resolution of 61 nm and an axial sensitivity of ±20 mrad. Using the combined system, we measured both the thickness (91.2 ± 43.5 nm) of sieve plates in liver sinusoidal endothelial cells and the size of the fenestrations (124 ± 41 nm).

In the latter part of the thesis, I show some initial and on–going research on how inhomogeneous excitation from multi–mode waveguides can be used for computational imaging. In particular, the deterministic nature of the patterns is used to enhance the resolution of images. This shows how a waveguide platform not only can enhance existing imaging techniques, but actually offer novel approaches as well.

Acknowledgements

There are too many people to acknowledge individually for their help and support—that I'll rather have to do in person. To all who offered innumerable hours for discussions; who demonstrated, facilitated and collaborated in the laboratory (both here and abroad); who read, provided feedback, re–read and overall drastically improved all I have produced during these years; who initiated and joined lunches, coffee breaks and other social gatherings—thank you! Your impact can not be overstated.

I produced this thesis under the supervision of Balpreet S. Ahluwalia, to whom I'm deeply grateful for supporting me through this journey. Thank you for not only helping with the science, but focusing on scientific training and helping me pursue my interests.

Finally, a massive thanks to Vilde. It might be a cliché, but without you, this work would truly not have been possible.

Contents

List of Figures

List of Tables

List of Abbreviations

CLSM confocal laser scanning microscope

CMOS complementary metal–oxide semiconductor

DIC differential interference contrast

dSTORM direct stochastical optical reconstruction microscopy

ESI entropy–based super–resolution imaging

FOV field–of–view

FRC Fourier ring correlation

HIC high refractive index contrast

IR infra–red

LSEC liver sinusoidal endothelial cell

MMI multi–mode interferometer

NA numerical aperture

OTF optical transfer function

PAINT points accumulation for imaging in nanoscale topography

PDMS polydimethylsiloxane

PIC photonic integrated circuit

PSF point spread function

QPI quantitative phase imaging

RBC red blood cell

SBR signal–to–background ratio

SERS surface enhanced Raman scattering

SIM structured illumination microscopy

SLM spatial light modulator

SMLM single molecule localisation microscopy

SOFI super–resolution optical fluctuation imaging

STED stimulated emission depletion

STORM stochastical optical reconstruction microscopy

TE transverse electric

TIR total internal reflection

TIRF total internal reflection fluorescence

TIRF-M total internal reflection fluorescence microscopy

TM transverse magnetic

WERS waveguide enhanced Raman spectroscopy

Part I

Introduction

1 Introduction

1.1 Background

The modern microscope is an essential tool in many research laboratories around the world. The first microscope was introduced in 1590, and although it opened up the microscopic world to investigation, the image quality was low. As lens fabrication technology advanced and more sophisticated microscope systems were developed, more and more scientists started embracing the new tool. Robert Hook published the famous work "Micrographia"[1] in 1665 with hand drawings of what he had seen through a microscope, and the work was received with great enthusiasm. Robert Brown used a microscope to peer into the microscopic world of atoms, unknowingly, while studying pollen in 1827, where he observed the random motion of the pollen in water. Despite a plethora of interesting applications, imaging certain biological specimens remained challenging as they were nearly transparent under white light. Over the last centuries many techniques have been developed to try to image biological samples such as cells, with varying levels of success. The introduction of the laser in the 1960s opened the door to completely new microscopy techniques. One that emerged, and has since grown to become ubiquitous in life sciences, is the fluorescence microscope.

Cells have a very small difference in refractive index compared to traditional immersion media, such as water, and will thus have very little contrast in bright–field microscopy. The solution in fluorescence microscopy is to use fluorescent markers that bind specifically to target structures in the sample.

Different structures in the cell can be marked with different markers, and these markers only light up under excitation of a given wavelength provided by a laser. This means that not only can the cell be imaged, but different labels can mark different cellular structures and thus give a plethora of functional information. Although it's a tried and true microscopy technique for biological research, there's still plenty of room for improvements. The confocal laser scanning microscope, a common version of a fluorescence microscope, has great versatility and offers a resolution at the highest possible limit—the diffraction limit. Resolution in optical microscopes has gradually improved over centuries, and has now reached the fundamental limit that Abbe presented in 1873[2]. The diffraction limit for visible light is around 250-300 nm, which is small compared to the size of a typical cell. It is, however, of increasing interest to study the inner workings of cells, where structures often can be far smaller than the diffraction limit. One solution has been to use electron microscopes, which can grant a far higher resolution than the diffraction limit in optical microscopes. Electron microscopes do, however, often put severe restrictions on the sample which can make it impossible to perform e.g. live–cell imaging to study the dynamics of the cells. Although electron microscopy offers an extremely high resolution, it does not break the diffraction limit; it's simply that electrons have a much shorter wavelength than light. In 1992, however, a theoretical approach was published that presented a way to circumvent the resolution limit through stimulated depletion of fluorophores[3]. An experimental verification[4] and several improvements[5, 6] of the technique outlined by Hell et al. came in the following years. In 2006, something remarkable happened, when three new super–resolution optical microscopy—or nanoscopy—techniques were published almost simultaneously[7–9]. The onset of super–resolution optical microscopy finally allowed biologists to image beyond the diffraction limit using visible light.

A recent addition to the now broad range of super–resolution optical microscopy techniques is chip–based super–resolution optical microscopy[10]. The idea behind chip–based imaging is to swap the entire excitation pathway from a free–space system to a fully integrated system on a photonic integrated circuit. This change removes a lot of constraints on both collection and excitation that are inherent to free–space optics. This can drastically increase the throughput, which historically has been a challenge for nanoscopy techniques. An equally interesting aspect is that the photonic chip can be retrofit into existing fluorescence microscopes to bring super–resolution techniques to laboratories around the world. Although the initial work on chip–based imaging was with the aim of developing an alternative to traditional nanoscopy techniques, there are endless more possibilities using chip–based excitation. Chip–based super–resolution imaging ties well in to a trend in photonic integrated circuits research where applications have moved into new territories such as biosensing.

Photonic integrated circuits were originally developed for telecommunication applications. They have, however, expanded to a multitude of applications since the early days. In particular, the last decades have seen an increasing interest in bio–applications. The chip–based nanoscope answers the challenge of throughput by employing an intrinsic property of photonic chips—the evanescent field. Whenever light is guided in a structure, a portion of the light will be guided outside the physical structure in the evanescent field. This is an essential part of chip–based nanoscopy, as it offers total internal reflection fluorescence imaging without the need for specialised optics. It is this evanescent field, and all the potential benefits it brings compared to free–space systems, that spurred an interest in photonic integrated circuits in the greater sensing field as well. Despite all the work done on e.g. biosensing with photonic chips, little work has been done with visible light, which is essential for fluorescence imaging. One hurdle on the way to widespread adoption of chip–based excitation is developing suitable platforms for visible light. Additionally, with the merger of photonic integrated circuits and imaging, there are bound to be many interesting new possibilities.

1.2 Scope of the Thesis

The scope of the thesis is to explore the possibilities that follow with waveguide–based excitation, especially in the visible range. This will include two main areas: 1) increasing the throughput of single molecule localisation microscopy, and 2) investigating other imaging and spectroscopy modalities that benefit from the waveguide–based platform. All of the work will be centred around the chip–based nanoscope, which appears in several different implementations throughout the thesis. An overarching focus will be on the challenges and uncertainties of visible light imaging and sensing, a scarcely explored part of photonic integrated circuits.

1.3 Structure of the Thesis

In the thesis, I will systematically go through the two themes outlined in the scope. The thesis is separated into four parts. Before presenting the results, I will cover the necessary fundamental theory in Part 1. In Part 2 and Part 3, I will cover the two main areas outlined in the scope. Part 4 contains my conclusions where I highlight the future challenges and opportunities with waveguide–based excitation.

Part 2 of the thesis will focus on expanding the throughput of chip–based

direct stochastic optical reconstruction microscopy (*d*STORM). This is mainly achieved through the separation of the excitation and collection pathways acheived with waveguide–based excitation, as it allows for arbitrarily large areas with total internal reflection fluorescence excitation. I will start the part with an analysis of two common waveguide platforms, silicon nitride (Si_3N_4) and tantalum pentoxide (Ta_2O_5), and evaluate their suitability for visible light imaging in Chapter 3. Wide Si_3N_4 waveguides are then used in Chapter 4 to demonstrate large field–of–view diffraction–limited and *d*STORM imaging. In the final part of Chapter 4, one of the main challenges of chip–based imaging—its 2D nature—is answered by adding a quantitative phase imaging system to enable highly sensitive morphological imaging.

Part 3 of the thesis will present results on other imaging and spectroscopy modalities that benefit from chip–based excitation. Based on the findings shown in Chapter 3, I present results on using Ta_2O_5 waveguides for resonance Raman spectroscopy in Chapter 5. Further studies of the background in Ta_2O_5 are also presented in this chapter. A significant difference between free–space optics and integrated optics is that integrated optics offers easy control of light modes. A novel approach to computational imaging is demonstrated in Chapter 6 using the deterministic excitation patterns of multi–mode waveguides. The results demonstrate how the mode patterns intrinsic to a multi–mode waveguide can be used to enhance the resolution.

Throughout the thesis work, several different versions of the chip–based nanoscope were made. Figure 1.1 is a composite schematic of all variations and can be used to emphasise the focus of each chapter. Chapter 3 and Chapter 6 focus on the excitation part of the system. and in particular the waveguide platforms. Chapter 4 expands the imaging capabilities of chip–based microscope. In Chapter 5, I show how the same setup can be used for waveguide–based resonance Raman spectroscopy.

1.4 Publications

The thesis is based on several research articles. Four research articles are published, two are in peer review and one being written. All except one article are either published or have been self archived. The final research article, termed Paper VII, is being written and the relevant results are included in Chapter 6. Beneath follows a list of the works found in the thesis:

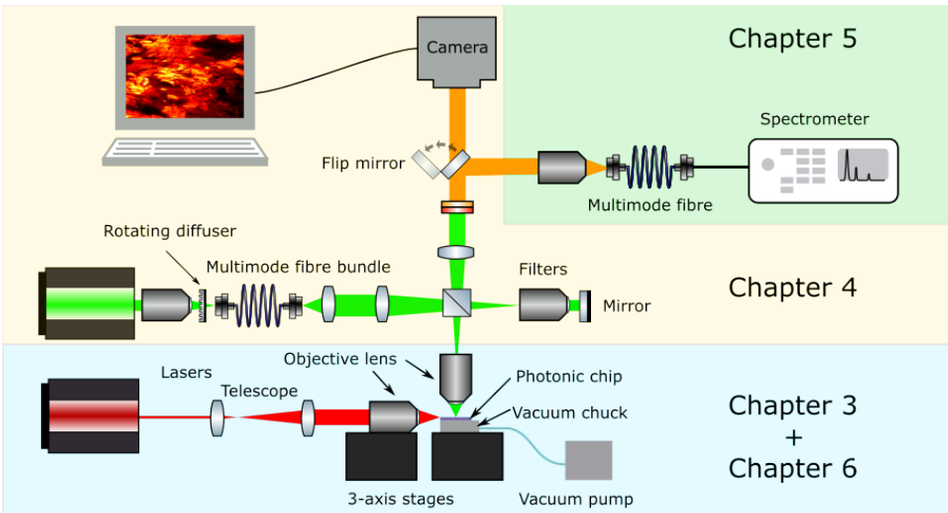

Figure 1.1: A composite schematic of the chip–based microscope used throughout the thesis. The entire system was never built into a single instrument, but it is useful to view it all together. The different chapters of the thesis focus on different aspects of the system. Chapter 3 and Chapter 6 (blue) emphasises the properties of the waveguide platforms; Chapters 4 focuses on the imaging part of the system; and Chapter 5 uses the same instrument for Raman spectroscopy.

Paper I **Study of Waveguide Background Signal at Visible Wavelengths for On–chip Nanoscopy.**
D. A. Coucheron, Ø. I. Helle, J. Wilkinson, G. S. Murugan, C. Dominguez, H. Angelskår, B. S. Ahluwahlia.
Selv archived at arXiv.org: 2101.10235
Submitted to Optics Express.

Author contribution: D. A. C. built parts of the set–up. D. A. C. performed the experiments and the data analysis. All authors contributed to writing the manuscript.

Paper II **Chip Based Nanoscopy: Towards Integration and High–throughput Imaging.**
D. A. Coucheron, Ø. I. Helle, C. I. Øie, F. T. Dullo, B. S. Ahluwalia.
Published in Proceedings of SPIE, the International Society for Optical Engineering (2017).

Author contribution: D. A. C. performed the experiments and analysed the data. All authors contributed to writing the manuscript.

Paper III **Nanoscopy On–a–chip: Super–resolution Imaging on the Millimeter Scale**
Ø. I. Helle, D. A. Coucheron, J. C. Tinguely, C. I. Øie, and B. S. Ahluwalia.
Published in Optics Express (2019).

Author contribution: D. A. C. contributed to the large field–of–view imaging and reconstruction. All authors contributed to writing the manuscript.

Paper IV **High-Throughput Total Internal Reflection Fluorescence and Direct Stochastic Optical Reconstruction Microscopy Using a Photonic Chip**
D. A. Coucheron, Ø. I. Helle, C. I. Øie, J. C. Tinguely, B. S. Ahluwalia.
Published in Journal of Visualized Experiments[1] (2019).

Author contribution: D. A. C. performed the experiments and the data analysis. All authors contributed to writing, filming and editing the manuscript.

Paper V **Multi-modal On-chip Nanoscopy and Quantitative Phase Imaging Reveals the Nanoscale Morphology of Liver Sinusoidal Endothelial Cells**
D. A. Coucheron[2], A. Butola[2], K. S., A. Ahmad, J. C. Tinguely, P. McCourt, P. Senthilkumaran, D. S. Mehta and B. S. Ahluwalia.
Self archived at arXiv.org: 2007.12263
Submitted to Proceedings of the National Academy of Sciences of the United States of America.

Author contribution: D. A. C. performed all experiments and the data analysis. All authors contributed to writing the manuscript.

Paper VI **Chip-Based Resonance Raman Spectroscopy Using Tantalum Pentoxide Waveguides**
D. A. Coucheron, D. N. Wadduwage, G. S. Murugan, P. T. C. So, B. S. Ahluwalia.
Published in IEEE Photonics Technology Letters (2019)

Author contribution: D. A. C. built the set–up, performed the experiments and did the analysis. All authors contributed to writing the

1. This publication is a video-based publication meant to thoroughly explain the imaging procedure. The full video can be viewed at jove.com, doi: 10.3791/60378
2. These authors contributed equally to the work

manuscript.

Paper VII **Resolution Enhancement with Computational Imaging using Waveguide Excitation**
D. A. Coucheron, B. S. Ahluwahlia, D. N. Wadduwage.
Manuscript in preparation. Partial results are included in Chapter 6.

Author contribution: D. A. C. performed the experiments and the FIMMWAVE simulations. All authors contributed to writing the manuscript.

1.5 Setting for the Thesis

The work in this thesis was done in 2016–2020 and funded by UiT – The Arctic University of Norway under the "Tematiske satsinger" initiative. The work was performed under the supervision of Prof. Balpreet S. Ahluwalia within the scope of the ERC project "Nanoscopy: High-speed chip-based nanoscopy to discover real-time sub-cellular dynamics". The work presented in Part 3 was initiated at The Massachusetts Institute of Technology (MIT) during a 6 month research stay in 2017 at the So Lab and the Laser Biomedical Research Center. All the work presented in Chapter 5 was performed during the stay at MIT, whereas the results in Chapter 6 were initiated there and have since continued as a collaboration between UiT and Harvard.

2

Properties of Light and Interactions with Matter

In this chapter, I will present the fundamental theory needed to understand the rest of the thesis. Sections 2.1 and 2.2 focus on fundamental light–matter interactions from a microscopic and macroscopic view, respectively. In Section 2.3, I briefly present how Raman scattering can be used in sample analysis through Raman spectroscopy. As most of the thesis is centred around chip–based imaging, the fundamentals of microscopes and diffraction–limited imaging will be covered in Section 2.4. Section 2.5 will focus on surpassing the diffraction limit for imaging, with particular focus on single molecule localisation microscopy (SMLM). Finally, a brief introduction to integrated photonics is presented in Section 2.6.

2.1 Interactions of Light with Matter—A Microscopic Approach

A large part of light–matter interactions can be understood from a classical theory of radiation and light–matter interactions. In this theory, matter is modelled as a collection of dipoles, i.e. a pair of oppositely charged point particles separated by an infinitesimal distance. An incident oscillating electric

field is described by $\vec{E} = \vec{E}_0 e^{i\omega_0 t}$. Such an electric field can drive oscillations in the dipoles, which in turn radiate power into the environment according to the normal modes that are excited. The intensity of the oscillations in the material is described by the induced dipole moment, $\vec{p}$, which is a function of the electric field and a material specific quantity called the polarisability tensor, α. The linear induced dipole moment is thus given by:

$$\vec{p}^{(1)} = \alpha\vec{E} \tag{2.1}$$

The polarisability of a molecule depends on its molecular properties. In general, larger molecules will have less tightly bound electrons, and thus a higher polarisability. In case of atoms in the periodic table, polarisability increases from right to left and from top to bottom of the periodic table. Negatively charged ions will have a high polarisability, whereas positive ions have a low. Polarisability can be expanded to the static polarisability, α_0, and dynamic components described by a set of normal coordinates, Q_j. The polarisability can be written as:

$$\alpha = \alpha_0 + \sum_k \left(\frac{\partial\alpha}{\partial Q_k} Q_k\right) + \frac{1}{2}\sum_{k,l}\left(\frac{\partial^2\alpha}{\partial Q_k \partial Q_l} Q_k Q_l\right)\ldots \tag{2.2}$$

By using the electrical harmonic approximation, the higher order terms can be disregarded and the polarisability of the k–th vibrational mode will be given by:

$$\alpha_k = \alpha_0 + \sum_k \left(\frac{\partial\alpha}{\partial Q_k}(Q_{k_0}\cos\omega_k t + \partial_k)\right) \tag{2.3}$$

The induced dipole moment for the k-th vibration under the influence of an oscillating electric field will then be:

$$\vec{p} = \alpha_0\vec{E}_0\cos\omega_0 t + \left(\frac{\partial\alpha}{\partial Q_k} Q_{k_0}\cos(\omega_k t + \partial_k)\vec{E}_0\cos(\omega_0 t)\right) \tag{2.4}$$

$$= \alpha_0\vec{E}_0\cos\omega_0 t + \frac{1}{2}\frac{\partial\alpha}{\partial Q_k}\vec{E}_0 Q_{k_0}(\cos(\omega_0 t \pm (\omega_k t + \partial_k)) \tag{2.5}$$

The induced dipole moment thus has three separate components oscillating at different frequencies.

2.1.1 Scattering

From Equation 2.5 it is clear that an oscillating electric field can induce a dipole moment with three components, which can be presented in short hand as

$$\vec{p} = \vec{p}_{\omega_0} + \vec{p}_{\omega_0+\omega_k} + \vec{p}_{\omega_0-\omega_k} \tag{2.6}$$

where ω_0 is the frequency of the incident wave and ω_k is the frequency of the k–th vibrational mode. The above derivation shows that excitation with light of a single frequency ω_0, will cause oscillations at three distinct frequencies from the k–th mode. The three scattered frequencies are the the same as the incident light, as well as at $\omega_0 + \omega_k$ and $\omega_0 - \omega_k$.

Elastic Scattering

Scattering where no energy change occurs is called elastic scattering. The specific type described above, with angular frequency ω_0, is called Rayleigh scattering. As Rayleigh scattering only depends on the static polarisability it will dominate the scattered light. It is common to separate the elastic scattering described above into two components: 1) coherent, in–phase scattering in the forward direction, commonly called the transmitted or forward propagating light; and 2) incoherent scattering in all directions, which is commonly referred to as Rayleigh scattering. Light propagation through an ordered solid occurs through elastic scattering and will be in phase with the incident light. Any real solid will have a degree of anisotropy, which causes the incoherent scattering.

Inelastic Scattering

The two angular frequencies at $\omega_0 \pm \omega_k$ will have an energy difference to the incoming light, and is therefore a type of inelastic scattering. This particular type of inelastic scattering is called Raman scattering[11] The higher energy scattered light at frequency $\omega_0 + \omega_k$ is called anti–Stokes Raman scattering, whereas the lower energy scattered light at frequency $\omega_0 - \omega_k$ is called Stokes Raman scattering. Both are collectively known as spontaneous Raman scattering, to distinguish them from other types of Raman scattering, such as resonance Raman scattering. Raman scattering is a far weaker effect than Rayleigh scattering, since it depends on the dynamic polarisability.

It is worth noting that although the scattered light can have three different frequencies for a given vibrational mode, it does not have to occur. For Rayleigh scattering to occur, the molecule must have a static polarisability. All molecules have this to some extent and thus there will always be Rayleigh scattering. Raman scattering, however, requires the second term in Equation 2.3 to be non–zero for the given vibrational mode. This requirement is known as the selection rule for Raman scattering. Also, it is important to remember that the electrical harmonic approximation was used to determine the frequency shift, whereas for an actual vibrational mode can have e.g. overtones, giving more possible frequencies.

2.1.2 Absorption and Emission

Scattering is not always the only result whenever an electric field is incident on a molecule. If the wavelength is close to a resonant frequency for an electronic transition the photon can get absorbed. Understanding absorption and emission from atoms and molecules requires a quantum mechanical theory of light–matter interactions. Atoms and molecules are quantum systems, and thus have discrete energy levels that they can occupy. The lowest energy level is commonly referred to as the ground state, and all higher are termed excited states. It is common to denote the energy levels with S_0, S_1 etc. Each energy level is split into several vibrational levels, commonly denoted ν_{n}, which differ slightly in energy. Each vibrational level is furthermore split into several rotational energy levels.

Absorption

Absorption is the process where an incident photon is absorbed by matter. In order for this to occur the energy of the photon must be similar to an electronic transition in the sample. For a molecule in an electronic state S_i, the electrons will be distributed following the Boltzmann distribution between the different states. Thus, absorption of a photon can excite a molecule from one electronic state to another electronic state can take many forms, as it can go between different vibrational states. A simultaneous transition in electronic and vibrational energy levels is called a vibronic transition. A Jablonski diagram of spontaneous Raman scattering, absorption and resonance Raman scattering (see Section 2.1.2 for more details) is presented in Figure 2.1a. From a quantum mechanical point of view, the scattering processes can be thought of as entering a virtual state, as shown in the figure. The vibronic transitions are more likely to occur between levels that have the highest overlap of wave functions, according to the Frank–Condon principle. Panel b in Figure 2.1 shows the energy levels with the wave functions of the different vibrational states. Absorption from the ground state to an excited state with a high degree of overlap is represented with the green arrow.

Fluorescence

Following absorption, a multitude of processes can take place. The excited molecule will, without outside interference, relax back to the ground state with time. This can occur in several ways, with one being fluorescence. Fluorescence is when the molecule emits a new photon to disperse of the energy to return to the ground state. This is done through a transition from a higher singlet state to a lower singlet state. The energy of the emitted photon usually has a lower

energy than the absorbed photon. According to the Frank–Condon principle, the molecule is usually excited to a higher vibrational state in the excited electronic state. It then transfers some energy to kinetic energy in order to satisfy the Boltzmann distribution. The molecule will then re–emit a photon of lower energy, usually returning it to an excited vibrational state in the ground state with a high degree wave function overlap. Two different emissions are shown in Figure 2.1b by blue arrows. The end result is that the emitted photon will be red–shifted compared to the absorbed photon. A typical excited singlet state has a lifetime in the nanosecond range, which means fluorescence is a relatively rapid process.

Resonance Raman Scattering

Raman scattering is, as the name implies, a scattering process and not related to absorption. The same goes for resonance Raman scattering, but due to the characteristics of resonance Raman scattering it is discussed together with absorption. Resonance Raman scattering can occur if the wavelength of the excitation light matches, or is close to an electronic transition in the sample, which can cause a resonance effect that increases the scattering by a factor 10^2–10^6. It can thus effectively increase the scattering cross section of Raman scattering, which is very small for spontaneous Raman scattering. The main challenge is that when the excitation light matches an electronic transition, absorption and fluorescence can also occur. All samples do not exhibit resonance effects, and thus resonance Raman scattering is highly sample specific. A resonance Raman process is sketched in Figure 2.1a.

Non–radiative Relaxation

Non–radiative relaxation can occur through several pathways, but consists of small releases of energy that leads to a lower state. It is a broad category, but usually occurs by transfer of vibrational energy to the kinetic energy of the molecule. The result is a relaxation that does not emit a photon. Two different non–radiative relaxations are shown in Figure 2.1 as black arrows.

Intersystem Crossings and Phosphorescence

Absorption processes can only excite the singlet ground state to an excited singlet state due to quantum mechanical selection rules. An excited singlet state can, however, through an intersystem crossing end up in a triplet state. A triplet state is a degenerate state of spin quantum number 1. As the selection rules prohibit direct relaxation to the singlet ground state, the triplet state is long

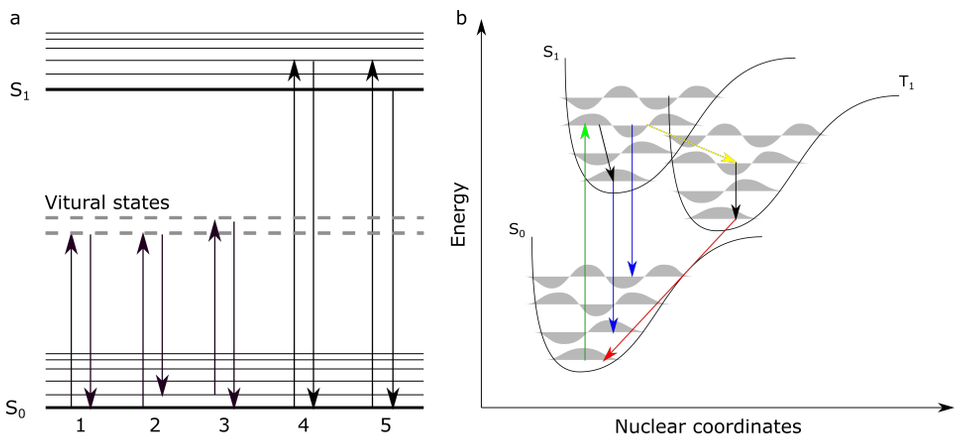

Figure 2.1: (a) A Jablonski diagram of Rayleigh scattering (1), Stokes Raman scattering (2), anti–Stokes Raman scattering (3), resonance Raman scattering (4), and absorption and fluorescence (5). (b) A schematic showing different transitions in anharmonic energy potentials. Green arrow = absorption, blue arrows = fluorescence, black arrows = non–radiative relaxation, yellow arrow = intersystem crossing and red arrow = phosphorescence.

lived compared to an excited singlet state. Relaxation back to the singlet state through emission is called phosphorescence and is similar to fluorescence but much slower and can take up to several minutes. The result is that fluorescence stops almost instantaneously after excitation stops, whereas phosphorescence can occur a long time after. An intersystem crossing is shown in Figure 2.1b as a yellow arrow, and phosphorescence is shown as a red arrow.

2.2 Interactions of Light with Matter—Bulk Properties

In this section I will relate the microscopic processes described in the previous section to bulk properties in matter. Other relevant bulk properties of matter, such as the refractive index, will also be introduced.

2.2.1 Phase Velocity and Refractive Index

When light propagates through matter it occurs through Rayleigh scattering (see Section 2.1.1). The propagating light will, however, have a change in phase velocity compared to the incident light. The phase velocity of light in matter

will be given by

$$v_{\mathrm{p}} = \frac{c_0}{n} = \frac{1}{\sqrt{\epsilon_0 \mu_0 \epsilon_r \mu_r}} \tag{2.7}$$

where c_0 is the speed of light in vacuum, ϵ_0 the permittivity of vacuum, ϵ_r the relative permittivity of the material, μ_0 the permeability of vacuum, μ_r the relative permeability of the material, and n is the refractive index of the matter. The refractive index is dependent on wavelength and this dependency is called dispersion. The refractive index of a material is, from Equation 2.7, a measure of light's phase velocity in the material compared to vacuum. The phase velocity change when passing through a material means that if two parallel beams pass through two different media of equal length, they will be phase shifted. If the beams are combined they will interfere and the resulting interference can reveal the refractive index difference of the materials. An illustration of the change in phase velocity can be found in Figure 2.2.

2.2.2 Snell's Law of Refraction

When light passes from one transparent medium to another transparent medium the phase velocity will change. This change in phase velocity causes a change in propagation direction from the incident beam (except for normal incidence), which is expressed through Snell's law of refraction:

$$\frac{\sin\theta_1}{\sin\theta_2} = \frac{v_{\mathrm{p},1}}{v_{\mathrm{p},2}} = \frac{n_2}{n_1} \tag{2.8}$$

Thus, the material–specific refractive index is a very useful property that can be determined experimentally. The bending of light when passing from one refractive index to another is called refraction and forms the basis of fundamental optical components such as lenses.

2.2.3 Light Attenuation

The above section describes the behaviour of light in transparent media, however, many materials are not transparent. The light beam will be attenuated gradually in the material. The attenuation of light in a given medium is given by the attenuation coefficient, μ, of the medium. The attenuation coefficient is in its simplest form a combination of the component of elastic scattering that is not forward–propagating, as well as the absorption in the medium. This can be expressed as:

$$\mu = \mu_s + \mu_a \tag{2.9}$$

where μ_s is the scattering coefficient and μ_a is the absorption coefficient. The light intensity at any given point, z, in the medium will then be given by:

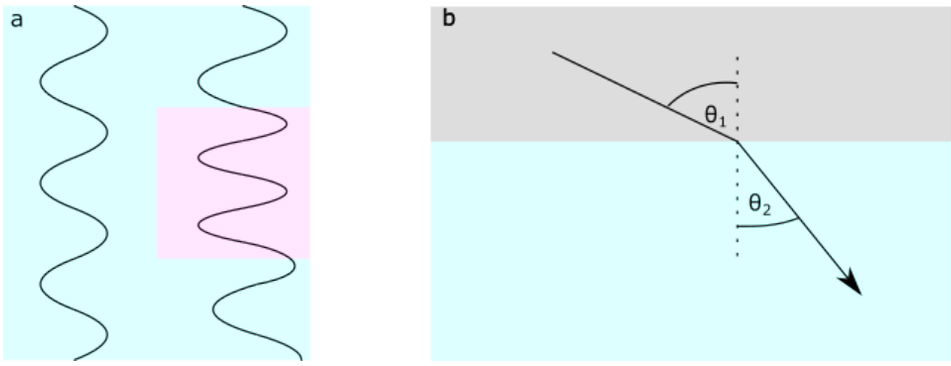

Figure 2.2: (a) Illustration of how two in–phase parallel beams can be phase shifted when they pass through regions of different refractive index (illustrated with different colours). (b) A sketch demonstrating refraction of a light ray when passing from a region of one refractive index to a region with a different refractive index.

$$I(z) = I_0 e^{-\mu z} \tag{2.10}$$

The scattering coefficient scales roughly as λ^{-4}. This means that shorter wavelengths will experience more scattering in a medium. The absorption coefficient does not have a simple behaviour, but depends on the electronic structure of the sample. It can have a very strong dependence on wavelength, as some wavelengths simply can't excite the sample.

2.3 Raman Spectroscopy

The Raman scattering described in Section 2.1.1 means that each molecular vibration in a molecule will oscillate at the incident lights frequency, as well as two distinct additional frequencies for all Raman active vibrational modes. It is, however, apparent from Equation 2.2 that higher order terms can exist and lead to more frequencies. The emitted frequencies of a molecule will be a collection of all molecular vibrations, with a couple of example vibrations shown for a bent triatomic molecule such as CO_2 in Figure 2.3a. By exciting a sample with a laser and measuring the scattered light, the chemical fingerprint of the sample can be obtained. The output spectrum will be dominated by the Rayleigh scattered light, but will also have the Stokes and the anti–Stokes Raman scattered light, as shown in Figure 2.3b. For spectroscopy, the anti–Stokes Raman scattered light is commonly filtered out, along with the Rayleigh scattered light. The anti-Stokes scattered light carries no additional information to the Stokes scattered light, as they are symmetric, except that the anti-Stokes signal is weaker due to the thermal distributions in the molecule, as explained in Section 2.1.2. An

important property of spontaneous Raman scattering is that the frequency shifts of the scattered light do not depend on the wavelength of the incident light, as they only depend on the vibrational energy levels. This is in contrast to a fluorescence signal.

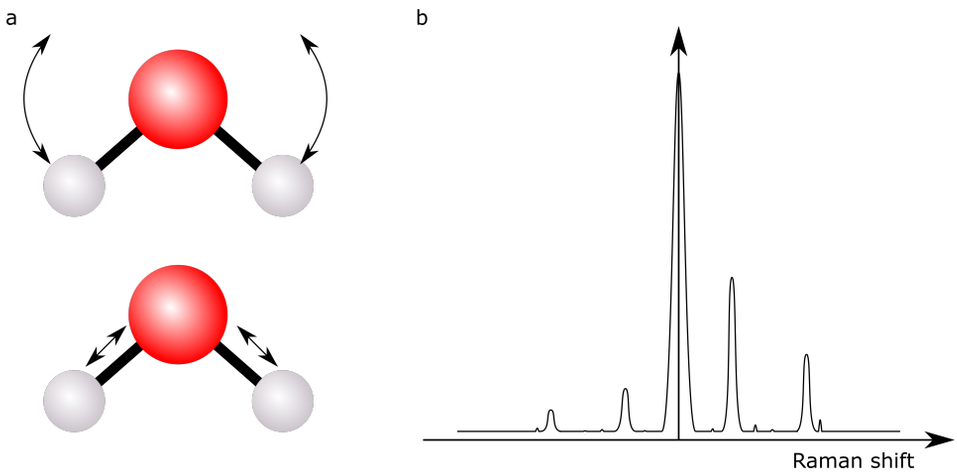

Figure 2.3: (a) Two examples of vibrational modes in a bent triatomic molecule, such as CO_2. (c) A sketch of a Raman spectrum. The central beam is the Rayleigh scattering and will by far be the strongest. The spectral parts at positive and negative Raman shifts will be symmetric, but the Stokes Raman scattered light will be stronger.

Scattering is a linear process and as such it will scale linearly with excitation power. Raman spectroscopy can be performed with any wavelength excitation and has to be chosen based on application, although the scattering intensity scales as λ^{-4}, which means that the intensity of the Raman signal drastically increases with shorter wavelengths. Many samples will, however, experience a strong fluorescent signal in the visible range. This has led to typical Raman spectrometers using a 785 nm laser, as it offers a sweet spot of a high scattering intensity while avoiding a strong fluorescence signal.

In a typical Raman spectroscopy set–up, the laser usually passes through e.g. a cuvette containing the sample and the scattered light is measured. This can be done e.g. by collecting backscattered light through the excitation lens, or using a collection lens at an angle. The collected signal is then passed through a long pass filter and a notch filter to the move the Rayleigh scattering as well as the anti–Stokes Raman. Further filters, such as band pass filter, can be used to collect only the spectral region of interest. The filtered light is then passed into a spectrometer and analysed.

2.4 Optical Microscopy

A microscope is a tool used to observe the microscopic world. The function of a microscope is to generate a magnified image of a sample so that more details can be observed by the user, compared to viewing it with the naked eye. This is usually done with lenses, although a plethora of different techniques and variations exists today, from the simple magnifying glass to the most advanced transmission electron microscopes. The original microscope, and the most common implementation, is the light microscope. The basic principle behind a light microscope is to illuminate a sample with light and then image the contrasts generated by the sample through a lens set–up which magnifies the sample significantly. Light microscopy was pioneered in the 1600s and the advent of the first optical microscopes opened a door to an unexplored world: the microscopic world. The simplest microscope is really a magnifying glass with just a simple lens, but development quickly turned to compound microscopes containing several lenses with a sample stage and other practical solutions. Optical microscopy is today a very broad category of microscopes, all using light for imaging.

There are many ways to classify the different microscopy techniques that exist. One way is through broad categories based on the imaging principle, with the three main types being optical microscopy, electron microscopy and scanning probe microscopy. Only optical microscopy is discussed in this thesis. Optical microscopy can be sub–divided based on e.g. excitation type into widefield illumination, structured illumination or point illumination, although point illumination is just a type of structured illumination. Another interesting division is based on the mechanism of generating contrast, with some options being bright–field, dark–field, phase or polarisation. In the following section, I will present the fundamental working principles of optical microscopes. This will lead into a discussion on resolution in a microscope and then a brief introduction to several types of microscopy. This will form the basis for Section 2.5, where I will introduce super-resolution optical microscopy, a major topic of this thesis.

2.4.1 Seeing the Microscopic World

Modern optical microscopy includes a lot of different techniques, but they all form images using light from the sample. The light from the sample, however, can be reflected light, transmitted light, scattered light, emitted light or many other options. Whenever light interacts with a sample, each point on the sample will emit light as a point source according to the Huygens principle. A lens can be used to capture the light and, through refraction, form a magnified image of the sample. Any lens has a property called the focal length, which is the length

at which the lens will focus collimated light. If a lens is used for imaging the image will occur at a distance given by the following equation:

$$\frac{1}{d_0} + \frac{1}{d_1} = \frac{1}{f} \tag{2.11}$$

where d_0 is the distance from the sample to the lens, d_1 is the distance from the lens to the image, and f the focal length of the particular lens. The magnification, m, of a single lens depends on the distance from the lens and is given by:

$$m = -\frac{d_1}{d_0} \tag{2.12}$$

The magnification is simply how much larger the sample will appear in the image compared to the actual size. For compound lenses, such as objective lenses, the magnification is usually quoted directly as e.g. 60x.

The main component of a microscope is the lens. Lenses are typically finely polished glass structures that are either concave or convex in order to refract the sample and create a magnified or demagnified image. The simplest microscope is the magnifying glass, which uses a single lens to form a magnified image of a sample. Most microscopes today are compound microscopes, where two or more lenses are used together to form an image of the sample. An example of imaging through two lenses can be seen in Figure 2.4a. The objective lens can e.g. provide a 60x magnification, and an additional lens in the eyepiece can provide a further 10x magnification, resulting in a 600x magnification of the sample. A simple schematic using with the geometrical optics approximation is presented in Figure 2.4a.

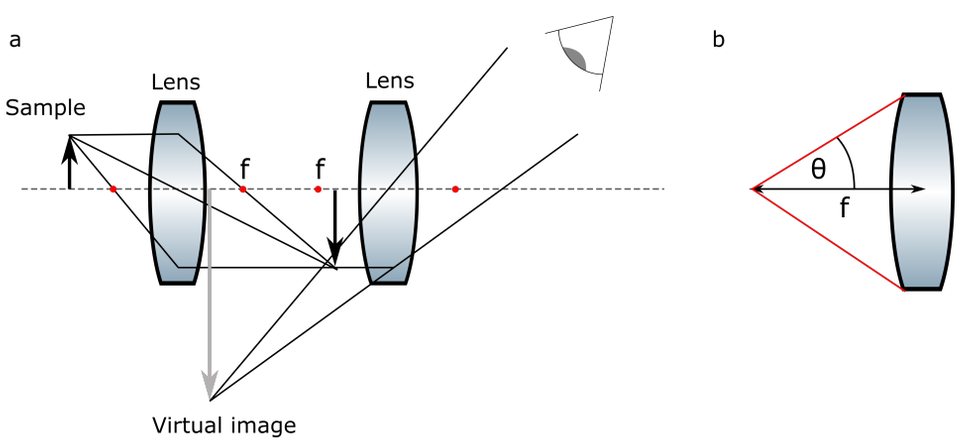

Figure 2.4: (a) Simple schematic of image formation through a compound microscope. (b) Sketch showing the maximum angle that a lens can collect light through.

2.4.2 Resolution in Optical Microscopy and The Diffraction Limit

Although a microscope allows the user to magnify an object as much as desired, it will reach a point beyond which no additional information is gained through magnification. The resolution of a microscope is defined as the shortest distance between two points on a sample that still can be separated in the image. The imaging process does not recreate the sample perfectly—it is in fact blurred by the imaging process. In 1825 Ernst Abbe gave a theoretical description of imaging a point source through a circular aperture and showed that the point would result in an intensity distribution called an Airy disk. The reason for the limited resolution is that although point emitters will emit in all directions, a lens can only capture a certain portion of it, as shown in Figure 2.4b. The imaging process does not capture all spatial frequencies from the sample and will in practice function as a high pass filter in Fourier space. The maximum angle at which a given objective lens can capture light is described by the numerical aperture (NA), given by:

$$\mathrm{NA} = n \sin \theta \tag{2.13}$$

where n is the refractive index and θ the maximum angle that the lens can accept, as illustrated in Figure 2.4b. In a real microscope, there will also be aberrations present, which cause a diversion from the Airy disk. The actual distribution that a point will take in a given microscope is called the microscopes point spread function (PSF). When imaging, every point on the sample acts as a single emitter and the resulting image will be a convolution of the sample and the point spread function of the microscope. Mathematically, this is described by the following convolution:

$$I(r) = [O(r) \cdot E(r)] * \mathrm{PSF}(r) \tag{2.14}$$

where $I(r)$ is the image, $O(r)$ the sample, $E(r)$ the excitation light distribution, and $\mathrm{PSF}(r)$ the PSF of the system. A simulation of this process is shown in Figure 2.5.

The diffraction limit means that two points will not be distinguishable in the image if they are closer together than the diffraction limit. This is demonstrated in Figure 2.5. The threshold for separating point sources has been formulated in different ways by different scientists. Lord Rayleigh formulated the most conservative definition of resolved as when the maximum of one point source overlaps with the first minimum of the next one. This can be expressed as:

$$d_{\mathrm{Rayleigh}} = 0.61 \frac{\lambda}{\mathrm{NA}} \tag{2.15}$$

This is more conservative as the limit expressed by Abbe, which was based on the distance two point sources can have while still having a distinct dip in

intensity in the resulting intensity distribution. This was formulated as:

$$d_{\text{Abbe}} = 0.5\frac{\lambda}{\text{NA}} \tag{2.16}$$

A related formulation, which is based on when the resulting intensity profile is flat at the maximum was proposed by Sparrow. This can be expressed as:

$$d_{\text{Sparrow}} = 0.47\frac{\lambda}{\text{NA}} \tag{2.17}$$

The different formulations give different resolution limits, but they are all linearly related and all scale as $\frac{\lambda}{\text{NA}}$. This means that the resolution of an optical microscope improves with a higher NA of the system, and shorter wavelengths. A quick note on nomenclature: an increase in e.g. the NA of a system will result in shorter distances being separable, and this will be referred to as an increase in resolution and vice versa.

The above derivations show that the resolution of an imaging system will have a lower limit imposed by the diffraction of light. There are, however, other effects that can cause a departure in performance compared to the theoretical maximum. These effects are collectively termed aberrations and will lead to blurring or distortion of the image. A common type of aberration is spherical aberrations, where light passing through the outer periphery of a lens is refracted more than the light passing through the central region, resulting in a blurred focus. If the imaged light contains several wavelengths, chromatic aberrations can occur where different wavelengths are refracted differently in a lens due to dispersion in the material. The result is that each wavelength will have a different focal length. Other types of aberrations include coma, astigmatism and field curvature. All microscopes will have aberrations, but they can be reduced through e.g. proper alignment and technical improvements.

2.4.3 White Light Imaging

So far we have seen how a basic microscope can image a sample and how the resolution of the image is limited by the imaging process. In order to generate an image, the microscope needs to be made with a method of generating contrast in the sample. In the following subsection, I will present the contrast mechanisms for a few common white light imaging techniques.

Bright–field

The very first microscope invented, which remains extremely popular, is the bright–field microscope. The sample is illuminated by a light source and

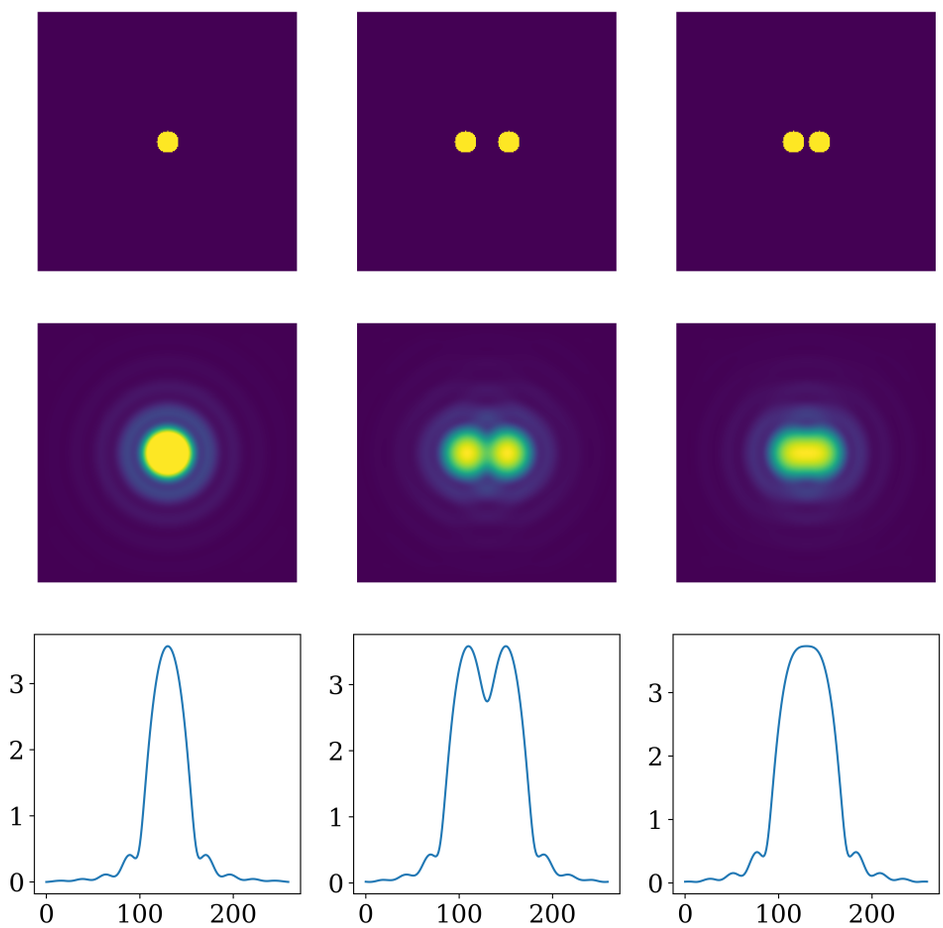

Figure 2.5: Simulated imaging of fluorophores through a microscope. The first column shows how the fluorophore will be imaged as a Airy disk. The second and third columns show how the distance between two spots will determine if the two spots are resolvable or not. The bottom row is a line plot through the centre of the fluorophores. All panels are shown with logarithmic axes to make the patterns easily visible.

contrast is generated by a difference in transmittance/reflectance. Transmitted light will be the forward propagating light, so the contrast is generated through losses such as incoherent Rayleigh scattering and absorption in the sample. The sample will thus appear dark on a bright background, and thus the name bright–field microscopy.

Dark–field

An alternative version is dark–field microscopy. As with bright–field, the name dark–field references the general image look—a dark background with sample structures being bright. In dark–field microscopy, the forward propagating light beam is blocked out and instead the incoherent scattered light is imaged. Contrast is thus generated based on the amount of incoherent scattering that different parts of the sample generates.

Phase Microscopy

Whenever Rayleigh scattering occurs, the forward propagating light will be coherent. It will, however, be out of phase with the incident light due to a change in phase velocity. The change in phase velocity depends on the refractive index, n.

For samples that are transparent to light, using the phase change can be a way to image them. This is called phase microscopy. A particular type is the phase contrast microscope, where phase differences in the specimen and surroundings are used to create contrast in the image. The basic idea is to separate the unscattered light from the scattered light, which contains information of the sample. The unscattered light is phase shifted 90 degrees and then recombined with the scattered light (could be other way around too). The amount of phase change incurred by the sample will then determine the contrast. The final image is thus an image of the refractive index. Another popular phase microscopy technique is differential interference contrast (DIC) microscopy. In DIC microscopy, the excitation beam is split into two parallel beams with a Wollaston prism. The two beams then pass through the sample in very close proximity, and are recombined again. The interference between the two beams with then give rise to contrast depending on the difference in refractive index between the two spots the beams passed through.

2.4.4 Fluorescence Microscopy

The low refractive index difference between many biological samples and the immersion media is of great concern for biologists and medical researchers. Phase microscopy can be used to image such samples, but a more popular technique is fluorescence microscopy. In fluorescence microscopy the sample is labelled with fluorescent markers, i.e. molecules that fluoresce under excitation of a given wavelength range. There are two common sources of fluorescent markers: 1) engineered molecules that fluoresce strongly under the correct excitation and 2) fluorescing proteins such as the green fluorescent protein[12]. The fluorescent markers bind only to very specific sites in the sample, e.g. the actin network of a cell, which means that fluorescence microscopy actually offers functional imaging. A plethora of fluorescent markers exist today that bind to different sites with a range of different excitation and emission spectra, making multi–colour imaging of several components straightforward. The fluorescent markers are made to excite within a range of wavelengths and will emit a red–shifted and often mirrored spectrum to the excitation spectrum due to the Frank–Condon principle. The nature of the fluorescent markers makes fluorescent microscopy useful for both qualitative imaging and quantitative measurements. The versatility of fluorescence microscopes have made them an integral part of biological research laboratories around the world. A fluorescence microscope, in its simplest form, uses a laser to excite the sample through an objective lens. The emitted light is collected through the same lens and passed through a dichroic beamsplitter to remove the excitation wavelength. It is then imaged with a lens onto a camera. Such a set–up is presented in Figure 2.6a. An example fluorescent image is shown in Figure 2.6c, where the nucleus and the plasma membrane of cardiomyocytes have been labelled.

Total Internal Reflection Fluorescence Microscopy

The entire volume that the laser passes through will have fluorescent excitation, but it's only the signal in the focal plane that is of interest. The out–of–focus light will appear as a background and reduce the contrast and resolution. One common way to avoid this problem is to use a total internal reflection fluorescence microscopy (TIRF-M), where only a few 100 nm of the sample will be excited. In TIRF-M, the microscope does not change much, but the excitation is done through an evanescent field rather than through free–space. The evanescent wave can be achieved in several ways. One common way is by passing the light through a prism, with the sample on top[13]. The light will experience total internal reflection in the prism, which generates an evanescent field that can interact with the sample. Another method is simply to use a total internal reflection fluorescence (TIRF) objective lens. This is a high NA lens

that, when light is passed in at the right angle, will generate an evanescent field through total internal reflection in the lens. More details on total internal reflection and evanescent fields can be found in Section 2.6. The result is that only the focal plane is excited and the out–of–focus fluorescence is thus drastically reduced. A schematic is shown in Figure 2.6.

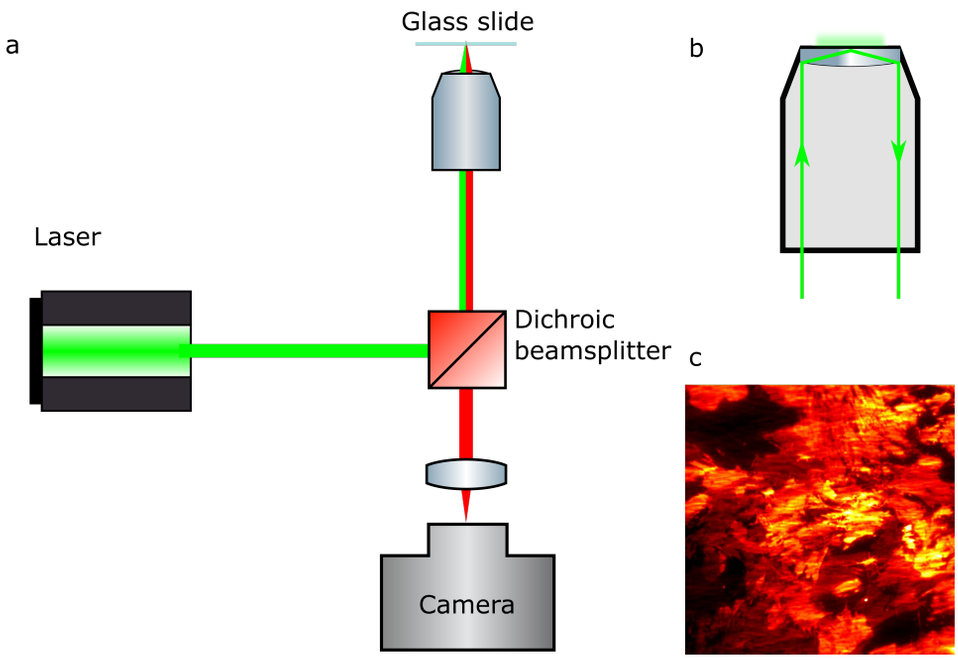

Figure 2.6: (a) A schematic of a simple fluorescent microscope. The sample is placed on a glass slide. The laser beam is reflected off a dichroic beamsplitter into the objective lens and excites the sample. Any fluorescent signal is collected by the objective lens and will pass through the dichroic beamsplitter and is focused onto a camera. The beamsplitter works as a filter to remove the laser light, but usually additional filters are used as well. (b) Illustration of how a TIRF lens works. The laser light experiences total internal reflection in the objective lens, which generates an evanescent field outside of the lens. (c) A TIRF image of cardiomyocyte cells labelled with CellMask Deep Red.

2.5 Super–resolution Optical Microscopy

Abbe theorised the diffraction limit in 1883, but for a long time this limit was out of reach. Microscopes were suffering from severe aberrations and other challenges that limited resolution. With time, these challenges were solved and the diffraction limit of resolution was finally reached. As it is a fundamental limit of nature, it was believed that to image beyond the diffraction limit was impossible.

From the limits of resolution presented in Equations 2.15, 2.16 and 2.17, one simple way to improve the resolution of microscopes is to use shorter illumination wavelengths. UV microscopes employ this to achieve a high resolution. Even shorter wavelengths are used in X–ray microscopes, yielding a resolution below 15 nm[14]. In fact, electron microscopes are just taking this to the extreme, as electrons are waves of extremely short wavelength through the wave–matter duality. Although an extremely high resolution can be achieved in this way, it never goes beyond the diffraction limit—it simply lowers the limit. Many of these techniques are limited in applications, either through it being biologically damaging radiation, or technical constraints such as vacuum.

Another way to increase the resolution is to increase the NA of the objective lens. The numerical aperture is a measure of the amount of light captured by a lens. In any realistic lens this angle will at a maximum be 90 degrees from the optical axis, which would give a maximum NA of 1.0 in air (refractive index 1.0). The highest realistic value, however, is around 0.95. There are ways of further improving this, e.g. by changing the refractive index that the light passes through. Today, water immersion lenses that have an NA of 1.2 are commonplace, and oil immersion lenses can achieve 1.4. Going beyond this, however, is challenging.

The following sections will present a brief summary of the beginnings of super–resolution optical microscopy as a means of actually surpassing the diffraction limit. Special attention will be given to single molecule localisation microscopy, and in particular direct stochastical optical reconstruction microscopy (dSTORM), as this thesis is to a large extent based on it.

2.5.1 Surpassing the Diffraction Limit

One of the first optical microscopy techniques to surpass the diffraction limit was the confocal fluorescence microscope—a technique that today has become an essential part of a biomedical research environment, although interestingly not due to the high resolution. In confocal microscopy a small pinhole is placed in a conjugate focal plane to block out any out–of–focus light. A common implementation of the confocal microscope is the confocal laser scanning microscope (CLSM), which scans the sample with a focused laser. The main reason confocal microscopes are used today is that they greatly increase contrast by removing most of the out–of–focus light. It is, however, possible to increase the resolution past the diffraction limit by reducing the pinhole size to 1 airy unit or below, at the cost of signal strength. Additionally, the pinhole can be put off–axis for additional enhancement[15, 16]. The loss of signal is a steep price however. A recent application of similar principles is the AiryScan[17].

The modern super–resolution optical microscopy techniques are, however, a far more recent invention. In 1992, Stefan Hell proposed a theoretical imaging approach that could increase the resolution beyond the diffraction limit[18]. The proposed technique is today known as stimulated emission depletion (STED) and was first experimentally demonstrated in 1999[4]. The development of STED continued into the 2000s, but in 2006 there was a massive surge of techniques. Almost simultaneously, three new super–resolution techniques were published[7–9], all using the same principle of single molecule localisation microscopy, which will be covered in detail in the following section. The techniques presented in 2006 helped spark a great interest in super–resolution optical microscopy techniques, with many new approaches being publishes in the following years. In 2000, structured illumination microscopy (SIM) was introduced, where a structure excitation pattern is used to shift higher frequencies into the image, potentially doubling the resolution through a reconstruction algorithm[19]. Several fluctuation based techniques have been introduced, which offer unprecedented speed, but with a limited resolution enhancement[20, 21]. The field continues to explore a plethora of new approaches and advancements.

2.5.2 Single Molecule Localisation Microscopy

In 2006, the three original SMLM techniques were published. Since then, other variants have been presented, such as *direct* stochastic optical reconstruction microscopy (*d*STORM)[22] and points accumulation for imaging in nanoscale topography (PAINT)[23]. They all rely on the same fundamental principle of localising individual emitters, although they achieve this in different manners. Following the initial presentation of the techniques, several advances were quickly made. Multi–colour imaging was introduced to increase the throughput of the techniques[24]. The imaging speed has also been increased significantly[25]. Modern applications of SMLM range from single molecule counting[23], to live cell imaging[26].

General Principle

As shown in Section 2.4.2, imaging of a point emitter through a lens results in an image that is a convolution of the emission and the PSF. The main idea behind SMLM is that the emission profile of a single emitter is known. Thus, if a detected signal comes from a single emitter it is possible to perform a fitting procedure, e.g. by using a 2D Gaussian profile, and localise the emitter's position far more precisely than the diffraction–limited spot. This is illustrated in Figure 2.7. The idea came from single molecule spectroscopy[27], although it took a long time before it was used in imaging as fluorescence imaging ends

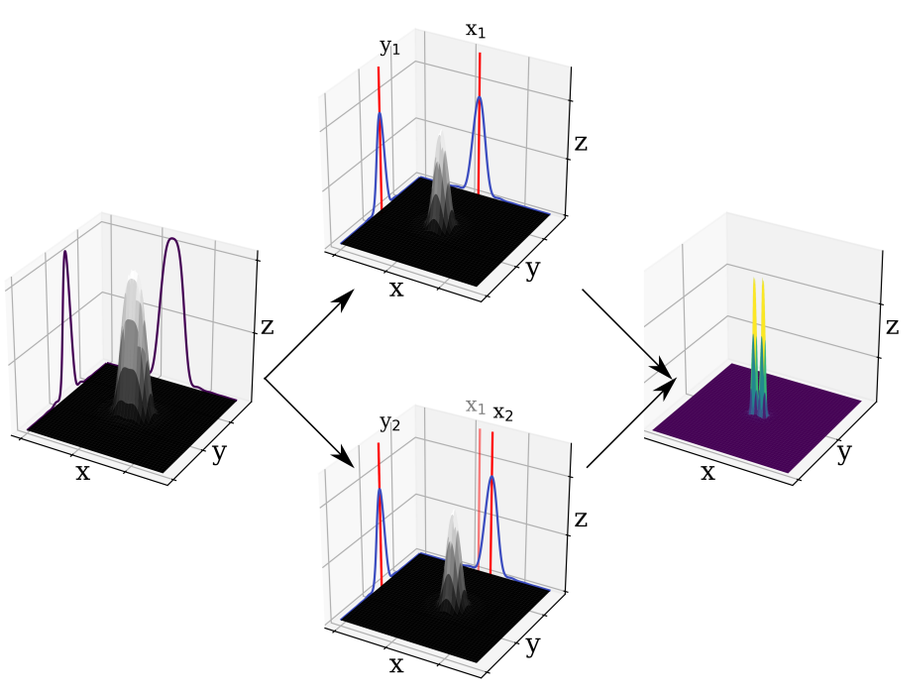

Figure 2.7: Illustration of single molecule localisation microscopy with a sample containing to fluorophores within the same diffraction–limited area. If the fluorophores can be imaged sequentially, each can be individually localised to a high degree and a super–resolved image can be reconstructed from two images.

up with many fluorophores within the same diffraction–limited spot.

In order to perform SMLM, the fluorophores have to be separated. This is done by introducing a temporal separation. Instead of having all fluorophores excited at the same time, sparse subsets are imaged sequentially and a localisation procedure is performed on the data. In practice, several thousand frames are imaged, with each containing a sparse subset of single emitters, where the density is tuned such that it is highly likely that there is no overlap. An example of such a stack is shown in Figure 2.8a. Each frame then goes through a segmentation to find emitters and then each emitter is fitted to e.g. a 2D Gaussian profile, similar to the process presented in Figure 2.7. The resulting fit parameters, such as position and intensity, are collected and re–plotted on a super–resolved image in the end. Examples of diffraction–limited and super–resolved images of liver sinusoidal endothelial cells (LSECs) are found in Figure 2.8b and c, respectively. The difference in SMLM techniques often comes down to how the separation is achieved[28].

Several different software options exist today for performing the actual emitter

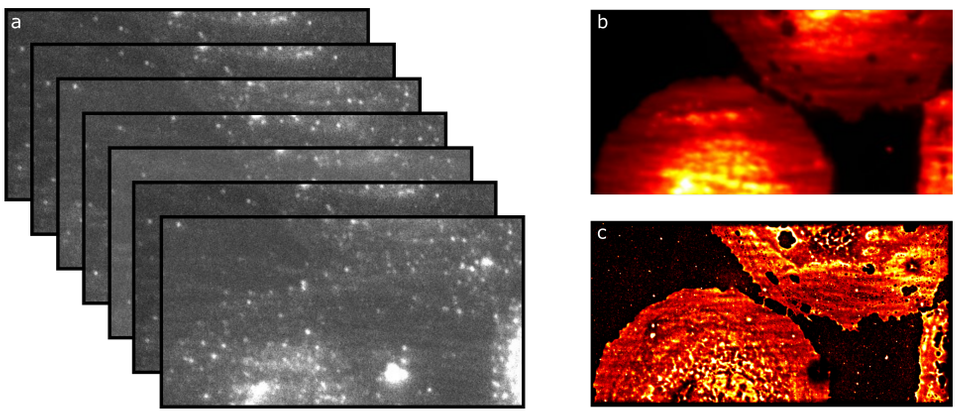

Figure 2.8: (a) A stack of images with well separated, blinking fluorophores that can be used for reconstruction. The sample is liver sinusoidal endothelial cells labelled with CellMask Deep Red. (b) A diffraction–limited TIRF image and (c) a super–resolved *d*STORM image of the sample in (a). The super–resolved image reveals nano–pores in the membrane of the cells that are not visible in diffraction–limited imaging.

fitting procedure and reconstruction of the *d*STORM data. The choice depends on many factors, such as computational speed, ease of use, multi–emitter fitting availability, drift correction etc. The localisation precision of a single emitter is, however, governed by the fitting procedure. Thompson et al. presented the following equation to describe the localisation precision, Δx:

$$\Delta x = \sqrt{\frac{\sigma^2 + \frac{a^2}{12}}{N} + \frac{8\pi\sigma^4 b^2}{a^2 N^2}} \tag{2.18}$$

where σ is the standard deviation of the PSF, a the pixel size of the camera, b the background signal, and N the number of photons collected from an emitter[29]. This means that any background signal will reduce the localisation precision, whereas a higher photon count will increase it. The blinking density can be tuned with excitation laser power, and the photon count will depend on the exposure time. The two parameters have to be tuned to get strong blinks that are well separated.

Any background signal will reduce the localisation precision and thus the resolution, as seen in Equation 2.18. Thus, minimising the background signal is essential for a high quality image. One common solution in SMLM is to use TIRF to reduce out–of–focus fluorescence. The modern TIRF objective lenses are easy to use, but they usually have a very high magnification and thus a very low throughput.

direct Stochastic Optical Reconstruction Microscopy

One implementation of SMLM that has seen great popularity since its introduction is *d*STORM[22]. *d*STORM is a simplification of stochastical optical reconstruction microscopy (STORM), and the main advantage is that the photoswitching is achieved in single fluorophores. STORM relies on the Cy3–Cy5 complex to get the desired blinking, but this limits the applicability since the range of fluorophores is limited. Over the years, several common fluorophores have been demonstrated to blink just by altering the imaging buffer[30, 31]. Several different blinking buffers are used, depending on the fluorophore and imaging conditions, but they all work by increasing the inter–system crossings from the singlet state to a dark state. Fluorophores will spontaneously end up in a triplet state occasionally, which can be reduced to lead to a long lived dark state. The formation of the dark state is affected by laser power and e.g. by addition of a thiol. A reduction of the fluorophore will relax it back to the fluorescing singlet state[32]. This is shown in Figure 2.9. Returning fluorophores from the dark state can be aided with a short wavelength laser, e.g. 488 nm[33].

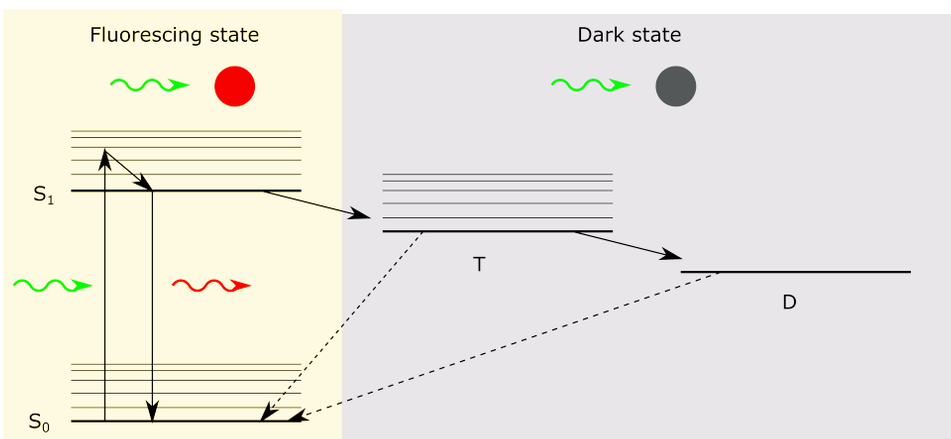

Figure 2.9: Jablonski diagram for *d*STORM imaging. A fluorophore in the fluorescing state will absorb and re–emit photons continuously. A portion of the fluorophores in the sample will fall into a triplet state, and from there be reduced into a long lived dark state. This process is enhanced by the blinking buffer.

*d*STORM makes SMLM easy to implement with minimal instrumentation needs. The main requirements to perform *d*STORM are suitable fluorophores, a blinking buffer, and a high intensity excitation source. An advantage with *d*STORM is that many of the common fluorophores used today have been shown to blink under the right conditions[22, 34], unlike for e.g. STORM. All SMLM performed in this thesis was done using *d*STORM due to these reasons.

2.5.3 Other Super-resolution Optical Microscopy Techniques

Although SMLM is a big category of nanoscopy techniques, there are several other widespread categories. The first proposed technique in 1992 was what today is commonly referred to as STED, which bears resemblance to CLSM. In CLSM the excitation light is focused into a diffraction–limited spot and imaging is done by scanning this spot along the sample and measuring the output intensity of each point. The resolution is thus limited by the size of the excitation spot. In STED, the imaging is done in a very similar way, but one additional component is added: a depletion laser. A longer wavelength laser with a torus shaped beam is aligned with the excitation laser and scanned along the sample. The excitation laser excites all the fluorophores inside the focal volume, but the coaligned depletion laser relaxes all fluorophores except those in the centre of the torus through stimulated depletion. The result is that only a very small central spot of the excitation volume will experience spontaneous relaxation. As stimulated depletion will occur much faster, gating can be used to separate the signal and the end result will be an extremely small excitation volume scanned across the sample.

Another technique that can provide a resolution twice that of diffraction–limited microscopy is SIM. It is a popular technique due to its versatility and fast image acquisition, but it has a limited resolution enhancement. SIM is a widefield technique, like *d*STORM. Unlike a traditional widefield technique, where a homogeneous excitation is wanted, SIM uses structured illumination. This shifts higher order frequency information into the optical transfer function of the microscope through the Moiré effect[19]. By imaging enough phases and angles, a high resolution image can be reconstructed of the sample.

All the work in this thesis is done using *d*STORM. *d*STORM requires very little modification to be performed, unlike SIM and STED, which makes it ideal for investigating the waveguide platform.

2.6 Integrated Photonics

The last decades have seen massive changes in optics with the emergence of integrated photonics. Electronics shifted to integrated electronics in the 1950s, and optics is now following along. This section will present some fundamental theory of integrated photonics.

Like the electrical wire forms the basis of an integrated electronic circuit, the optical waveguide forms the basis of a photonic integrated circuit (PIC). The

most common optical waveguide today is the optical fibre, which is essential for modern telecommunication. The integrated waveguide is the integrated equivalent to the optical fibre. Many different geometries and variants exists today, and common ones include the strip waveguide, the rib waveguide and the slot waveguide. If light is coupled into a waveguide at the correct angle it will be guided through the structure through total internal reflection (TIR). Section 2.6.1 will briefly present the theory of total internal reflection. In Section 2.6.2, I will show how the light will be guided in discrete modes in a 1D waveguide. Section 2.6.3 will briefly present an essential parameter for the evanescent field—the penetration depth—and finally a qualitative description of the mode behaviour in actual 2D waveguides is given.

2.6.1 Total Internal Reflection

When light is coupled into a waveguide it will be guided by a process called total internal reflection. When light is moving through a media of refractive index n_1 and hits the boundary of a second media of refractive index n_2 the light will then scatter of the boundary. Two things can occur from the interaction: 1) refraction of the beam, i.e. the beam passes into the new medium at a different angle, or 2) reflection of the beam back into the current medium. Often, both will happen. For total internal reflection, where all the light is internally reflected, the angle of incidence has to be below the critical angle. This can be expressed from Snell's law (see Section 2.2.2):

$$\theta_c = \arcsin\left(\frac{n_2}{n_1}\right) \tag{2.19}$$

An asymmetric waveguide will guide the light as long as the angle is below the critical angle of the lowest refractive index, as seen in Figure 2.10.

2.6.2 Guided Modes

Light will be guided inside a waveguide in discrete modes. This can be shown using a geometric optics approach[35]. Below, the modes and evanescent field of a 1D waveguide are derived from the wave equation. Light travelling through a non–magnetic, isotropic, linear dielectric medium the propagation will be described through Maxwell's equations:

$$\nabla \times \boldsymbol{E} = -\mu_0 \frac{\partial \boldsymbol{H}}{\partial t} \tag{2.20}$$

$$\nabla \times \boldsymbol{H} = \epsilon_0 n^2 \frac{\partial \boldsymbol{E}}{\partial t} \tag{2.21}$$

By insertion, the above equations can be written by only using E and H in each. By assuming that the refractive index only varies in one direction, the electric

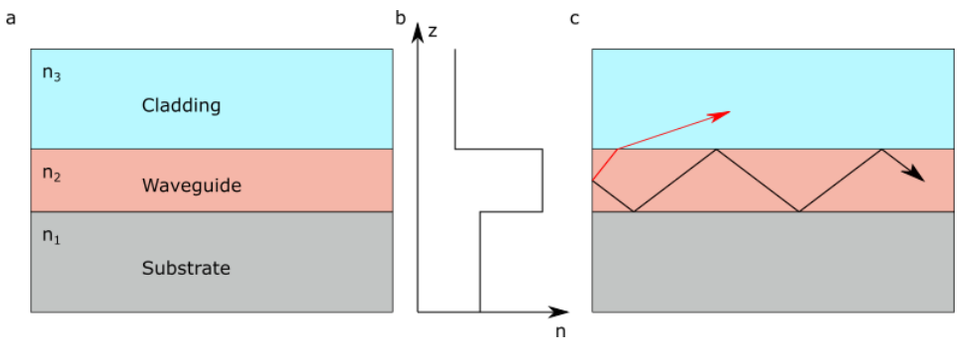

Figure 2.10: (a) A simple 1D asymmetric step–index waveguide. This is representative of e.g. an uncladded slab waveguide. (b) Refractive index profile of the waveguide in panel (a). (c) Illustration of total internal reflection. If the light has an angle below the critical angle, it will experience total internal reflection. For an asymmetric waveguide, the two different cladding materials will have different critical angles, which can lead to leaky modes.

and magnetic field take the following form:

$$E(\vec{r},t) = E(x)e^{i(\omega t-\beta z)} \tag{2.22}$$

$$H(\vec{r},t) = H(x)e^{i(\omega t-\beta z)} \tag{2.23}$$

where β is the propagation constant. If we assume that the electric field only has a perpendicular component to the incident plane, then the only electric and magnetic field components that are non–zero will then be E_y, H_x and H_z. Inserting Equation 2.23 into Maxwell's equations the following wave-equation is achieved:

$$\frac{\partial^2 E_y(x)}{\partial x^2} + [k_0^2 n^2(x) - \beta^2]E_y(x) = 0 \tag{2.24}$$

In order to solve the equation, the following boundary condition must be imposed: continuity of the tangential components of E and H at interfaces. A solution then for region j in the structure is given by:

$$E_j(x) = Ae^{i\gamma_j x} + Be^{-i\gamma_j x} \tag{2.25}$$

if we assume that

$$\gamma_j = \sqrt{k_0^2 n_j^2 - \beta^2} \tag{2.26}$$

We can then introduce the effective refractive index of a mode as $n_{\text{eff}} = \frac{\beta}{k_0}$. For guided modes the following requirement is applied:

$$k_0 n_s < \beta < k_0 n_f \tag{2.27}$$

The following expression for the electric field as a function of x is found by solving the wave equation:

$$E_y = \begin{cases} Ae^{-\gamma_c x} & x >= 0 \\ Be^{-i\kappa_f x} + Ce^{-i\kappa_f x} & -d < x < 0 \\ De^{\gamma_s x} & x =< -d \end{cases} \tag{2.28}$$

With the following relations:

$$\gamma_c^2 = \beta^2 - k_0^2 n_c^2 \tag{2.29}$$
$$\kappa_f^2 = k_0^2 n_f^2 - \beta^2 \tag{2.30}$$
$$\gamma_s^2 = \beta^2 - k_0^2 n_s^2 \tag{2.31}$$

By solving the transcendental equation the following expression for the electric field is:

$$E_y = \begin{cases} Ae^{-\gamma_c x} & x >= 0 \\ A(\cos \kappa_f x - \frac{\gamma_c}{\kappa_f} \sin \kappa_f x & -d < x < 0 \\ A(\cos \kappa_f x - \frac{\gamma_c}{\kappa_f} \sin \kappa_f x e^{\gamma_s (x+d)} & x =< -d \end{cases} \tag{2.32}$$

The three first transverse electric (TE) modes are shown in Figure 2.11a. The transverse magnetic (TM) modes can be derived by solving the wave equation for the transverse magnetic field. Once the magnetic field is know, the electric field can be determined using equation 2.21.

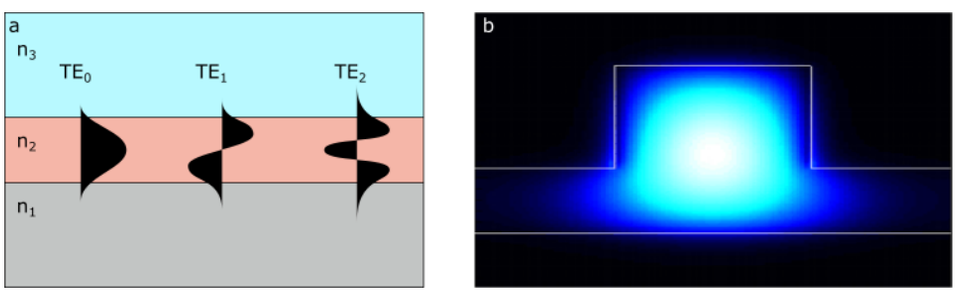

Figure 2.11: (a) An illustration of the mode intensity distribution for the first three TE modes in a slab waveguide. (b) A simulated mode distribution for a 2D waveguide structure.

2.6.3 Evanescent Field

The guided modes in the waveguide will have a component outside the waveguide core, called the evanescent field. This occurs because the light is trapped inside a finite energy well, resulting in a wave function with components outside the well. The light outside will experience exponential decay in the direction

normal to the waveguide surface. An important property of the evanescent field is the penetration depth, d, given by:

$$d_i = \frac{1}{\alpha_i} = \frac{1}{k_0\sqrt{n_f^2 - n_i^2}} \tag{2.33}$$

where n_f is the refractive index of the core and n_i the refractive index of the cladding. The penetration depth of the evanescent field is the depth at which the evanescent field strength has decayed to a value e^{-1} of the surface intensity. There are several other parameters that are of interest. The confinement factor gives the amount of the total power that is contained inside the waveguide structure.

2.6.4 Two–dimensional Waveguide Structures

All waveguides used in the work included in this thesis are 2D waveguides, such as strip and rib waveguides. The term 2D here refers to the fact that light is confined in two dimensions (the two directions perpendicular to the propagation direction). This introduces additional complexity in understanding the guided modes and the evanescent field. All the insights derived so far are from 1D waveguides. An exact analysis of modes in a 2D waveguide is not possible, and modes must thus be solved using approximations and numerical methods. There are today several commercial options, such as FIMMWAVE/FIMMPROP[1] that can simulate complex waveguide structures. An example of such a mode is shown in figure 2.11b.

1. Software from Photon Design

Part II

Increasing the Throughput of Chip–based *d*STORM

3

Waveguide Background and Its Effect on Imaging and Raman Spectroscopy

The main aim of this thesis is to investigate the opportunities arising from waveguide–based excitation. In particular, the focus will be on the use of waveguides for generating an evanescent field,as explained in Section 2.6.3, that can interact with samples in contact. It is therefore essential to start with an understanding of waveguide platforms and their use, before proceeding to applications.

All the work presented in this thesis was performed using either Ta_2O_5 or Si_3N_4 waveguides of different geometries. The choice of material depends on many factors, such as the components needed, propagation losses and fabrication infrastructure. Waveguide–based imaging, the topic of Chapter 4 and Chapter 6, requires visible light excitation, which can pose additional challenges with background fluorescence from the waveguide platform. The results presented in Chapter 5 on resonance Raman also employs visible light. A significant portion of the sensing applications that uses integrated photonics, however, tends to use longer wavelengths and thus there's a need for investigating how visible light works in the established platforms. In this chapter, I will present results on the background from Ta_2O_5 and Si_3N_4 when using visible light. The main reason for this work is to understand how it affects chip–based

imaging and spectroscopy, the main topics of the coming chapters, and the results presented here determined the platform selections for the rest of the thesis.

This chapter will start with a brief introduction to integrated photonics in Section 3.1. From there, I will explain how the evanescent field of waveguides has been used in several bio–sensing applications, highlighting the advantages of integrated photonic circuits versus free–space optics in Section 3.2. In Section 3.3.2, a brief overview of common platforms will be given and related to the platforms used in this thesis. I will follow this with a discussion on the waveguide background, including potential origins and effect on imaging and spectroscopy in Section 3.4. The last sections of this chapter will give an overview of the experimental set–up used, a summary of the findings and a discussion on the Si_3N_4 and Ta_2O_5 platforms.

3.1 A Brief History of Integrated Photonics

Integrated photonics is a sub–field of optics that is defined by a combination of waveguide technology with other disciplines such as electro–optics or non–linear optics. The field emerged in the 1960s as a consequence of several developments in related fields. The idea of integrated photonics is very similar to, and was highly influenced by, the rapid development in semiconductor physics and technology that lead to integrated electronics. Another integral part of the birth of integrated photonics was the advent of the first laser in 1960[36].

The development of integrated photonics was highly motivated by the telecommunications industry. Following the invention of the transistor, all processing and transmission of information was entirely based on electronics for several decades. Although it worked well with electronics based communications, the transmissions rates were very low. In the 1980s, the field gradually started moving into photonics, which enabled far faster communication. Modern long distance communications is entirely done through a vast arrays of optical fibres that are highly optimised to have extremely low losses. The field was further developed from optical fibres to integrated photonics, where waveguides and components were integrated onto a substrate, similar to integrated circuits in electronics. The result was the photonic integrated circuit, which can be used to guide and manipulate light on a thin wafer substrate.

Although the development of integrated photonics was spearheaded by the telecommunications field, a lot of new applications and interests arose from the developments. The following sections will discuss some of the novel applications

brought by the development of integrated photonics, and how they benefit from it. All the work in this thesis is based on using the intrinsic evanescent field of a waveguide to interact with the sample, similar to many other applications. Most of the focus will be on biology based applications, as it is most relevant for the work presented.

3.2 Waveguide Excitation

Optical waveguides will, due to quantum mechanical effects, have a portion of the guided light outside the geometrical structure. The electric field outside the waveguide structure is called the evanescent field and it is essential in many applications, from optical trapping[37], to sensing[38] and imaging[10]. The basics of the evanescent field was covered in Section 2.6.3. In the following section I will introduce waveguide–based excitation and discuss several of the advantages of using integrated photonics in general over free–space optics.

3.2.1 Excitation Through the Evanescent Field

In free–space optics, light–matter interactions often occur between a propagating laser beam and a sample. With evanescent field excitation it is the evanescent field that interacts with the sample, rather than the main propagating light. Evanescent field excitation is used extensively in microscopy and sensing, although the generation of the field varies. The contrast and quality of fluorescence imaging can be significantly improved by using TIRF, as explained in Section 2.4.4. The evanescent field used in TIRF microscopy is commonly generated either using a prism that the sample rests on, or with a specialised objective lens. A common spectroscopic application of evanescent field excitation is in attenuated total reflectance Fourier transform infra–red spectroscopy. In attenuated total reflectance Fourier transform infra–red spectroscopy, two major challenges of spectroscopy, namely sample preparation and spectral reproducibility, are solved by guiding light through a crystal and thus sampling only the part of the sample in contact with the crystal. The aim of this thesis, however, is to investigate how the evanescent field generated from waveguides—referred to as waveguide–based excitation—can be used for similar applications, and even be preferable over the other options. The evanescent field of guided light has seen many different applications. In general, two important types of applications of the evanescent fields in waveguides can be identified: 1) those where the evanescent field is used to interact with an external sample, and 2) those where the evanescent field is used for coupling purposes. Only the first category is of interest in this thesis.

For many waveguide applications, the evanescent field is purely an interesting fact, or perhaps even a nuisance. And for structures above a few hundred nanometers the evanescent field penetration depth becomes vanishingly small. There are, however, several fields today that make use of the evanescent field that the waveguides form. As the evanescent field can interact with anything in contact with the structure, it has been embraced in sensing applications. An example structure with three waveguides and an unclad region for the evanescent field interaction to occur is shown in Figure 3.1. The waveguide guides the light under a cladding, and the cladding is removed in the interaction area, which limits where the sample interaction occurs. Any light from the sample can then re–couple back into the waveguide and be measured for e.g. waveguide enhanced Raman scattering[39]. Alternatively, the refractive index change caused by the sample can be detected using e.g. a Mach–Zehnder interferometer. Today, a plethora of integrated photonics sensing devices have been developed using the evanescent field. Some include gas sensor[40] and Raman spectroscopy[41]. In novel applications, such as imaging, the evanescent field is simply used for excitation and not detection[10]. The following section will cover many reasons for using evanescent field excitation.

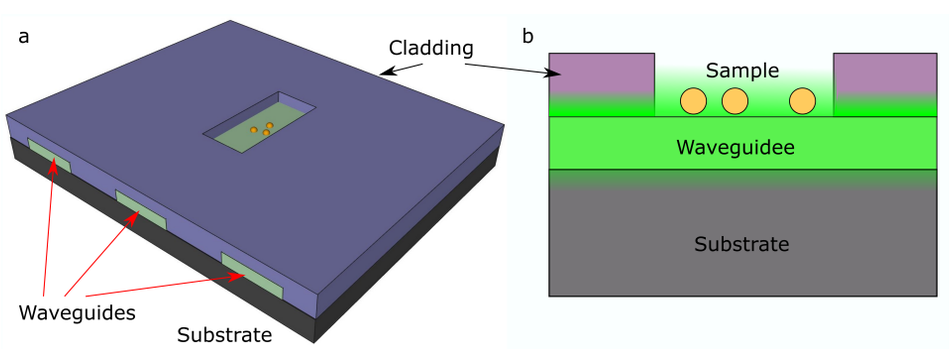

Figure 3.1: (a) Illustration of a PIC with three waveguides with a cladding. A portion of the cladding is removed so that the samples can come into contact with the evanescent field of the waveguide. (b) A cross section of the unclad portion of the waveguide, showing how the evanescent field can interacts with a sample.

3.2.2 Why Use Evanescent Field Excitation?

In the examples in the previous section waveguides guide the light and excite a sample through the evanescent field. There are several advantages with an integrated photonics platform compared to a free–space system. Some include:

→ **Integrated functions.** PICs brings both passive components, such as 1×2

MMI splitters and reflectors, and active components, such as lasers, onto a single substrate.

→ **Stable alignment.** All integrated components are immovable and thus highly stable. If the light source if off–chip, then coupling can lead to some uncertainty, but with a single–mode waveguide the result will only be an overall attenuation in intensity compared to a perfect coupling.

→ **High control of guided modes.** Tailoring modes can easily be done in waveguides, both due to the stable alignment and the power of the available components. Waveguides can be designed to have a given amount of modes, bends can filter modes etc.

→ **High optical power density.** For sensing and imaging applications, a very high power density can be achieved in the evanescent field with careful design of the structures. The evanescent field can be contained in a very narrow region by using achic waveguides, giving a high intensity. Other designs, such as the slot waveguide, can be used to increases the amount of light outside the structure drastically[42].

→ **Miniaturisation.** high refractive index contrast (HIC) waveguides can have very small bending radii and thus several components can be packed into very small areas. Not only can this save space, but it can also open up for new designs, such as a spiral waveguide for a drastically increased sensing area[43].

→ **Low cost.** Integrated photonics fabrications to a large extent is based on common complementary metal–oxide semiconductor (CMOS) fabrications techniques from the electronics industry, which through decades of optimisation has become very low prices.

While all of these properties are desirable for chip–based imaging, much of the advantage comes from how it changes the configuration of a nanoscope. In applications such as chip–based Raman spectroscopy, the photonic chip platform is used for both sample excitation and signal collection. In chip–based imaging, the photonic chip is only used for excitation. Collection is done through a traditional microscope. That means that the excitation and collection pathways are disconnected, unlike free–space microscopes where excitation and collection are both performed through the objective lens. This will be covered in depth in Chapter 4.

As described in Section 2.4.4, any out–of–focus light will deteriorate the resolution and contrast in imaging. A common solution is to use a TIRF objective lens, but this limits the throughput due to technical restraint in FOV. By sep-

arating the excitation and collection pathways using a photonic chip, a TIRF excitation can be performed over an arbitrarily large region, and any desired objective lens can be used for collection. The effect of this will be shown in Section 4.3.

3.3 Waveguide Platforms and Fabrication

There are today a plethora of available waveguide platforms, including silicon (Si), lithium niobate ($LiNbO_3$), tantala (Ta_2O_5) and silicon nitride (Si_3N_4). The work in this thesis uses tantala (Ta_2O_5) and silicon nitride (Si_3N_4), and the following sections will explain why.

3.3.1 Requirements from a Waveguide Platform

There are two different applications of waveguide–based excitation in this thesis, namely fluorescence imaging and Raman spectroscopy. Both applications require careful considerations with respect to choice of waveguide platform. A first condition for any real world clinical application is a compatibility to CMOS–fabrication techniques[39]. This will allow for cheap, mass–producible chips that can be one–time use. Secondly, high refractive index contrast (HIC) materials are preferable as they will increase the intensity in the evanescent field. HIC also allows for miniaturisation by reducing e.g. bend radii due to stronger trapping. Thirdly, the platform has to be transparent in the wavelength region of interest. For biosensing applications, the excitation light is often inside the therapeutic window of 750 – 930 nm, where there is negligible water absorption and minimal photo–damage[44]. Chip–based imaging, on the other hand, requires wavelengths below the therapeutic window, as fluorescent imaging is almost exclusively performed in the visible range 400-700 nm. For applications such as Raman spectroscopy, the amount of scattering increases drastically at shorter wavelengths, which means visible light can be of great interest. There are also many other requirements that vary with applications. When deciding on waveguide platforms for the work in this thesis, the main requirements were:

- High refractive index material.
- Low propagation losses.
- Transparent in the visible range.
- Low background, especially in the visible range.

- Live cell compatibility.
- CMOS fabrication compatibility.
- Relatively mature platform.

The following section will give a brief overview of common integrated photonics platforms and relate it to the requirements.

3.3.2 Common Platforms

Today, there exists a multitude of different platforms that are commonly used in integrated photonics. One of the first platforms that received attention, and that remains very popular today, is the lithium niobate ($LiNbO_3$) platform. Several other platforms that were developed with telecommunication in mind including silica on silicon (SiO_2/Si), indium phosphide (InP), gallium arsenide (GaAs) and silicon (Si). Of these platforms, Si has proven itself very useful for mid–infra–red (IR) sensing applications[45–47]. For waveguide enhanced Raman spectroscopy, it has not been of great interest, as it is opaque below 1.1 μm . Raman spectroscopy can be performed with any wavelength, but since it's such a weak effect it's often of interest to use the shortest possible wavelength, which usually is in the near–IR range.

A popular platform commonly used for Raman applications is Si_3N_4. With a refractive index of 2.0 it can allow for bend radii down to 40 μm and it is transparent over the range 0.4-5 μm [44]. Strip waveguides from Si_3N_4 have been fabricated with extremely low losses[48], and many other geometries have also been realised as well[49–52]. Additionally, a wide range of components have been fabricated with the platform, such as resonators[53]. Si_3N_4 is today a mature platform that has been adopted in many fields, such as waveguide–based Raman spectroscopy[39], super–continuum generation[54] and micro fluidic optical systems[55].

Another related platform is the TriPleX platform. In contrast to the previous platform, TriPleX is a Si_3N_4 box that has SiO_2 both inside and outside. Thus minimising losses, but maintaining the advantages of Si_3N_4. The platform has been used e.g. for optical trapping and Raman spectroscopy[56] and fluorescence biosensing[57]. Many important components have been realised in the Triplex platform, such as Mach–Zehnder interferometers and ring resonators[49]. The platform is a commercial platform from Lionix[1].

1. http://www.lionixbv.nl/wp-content/uploads/2011/09/LionixTriplex%20flyer.pdf

A third, interesting platform is Ta_2O_5. Ta_2O_5 has a high refractive index of 2.1, with low losses[58] and is transparent in the visible light range. Several different components have been fabricated with Ta_2O_5, such as ring resonators and grating couplers[38]. The platform has been used e.g. for Raman spectroscopy[59] and optical trapping[60, 61].

The work in this thesis is purely based on the Si_3N_4 and Ta_2O_5 platforms. Both platforms have a high refractive index, low propagation losses, are live cell compatible, are compatible with CMOS fabrication and are relatively mature platforms. The last requirement was a low background in the visible range. The background of the two materials has been studied in the near-IR and both have a weak background below[62, 63]. Using excitation wavelengths within the visible range can, however, significantly increase any fluorescent background. In this chapter, I will present results on how both of these platforms perform in the visible range, as it forms the basis of the following work. Perhaps the most important parameter is the background from the platform. The particular aim of this chapter is to investigate the background of the two platforms.

3.4 Waveguide Background

As discussed in Section 3.3.1, there are many different requirements to consider for a waveguide application. One that is of particular interest in this thesis, is background. Both Si_3N_4 and Ta_2O_5 are common platforms, but the visible light applications are limited. Therefore, it is important to study how the background changes when moving into shorter wavelengths.

3.4.1 Effect of a Background

For both imaging and spectroscopic applications, the two major themes of this thesis, a background can be detrimental. In this section, I will evaluate the effect of it on spectroscopy and imaging applications.

Raman Spectroscopy

Raman spectroscopy relies on analysis of spontaneous Raman scattering, a very weak process. Raman scattering scales approximately as λ^{-4}, thus using a short wavelength for excitation will maximise the signal. Too short wavelengths can be problematic, as they can induce fluorescence in a sample and thus increase the background drastically. Using too long wavelengths on the other hand can lead to water absorption. Thus, it is common to use near–IR wavelengths. Even

at the optimal wavelength, a background might still be present. Several different approaches have attempted to reduce the background and can be grouped into three different categories: 1) instrumental modifications, 2) experimental changes or 3) computational subtraction. Instrumental approaches include wavelength shifts and time–gated Raman spectroscopy[64]. An alternative version can be to increase the signal strength rather than decrease the background. This has been done through e.g. tip enhanced spectroscopy[65] and surface enhanced Raman spectroscopy[52, 66]. Experimental approaches can be e.g. in the sample preparation. Finally, it can often be possible to subtract the background using suitable algorithms[67].

The background challenges above are the same for waveguide–based Raman spectroscopy as for traditional Raman spectroscopy. An additional challenge with waveguide Raman is the added background from the waveguide platform. As light is guided in the waveguide, any background will also be guided and scattered out. Thus any measured signal will also contain any background from the waveguide platform.

Nanoscopy

SMLM is based of precisely localising single fluorophores. The reason this is possible is due to the fact that the emission profile of a single fluorophore is know, and thus by assuming that the measured emission is from a single fluorophore a peak fitting procedure can be performed and thus a precise localisation is found. Any background will reduce the signal–to–background ratio (SBR) and thus reduce the localisation precision, as described in Section 2.5.2. The resolution of SMLM can be described by Equation 2.18, which shows that the relationship clearly. Thus, to achieve the highest possible resolution the waveguide should not add any background.

The waveguides used in the thesis are all multi–mode and will therefore exhibit an inhomogeneous excitation pattern, which means that any background generated will have a distinct inhomogeneous pattern. An inhomogeneous background can lead to artefacts in single molecule localisation microscopy reconstruction algorithms and blinks will tend to be biased towards high intensity background areas. Figure 3.2 shows how a single fluorophore can be fitted with a Gaussian curve for a low background, high background and inhomogeneous background. It is clear that a higher background reduces the precision as predicted from Equation 2.18. For the fluorophore with an inhomogeneous background, here a linear gradient, the precision goes down, but it is also shifted towards the high intensity region. Localisation along in the orthogonal direction will be unaffected here. An important aim in the work included in this thesis was to investigate whether the waveguides used will have such an

effect on the localisation.

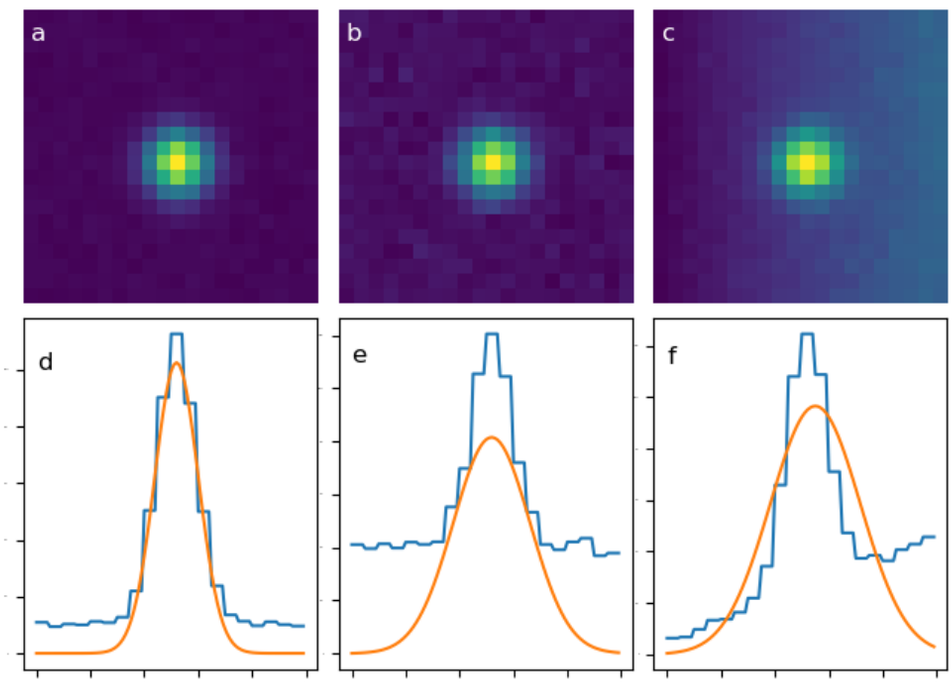

Figure 3.2: Simulated fluorophore with a low background intensity (a), high background intensity (b) and a inhomogeneous/gradient background (c). (d-f) Show the fitted curve (orange line) and the raw data (blue line) for a line passing through the centre of the fluorophore.

3.4.2 Origin of a Background

A background from a waveguide platforms can have many origins, including:

- A fundamental background due to random thermal refractive index fluctuations in the waveguide core[68].
- A Raman signal from the waveguide core or surrounding materials.[62].
- A fluorescence signal from the waveguide core or surrounding materials.
- A Raman or fluorescence signal from contaminants from the fabrications process.

Determining if the background is from a fluorescence signal or Raman signal

can be done by using different wavelengths, as a fluorescence signal will change with excitation wavelength, whereas the Raman shifts are unchanged. Determining whether a signal is from the material or from contaminants in the processing can be assessed by comparison with other fabrication methods for the platforms.

3.5 Results

All the work presented in this chapter is found in Paper I.

Summary of Paper I

The aim of the work was to evaluate the two waveguide platforms Si_3N_4 and Ta_2O_5 for visible light applications. Understanding the background from the two platforms is essential for both chip–based imaging and resonance Raman spectroscopy. Two different Si_3N_4 platforms were tested, one fabricated at Institute of Microelectronics Barcelona (referred to as Si_3N_4-B) and the other fabricated by SINTEF (referred to as Si_3N_4-S). The findings can be split into two parts: 1) how the background changes with wavelength and 2) how this affect *d*STORM imaging.

To investigate the strength of the background with varying excitation wavelengths a non–destructive method was used. Sparse samples of fluorescent beads were excited with the evanescent field and imaged from the top. The resulting images are presented in Figure 3.3 From the images, the signal and background could be calculated by localising all the beads with a local thresholding algorithm (Phansalkar) in ImageJ[2]. The maximum value of the beads was used to reduce uncertainty in the threshold values. In order to adjust for differences in guided power the background measurements were adjusted to a matching signal strength from the beads. The dark current from the camera was subtracted during this procedure. The results are presented in Table 3.1. The images of the beads are presented in Figure 3.3. For 640 nm excitation there was no big difference between Si_3N_4 and Ta_2O_5, but for shorter wavelengths the difference increased. We investigated Si_3N_4 from two different fabrications facilities and found the same trend in both, however there was a difference in background intensity.

The next step was to determine the spectral characteristics of the background. In Figure 3.4a, the Raman background measured for Ta_2O_5 at 532 nm excitation

2. Image processing software.

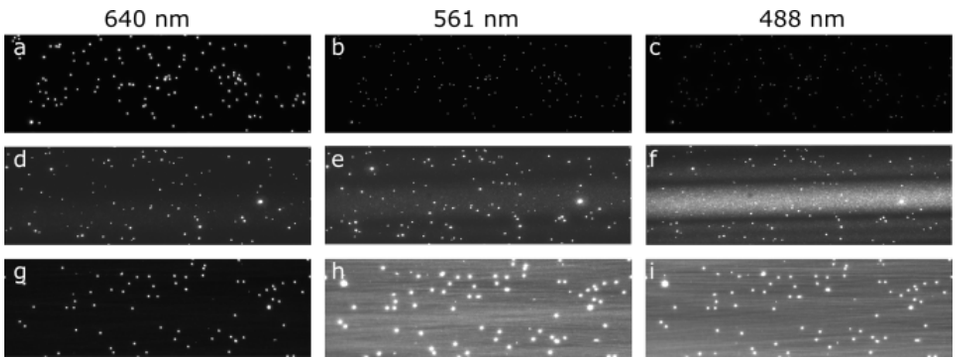

Figure 3.3: Images of fluorescent beads on the different waveguides. All three platforms are imaged, with (a-c) being Ta_2O_5, (d-f) Si_3N_4-S and (g-h) Si_3N_4-B. All images are adjusted to have the same contrast.

Table 3.1: Results from beads measurements. The background measurements were all adjusted to the average beads intensity, $\overline{S}$, of Ta_2O_5. All measurements are given in counts from the camera.

λ (nm)	$\overline{S}$	Ta_2O_5 BG[a]	Si_3N_4-S BG[a]	Si_3N_4-B BG[a]
640	5132	100[b]	102	107
561	1478	100[b]	107	127
488	2711	100[b]	150	202

[a] background
[b] Average dark current value for the camera

is presented. This measurement is not presented in Paper I, but rather in Paper IV, thus a more detailed analysis of this spectrum can be found in Chapter 5. This is a narrow background, and weak as it is not detectable in the imaging. The fluorescence background measured for Si_3N_4 at different wavelengths are presented in Figure 3.4b. It's worth noting that the spectrum for Ta_2O_5 is presented as a function of wavenumber, whereas for Si_3N_4 is presented as a function of wavelength as it spans over such a broad range. The approximate wavelength range for the plotted Raman background with a 532 nm excitation wavelength is 532-614 nm, although the background is very low above approximately 560 nm. The results are presented with arbitrary units for counts, as they were captured with different systems and the absolute counts won't compare well. The two most important findings here are that the Ta_2O_5 background is a Raman signal, as it agrees with previous literature[63, 69], whereas the Si_3N_4 background is fluorescence based as it is very wide and changes with excitation wavelength.

The next experiments investigated how the increased background affected *d*STORM. This was done by imaging monolayers of fluorophores and looking

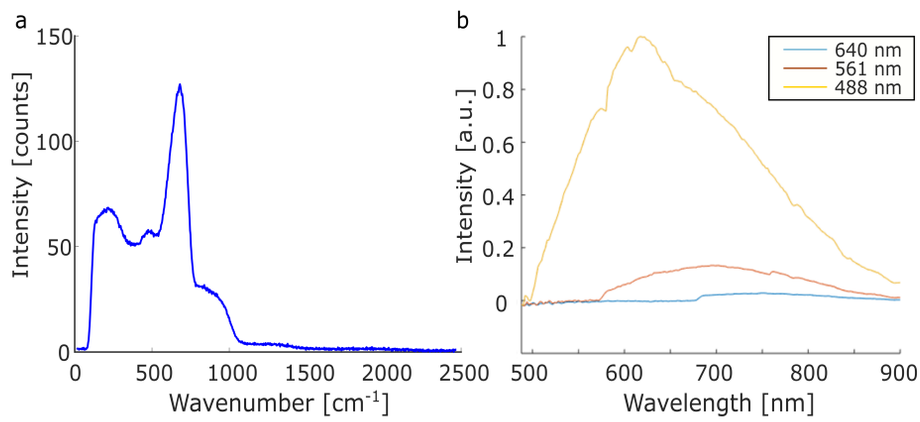

Figure 3.4: (a) background from Ta_2O_5 excited with a 532 nm laser. Note that the spectrum is plotted as a function of wavenumber. (b) background from Si_3N_4-B excited with a 640 nm, 561 nm and 488 nm laser. All the spectra have been normalised to the maximum value of the 488 nm spectrum.

at the localisation statistics for 640 nm and 488 nm excitation, both commonly used for *d*STORM imaging. The increased background in Si_3N_4 at shorter wavelengths is problematic for imaging, as it deteriorates the localisation precision and thus the resolution, as discussed in Section 3.4.1. The effect of the most important parameters is presented in Figure 3.5. It is clear that the background is challenging for 488 nm imaging. Imaging at e.g. 640 nm can sometime require addition of shorter wavelengths to aid blinking, but adding a 488 nm laser at 10% power of the 640 did not alter the result.

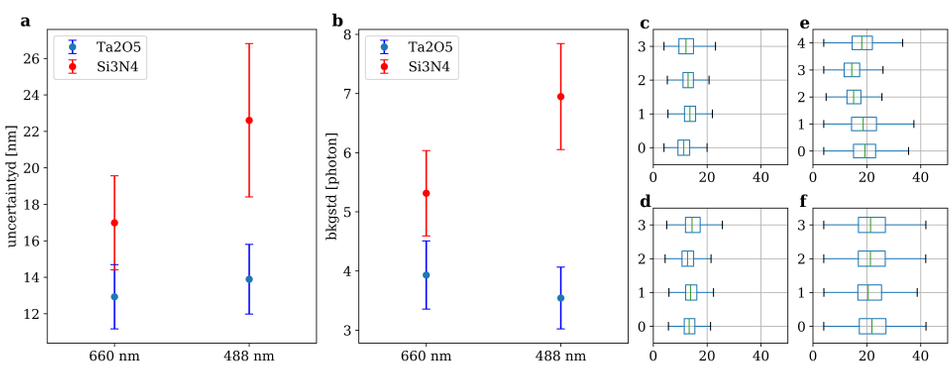

Figure 3.5: (a) Average uncertainty from all localisations for Ta_2O_5 and Si_3N_4 at 640 nm and 488 nm. (b) Background standard deviation for the same combinations. (c-f) Box plot of the localisaiton uncertainty for all individual experiments for Ta_2O_5 at 640 nm (c) and 488 nm (d), as well as Si_3N_4 at 640 nm (e) and 488 nm (f).

It is also worth noting that the multi mode patterns can induce some localisa-

tion bias, as they exhibit a clear directionality. An example of this is presented in Figure 3.2. This effect is not large for Si_3N_4, and for Ta_2O_5 it's non-present since the background is so weak. These results were based on pseudo experiments where blinks were simulated onto experimentally measured excitation patterns.

3.6 Discussion and Conclusion

From the presented results, it is clear that the Si_3N_4 platforms used in this work have a challenge with an increasing background for shorter wavelengths. The background has been investigated thoroughly before, but mostly at near–IR wavelengths[62, 63, 70], which found a weak background on the level of Ta_2O_5. Due to technical constraints, the platforms investigated in this work could not be tested with 785 nm for this work. Si_3N_4 is a mature platform today and can offer a wide selection of structures, as well as high quality waveguides. Much of the imaging in this thesis is therefore done using Si_3N_4. This works very well, as the best performing *d*STORM fluorescent labels have optimal excitation in the 640–660 nm range. For multi–colour imaging, Ta_2O_5 will perform better as it has very little background throughout the visible range. Si_3N_4 is also a well established platform for waveguide–based Raman spectroscopy[71], but for e.g. resonance Raman of haemoglobin, which will be presented in Chapter 5, Ta_2O_5 will be preferable due to the shorter wavelength.

We have demonstrated that the background from Si_3N_4 is fluorescence, as it is both very broad and changes with excitation wavelength. However, we have not investigated the origin further. There is a difference in the two Si_3N_4 platforms tested, as seen in Table 3.1, and thus an unknown potential for improvement by optimising the fabrication from visible light applications. This is an important limitation of the work presented. The fact that the two fabrications processes yield a different background could suggest that at least parts of the background comes from contaminants and fabrications residue, rather than from the Si_3N_4. In future works, both platforms should be investigated at 785 nm excitation to compare with the work of e.g. Raza et al.[63]. Also, the comparison between all platforms is done using a non–destructive approach with fluorescent beads. The variation in waveguide geometry is a source of uncertainty in the measurements, as it can change parameters such as the evanescent wave penetration depth. The beads used are only 100 nm and will thus most likely fall within the penetration depth of the evanescent field and should thus reduce the uncertainty. This, combined with the fact that the fluorophores are located on the surface and as such most of it will be significantly closer than the maximum distance of 100 nm, mitigates the uncertainty.

The *d*STORM measurements performed can also have a significant uncertainty to it. This can come from many different sources, such as variations in the blinking buffer used, as well as variations in monolayer quality and reconstruction parameters. The two different fluorescent dyes used at 640 nm and 488 nm makes a direct comparison between the wavelengths impossible, as the two different dyes have differences in e.g. quantum yield. However if the background did not change with wavelength, the ratio between the two platforms should have remained the same for the two wavelengths. On the other hand; the reconstruction algorithm underestimates any difference, as it performs a filtering in the localisation process through the detection threshold. It is thus fair assume that the actual effect of the increased background for Si_3N_4 at 488 nm excitation on *d*STORM imaging is underestimated in this work, and the effect can be much larger. As a final note, all the imaging here was performed on monolayers. Imaging through e.g. a cell can lead to multiple scattering of the signal through the cell which will magnify the effect of the background.

The work presented in this chapter is an initial investigation into the Si_3N_4 and Ta_2O_5 platforms for visible light excitation. It is clear that the Si_3N_4 platforms used is not well suited for 488 nm *d*STORM imaging. The fact that there's a significant difference between the two fabrication methods, however, shows that the extrinsic factors have a part in the background. There is a need for further studies to determine the exact origins of the background in order to completely evaluate Si_3N_4 as a candidate for low wavelength applications. There are also other interesting platforms that are being explored. One particularly interesting is TiO_2. Evans et al. have developed this platform for waveguide enhanced Raman spectroscopy and shown very promising results[72–74].

For the work in this thesis the findings presented in this chapter suggests that Si_3N_4 can be used for 640 nm excitation without any problem, whereas for shorter wavelength applications Ta_2O_5 should be chosen. Si_3N_4 does have a lower demonstrated propagation loss than Ta_2O_5 and could be preferable at longer wavelengths. Based on the findings presented above, Si_3N_4 is used in *d*STORM work in this thesis and Ta_2O_5 for waveguide–based resonance Raman spectroscopy.

4

Waveguide–based *d*STORM

Fluorescence microscopy is today a staple technique of biological and medical research laboratories all around the world. It solves the problem of cells being almost transparent under white light while also providing functional information through specific labelling. The last decades have seen the resolution of fluorescence microscopes pushed beyond the diffraction limit with different approaches. One such implementation that's of particular interest for this thesis is *direct* stochastic optical reconstruction microscopy (*d*STORM). In the previous chapter, I presented how waveguide–based excitation has been used in different applications, and in particular why it's interesting for nanoscopy. In this chapter, I will show results that demonstrate how a chip–based nanoscope can drastically increase the throughput of *d*STORM. Despite the advantages of chip–based TIRF imaging, it does impose an important restriction over e.g. a TIRF objective lens: the imaging is restricted to the waveguide surface and thus essentially a 2D imaging technique. A modified system that uses quantitative phase imaging for morphological imaging is presented in the latter part of the chapter as one solution to the 2D nature of TIRF imaging.

The chapter starts with a general introduction to chip–based imaging and its development, although several of the fundamental principles will be found in chapters 2 and 3. In Section 4.1.2, I will introduce waveguide–based *d*STORM, focusing on the set–up and experimental considerations. Section 4.2 will introduce quantitative phase imaging and how it can be combined with the chip–based nanoscope to give morphological information about the sample.

4.1 Waveguide–based Microscopy

With the introduction of TIRF microscopy for improved contrast and resolution, there has been an increasing interest in alternative ways to generate TIRF. Evanescent wave excitation has been used in spectroscopy for a long time in e.g. attenuated total reflection infra–red spectroscopy[75], where light is guided inside a crystal and the evanescent field generated interacts with the sample on top. A common way today to use TIRF in microscopy is through TIRF objective lenses. An alternative way that offers several advantages over TIRF objective lenses is waveguide–based excitation, as explained in Section 3.2. By designing waveguides correctly, a high intensity evanescent field can be achieved close to the waveguide surface. Chip–based nanoscopy uses the evanescent field to excite thin sections of the sample for *d*STORM imaging over large areas. The following section will present a brief summary of the early developments of chip–based imaging and then go into details of how it works.

4.1.1 Introduction to Chip–based Imaging

TIRF microscopy is highly sensitive due to the use of the evanescent field, as it effectively removes out–of–focus light. However, imaging through a TIRF lens gives a small FOV, due to technical limitations. Over the last decade, the use of waveguides for fluorescence excitation has been of explored. Some advantages of using waveguide–based excitation are high surface specificity, large area illumination and simultaneous guiding of several wavelengths. It can also be used to combine imaging and sensing. The key concept is that laser light is guided in a waveguide with the sample attached to it, creating an evanescent field that excites a a sample labelled with suitable fluorophores (see Figure 3.1 for a schematic). The emitted fluorescence from the sample can then be captured with a microscope and imaged. The penetration depth of the field is determined by the relationship between the refractive indices of the sample, substrate and waveguide materials, as described in Section 2.6.3. Grandin et al. first introduced a waveguide–based excitation fluorescence microscope for sensing and imaging bio–interfaces[76]. A flow–through cell was placed on top of a waveguide and laser light was coupled in through a grating. Imaging was done using a microscope objective and detector perpendicular to the waveguide. However, the set–up experienced line artefacts during imaging, attributed by the authors to coupling problems in the grating. A very similar set–up was later used by Hassanzadeh et al. to experimentally verify the exponentially decaying evanescent field by measuring the fluorescence using different thickness spacers between fluorophores and the waveguide surface. Using the same set–up, osteoblasts were imaged to prove the biological applicability, clearly showing the pin points[77]. The same group later used multi–mode waveguides to measure cell–substratum distances by using the

differential decay on different TM modes with distance[78]. The high surface specificity from waveguide–based excitation is highly beneficial for studying e.g. the contact areas between a cell and the substrate. On the other hand, for a micron sized cell most of the cell can't be probed using such a set–up. In 2002 Horvath et al. introduced the reverse waveguides, where the where the substrate has a lower refractive index than the refractive index of the medium covering the surface[79], allowing for tailoring of the extent of the evanescent field, from around 200 nm to infinity[80]. Multi–depth screening using different modes in a reverse waveguide was demonstrated by the same group, however they did not perform imaging[81]. In 2009 Agnarsson et al. introduced symmetric planar waveguides for fluorescent imaging, where the refractive index of the substrate was matched to the cover medium[82]. This geometry has several advantages: highly effective end–fire excitation makes coupling easier, a large range of possible polymer waveguide materials, and the possibility to tune the penetration depth. This gives better imaging quality and is compatible with optical fibres for e.g. coupling. Later, a Mach–Zehnder interferometer was introduced into the chip to enable on–chip modulation of the excitation light by controlled heating of the non–sensing arm[83]. In 2014 Ramachandran et al. introduced a set–up using LEDs for illumination and a simple glass slide as waveguide. By using an inverted microscope system, they performed simultaneous waveguide–based excitation fluorescence microscopy and atomic force microscopy[84].

Several of the groups managed to perform chip–based diffraction–limited imaging, however the results experienced different artefacts and challenges. This all changed in 2016 with the use of HIC waveguides that were used to image liver sinusoidal endothelial cells[85]. In 2017, the first realisation of chip–based *d*STORM was presented[10]. *d*STORM requires a high intensity to achieve proper blinking and the Si_3N_4 waveguide platform could provide this. The next step is to really take advantage of the platform, as well as explore other imaging modalities using a waveguide platform.

4.1.2 Waveguide–based *d*STORM

A common TIRF microscope has three important parts: 1) the excitation pathway, 2) the sample holder and 3) the collection pathway. In a traditional free–space system the sample is held by a microscope slide and the sample excitation and collection are both done through the same objective lens. The excitation and collection pathways are thus the same. In the chip–based microscope, the sample is held by a photonic chip rather than a microscope slide. The photonic chip doubles as both the sample holder and part of the excitation pathway, as illustrated in Figure 4.1a. Waveguides on the photonic chip guide the excitation light under the sample and the intrinsic evanescent field will

then provide TIRF excitation to the sample. Collection is done through an objective lens with a simple microscope. The excitation and collection arms of the system has thus been separated.

The chip–based platform has many advantages, as outline in Section 3.2.2. It is, however, the separation of the excitation and collections arms that is essential for many of the advantages with chip–based imaging. When the evanescent field excitation is done through a TIRF lens, the imaging FOV will be limited due to the high magnification of the lens. For waveguide–based excitation, the evanescent field is present all over the waveguide structure. With a low loss platform such as Ta_2O_5 or Si_3N_4, the waveguide can be made centimetres long and millimetres wide. Thus, by separating the excitation and collection the throughput can be drastically increased, since the excitation can be made arbitrarily large through the waveguide, allowing collection with any objective lens. The system can be used for any TIRF applications. SMLM, however, requires a very high intensity for proper blinking. By using HIC materials with a structures a height of 100-250 nm a sufficiently high intensity for *d*STORM can be achieved (1-10 kW/cm^2)[10].

Set–up

As mentioned above, a typical *d*STORM microscope consists of the excitation and collection pathways, as well as the sample holder. The collection pathway in a chip–based nanoscope is the same as in any free–space microscope. It consists, in its simplest form, of an objective lens, followed by suitable fluorescence filters, a tube lens and a camera. The sample holder and excitation pathway are significantly changed.

The sample holder is changed from a glass slide to a photonic chip. The photonic chip is then part of the excitation pathway, as it is used to deliver the light to the sample. No special measures are needed during sample preparation on a photonic chip compared to a glass slide, however the facets of the waveguides can be fragile and some additional care must be taken. For sample preparation, the sample is simply placed directly onto the photonic chip. In order to restrict the sample region, a frame of polydimethylsiloxane (PDMS) is attached to the surface to define the sample and imaging region. The sample will then be restricted to inside the frame. All sample preparation, such as fluorescent labelling, is done inside the PDMS frame. When the sample is ready, the imaging buffer is added and a cover glass used to seal it off. The whole chip can then be mounted in the microscope for imaging. The chips are multi use and can be cleaned with a 10 minute soak in a 5% Hellmanex[1] in deionised

1. Cleaning solution

water solution at 70°C.

The excitation pathway is similar to a free–space system, although it has some significant changes. The most important aim is to couple laser light into the waveguide. Once light is inside the waveguide, the sample will be excited correctly. There are several ways to couple the light in. All the work in this thesis is done using end–fire coupling, where a lens, called the coupling lens, is used to focus a collimated laser beam onto the end facet of the waveguide. A portion of the laser light will then be coupled into the waveguide, depending on the modal overlap between the free–space and the guided modes. The light can be brought to the coupling objective in different ways, including through the use of free–space optics or with an optical fibre. The waveguide chip will then both hold the sample and excite it, as shown in Figure 4.1a. The photonic chip is held in place using a vacuum chuck, which is mounted on a 3–axis piezo stage. Optimal coupling requires a high mode overlap between the focused spot and the waveguide, which is achieved by adjusting the objective and the chips position to maximise coupling. To control the imaging process, either the excitation pathway and sample can be translated relative to the collection pathway, or the other way around. A simple schematic of a chip–based nanoscope is presented in Figure 4.1b. The work in this thesis will have several variations in the set–ups.

Mode Averaging

For large FOV imaging, the waveguide imaging area must be wide. Ideally, the waveguides should start as single mode and then adiabiatically taper out to the desired width to give homogeneous excitation. The fabrication processes used for the waveguides in the thesis did not allow for such specifications. Additionally, waveguides as wide as 500 μm were used, which would require an unpractical long adiabatic taper to maintain the single mode condition. The waveguide designs used throughout the thesis are all multi–mode waveguides and will thus have distinct excitation patterns due to multi–mode interference. An example of a multi–mode interference pattern is presented in Figures 4.2a and b, where panel b shows the effect with cells on top of the waveguide. In order to remove this effect, several images with different patterns can be averaged. Several approaches can be used to average out the effect of the patterns in order to achieve homogeneous intensity in the final image. Most of the thesis work was done using a piezo stage, as shown in Figure 4.1. A piezo controller was used to loop the coupling objective along the coupling facet of the waveguide while imaging. Over the course of the imaging procedure, enough patterns will be imaged to average out the effect. For diffraction–limited imaging, which usually is one–shot, the averaging does add time as it requires a couple of hundred images to give a homogeneous average image.

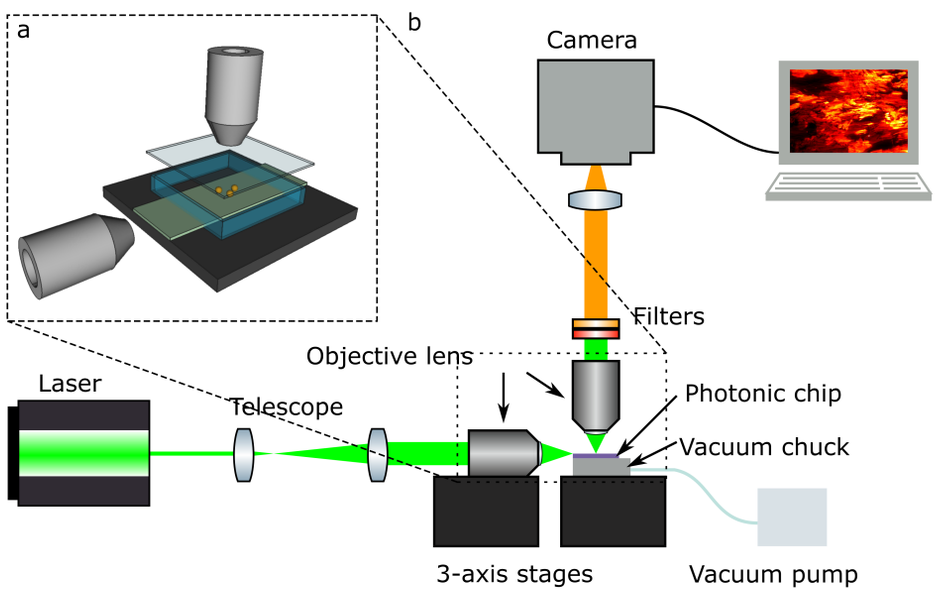

Figure 4.1: (a) An illustration of how a photonic chip is used for imaging. A PDMS frame is used to define the imaging region on a strip waveguide with some beads inside. The imaging area is sealed with a cover slip. An objective lens is used to couple the laser light into the waveguide, and another objective lens is used to image from the top. (b) A schematic of a chip–based nanoscope. The laser light is coupled into the waveguide with a coupling lens. The lens is mounted on a 3-axis piezo stage for easy coupling optimisation. The waveguide chip is mounted with a vacuum chuck. Imaging is done by a simple upright microscope.

For *d*STORM, where thousands of images are needed, it makes no difference. No synchronisation between the camera shutter and the piezo stage is needed. The piezo stage scanning can be tuned with step length, wait time, step velocity, and the start and stop positions.

Another way to average the patterns is to use a spatial light modulator (SLM) in the beam prior to the coupling objective. The laser beam shape and position in the objective back aperture can be altered by changing the SLM, which will change the coupling position into the waveguide. By scanning the SLM, mode averaging can be performed. The SLM has the advantage of being able to reproduce coupling patterns due to little uncertainty. Piezo stages will often exhibit hysteresis, which will limit the reproducible of the steps. We tested the reproducibility of patterns with an SLM by repeating five different patterns over several minutes. The mean square error between the initial pattern and all following patterns is presented in Figure 4.2c.

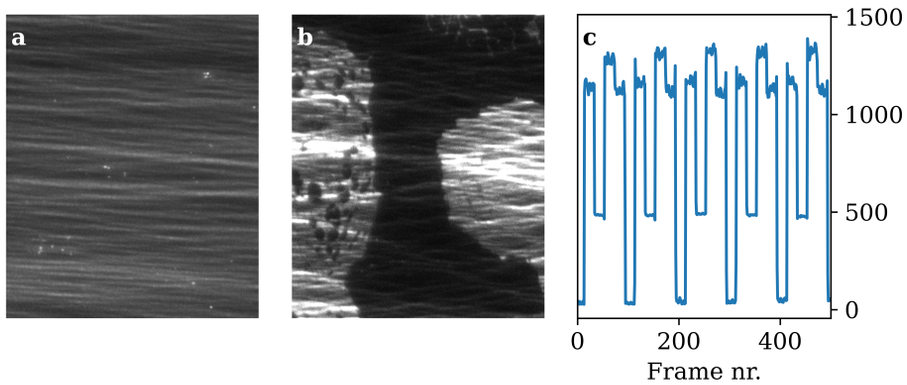

Figure 4.2: (a) An example of a multi–mode interference pattern imaged from above. The sample is simply a monolayer of fluorophores. The pattern will change with changes in the coupling. (b) An example of a multi–mode interference pattern with cells with a labelled plasma membrane on top. Most of the fluorophores have attached to the cells, and as such they appear brighter. (c) The mean square error between a set of different mode patterns in a waveguide that are precisely looped using a spatial light modulator.

4.2 Quantitative Phase Imaging

Chip–based imaging offers many advantages compared to using e.g. a TIRF objective. One significant drawback with chip–based imaging is that only parts of the sample that are in contact with the waveguide will be excited, and unlike a TIRF objective lens, the waveguide can't be moved. As such, it will only image up to a few hundred nanometres thickness of the sample, essentially reducing it to a 2D technique. However, if combined with a QPI system, nanometric sensitivity in the axial dimension can be achieved over large ranges. Parts of the results presented in this chapter is such a combined system. As such, the following sections will present the fundamental theory of QPI

4.2.1 Fundamental Principle

Phase microscopy was briefly presented in Section 2.4.3 as a way to image samples where bright–field microscopy struggles. Common phase microscopy techniques, such as DIC, provides qualitative phase images. The contrast generated is based on phase difference, but it is not quantifiable. Quantitative phase imaging measures the actual phase changes caused by the sample. It can thus be used to measure the morphology of a sample.

In QPI, the excitation beam is split into two. One path interacts with the sample,

which will then change the phase of the beam, according to the sample. The other path is simply the reference beam, which is unchanged from the excitation light. The two beams are then combined. The result will be an interferogram based on the interference between the two beams, which is then imaged (an example interferogram is shown in Figure 4.5). The intensity distribution of the interferogram can be written as:

$$I(x,y) = a(x,y) + b(x,y)\cos 2\pi i(f_x x + f_y y) + \phi(x,y) \tag{4.1}$$

where $a(x,y)$ and $b(x,y)$ represent the background and the modulation term, respectively. $f_x x$ and $f_y y$ are the spatial frequencies of the pattern along the x and y directions. $\phi(x,y)$ is the phase difference between the reference and object beams. Equation 4.1 can be rewritten using complex conjugates:

$$I(x,y) = a(x,y) + c(x,y)e^{[2\pi i(f_x x + f_y y)]} + c^*(x,y)e^{[-2\pi i(f_x x + f_y y)]} \tag{4.2}$$

where $c(x,y) = b(x,y)\exp i\phi(x,y)$. The sample data can be extracted by taking the Fourier transform of the sample and filtering so that only the first order is kept. The phase data is then retrieved by calculating the inverse Fourier transform of the first order and gives:

$$\phi = \arctan\left(\frac{Im\{I_{\text{filtered}}\}}{Re\{I_{\text{filtered}}\}}\right) \tag{4.3}$$

The phase difference will depend on the optical path difference in the following equation:

$$\phi(x,y) = \frac{2\pi}{\lambda} * 2h(x,y) * [n_s(x,y) - n_0(x,y)] \tag{4.4}$$

Using this, a phase map of a sample can be generated. If the refractive index profile of the sample is known, or can be estimated, a height map of the sample can be generated by solving Equation 4.4 for the height.

4.2.2 Instrumentation

QPI can be implemented in many different ways, but in this work it has to be combined with a the chip–based nanoscope. The QPI was done using a Linnik type interferometer, which is similar to a Michelson interferometer. In a Michelson interferometer, the beam is split with a beamsplitter into a sample arm and a reference arm. The reference beam is then simply reflected off a mirror at a fixed distance, whereas the beam in the sample arm is modulated by the sample. For imaging purposes, an objective lens is used in the sample arm and the sample placed in the focal plane of the objective, which will then modulate the sample. The difference in the Linnik type interferometer is that imaging optics are included in the reference arm as well, rather than just a

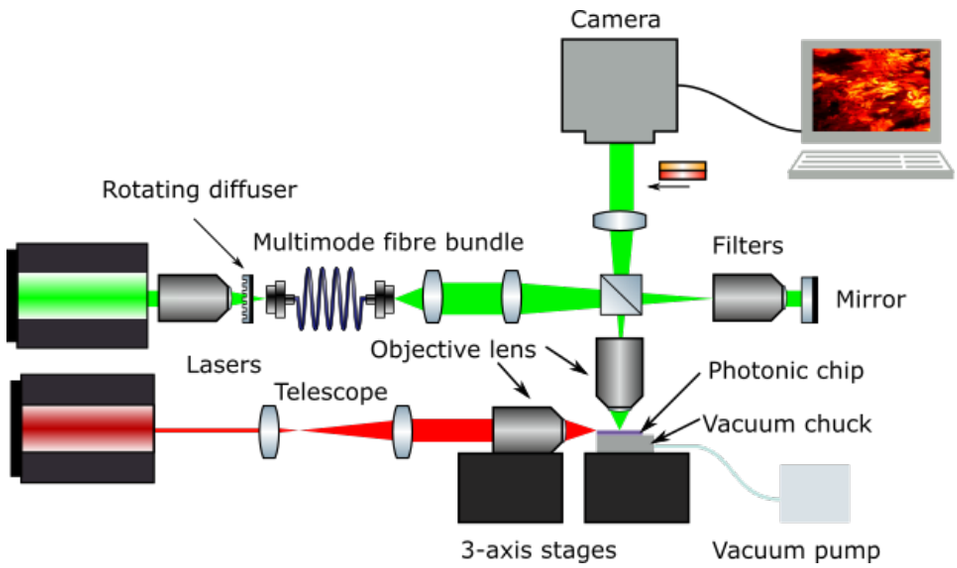

Figure 4.3: A schematic of the combined QPI and chip–based nanoscopy system. The QPI is simply integrated as a modular component and the only modification needed to the nanoscope is a beamsplitter in the infinity space.

reflector. The inclusion of imaging optics in the reference arm reduces the optical aberrations.

The interferometer was easily integrated with the chip–based nanoscope. A beamsplitter was added into the infinity space of the imaging optics of the nanoscope. As light is collimated here, it does not have any significant effect on the imaging properties. There will, however, be a loss through the beamsplitter which will reduce the maximum obtainable resolution for the *d*STORM imaging, as the localisation precision depends on the number of collected photon, as shown in Equation 2.18. The entire interferometer was built on a mechanical support from the beamsplitter and is thus does not affect the nanoscope in any way. A schematic of the modified, chip–based imaging system is presented in Figure 4.3.

4.3 Results

The work performed in this chapter covers several topics. I will start by presenting some general findings from the work, leading into a summary of all the included papers. The manuscripts included in this chapter are Paper II, Paper III, Paper IV and Paper V.

4.3.1 Imaged Cells

Chip–based imaging is ideal for e.g. membrane studies, as it offers excellent optical sectioning at the intersection between the cells and the waveguide surface. Much of the work done in this thesis is performed on liver sinusoidal endothelial cells (LSECs), as they have an interesting plasma membrane morphology. LSECs have small pores, called fenestrations, in the plasma membrane that are localised together in regions called sieve plates[86]. The pores are only 50-300 nm and thus mostly not visible with diffraction–limited techniques. An example of a *d*STORM image clearly showing the fenestrations can be found in Figure 4.4a. The cell was labelled with CellMask Deep Red, a plasma membrane label that works well with *d*STORM.

It is also possible to image other types of cells. In Figure 4.4b, cardiomyocytes were imaged using a microtubulin label. An image of the plasma membrane of an HTR-8 cell is presented in panel c. The cell has several clearly visible filopodia

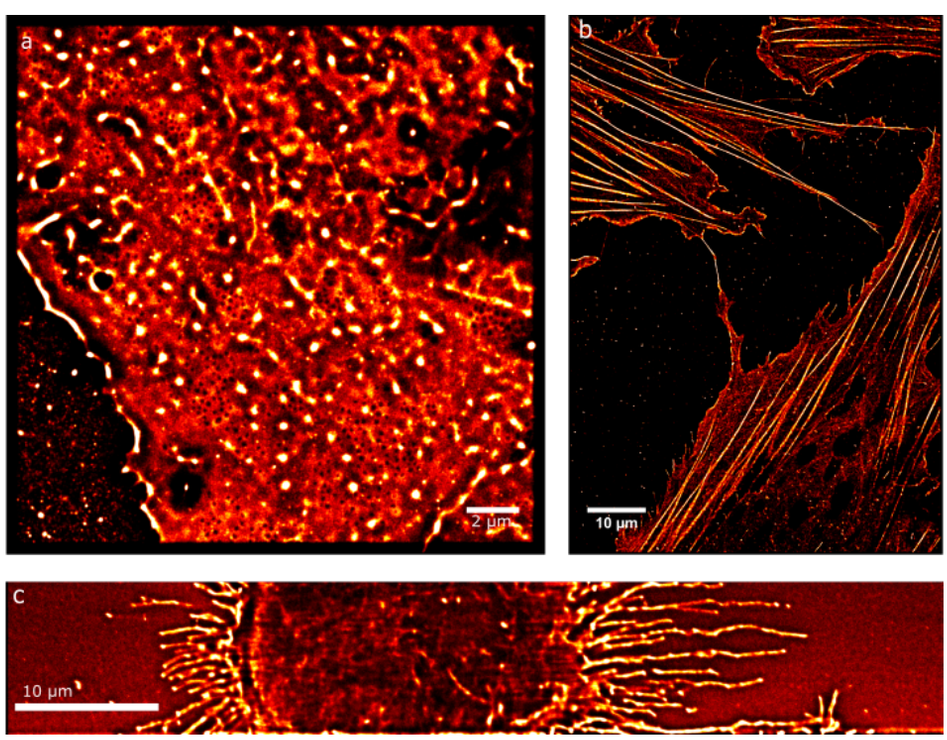

Figure 4.4: (a) Image of the plasma membrane of LSECs. The cells have nanosized holes in the membrane, called fenestrations, that are only visible with super–resolution optical microscopy. (b) Microtubulin labelled cariomyocytes. (c) Plasma membrane labelled HTR-8 cells with many filopodia.

4.3.2 Calibrations of the System

Chip–based *d*STORM can achieve a very high resolution, with a demonstrated resolution below 50 nm[10]. The combined *d*STORM and QPI system will has a lower resolution due to the beamsplitter in the system. Characterisation of the resolution with Fourier ring correlation (FRC) resulted in a resolution of 61 nm for the combined system, as seen in Figure 4.5c. The phase sensitivity was calculated by imaging a mirror, giving ±20 mrad.

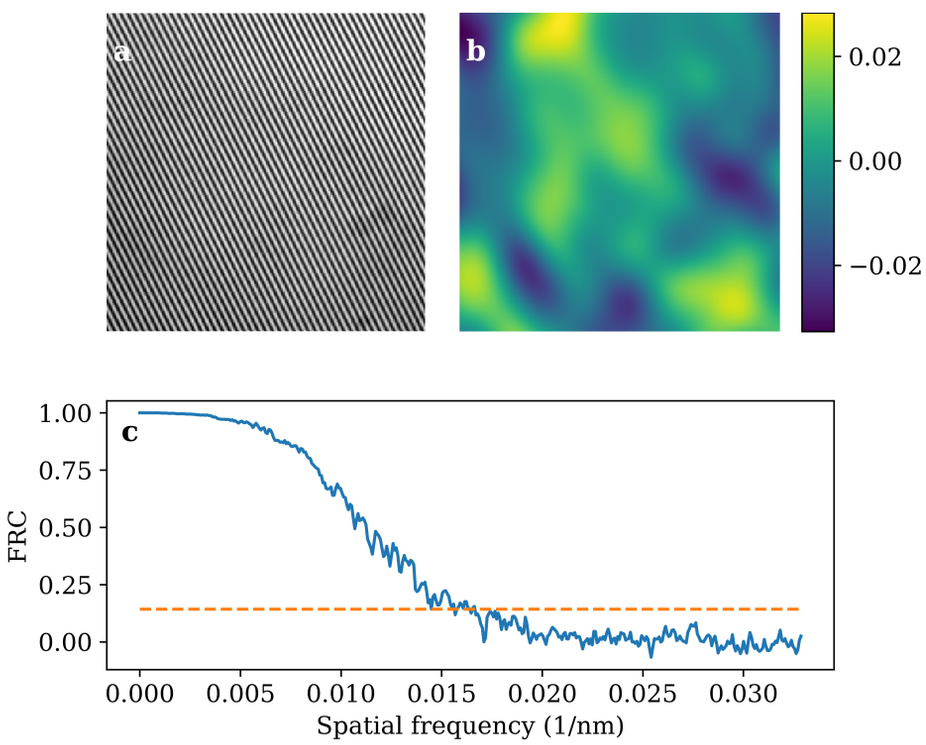

Figure 4.5: (a) Example image of an interferogram. (b) Phase map of a mirror used to calibrate the sensitivity of the system. (c) FRC results from the *d*STORM imaging.

The achievable resolution of the system will depend on the collection objective used. Separating the collection and excitation pathways gives the user the freedom to select any collection objective, which can be used to image an extremely large field of view, as presented in Paper II and Paper III. Lower magnifications lenses, however, tend to have a lower NA, which means that the resolution will be lowered as a consequence. Despite its FOV, the image presented in **??** still has a resolution of 75 nm.

4.3.3 Effect of *d*STORM on Sample

*d*STORM requires high intensity light when imaging, which can potentially be disruptive to biological specimen. In order to evaluate the effect of a chip–based *d*STORM measurement on the fixed LSECs, a phase image was acquired before and after *d*STORM imaging. To quantify the difference before and after the structural similarity index[87] was calculated to be 0.91, which indicates a high similarity. The correlation between the before and after images was calculated and is presented in Figure 4.6c. Additionally, the difference image of the before and after phase images was calculated and is shown in Figure 4.6d. Based on the difference image, it seems that the small change before and after can be attributed mostly to sample drift. This can be deduced by the fact that many of the image structures are visible in the difference image, but with a bright and dark border, which indicates a slight offset when subtracting.

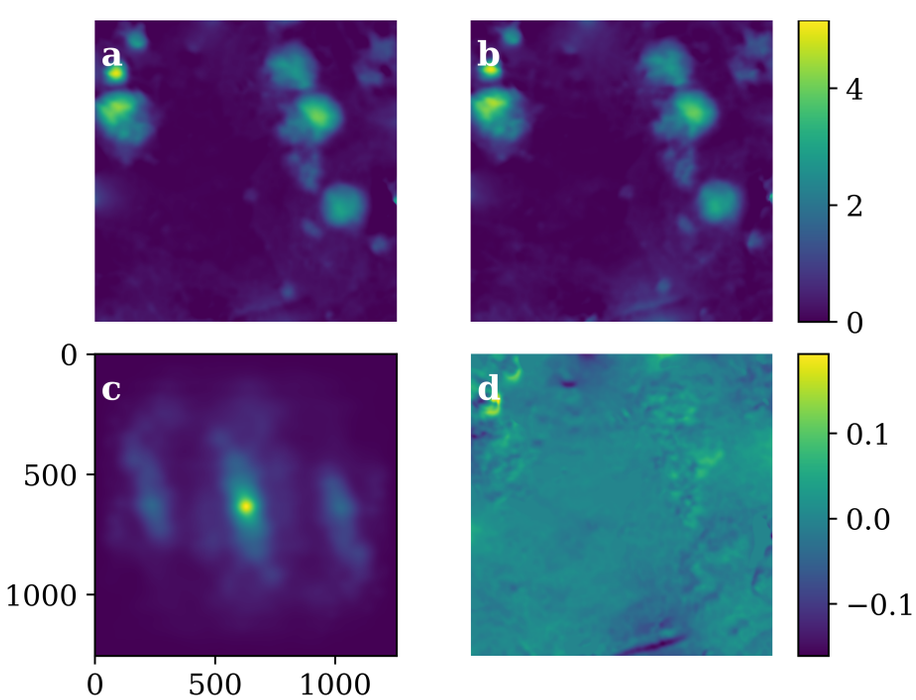

Figure 4.6: (a) Phase image of cells before *d*STORM imaging. (b) Phase image of cells before *d*STORM imaging. (c) Cross–correlation of the two images in panels (a) and (b). (d) Difference image between the two images in panels (a) and (b). The colourbar shows the phase in radians.

4.3.4 Summary of Papers

The manuscripts attached in this chapter focus primarily on expanding the capabilities of chip–based *d*STORM. This is partly done by increasing the

throughput with unprecedentedly large FOV imaging. Paper II presents large FOV diffraction–limited TIRF imaging of LSECs. By decoupling the collection and excitation pathways, an arbitrarily large area of the sample can be excited, as the excitation is only determined by the waveguide geometry. The large FOV was made possible by using a high NA, low magnification objective lens (25x/0.85 NA). An objective lens with these specifications has a large depth–of–field and is not readily available for TIRF imaging. This is where the inherent evanescent field of the waveguide platform enables large FOV high resolution TIRF imaging, as demonstrated in the paper.

In Paper III, the large FOV imaging was extended to include *d*STORM. The same system was used, and with the thin, high refractive index waveguides a high enough intensity for *d*STORM was obtainable. We imaged a 500 μm × 500 μm region with microtubulin labelled LSECs at a resolution of 75 nm, as seen in **??**. Paper IV is a video article that focuses on the technical aspects of chip–based imaging. The main motivation behind the publication was to disseminate the technique to the broader scientific community.

Finally, a combined system with QPI and chip–based nanoscopy is presented in Paper V. A chip–based nanoscope was modified to include a Linnik type interferometer for quantitative phase imaging. With the combined system, both spatial super–resolution images can be captured, together with nanometric sensitivity in the axial direction. We measured both the size and thickness of fenestrations in LSECs using the simple system. The resulting measurements gave a fenestration diameter of 124 ± 41 nm and sieve plate thickness of 91.2 ± 43.5, which agrees well with previous literature[86]. Images of the cells and the phase measurements are presented in Figure 4.8.

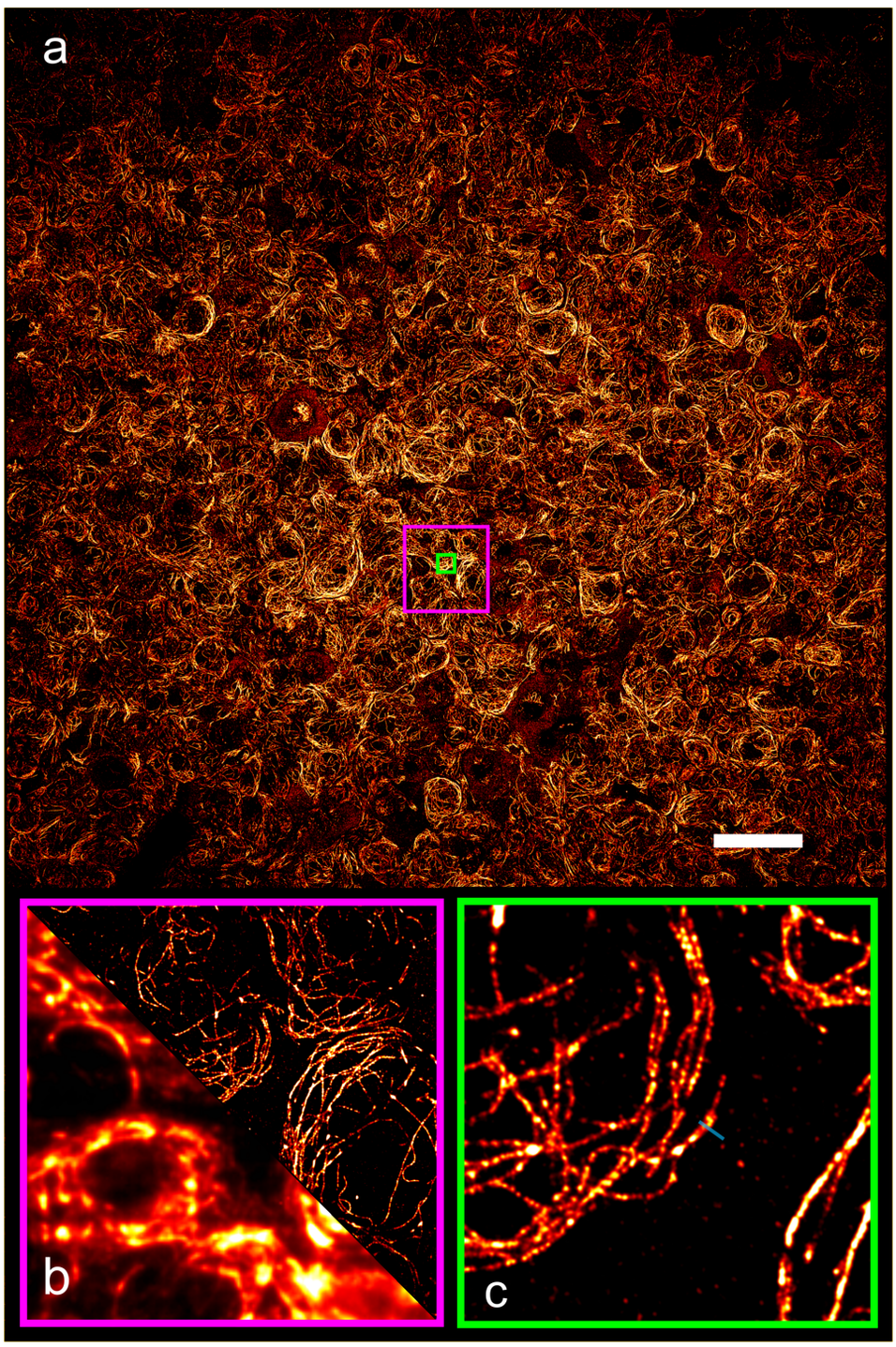

Figure 4.7: (a) A 500 μm × 500 μm FOV image of microtubulin labelled LSECs. (b) Inset from panel (a) showing a typical FOV with 60x objective lens, with both super–resolution and diffraction–limited. (c) Inset used to determine the resolution.

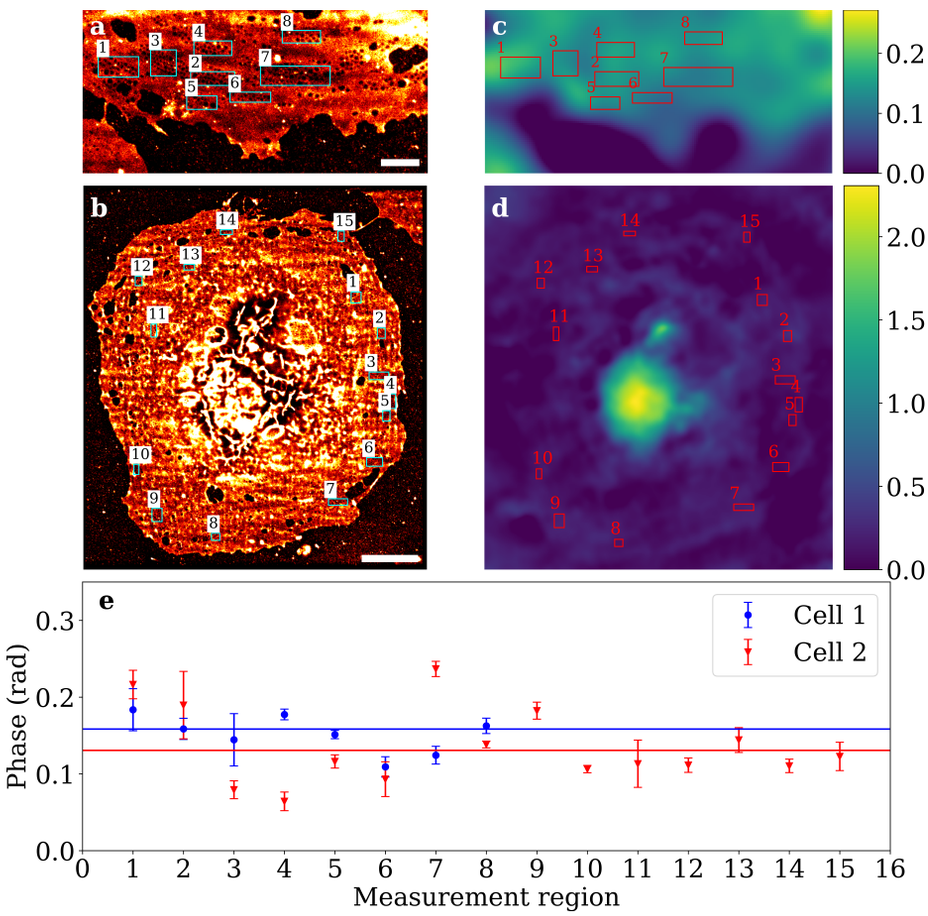

Figure 4.8: (a-b) *d*STORM images of two different LSECs, with several sieve plates marked. (c-d) QPI of the same regions. (e) Measured phase values for all marked regions in both cells, together with the average value and standard deviation for both cells.

4.4 Discussion and Conclusion

As outlined in Section 3.2.2, using a photonic chip platform can have a lot of advantages. However, as with all microscopy techniques, there's no single technique that can solve all problems. Here, I will try to clarify the areas where chip–based can have a great advantages, and also where the limitations lie.

One of the defining features of chip–based imaging compared to free–space imaging is that the sample holder is an integral part of the imaging system in the chip–based microscope. The photonic chip serves a dual purpose as both

the sample holder and delivering the excitation light. The collection pathway is the same as many common microscopes found around the world. Photonic chips can thus be used to retrofit common microscopes to TIRF microscopes at a very low price. When mass produced, photonic chips can be made affordable single use items.

Perhaps the most significant difference between a traditional nanoscope and a chip–based nanoscope is that the free–space system often has a shared excitation and collection pathway, whereas in a chip–based system the two are separated. This opens up several opportunities, which is perhaps most clear in TIRF imaging. A lot of nanoscopy applications today are based on TIRF excitation, which is commonly performed using a TIRF objective lens. Due to technical challenges, these objectives have a very limited FOV, which restricts the throughput. In chip–based nanoscopy, the separation of the excitation and collection pathways means that any objective lens can be used for imaging. In the presented results, this is used to image extremely large areas.

The waveguide–based excitation is perhaps the most significant advantage of chip–based nanoscopy, but it is also an important limitation. The excitation light will be restricted to the evanescent field, which means that it is more or less a 2D imaging technique. In particular, the imaging is restricted to the section of the sample that is in contact with the waveguide surface. Applications such as volumetric scanning of samples would thus not be possible with a typical chip–based nanoscope. Membrane studies, on the other hand, are perfectly suited for the system. As with all microscopes, the applications will determine whether chip–based is correct or not. The combination of QPI and nanoscopy presented in this chapter, however, is an attempt at circumventing the limitation. The instrumentation does not require any changes to the *d*STORM set–up, besides a beamsplitter in the optical path. The interferometer is thus seamlessly implemented with the current system. The same data could be achieved by sequentially imaging with a chip–based nanoscope and then a QPI microscope through use of image registration algorithms. It would, however, be challenging as the major advantage of the photonic chip platform is the extremely large imaging area. Going forward, the integrated system is essential for live cell studies where .e.g TIRF and QPI can be combined. One such applications could be studying LSECs treated by chemicals, as that can change the fenestrations[88]. The current combined version uses a beamsplitter in the optical path, which reduces the collected photons for *d*STORM and will thus reduce the resolution. Changing the beamsplitter with a flip mirror would be advantageous, if a higher resolution is needed. The current QPI version has a sensitivity of ±20 mrad, but it would be possible to improved it further by using white light illumination. A common advantage with chip–based solution is the compactness it can provide. The system is not particularily compact as presented here, but the excitation pathway can be

made very compact[89].

Although the systems presented in this thesis use exclusively evanescent field excitation, it is possible to launch the excitation light out of the waveguide and open up for 3D imaging. Several ways could be used. One possibility is using axicons or similar structures to launch the light out of the end facet[90]. By launching a light sheet out of the edge, one could e.g. make a flow cytometer with a microfluidic device to flow the sample passed the edge. Another approach could be to launch the light using diffraction grating and scan it in 3D[91].

All the systems presented in this thesis are upright microscopes, meaning that all imaging is done through the sample. This can be problematic for thick samples, as the samples can distort the image through multiple scattering. This can be seen in Figure 4.8, as the membrane under the nucleus can't be localised. A simple solution to this is to use an inverted microscope and image through the chip. The Si wafers used here are not transparent in the visible range, though, so this is not possible. It is, however, possible to use a transparent substrate and image through the chip[92].

A challenge with the use of the microscope, as shown in Paper IV, is that it can be complicated to use for untrained personnel. It does not require much training to learn how to use the system, but of course time is often scarce. There are several ways to improve the usability, such as automatic coupling[89], butt coupling (with glue), etc. It is thus possible to make it a lot more used friendly, but that was not a priority in this work as all users were trained personal.

In this work the system only contains a single camera and thus making simultaneous phase and fluorescence imaging challenging, but a system could easily be made with two separate, small inexpensive cameras[93]. This could also be a benefit for multi–colour imaging. Waveguides can guide several wavelengths simultaneously, so simultaneous multi–colour imaging can be implemented with dichroic beamsplitters.

Chip–based excitation offers many desirable properties for both diffraction–limited and super–resolution optical microscopy. In this chapter, I have demonstrated how simple waveguide structures can be used to expand the throughput of *d*STORM by increasing the FOV drastically. The platform is versatile and can be used to image several different samples. In addition, a combined system that uses phase imaging to circumvent a limitation with chip–based imaging—it's 2D nature—was presented and used to measure both the size and thickness of LSEC fenestrations.

Part III

Investigating Other Modalities That Can Benefit From Waveguide–based Excitation

/5

Waveguide–based Resonance Raman

The results presented so far in this thesis have shown how waveguide–based excitation can be used to increase the throughput of *d*STORM. The following two chapters will focus on other applications that also can benefit from waveguide–based excitation. In this chapter, I will present results on resonance Raman spectroscopy, whereas the next chapter will go back to imaging. The aim of the work was to use the chip–based platform with a near–common–path interferometer for wide–field Raman imaging[94]. Widefield Raman imaging requires very high intensities, and the plan was to use waveguide–based excitation together with resonance Raman effects as a possible solution. The first step was to demonstrate chip–based resonance Raman spectroscopy, which is presented in this chapter.

The Raman effect was first described in the 19th century, yet general applications of Raman spectroscopy remain limited to this day. The major challenge for Raman spectroscopy is the extremely low scattering cross–section. The cross–section for Raman scattering is around 15 orders of magnitude less than that of fluorescence. Because of this limited signal strength, a long time passed between its discovery and the first specialised applications that came in the 1980s with the emergence of high quality lasers. Since then, a significant effort has been put into enhancing the Raman scattering from a sample. One way to make Raman scattering more viable is to improve the instrumentation.

Advances in detectors, lasers and filters has helped with detecting more of the Raman scattering. Despite the advances, Raman spectroscopy has found few general applications and is mostly limited to specialised uses. The second option is to increase the Raman scattering. A novel direction that aims to improve signal strength in different ways is waveguide–based Raman spectroscopy. In this chapter, I will present work on waveguide–based resonance Raman spectroscopy.

5.1 Waveguide–based Raman Spectroscopy

There have been a lot of techniques developed in order to increase the signal strength from Raman spectroscopy, including surface enhanced Raman scattering (SERS)[95], tip–enhanced Raman spectroscopy[96] and stimulated Raman scattering[97]. A particularly interesting enhancement technique for this thesis is using waveguides to enhance the signal. This can be done in several ways. The following section will introduce the concept, and briefly present previous work on the topic.

5.1.1 Waveguide–enhanced Raman Spectroscopy

Waveguide–based Raman spectroscopy has seen several different implementations. The simplest is perhaps what is termed waveguide enhanced Raman spectroscopy (WERS), where the intrinsic properties of the waveguide leads to an enhancement. An important aspect of the waveguide is that it can increase the electric field intensity through the Purcell effect[98]. Thus, any sample in contact with the waveguide can be exposed to a high intensity evanescent field, in the same way described in the previous chapters. The evanescent field can then cause Raman scattering from the sample, which can be detected for Raman spectroscopy.

The emission from a sample on a waveguide under a cover glass can follow two paths:

1. Re–couple into the waveguide.

2. Free space emission.

Two different approaches can be used to detect the resulting spectrum from the sample. The light that is re–coupled into the waveguide can be detected at the edge of the waveguide, which is commonly termed end– or edge–detection. Alternatively, the light emitted to free–space can be detected with an objective

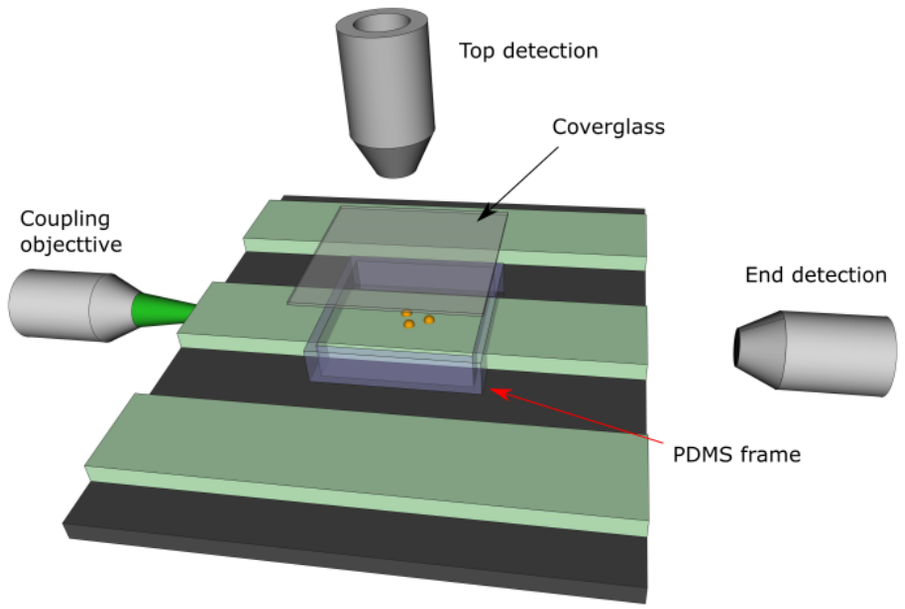

Figure 5.1: Illustration of top– and edge–detection for Raman spectroscopy.

lens from above, in the same way as for chip–based nanoscopy, which is commonly termed surface– or top–detection. The two different collection schemes can be seen in Figure 5.1. In a realistic system, any scattered light can of course take other paths such as guiding in the cover glass etc, which will lead to less signal detected from the top or side.

Using a waveguide platform can offer two enhancement factors:

→ **Radiative enhancement factor.** The power coupled back into the fundamental mode of the waveguide can exceed the free–space emission with the right geometries due to Purcell enhancement[59, 71]. Raman scattering can be described as dipole radiation, and as such it can be enhanced by ways of dipole radiation enhancement. Purcell discovered that dipole radiation is not a purely intrinsic effect for the dipoles, but depends on the local environment. For waveguides, the local environment at the waveguide surface gives a large enhancement in the local field. Basically, the large refractive index difference enhanced the electric field close to the waveguide surface.

→ **Area enhancement factor.** In confocal microscopy, the Raman signal is collected from a diffraction–limited spot, whereas for waveguides, the emission is collected for all of the waveguide surface that is covered with

sample material. Thus, arbitrarily large sensing areas can be designed simply by increasing the length and/or width of the waveguide structure. HIC waveguide are particularly interesting as they can allow for very long waveguides on small footprints due to a tighter confinement. The increase area is particularly relevant for thin samples, such as monolayers, as only a small portion of the focal volume of a confocal system would not interact with the sample, unlike the evanescent field.

Raman spectroscopy with edge–detection is usually referred to as WERS[41], due to these enhancement factors. As top–detection only measures the freely propagating light, and not the re–coupled Raman signal, it will not benefit from the area enhancement. WERS is commonly used to explain waveguide systems where excitation and collection are both done through the waveguide. I will use an expanded definition where WERS will refer to waveguide–based excitation through the evanescent field, independent of whether it's edge–detection or top–detection. Part of the enhancement comes solely by using a waveguide for excitation and will thus be independent of detection scheme.

Raman scattering can be modelled as a classical dipole emission problem in a layered medium for waveguides. The emission is not purely intrinsic to the dipole, it also depends on waveguide geometries and material properties. Dhakal et al. showed that the absorption of the pump light by a dipole on a slab waveguide varied significantly with slab waveguide thickness, with a much higher absorption for TM mode excitation compared to TE mode excitation[99]. It was also calculated that the higher the effective index contrast, the higher the emission and absorption efficiency. A similar analysis has been performed on strip waveguides[100, 101], calculating the overall efficiency of Raman emission by η, defined as the coupled signal power over the pump power. In this work, the authors concluded that the TE mode is the most efficient for a strip waveguide, reaching a maximum at approximately $w = 250$ nm and $h = 300$ nm. However, for widths over 450 nm, the TM mode was more efficient. In fact, for wider strip waveguide the Raman signal using the TM mode was shown to be several times higher than from the TE mode[102]. In later work, the group estimated a 6 fold increase in efficiency by using a slot waveguide ($s = 150$ nm) compared to strip, due to a significant field enhancement close to the waveguide surface due to the slot[103]. Wang et. al performed a rigorous theoretical analysis of waveguide–based excitation with a Ta_2O_5 platform, and compared it to traditional Raman spectroscopy and also estimated an enhancement of more than three order of magnitude that compared to free–space[104]. These estimates are, however, all made with edge–detection in mind. Later work by the same group compared surface–detection to edge–detection, showing a 40–fold increase when collecting from the edge– compared to the top[59], due to the far larger interaction area.

End–detection

The first experimental demonstration of WERS was done by coupling a 90 mW 785 nm laser into a looped waveguide[105]. The waveguide used was strip waveguide of Si_3N_4 (500 nm x 220 nm) on SiO_2 on a Si substrate. Iso–propanol was excited and the emission evanescently coupled back into the waveguide and analysed using a spectrometer. The back–propagating light was collected through the coupling lens. By using a loop structure, the authors achieve a long interaction length in a small area. Later iterations collected the forward propagating light[71]. Comparing to confocal Raman microscopes, Dhakal et. al state a 300 times higher experimental signal for waveguide Raman for slot waveguides, but hypothesised that up to 2000 times higher is theoretically achievable. For strip waveguides the numbers are 50 and 500, respectively[106].

All collected spectra contained a strong Si peak, as well as a broad fluorescent background from the substrate of the waveguide, but the background could be filtered away. Further investigations of the background revealed that the broad peak around 2100–2400 cm^{-1} is due to Si_3N_4 and that a broad luminescence below 1200 cm^{-1} is likely due to fluorescence from the SiO_2[100]. Evans et. al have demonstrate a WERS implementation using a TiO_2 platform with visible light that achieved over 50 times the signal enhancement of Si_3N_4[74].

Top–detection

An alternative collection scheme is to use top–detection with an objective lens or fibre. Wang et. al used on Ta_2O_5 strip waveguides for chip–based Raman spectroscopy. The authors have presented top–detection Raman using 110 nm thick Ta_2O_5 slab waveguide on silica with a 637 nm laser[104]. Coupling was done using prism coupling. A signal increase of more than 1000 was observed for the 1002 cm^{-1} line of toluene, compared to confocal Raman. Wang et al. have also compared edge–detection and top–detection and found that edge–detection offers approximately 40 times stronger signal[59].

Propagating Field

A third alternative is to use a propagating field. Boerkamp et. al used the TriPleX platform to perform trapping and Raman spectroscopy of polystyrene beads in a waveguide loops with 5 μm gaps for trapping[56]. The waveguides were 1.1 μm wide at the base and 1.0 μm high. The Raman signal was collected from the top using a 0.8 NA objective lens (water immersion). A 785 nm laser is used to excite the TE fundamental mode by fibre coupling. A microfluidic channel had

a flow of polystyrene beads passing through the waveguide gap, with the laser both trapping beads and inducing a Raman signal. The approach is similar to top–detection, and in fact uses top–detection, but is separated as the sample interaction is with freely propagating light rather than an evanescent field interaction. Using the propagating field is not of interest in the thesis work, however, and will not be discussed further.

5.2 Other Enhancement Methods

WERS offers an increase in signal strength for Raman spectroscopy due to the two enhancement factors discussed above. However, most of the enhancement is due to the increased interaction volume when using edge–detection[59, 71]. As Raman imaging will not carry the benefit of increased volumes, and only the field enhancement, additional enhancement can be achieved from other techniques.

A related enhancement method to WERS is SERS. SERS is based on the enhanced interaction observed between metallic structures and molecules in its vicinity. The nanostructuring required for the metallic structures combines well with waveguide–based excitation. Peyskens et al. used periodically spaced gold bow tie antennas on Si_3N_4 strip waveguides to achieve an $8 \cdot 10^6$ enhancement compared to free–space[107]. The enhancement was measured for the emission coupled back into the waveguide. A theoretical investigation of the phenomenon was performed prior to the experimental study[108]. In a different application, suspended Si_3N_4 waveguides together with a film of nanoporous gold[66]. SERS can give an increased Raman scattering signal in the order of 10^8. A challenge with SERS, however, is that the metallic structures often are fragile. Additionally, it's a very short range effect and thus any damaged regions can cause a signal loss from that region. This makes it less suited for wide–field imaging purposes, as the entire sample must be excited.

A possible solution to enhance the signal further than from WERS is to use resonance Raman effects. Resonance Raman can provide a significant increase in signal strength, as described in Section 2.1.2. Combining it with WERS can thus give a significant signal enhancement. It will, however, only be possible for certain samples that have suitable resonance effects. Thus, a strong enhancement can be achieved using top detection with resonance Raman spectroscopy. The work presented in this chapter uses simple strip waveguides with resonance Raman for top detection Raman spectroscopy.

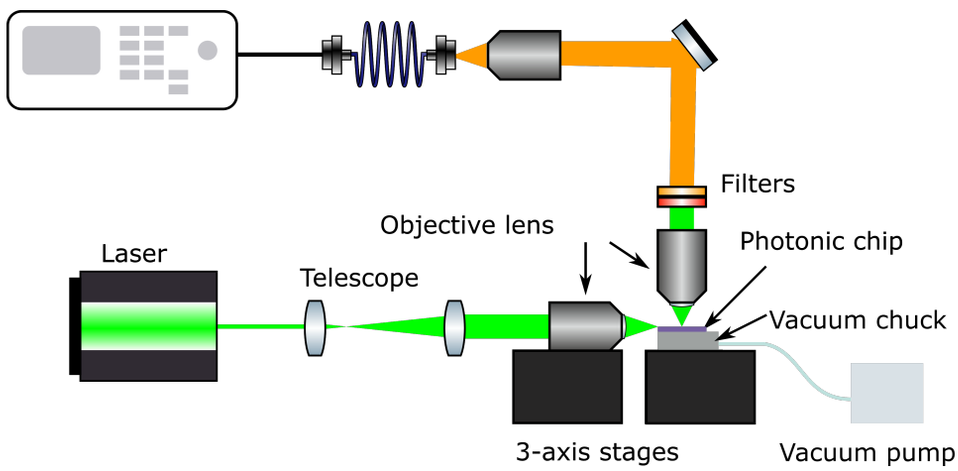

Figure 5.2: A schematic of the system used for waveguide–based Raman spectroscopy. The system is the same as used for chip–based *d*STORM , except that the collected signal passed to a spectrometer rather than a camera.

5.3 Set–up

The aim of this work was to investigate the possibility of modifying the chip–based nanoscope so that it could also perform Raman imaging of the sample. The first step, however, was just to perform spectroscopy. As such, top–detection was the most suitable detection scheme, despite offering less enhancement compared to edge–detection. The system was similar to that described in Chapter 4, but the collection pathway was modified to couple the scattered light from the sample through suitable filters and into a spectrometer, as seen in Figure 5.2. The mirror in the collection pathway was a flip mirror so the system could be used both for spectroscopy and imaging purposes.

The aim of the work was to investigate the possibilities of waveguide–based resonance Raman spectroscopy of haemoglobin, and thus a 532 nm excitation laser was needed[109]. Based on the results from Chapter 3, we opted for the Ta_2O_5 platform. All the work was done using strip waveguides of varying widths. In addition, some Ta_2O_5 waveguides on MgF_2 were fabricated to further investigate the origin of the background signal. All fabrication details are found in the manuscript.

5.4 Results

The aim of this chapter was to investigate if the chip–based system developed for *d*STORM could be used for Raman spectroscopy as well. The following sections

will demonstrate how the same system can be used for spontaneous Raman spectroscopy. Furthermore, chip–based resonance Raman of haemoglobin is shown. I will start by presenting some general findings, leading into a summary of Paper VI.

5.4.1 Background Analysis

The background signal from Ta_2O_5 and Si_3N_4 in the visible range was studied in Chapter 3. It is clear that Ta_2O_5 has a very weak background signal. The spectrum is presented again in Figure 5.3a. There are four discernible peaks: 1) A peak at 196 cm^{-1}, 2) a peak at 488 cm^{-1}, 3) a sharp peak at around 680 cm^{-1}, and 4) a shoulder at around 899 cm^{-1}. This agrees well with previous literature[69]. For narrow waveguides, an additional peak arose at around 523 cm^{-1}. This is a typical Si–Si peak. The size of the peak increased with narrower waveguides, as seen in Figure 5.3b and c.

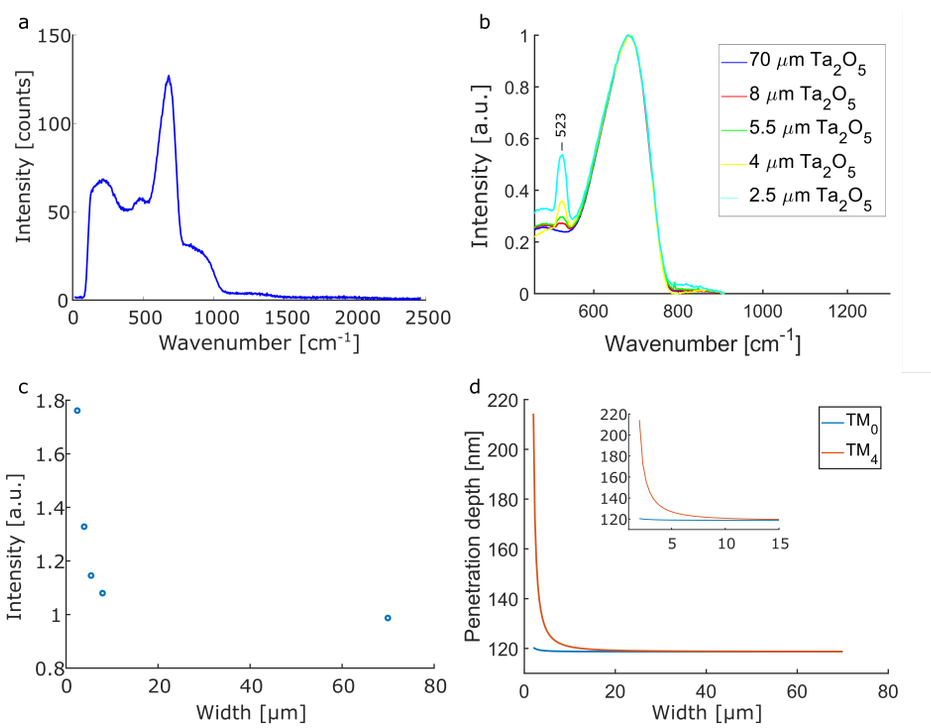

Figure 5.3: (a) Spontaneous Raman spectrum from a Ta_2O_5 waveguide. (b) Zoomed in region of the spectrum from Ta_2O_5 strip waveguides of different widths. (c) The ratio of the 523 $cm^{-}1$ peak to the surrounding level. (d) Simulations of the confinement factor for the TM_0 and TM_4 modes for strip waveguides of varying widths.

The confinement factor of the guided modes is dependent on the geometrical sizes of the waveguide structure. All work done here was performed with 220 nm thick waveguides, however, a wide range of different waveguide widths were available. FIMMWAVE was used to simulate the confinement factor for different widths for both the TM_0 and TM_4 modes, as shown in Figure 5.3d. Higher order modes have a lower effective refractive index, which means a lower confinement factor, which means a greater penetration depth of the modes. A drastic increase for narrow widths was observed, with a clear increase in the TM_4 mode around 5 μm , as seen in the inset in Figure 5.3d. This agrees well with the observed changes in spectrum with smaller widths. We can thus attribute the overall background to Ta_2O_5, whereas the weak peak is from the SiO_2.

5.4.2 Polarisation

Polarisation can have a significant effect on several relevant properties, as discussed above. The three most important properties for waveguide–based Raman spectroscopy are coupling efficiency, interactions with the sample, and amount of recoupling. Since we are doing top detection, the latter is not relevant. We investigated the coupling efficiency into the strip waveguides. In Figure 5.4b the spectrum from a Ta_2O_5 waveguide with fluorescent beads is measured for the TM and TE polarisation. The TM mode gave the highest SBR ratio, due to a lower confinement[70], and was used for the experiments.

5.4.3 Summary of Paper

One of the aims of this work was to investigate the background signal from Ta_2O_5 at 532 nm excitation. In particular, the aim was to investigate the origin of the signal. Spectra from clean waveguides were measured, and several different widths were measured in order to determine which part of the platform the signal originated from. From the simulations presented in Figure 5.3 the penetration depth increases significantly around 5 μm . We observed a change in the background spectra with an emerging peak in lower numbers, which matches to an SiO_2 peak. It was thus concluded that the weak background from the platform is mostly from Ta_2O_5 and thus can't be reduced much further. This was further confirmed by fabricating Ta_2O_5 waveguides on MgF_2 substrates where we observed MgF_2 peaks instead. The platform performs much better than the Si_3N_4 used in this thesis in lower wavelengths, as shown in Chapter 3.

We successfully demonstrated spontaneous Raman spectroscopy of methanol and iso–propanol. Furthermore, we demonstrated, to the best of our knowledge,

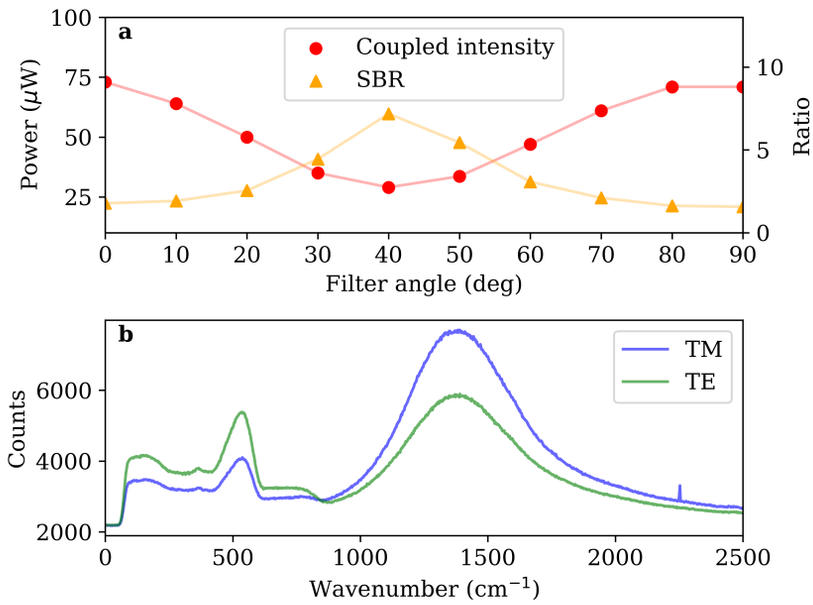

Figure 5.4: (a) Plot of the guided light intensity and signal–to–background ratio for different polarisations. (b) Spectra from fluorescent beads on a Ta_2O_5 platform for TE and TM polarisation in the waveguide. For TM the background signal is weaker, yet the signal is stronger than for TE.

the first waveguide–based Resonance Raman spectroscopy. A Resonance Raman spectrum of haemoglobin is presented. The resonance effect provided a massive signal improvement. Spectra from the samples can be found in Figure 5.5. All the measurements were performed using Ta_2O_5 chips that could be used for imaging as well, and the instrument was a modified version of the chip–based nanoscope.

5.5 Discussion and Conclusion

The main result of the work presented in this chapter is a demonstration of waveguide–based resonance Raman spectroscopy. It is important to view these results together with Chapter 3, as the platforms performance in the visible range in essential. Ta_2O_5 is well suited for this application, as it has little background signal at shorter wavelengths. Another important finding was that the background signal detected originated from Ta_2O_5, and thus it will be hard to reduce further. The detected signal is, however, far weaker than that form Si_3N_4 at short visible wavelengths, as seen in Chapter 3.

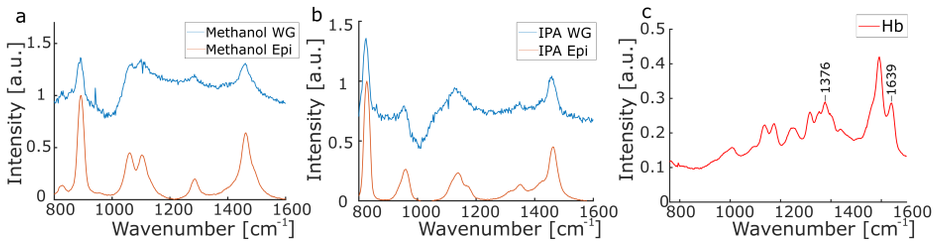

Figure 5.5: (a) Raman spectrum of methanol from both waveguide–based and free–space for reference. (b) Raman spectrum of iso–propanol from both waveguide–based and free–space for reference. (c) Resonance Raman spectrum of haemoglobin.

There are, however, several limitations in the work. Resonance Raman spectroscopy is by nature of limited applicability as it is both sample and wavelength dependent. It is however clear that haemoglobin is a very important marker in medical research and thus has great value[109]. There are several other relevant samples where resonance Raman can be used[110, 111].

For the highest possible enhancement, edge–detection should be used as the area enhancement can be made arbitrarily large simply by increased the interaction area. In the work presented, we opted for top detection. The main reason for this lies in future applications. The overall aim of the work was to develop widefield chip–based Raman imaging of red blood cell (RBC). In order to form an image, top detection was used. To compensate for the loss in enhancement, a 532 nm laser was used to benefit from the resonance effects of haemoglobin, the major component of RBCs. A combined imaging and spectroscopy system that employs resonance Raman spectroscopy could e.g. be of interest when studying sickle–cell anaemia, where imaging identifies key samples and spectroscopy can analyse the haemoglobin. However, for purely spectroscopic applications, edge–detection should be preferred.

As with all the previous work, multi–mode waveguides were used. Ideally, the waveguides should have been single mode, as it would give homogeneous excitation. For spectroscopy it does not cause a problem, assuming that the sample has a uniform coverage on the waveguide, but for imaging spectroscopy the waveguides should be made single mode. An alternative is to scan the coupling objective to average the excitation, as described in Section 4.1.2.

We have for the first time, to the best of our knowledge, demonstrated waveguide–based resonance Raman spectroscopy. We have also shown that Ta_2O_5 can be an attractive platform for spontaneous Raman spectroscopy with shorter wavelengths in the visible range. The background observed in Ta_2O_5 appears to be from the Ta_2O_5 and thus hard to reduce further, but for applications above

approximately 1000 cm^{-1} the platform has virtually no detectable background. This makes it perfectly suited for haemoglobin analysis. There is, however, still more work needed to investigate other potential platforms. From the results presented in Chapter 3, it is possible that Si_3N_4 could be a suitable platform through improvements in fabrication to reduce the background signal. There are several interesting options for increasing the available power, e.g. by increasing the coupling efficiency through inverse tapering[112] or 3D tapering[113]. Furthermore, optimisation of the waveguide geometries can further increase the signal strength. Implementing such strategies is essential for waveguide–based Raman imaging to succeed.

6

Computational Imaging Using Waveguides

Whenever waveguide imaging is performed with multi–mode waveguides, the guided light will have an inhomogeneous spatial distribution due to multi–mode interference. An example with visible light was shown in Figure 4.2. The result can be an inhomogeneous illumination in the final image, unless accounted for. This can be overcome e.g. by looping the coupling objective lens along the coupling facet to generate a wide range of patterns that average out to a homogeneous image, as done throughout Chapter 4. In the results presented here, I will show how the multi–mode interference patterns actually can be used as an advantage in chip–based imaging to improve the resolution, rather than a nuisance that must be accounted for. In particular, we demonstrate how known excitation patterns from the waveguide can be used to increase the resolution of an image through computational imaging. The multi–mode interference pattern occurring in a waveguide contain high frequency components that can alias sample frequencies normally outside the optical transfer function (OTF) back into the OTF of the system. Normally the spatial distribution of the patterns is not known in detail, and thus the patterned images are simply averaged in the end to provide homogeneous illumination in the final image. Here, we imaged the patterns from Si_3N_4 waveguides using the background observed from short visible length excitation to achieve the high–resolution details of the patterns. Using the experimentally determined patterns, a fluorescent sample was simulated and it is demonstrated how the computational imaging

procedure can reconstruct a higher resolution image of the sample.

From the results presented in Chapter 4, it is clear that waveguide–based excitation makes very large FOV imaging possible, but the price to pay is a decrease in resolution due to lower NA collection optics. The results presented here, however, offer a way to achieve the same high FOV, but avoid a loss in resolution through computational imaging, as long as the interference patterns are known. Although the work presented here was only performed on a simulated sample, it provides a proof of concept for future development. Furthermore, simulations of a multi–mode interferometer (MMI) structure that can provide highly repeatable patterns is presented as a solution to the challenges with the current implementation. The work presented here is ongoing and a manuscript is in preparation, but not included in the thesis.

I will start the chapter with a brief introduction to patterned excitation and fundamental theory in Section 6.1. The experimental methods will be covered in Section 6.2. Finally, Section 6.3 will present the results and Section 6.4 a discussion of the results.

6.1 Patterned Excitation

6.1.1 Introduction

Patterned, or structured, excitation is well known from SIM, which was briefly introduced in Section 2.5.3. The basic idea of SIM is to use a high–frequency sinusoidal excitation pattern to alias higher frequencies in the sample into the OTF of the system, which are then imaged. A reconstruction algorithm can reconstruct an image with a resolution twice that of the diffraction limit from a set of images. Patterned excitation has, however, seen several other implementation. One recent implementation is the use of patterned excitation for de–scattering in two–photon microscopy[114].

Optical waveguides guide light through total internal reflection. The light will, however, only be guided in discrete modes, as described in Section 2.6.2. As a result, the light distribution varies along the propagation direction of the waveguide, essentially resulting in patterned excitation of any sample in contact with the waveguide. Often, these variations are unwanted and waveguides will be designed to achieve the single mode condition, where only the fundamental mode is guided. In other cases, it is of great help. A MMI is a structure where a single mode waveguide abruptly changes to a slab section. This will lead to an interference pattern from the modes and the pattern will self–image along the propagation direction due to the Talbot effect. By careful design of the slab

section and correct placing of the outgoing waveguides, a very efficient $1 \times N$ splitter can be made[115].

Recently, multi–mode patterns have been investigated as a potential benefit for chip–based imaging. Scrambling the modes during acquisition can be used for fluctuation based super–resolution optical microscopy techniques such as super–resolution optical fluctuation imaging (SOFI)[20] and entropy–based super–resolution imaging (ESI)[21]. Both SOFI and ESI have been demonstrated for chip–based imaging[10, 116]. All fluctuation based techniques use different statistical properties of the fluctuations to produce super–resolution images. Recently, SIM was successfully implemented with chip based excitation by using counter–propagating light in waveguides[117].

In this work we explore an unorthodox advantage of interference patterns generated by multi–mode waveguides, by treating them as highly resolved excitation patterns for computational imaging. High–resolution excitation patterns can encode any spatial frequency in an image to its other frequencies through aliasing effects. Thus one can use this effect to generate high–resolution images using collection optics with lower NA, and hence at low resolution. This is the same principle used in SIM[19] and single–pixel imaging[118]. In SIM, unresolved frequencies are aliased back to the OTF to generate a super–resolved image. In single–pixel imaging, all high frequencies are aliased to the DC (i.e. the zero frequency), and are computationally resolved through multiple such measurements. Importantly, given enough measurements, the reconstructed image can be at (or even beyond) the maximum resolution of the excitation pattern, and is independent of the NA of the collection optics. Patterned excitation can thus be used with a low magnification lens in order to perform high–throughput imaging. However, building such systems in free–space for fluorescence microscopy typically requires two microscope objectives: one with a high NA for generating known, high–resoltuion excitation patterns, and one with a low NA for large FOV collection. The high NA objective lens usually covers a limited FOV compared to the low NA objective, and hence limits the advantages that can be achieved through computational imaging. The waveguide platform is an ideal candidate for computational imaging systems of this kind. First, the excitation and collection optics are inherently separated, which makes large area excitation easily achievable, as demonstrated in Chapter 4. Second, the excitation patterns can have a higher resolution than in free–space due to the high refractive index of the waveguide materials. The final result is a high NA excitation pattern that extends over arbitrarily large areas.

One of the greatest advantages of a chip–based imaging system is that TIRF imaging can be done over large areas compared a TIRF objective. However, the price to pay for the large FOV is a loss in resolution due to a lower NA objective lens. With this computational approach we aim to use the excitation

patterns in multi–mode waveguides to perform the same large FOV imaging, but without the loss in resolution. The imaging procedure used in previous chapters already requires several images with different patterns in order to get an end result with homogeneous excitation, so implementing computational imaging does not add any requirements.

6.1.2 Theory

A general imaging process was described in Section 2.4.2. For patterned excitation, the resulting image will be given by:

$$Y_i(x,y) = \big(E_{p,i}(x,y) \cdot O(x,y)\big) * \mathrm{PSF}(x,y) \tag{6.1}$$

where $Y_i(x,y)$ is the captured image, $E_p(x,y)$ the patterned excitation, $O(x,y)$ the sample and $\mathrm{PSF}(x,y)$ the PSF of the system. $*$ marks the convolution. The captured image, $Y_i(x,y)$, will thus be of an inhomogeneously excited sample which is blurred by the system PSF. In Chapter 4, several such images were captured in order to generate the final image, which is the average of all captured images. The aim of this work is to solve the equation for the sample, $O(x,y)$, to get the high resolution information about the sample.

It can be useful to consider the situation in Fourier space. Equation 6.1 can be written in the Fourier space, using the convolution theorem, as:

$$\tilde{Y}_i(kx,ky) = \big(\tilde{E_{p,i}}(kx,ky) * \tilde{O}(kx,ky)\big) \cdot \mathrm{OTF}(kx,ky) \tag{6.2}$$

Where tilde ($\sim$) represents the Fourier transform. The Fourier transform of the system PSF is the OTF and is denoted as such in the equation. The sample will contain very high frequencies, only limited by the labelling density of the fluorophores. The excitation pattern can be approximated with a Fourier series, limited by the wavelength of the guided light and the refractive index of the waveguide. The OTF will function as a low–pass filter determined by the NA of the objective lens. Assuming a total pixel count of $n_x \cdot n_y = N$, Equation 6.2 will have N unknowns. From Equation 6.1, it appears every image will produce N equations. The OTF will, however, filter the image and only M<N pixels will be supported, meaning that each image only produces M equations. In order to solve the problem, in the order of $\frac{N}{M}$ images are needed.

The complete imaging process uses an ensemble of excitation patterns, $\{E_p\}$, resulting in an ensemble of corresponding images, $\{Y\}$. The result is a linear set of equations in the form of Equation 6.1, that can be solved through matrix operations. The procedure will be covered in details in the following section, but the basic idea is sketched in Figure 6.1a.

6.2 Methods

The results presented in this chapter are based on simulated experiments. The excitation patterns were captured using waveguide structures with the chip–based nanoscope, but the sample was simulated. Simulated experiments were used as we were not able to image the patterns with a fluorescent sample on top of the waveguide in a suitable matter, which will be further discussed in Section 6.4.

6.2.1 Imaging High–resolution Excitation Patterns and Generating Images

The chip–based nanoscope was used without any modifications for imaging the multi–mode interference patterns. Unlike the work presented previously, a crossing waveguide was used rather than a straight. The loop structure was a 25 μm wide Si_3N_4 strip waveguide. A schematic of the structure used can be found in Figure 6.1b. The waveguide crossing was used as the imaging region. Crossing waveguides were used to reduce the directionality of the patterns observed in straight waveguides.

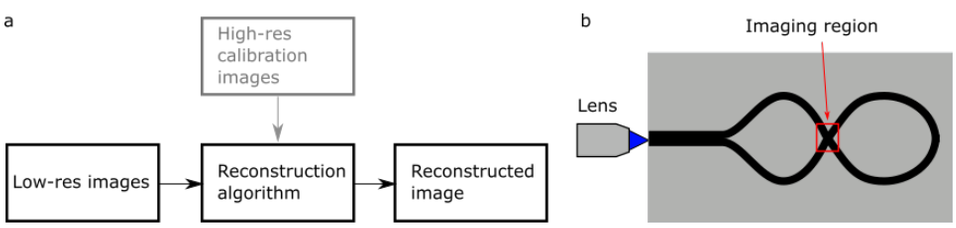

Figure 6.1: (a) Image reconstruction pipeline. (b) Schematic of waveguide used to generate high–resolution calibration images of patterns for computational imaging. An objective lens was used to couple light into the waveguide. By changing the position of the objective lens along the edge different patterns can be generated.

Si_3N_4 waveguides exhibit a background fluorescence signal when excited by short wavelength visible light, as shown in Chapter 3. The excitation patterns could thus be imaged directly without any fluorescent labelling of the waveguide. A 532 nm laser was used to excite the patterns and a 60x/1.2 NA water immersion objective lens was used to image the patterns. These imaged patterns constitute the known high–resolution patterns required for the reconstruction algorithm. The light was coupled into the waveguide using end–fire coupling. The different patterns were excited by using a piezo stage controller to change the position along the coupling facet of the waveguide. A 532 long pass filter was used to remove the scattered laser light. The resulting excitation patterns used was approximately 15 μm x 15 μm .

A fluorescent object of the word "Harvard" was simulated. then the experimentally measured patterns were used to simulate the patterned excitation process by multiplying the object with the pattern. The resulting images (one for each pattern) was then down sampled to mimic the low NA collection. Then Poisson noise was added to simulate the photon detection process on a camera.

6.2.2 Sample Reconstruction Process

The general idea of the techniques is presented in Figure 6.1a. In order to reconstruct a high resolution image, the set of equations, on the form of Equation 6.1, generated by each individual patterned excitation must be converted to a suitable set of matrix operations. This was first done for each individual captured image. The image was converted to a 1D vector of length N, V_Y, by stacking all N pixel values in a single column. A similar vector can be made for the sample, V_O, altough with unknown values. The multiplication of the excitation pattern with the 1D sample vector can be represented by changing the excitation pattern matrix from a $n_x \times n_y$ matrix to a matrix of size $N \times N$ with the values only on the diagonal, which can be called $\boldsymbol{M}_{\boldsymbol{E_p}}$. Finally, the convolution of the PSF with the product can be represented as a matrix multiplication by converting it into a Toeplitz matrix, which can be called $\boldsymbol{M}_{\text{PSF}}$. The result is that Equation 6.1 can be written as:

$$\boldsymbol{V_Y} = \boldsymbol{M}_{\text{PSF}} \cdot \boldsymbol{M}_{\boldsymbol{E_p}} \cdot \boldsymbol{V_O} \tag{6.3}$$

The result is then L equations in the form of Equation 6.3, where L is the number of images captured. One combined equation can be made from all L equations in the following way. All $\boldsymbol{V_Y}$ were added one after another to a 1D vector $\boldsymbol{V}_{\{Y\}}$ of length $L \cdot N$. The same was be done for the sample. All the excitation pattern matrices, $\boldsymbol{M}_{\boldsymbol{E_p}}$, were stacked on top of each other, forming a $(L \cdot N) \times N$ matrix. The convolution matrices, $\boldsymbol{M}_{\text{PSF}}$, form the diagonal of a new matrix of size $(L \cdot N) \times (L \cdot N)$. Finally, the convolution matrix and the excitation pattern matrix is multiplied together, forming a matrix $\boldsymbol{A}$, giving the following matrix equation:

$$\boldsymbol{V}_{\{Y\}} = \boldsymbol{A}\boldsymbol{V_O} \tag{6.4}$$

This was solved in Matlab through a linear optimisation method.

6.3 Results

The results presented in this chapter serve as a proof of concept. A simulated sample used together with experimentally imaged excitation patterns are used for the demonstration.

6.3.1 Simulated Experiment

The experimental patterns collected with the looped waveguide were used with a simulated sample to test the idea. Figure 6.2a shows examples of the patterns used. These form the known, high–resolution patterns in the reconstruction algorithm. In panel b, the resulting simulated fluorescent image is shown for the corresponding patterns in panel a with a downscaled resolution, similar to imaging with a 20x objective lens. The reconstructed image is presented in panel c. There is a clear improvement in the final resolution compared to the individual images of panel b.

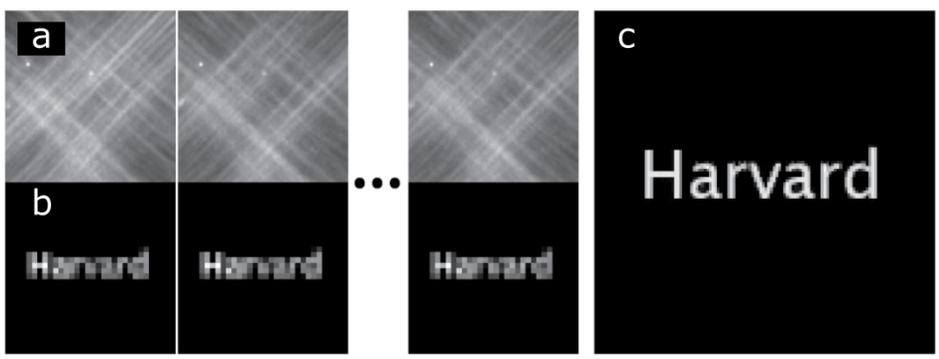

Figure 6.2: (a) Example excitation patterns. The patterns are approximately 15 μm x 15 μm large. (b) Resulting images of simulated sample excited by the patterns in (a) with low resolution. (c) Reconstructed high resolution image of the simulated sample. The imaged size is the same as in panels a and b, but the panel is enlarged to make the text more visible.

6.3.2 Excitation Patterns From a MMI

The results presented in the previous section used experimentally imaged excitation patterns from a crossing, multi–mode waveguide with a simulated sample. It was not possible to image a real sample, as the sample preparation requires the chip to be removed and thus achieving the same patterns is not experimentally possible. The challenge is that the waveguide is multi–mode from the start, which means that any change in coupling changes the entire excitation pattern. A single–mode waveguide, on the other hand, provides only homogeneous excitation and is therefore not useful. A possible solution is an $N \times N$ MMI, with N single mode waveguides from each side entering the slab section. An N X N MMI, where N single mode waveguides connect from each side to a slab region, can generate N^2 patterns if only one arm from each side guides light. By using several arms, a far higher number can be acheived. FIMMWAVE was used to simulate patterns using for a MMI. The structure

was 15 µm wide and 400 µm long, so that a 15 µm x 15 µm imaging area in the middle could be used. The entire structure was 220 nm high, and each single mode seegment was 500 nm wide. Realistic values were chosen for the refractive indices, with the waveguide having 2.0, the substrate 1.45 and 1.33 in the cladding. The structure, sample patterns and imaging region is shown in Figure 6.3.

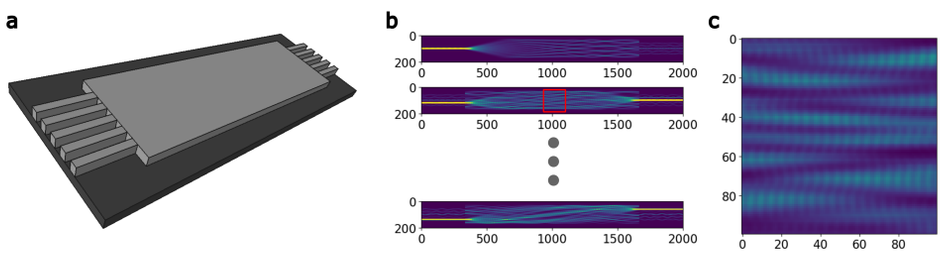

Figure 6.3: (a) Sketch of a MMI structure with 5 single mode waveguide inputs from each side. (b) Simulated multi–mode patterns from an MMI with inputs both from one side and two sides. (c) Inset from b showing the pattern over an imaging region.

6.4 Discussion and Conclusion

Chip–based imaging in it simplest form changes the excitation from free–space to waveguides. The interference patterns in multi–mode waveguides can be used for different fluctuation–based techniques, which offers a possible advantage over free–space. In this work, we use known excitation patterns to reconstruct high–resolution images from low–resolution images.

In the presented results, the excitation patterns were imaged and then used for the reconstruction of a simulated sample. Ideally, a real sample, such as a fluorescently labelled cell, should have been used. This, however, was not experimentally possible with the current set–up, as the patterns can't be imaged without the sample on the waveguide. If the patterns are imaged prior to adding the sample, it would not be practically possible to re–couple in a proper manner to get the exact same patterns. It was attempted to circumvent this problem by imaging a sample and the patterns in two different channels. This approach was attempted by labelling a sample with quantum dots with an excitation wavelength $\lambda_{ex} \approx 532$ nm and an emission wavelength $\lambda_{em} \approx 900$ nm. The background signal from Si_3N_4 when excited with a short wavelength laser is strong, and mostly located below 900 nm, as shown in Chapter 3. The multi–mode interference patterns were thus imaged using a 593 ± 46 bandpass filter, capturing a significant portion of the background signal. A 785 nm long–pass filter was used to image the quantum dots. All measurements

were performed with a 532 nm longpass to filter out the laser. The separation of signals was, however, not sufficiently high, with the sample bleeding through to the background channel. An alternative could be to use a transparent substrate and image the patterns from the bottom and sample from the top.

A simpler solution can be to use a structure like an MMI which will produce reproducible patterns, such as shown in Section 6.3.2. A challenge with a waveguide only guiding in one direction is that the excitation pattern will have a strong directionality. There will be higher frequencies perpendicular to the propagation direction. We solved this by crossing two waveguides. A typical MMI will have a directionality along the propagation direction, but one solution that will be pursued is to use crossing MMIs[119]. Further simulations of MMI structures will be performed and a structure fabricated based on the results.

One of the most important aspects of waveguide–based imaging is the arbitrarily large TIRF excitation for imaging. Using this, large FOV imaging is achievable. The throughput can be increased by using an objective lens with a lower magnification, but the loss in NA will lead to a loss of resolution. However, by using known waveguide patterns to increase the resolution, we hope to be able to do extremely large FOV imaging without sacrificing resolution. Such an applications would be beneficial for e.g. tissue analysis, where high–throughput imaging is beneficial. The results presented in this chapter point towards a new direction for chip–based imaging. It falls in line with recent developments with fluctuations–based imaging using waveguide–based excitation, but employs known patterns rather than random patterns, similar to chip–based SIM[117]. If the method is combined with compressive sensing, the amount of patterns needed could be reduced and thus the throughput further increased.

A common reason for using a photonic integrated circuit is for miniaturisation. The current system requires a traditional microscope for imaging, which limits the possibilities for miniaturisation. A natural next step, based on the results presented here, is to investigate the possibilities for single–pixel imaging with the excitation patterns. The reconstruction performed for the work presented here could be used with minor modifications for single–pixel imaging. This could provide a lens–less system which only needs an integrating detector and not a microscope. If the detector is integrated to the chip, a completely integrated microscope could be made.

Computational imaging with waveguides is just emerging and there are a lot of possibilities, either as a compliment to existing technique or as novel applications. The work presented in this chapter is a proof–of–concept and the use of known patterns will be further explored in future works.

Part IV

Conclusion

7

Conclusion

In this thesis, I have investigated waveguide–based excitation for different applications, mainly focusing on fluorescence microscopy. The aim of the thesis was two–fold: 1) to investigate how waveguide–based excitation can benefit *d*STORM, and 2) to explore new opportunities arising with waveguide–based excitation. In Part II, it was shown how the separation of the excitation and collection pathways in chip–based microscopy enables imaging at arbitrarily large FOVs, only limited by the available collection optics. In Part III, two different applications were shown using different versions of the chip–based microscope. First, chip–based resonance Raman spectroscopy was performed using a Ta_2O_5 waveguide. Second, a new approach to computational imaging was introduced using excitation patterns from multi–mode waveguides to enhance the resolution.

The backbone of the entire thesis is the photonic chips. The chips serve a dual purpose as both the sample holder and part of the excitation pathway. This gives a unique advantage over common ways of generating TIRF excitation. With a TIRF objective lens, the collection and excitation pathways coincide, which limits the set–up to the objective lens' performance. With prism TIRF, the excitation and collection pathways are separated, but the prism offers little versatility. PICs can include a plethora of active and passive components, giving a unique ability for tailoring that a prism can't achieve. The tailoring of the excitation from the waveguides enables unprecedentedly large FOV diffraction–limited and super–resolution imaging, as shown in Chapter 4. The large area excitation is also highly beneficial for patterned excitation—such as

SIM, single–pixel imaging or the computational imaging presented in Chapter 6—where a high NA objective lens is typically used to generate patterns of sufficient resolution and then imaged with the same lens, limiting the FOV. With waveguides, the excitation pattern is generated independently of the collection optics, thus granting significant freedom both for excitation and collection. Additionally, the high refractive index of the waveguide materials means they can produce excitation patterns carrying spatial frequencies that surpass that of free–space optics, thus further increasing the resolution for patterned excitation. One such example is the use of waveguide–based excitation for generating super–resolved fringes for SIM.

The waveguides can provide excitation over arbitrarily large areas, however the throughput will still be limited due to the collection optics. The results presented in Chapter 4 used a state–of–the–art objective lens with high NA and low magnification, but field flatness can cause problems for such lenses. Additionally, the lower NA results in a slight loss of resolution. The computational method presented in Chapter 6 can be used to increase the resolution by using the excitation patterns that are present from the waveguide. This can potentially allow for objectives with even lower magnification, and thus larger FOV, as the decrease in NA could be compensated to avoid a loss in resolution. An alternative approach to further increase the FOV to the centimetre scale could be to use a micro–lens array together with a camera with a large sensor. Pursuing high–throughput imaging is of great interest, especially for applications such as tissue analysis, which is an essential tool in both medical research and work. Tissue imaging, however, typically requires a high throughput, making implementation of traditional super–resolution imaging challenging. A chip–based nanoscope that can deliver the same throughput at a low cost could be an attractive route from diffraction limited to super–resolution imaging, especially for point–of–care analyses.

As with any new technique that is introduced, it does not exist in a vacuum. The chip–based nanoscope exists in a world of incredible instrument diversity. The main advantages of waveguide–based excitation were covered above. There are, however, some significant limitations. An important limitation is that the optical sectioning makes it essentially a 2D technique. Unlike a TIRF objective lens, which can investigate different planes of the sample e.g. by using highly inclined thin illumination, the waveguide–based excitation will only interact with the sample that is within the evanescent field's penetration depth. This is simply a restriction of the current technique, which can be advantageous in some cases and limiting in other cases. A modified chip–based nanoscope with QPI was shown in Chapter 4 to image the 3D structure of LSECs with high axial sensitivity, as well as reconstruct the super–resolved spatial information from *d*STORM . It is, however, not the same as 3D super–resolution fluorescence imaging. It will be well worth investigating potential methods of projecting

light out from the waveguides, e.g. with diffraction gratings or axicons, in order to perform 3D *d*STORM.

An attractive part of the presented system is that it can be retrofit into existing microscopes all over the world—the complexity, however, limits its use to trained personnel who can provide manual input, e.g. when coupling light into the waveguide. This can be solved through technical improvements, such as automatic coupling. A more significant challenge is that the current version uses opaque chips, which means imaging is done from the top. Any fluorescence from the sample must thus pass through the entire sample before it's collected by the objective lens. First, this means that systems using trans–illumination won't work—only epi–illumination works; and second, that the scattering through the sample can reduce the quality of the final image. As such, it is important to study other alternatives that can make it more accessible. Waveguides on a cover glass substrate is a suitable choice, as it is familiar to the average user and brings all the advantages of a transparent substrate. It is, however, also important to further investigate common PIC platforms, such as Si_3N_4, Ta_2O_5, or TiO_2.

One of the original goals of this thesis was to perform widefield Raman imaging by using waveguide–based excitation. Despite taking advantage of resonance Raman effects to perform Raman spectroscopy, as presented in Chapter 5, the power available through the waveguide was insufficient for imaging. Implementing STED on a chip would also require very high intensities, which can not currently be achieved. A straight forward way of increasing the evanescent field intensity is to increase the laser power, however, with the current chips, the relatively low coupling efficiency causes the waveguide facet to be damaged at higher laser powers. As such, it is important to investigate ways of increasing the evanescent field intensity. The initial steps can be optimisation of the waveguide geometry, in combination with improved coupling through either inverse tapering or 3D tapering. Furthermore, alternative materials, geometries and fabrication techniques optimised for high power applications could help. Exploring the use of surface plasmons on top of waveguide surface could also be a way to increase the evanescent field intensity.

The chip–based imaging system is still in its infancy, and there are many unanswered questions to be tackled. Some of the more promising directions for future research include integration with e.g. microfluidics as part of a general lab–on–a–chip device, implementation of additional advanced imaging techniques such as stimulated emission depletion microscopy, and developing new techniques based on the multi–mode interference patterns. The combination of a microfluidic flow cell with an integrated single–pixel camera based on the results from Chapter 6 would be an interesting next step. A fully integrated lens–less single–pixel microscope, with the laser and detector integrated on to

the PIC, could provide an ultra–portable imaging platform for e.g. field studies of bacteria. While this thesis demonstrates some of the potential uses of both waveguide–based excitation and chip–based microscopes, it should be viewed primarily as a stepping stone and hopefully spur interest for further research into the many possibilities, such as those outlined above.

Paper I

Study of Waveguide Background Signal at Visible Wavelengths for On–chip Nanoscopy.

D. A. Coucheron, Ø. I. Helle, J. Wilkinson, G. S. Murugan, C. Dominguez, H. Angelskår, B. S. Ahluwahlia.

Study of waveguide background at visible wavelengths for on-chip nanoscopy

DAVID A. COUCHERON,[1] ØYSTEIN I. HELLE,[2] JAMES S. WILKINSON[3], GANAPATHY SENTHIL MURUGAN[3], CARLOS DOMÍNGUEZ[4], HALLVARD ANGELSKÅR[5] AND BALPREET S. AHLUWALIA[1]

[1]*UiT The Arctic University of Norway, Klokkargårdsbakken 35, 9037 Tromsø, Norway*
[2]*Chip NanoImaging AS, Sykehusvegen 23, 9019, Tromsø, Norway*
[3]*Optoelectronics Research Centre, University of Southampton, Southampton SO17 1BJ, U.K.*
[4] *Instituto de Microelectrónica de Barceloana (IMB-CNM, CSIC), Campus UAB, 081930-Bellaterra, Spain*
[5] *SINTEF Digital, Dept. of Microsystems and Nanotechnology, Gaustadalleen 23C, 0373 Oslo, Norway*
balpreet.singh.ahluwalia@uit.no

Abstract: On-chip super-resolution optical microscopy is an emerging field relying on waveguide excitation with visible light. Here, we investigate two commonly used high-refractive index waveguide platforms, tantalum pentoxide (Ta_2O_5) and silicon nitride (Si_3N_4), with respect to their background with excitation in the range 488-640 nm. The background strength from these waveguides were estimated by imaging fluorescent beads. The spectral dependence of the background from these waveguide platforms was also measured. For 640 nm wavelength excitation both the materials had a weak background, but the background increases progressively for shorter wavelengths for Si_3N_4. We further explored the effect of the waveguide background on localization precision of single molecule localization for *direct* stochastic optical reconstruction microscopy (*d*STORM). An increase in background for Si_3N_4 at 488 nm is shown to reduce the localization precision and thus the resolution of the reconstructed images. The localization precision at 640nm was very similar for both the materials. Thus, for shorter wavelength applications Ta_2O_5 is preferable. Reducing the background from Si_3N_4 at shorter wavelengths via improved fabrication will be worth pursuing.

1. Introduction

Integrated photonics is a rapidly expanding field of research. It started out with integration of optical devices onto 2D substrates for telecommunications [1], but soon expanded to much more complex components. Today, both passive components such as multi-mode interference devices [2], as well as active components such as lasers [3] have been implemented. This has greatly increased the usefulness of the technology and now encompasses not only telecommunications, but diverse fields such as quantum mechanics [4] and optical trapping [5,6]. An important biological application has been waveguide-based biosensors [7]. A wide range of applications have been shown, ranging from Raman spectroscopy [8–10] to fluorescence imaging [11]. For sensing applications, integrated photonics can offer signal enhancement [8], size reductions [12] and many other benefits. High refractive index materials are of particular interest as they offer high sensitivity in smaller footprints [13]. The choice of waveguide material is based on several criteria, such as the wavelength of interest. Traditionally, integrated photonics have been developed for near infra-red wavelength for telecommunications applications. However, the increased interest in bio-applications is pushing the field closer to and into the visible range. For visible wavelengths, different material platforms have been investigated, with popular platforms being silicon nitride (Si_3N_4) [8,14], tantalum pentoxide (Ta_2O_5) [10,15] and titanium dioxide (TiO_2) [9].

Development of Raman spectroscopy using photonic chips has seen a surge of interest over recent years [8,9,15–18]. Different waveguide designs [5,16,19] and collection methods [5,20] have been suggested. Highly efficient waveguides based Raman sensors have been made,

rivalling the sensitivity of the traditional confocal Raman microscope [21]. Dhakal et al. have recently measured biological sub-monolayers using a spiral waveguide design [8]. Most of the chip-based Raman spectroscopy work until now has been performed using a 785 nm laser. Lately, there has been a growing interest in visible light for Raman spectroscopy [10,15,22]. A lower excitation wavelength increases the signal strength, as Raman scattering scales with λ^{-4}. Furthermore, visible wavelengths are also demonstrated to be useful for resonance Raman spectroscopy, such as 532 nm for hemoglobin [10,23,24]. The shorter wavelength can, however, also increase any background from fluorescence.

Recently, fluorescence based super-resolution optical microscopy using photonic integrated circuits was introduced [25], which exclusively uses visible wavelengths. Until now, three different well-established super-resolution methodologies have been demonstrated using a waveguide platform. These are: 1) single molecule localization microscopy (SMLM) such as direct stochastic optical reconstruction microscopy (*d*STORM) [25,26], 2) structured illumination microscopy (SIM) [27] and 3) fluorescence intensity fluctuations based methods, such as on-chip super-resolution radial fluctuation microscopy (SRRF) [28], on-chip super-resolution optical fluctuation imaging (SOFI) [29] and on-chip entropy-based super-resolution imaging (ESI) [25]. Among the existing methods, on-chip SMLM has provided the highest resolution. The SMLM techniques rely on precise localization of individual fluorescent probes [30–34]. In traditional fluorescence imaging, the entire sample is labelled with a fluorescent dye that is excited by a laser and emits red-shifted light, which can then be collected to create an image of the sample. The imaging process introduces a fundamental resolution limit known as the diffraction limit. SMLM techniques can surpass this limit. This is achieved by imaging subsets of fluorophores that are well separated and fitting the data in order to determine the localization precisely. A peak fitting procedure is then used to localize all the different fluorophores at very high precision, and from the localizations a super-resolved image is generated. Super-resolution imaging is often performed using evanescent field excitation from total internal reflection objective lenses. This removes most of the out of focus background and thus gives an improved result. In 2017 Diekmann et al. performed super-resolution imaging using optical waveguides for excitation [25]. The new approach offered miniaturization and high throughput imaging. A major advantage is the separation of the excitation and collection pathways. The evanescent field excitation is provided by the waveguide, removing any restrictions on collection optics. As such, arbitrarily large fields-of-view can be imaged [35]. The platform is also live-cell compatible and the same platform can be used for other applications such as Raman spectroscopy [10] or optical trapping [6]. Thus, several research fields are looking towards visible light applications with integrated photonics, and to this end performing systematic investigation of the background at visible lights for these waveguide platforms is useful.

Whenever light is guided in a waveguide it will also interact with the waveguide platform. Thus, any background from the waveguide material will have implications on the performance for on-chip spectroscopy and on-chip nanoscopy. Two important origins for background in these applications are Raman scattering and background fluorescence from the waveguide platform itself. Raman scattering will yield the same spectrum (frequency shift) independent of excitation wavelength, except for a scaling in intensity. Fluorescence, however, is strongly dependent on excitation wavelength. Any background, be it Raman or fluorescence based, can cause problems for Raman spectroscopy applications. The particular implications of a background depend on the actual spectrum – there might be applications where a Raman background can be filtered out, whereas a broadband fluorescence background is hard to eliminate. For imaging applications, the spectral distribution does not matter as the camera sensor only measures the total intensity. As fluorescent samples usually emit very strongly, imaging applications should tolerate a background better than spectroscopic applications. However, in case of SMLM the signals come from single fluorophore molecules and therefore the number of photons reaching the camera is usually low. Thus, any background from the

waveguide platform will reduce the localization precision as the data fitting will be done over a higher base level [36]. Furthermore, an inhomogeneous background is particularly challenging, as it can lead to a bias in localizations where the localization precision is different in the two lateral dimensions. Fluorescence emission is stronger when pumped in the visible range. As such, the signal-to-background (S/B) ratio for Raman spectroscopy might fall despite the increased Raman scattering at shorter wavelengths.

As interest in waveguide-based optical nanoscopy and Raman spectroscopy keeps growing, it is important to investigate the most relevant platforms for these applications and how any potential background will affect the measurement results. Fluorescence-based nanoscopy is performed solely in the visible range and is thus potentially subject to strong background fluorescence from the waveguide platform. In this work, we have investigated Ta_2O_5 from one fabrication procedure and Si_3N_4 from two different fabrication procedures as potential candidates for short visible wavelength imaging, as well as for use in Raman spectroscopy. The background is first assessed by imaging fluorescent beads to obtain an estimate of signal-to-background ratio for the different platforms at 640 nm, 561 nm and 488 nm excitation. The spectra for the Si_3N_4 with strongest background was measured to investigate the origin. Finally, we investigated the effect of a background on *d*STORM reconstruction by performing blinking experiments at 640 nm and 488 nm. The results show a noticeable difference in background both between platforms and with varying excitation wavelength.

2. Methods

2.1 Experimental set-up

The waveguide chips were mounted on a vacuum chuck and light was coupled into them using a 50x/0.5 NA coupling lens. A PDMS frame was put on top of the waveguide region of interest to contain the imaging medium and sealed off with a cover slip. We used an upright microscope for imaging. The chip set-up is illustrated in Fig. 1a.

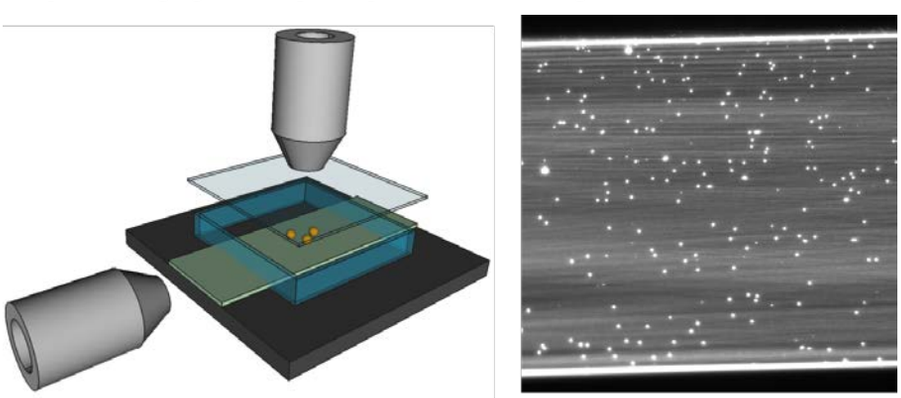

Figure 1: (a) Schematic of the waveguide structure with beads on top. The sample is contained in a PDMS frame with imaging medium and sealed off with a cover slip. The horizontal coupling lens is used to couple light into the waveguide of interest. (b) An example of TIRF imaging of fluorescent beads with a silicon nitride waveguide with a relatively strong background. The multi-mode pattern is clearly visible.

2.2 Waveguide fabrication

Three different waveguide platforms were used in this work. The Ta_2O_5 platform was fabricated at the Optoelectronics Research Centre (ORC), University of Southampton. Two different Si_3N_4 platforms were used in this work: 1) Si_3N_4 fabricated at the Institute of Microelectronics Barcelona termed Si_3N_4-B and 2) Si_3N_4 fabricated by SINTEF, MiniLab, Oslo termed Si_3N_4-S.

The optimization of fabrication procedures for Ta_2O_5 waveguides can be found in previous literature [37]. A thin layer (150 to 220 nm) of Ta_2O_5 was sputtered onto an oxidized silicon substrate (SiO_2 thickness ~ 5 µm). Magnetron assisted RF sputtering was employed and the deposition was optimized using an iterative process. The optimized parameters were substrate temperature, magnetron power and the oxygen flow rate. The optimized parameters chosen were 200°C substrate temperature, magnetron power of 300 W, chamber pressure of 10 mTorr and O_2 and Ar flow rates of 5 and 20 sccm, respectively. Post-deposition, standard photolithography was used to pattern a photoresist mask with straight channels and ion-beam milling was used to fabricate fully etched channel waveguides. The sidewall roughness, which is the major source of propagation loss, was reduced by optimization of the ion-beam milling process. Finally, plasma ashing was performed to remove the remaining photoresist after the etching process. Post-fabrication, the waveguides were annealed for 5 hours at 600°C to reduce the propagation loss.

Various silicon nitride technologies for photonic applications have spread in the past decade by means of foundry models that mirror electronic integrated circuit industry developments of the past century [38]. Many of the devices and circuits developed with this technology have been employed in biomedical and chemical sensing applications within the visible wavelength range [39]. The Si_3N_4-B waveguides were fabricated first by thermally growing a silicon dioxide layer with a thickness of 2 µm on silicon wafers. The thin Si_3N_4 layer (150 nm thick) was deposited using low-pressure chemical vapor deposition (LPCVD) at 800°C. Conventional photolithography processes were followed to deposit photoresist, UV-exposure and for defining the waveguide geometry. Photolithography was followed by reactive ion etching (RIE) to fabricate the waveguides. The remaining photoresist was then removed, and a top cladding layer was deposited by plasma-enhanced chemical vapor deposition (PECVD) at 300°C of thickness 1.5 µm. At the imaging areas, the top cladding was opened using RIE and wet etching to enable seeding of the cells. Further details of the fabrication process for Si_3N_4 waveguides can be found elsewhere [40] .

The Si_3N_4-S waveguides were fabricated by first growing a thermal oxide of 2.4 µm on silicon wafers. A thin Si_3N_4-layer of 140 nm thickness was deposited by low-pressure chemical vapour deposition (LPCVD) at 770°C. These samples were studied further as slab waveguides.

2.3 Imaging of fluorescent beads

The background intensity was first investigated by imaging a sparse sample of fluorescent beads using all three platforms (one for Ta_2O_5 and two for Si_3N_4). 500 µm wide strip waveguides were used for Ta_2O_5 and Si_3N_4-B whereas a slab waveguide was used for the Si_3N_4-S. The waveguides were treated for 30 s in a plasma cleaner to make the surface more hydrophobic, then 0.5 µL of 100 nm TetraSpeck beads was added and allowed to dry. Once the sample was dried, DI water was added to fill the PDMS chamber completely and sealed it off using a cover glass. Since the waveguides were multi-moded, approximately 1000 images were captured for each wavelength while looping the coupling objective along the coupling facet to reduce the mode pattern. For the slab waveguide, only a single image was used. All platforms were imaged with 640 nm, 561 nm and 488 nm excitation sequentially, through a matching band pass and long pass filter that would be used for fluorescence imaging.

A local thresholding algorithm (Phansalkar [41]) in ImageJ image processing software was used to identify all beads in each image. The average maximum beads intensity was measured. The maximum intensity of each bead was used in order to reduce the measurement uncertainty by averaging varying sizes of beads. An average background intensity was measured by excluding the localized beads with a 7 pixel padding.

2.3 Measuring background spectra

The background spectrum of the Si_3N_4-B was measured for excitation at 640 nm, 561 nm and 488 nm. The light was coupled into 500 μm wide strip waveguides using a 50x/0.5NA objective lens. Spectroscopic measurements were done by coupling the guided light out of the end of the waveguide and passing it through a suitable long-pass filter to remove the excitation light. The filtered signal was then coupled into a multi-mode optical fiber and passed into a Yokogawa spectrometer (AQ6373B). The spectra were collected using a collection time of 30 s and averaged over 5 measurements.

2.4 dSTORM imaging and reconstruction

The effect of the background emission on *d*STORM imaging was measured by investigating fluorophore monolayers. The monolayers were prepared on clean waveguides inside an approximately 170 um thick PDMS frame. The PDMS frame was filled with 0.01% Poly-L-Lysine (PLL) and incubated for 10 minutes. All the PLL was then drained from the chamber and the chamber was rinsed with deionized water. AF-647-dextran conjugate was then added at a concentration of 0.2 μg/ml. For imaging at 488 nm AF-488-dextran conjugate was added instead. Imaging was performed with 70 mW power from the laser coupled into the waveguides and with 30 ms exposure time. We used the following blinking buffer: 22.5 μL PBS, 20.0 μL glucose, 5 μL MEA and 2.5 μL enzymes. The measurements were performed both on the Si_3N_4-B and Ta_2O_5 waveguides.

In single molecule localization microscopy, sometimes it is desirable to simultaneously excite with a shorter wavelength, e.g. 488 nm even when imaging is performed with longer excitation wavelength, 647 nm. Activation with shorter wavelength assists to increase the blinking events and to get more fluorophores back into a fluorescing state. We investigated the effect of adding 488 nm excitation while imaging with 640 nm. Monolayers were prepared using AF-647 on the Si_3N_4-B waveguides. Half of the dataset was acquired using only 640 nm and for the latter half we added 488 nm excitation at 10% of the 640 nm power.

We also performed simulations to determine whether the multi-mode pattern of the background introduces any localization bias to the reconstruction. First, we generated a density filter for simulating realistic blinking data in ImageJ with a patterned excitation light. This was done by loading an image of the multi-mode pattern without any beads into ImageJ. The camera offset was subtracted, since parts of the waveguide will have zero intensity and thus no blinks. A Gaussian blur was then applied. The resulting image was used as the density filter. Simulated data stacks of 100 images were generated in the Thunderstorm plugin with both a low blink intensity distribution (200-500 photons) and a high (1200-1500 photons) with zero camera offset. The background pattern image was then added to the stack to give a realistic background pattern and then finally we reconstructed the stacks. Using the built-in evaluation function on the reconstructed data and the ground truth data from the simulation, we got a root mean square error (RMSE) in both the vertical and horizontal direction.

Thunderstorm [42], a plugin for ImageJ, was used for all *d*STORM image reconstruction. The datasets were filtered to remove hot pixels.

3. Results

3.1 Background

The first measurement performed was imaging of TetraSpeck beads in order to gauge the background intensity. The resulting images are presented in Figure 2. Representative waveguides were chosen from a batch and checked for damage and contaminants. The multi-mode interference patterns are clearly visible in Si_3N_4 for shorter wavelengths. Si_3N_4-S exhibits strong lines along the waveguide, which is expected as it is a slab waveguide. Si_3N_4-B on the other hand has a typical multi-mode pattern. In order to quantify the background intensity, we compared the average maximum bead intensity to the average background intensity. The beads

were localized using a local thresholding algorithm, due to the inhomogeneous background in the slab waveguides. The average bead intensity can be used to gauge the guided power inside the waveguide, so all background measurements were adjusted for differences in guided intensity between the platforms for the same wavelength. All measurements were adjusted were to the bead intensity of Ta_2O_5. The resulting measurements are presented in Table 1. It is, however, not straightforward to compare bead intensities at different excitation wavelengths as several factors that determine bead signal strength depend on wavelength, such as waveguide confinement factor and quantum yield of the beads. Ta_2O_5 has no detectable background besides the camera offset (approximately 100 counts). The background for Si_3N_4 is larger than for Ta_2O_5 at all wavelengths, although by a very small amount at 640 nm excitation. For shorter wavelengths, Si_3N_4 is increasingly challenging due to increasing background. The disparity between the platforms at all excitation wavelengths, and especially at 488nm is important to note.

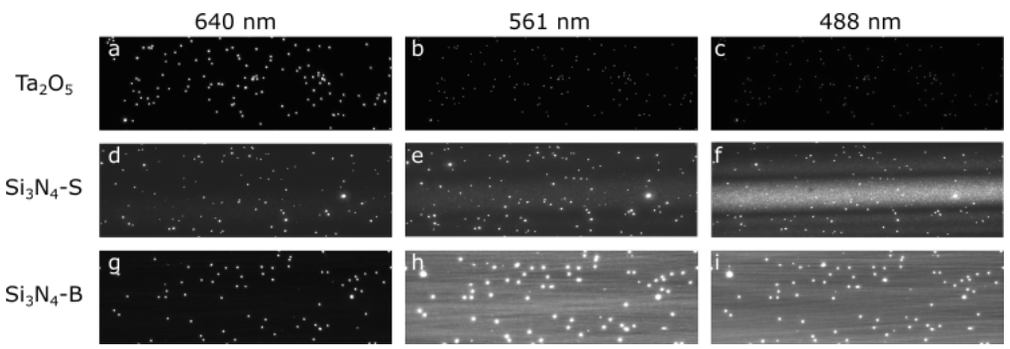

Fig. 2. Fluorescent beads imaged with waveguide excitation using different waveguide platforms with different excitation wavelengths. (a-c) Beads on Ta_2O_5 waveguides, (d-f) on Si_3N_4-S and (g-i) on Si_3N_4-B. Panels e and f exhibit a region of stronger background and this is because it is a slab waveguide and only a single image was acquired. All images are approximately 15 μm by 50 μm.

Table 1: Overview of background from the different waveguides with different excitation wavelengths. Fluorescent beads were used to adjust for similar guided power for the different waveguides at the same excitation wavelength. The backgrounds given are adjusted for similar beads strength for each wavelength. The camera used for the experiments has an offset of 100 counts. BG = background.

Wavelength (nm)	Average beads signal (counts)	Ta_2O_5 BG (counts)	Si_3N_4-S BG (counts)	Si_3N_4-B BG (counts)
640	5132	100*	102	107
561	1478	100*	107	127
488	2711	100*	150	202

It is imperative to understand the spectrum of the detected background: A background that is not spectrally overlapping with the sample could easily be filtered out with the correct filter set. We have previously studied the background from Ta_2O_5 at 532 nm excitation [10] and found a weak Raman background, which is located at short wavelengths. As the Si_3N_4-B had a stronger background than the Si_3N_4-S, we decided to only study the Si_3N_4-B further to obtain ab upper bound on the background emission. The Si_3N_4-B was further investigated by measuring the forward propagating light with a spectrometer. The intensity of the forward propagating background depends on the propagated distance, and more importantly, it varies with wavelength due to changes in propagation loss with wavelength. The coupled light will decay exponentially along propagation distance, but the background will have a maximum at the saturation distance $L_s=1/\alpha$, where α is the propagation loss. The measured spectrum thus has to be adjusted for the saturation length of the waveguide platform for the given wavelength.

The resulting spectra for 640 nm, 561 nm and 488 nm excitation is plotted in Figure 3a, with logarithmic axes. The spectra have been normalized in Fig. 3b, in order to more easily see the shape of the spectra. The spectrometer used in these experiments did not have high enough sensitivity to measure the weak background from Ta_2O_5, and since it did not have any effect on the imaging, it was not pursued further.

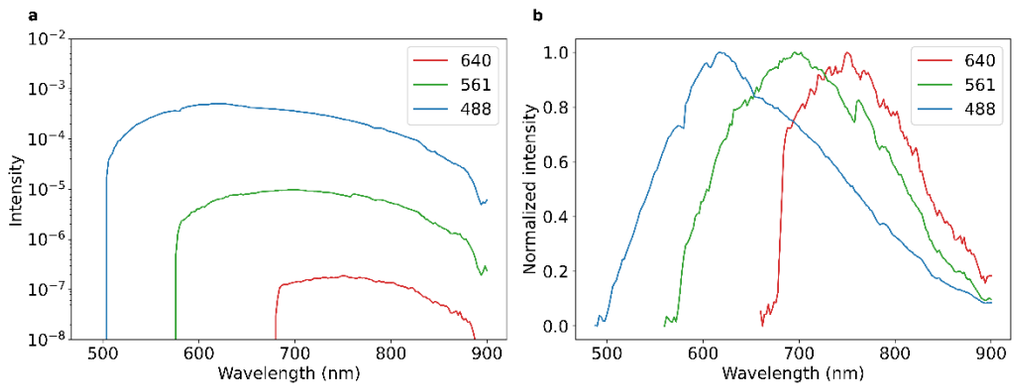

Fig. 3. (a) Background spectra for Si_3N_4-B for three different excitation wavelengths plotted on a logarithmic scale. (b) Normalized spectra.

3.2 Effect of background on super-resolution imaging

We investigated the background effect on single molecule blinking data fitting for Ta_2O_5, which exhibited the lowest background, and Si_3N_4-B, which exhibited the highest background. Each platform was imaged with 640 nm and 488 nm, as the background increases with shorter wavelengths. Example images of sparse blinks for each combination is presented in Figure 4, panels a-d. The localization uncertainty is of great interest in single molecule localization microscopy, as it determines the resolution of the image. Box plots of the localization uncertainty for each sample imaged are presented in panels e-h. The mean and standard deviation of the localization uncertainty, background standard deviation and intensity for all measurements are found in panels i-k. For Ta_2O_5, the average localization uncertainty is 12.9 ± 1.8 nm for 640 nm excitation and 13.9 ± 1.9 nm for 488 nm excitation. For Si_3N_4-B, the average blinking uncertainty is 17.0 ± 2.6 nm for 640 nm excitation and 22.6 ± 3.9 nm for 488 nm excitation. There is a difference in all parameters, even for 640 nm where Si_3N_4 has almost no background, but this may be due to differences in platform such as confinement factor. It is important to note that the fluorophores used for 640 nm and 488 nm are not the same, and as such the difference in parameters with wavelength can be expected. The most interesting point to note is that the parameters are consistent for 488 nm and 640 nm for Ta_2O_5, whereas for Si_3N_4-B the parameters are affected by the increased background at 488 nm compared to 640 nm.

The effect of a homogeneous background on the localization precision can be calculated using the following equation, assuming a background limited case [43]:

$$\langle(\Delta x)^2\rangle = \frac{4\sqrt{\pi}s^3b^2}{aN^2}$$

Where Δx is the localization error, s the standard deviation of the PSF, b the background noise, a the pixel size and N the number of photons collected. The values for a and s for the chip-based system is 106.5 nm and 113 nm, respectively. The number of photons and the background will depend on excitation wavelength for a background from the waveguide. Estimates of the background and photon counts for beads can be taken from Table 1 and converted into photons from counts. Typical values of AF647 blinks with the chip-based

platform is around 500-1000 photons, which results in a localization precision as low as 15 nm for Ta_2O_5 and 16 nm for Si_3N_4-B. These match closely with the experimental results shown in Fig. 4i. For AF488 typical blink intensity on chips is around 260 photons, which gives a resolution of 62 nm in Ta_2O_5. The higher background in Si_3N_4-B will result in a loss in localization precision at 488 nm, giving 115 nm resolution for the high background case. This is not in agreement with the experimental results, but during the reconstruction process poor fits are rejected automatically, and as such the localization precision from the experiments will be artificially inflated. This means that even though the signal-to-background ratio on average is poor, data can still be reconstructed from the high intensity blinks. However, due to rejection of poorer blinking images, it could require a larger number of images during bio-imaging experiments.

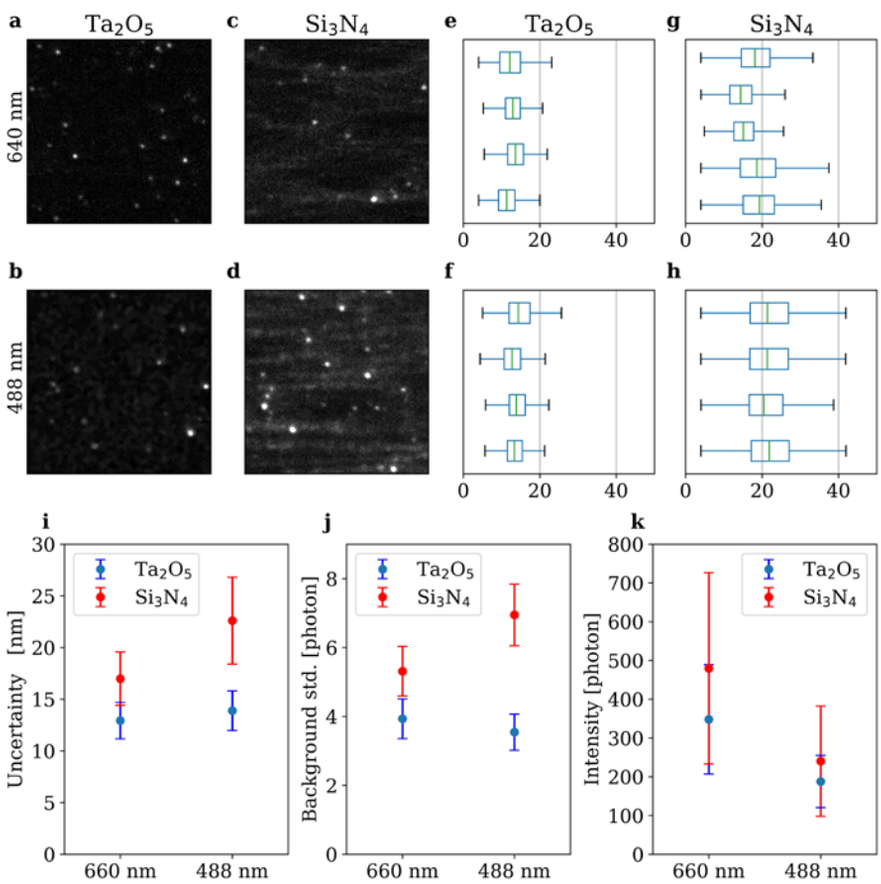

Fig. 4. (a-b) Representative image from *d*STORM data for Ta_2O_5 with AF647 and AF488. The imaged area is approximately 12 µm x 12 µm. (c-d) Representative image from *d*STORM data for Si_3N_4-B with AF647 and AF488. (e-f) Blinking statistics of reconstructed datasets for Ta_2O_5 with AF647 and AF488. Each box plot is a separate measurement; (g-h) Blinking statistics of reconstructed datasets for Si_3N_4-B with AF647 and AF488 image. The horizontal axis is in nanometers for panel (e-h). (i-k) Summary of localization uncertainty, background standard deviation and intensity for all measured samples.

The illumination generated by the optical waveguide is not uniform, thus the background and excitation distribution are not homogeneous, as assumed in the above calculation. There is

instead a distinct mode pattern as can be observed in Fig. 1b. The waveguides used in the work are highly multi-mode and will therefore exhibit patterns such as that in Fig 1b. The specific pattern will depend on the coupling into the waveguides, but due to the structure of the waveguide they will all have a directionality along the propagation direction. Such an inhomogeneous background can introduce a difference in localization precision along the propagation direction compared to the perpendicular direction. Analysis of simulated data with experimentally captured background patterns showed that the localization uncertainty was 18.0 nm in the vertical direction and 13.7 in the horizontal direction for the low intensity blinks (200-500 photons). In the high intensity sample (1200-1500 photons), the results were 9.2 nm in the vertical direction and 6.2 in the horizontal direction. This means that there is a small degree of bias introduced by the directionality and inhomogeneity of the pattern. A stronger background will increase this effect, whereas for low background the difference will disappear. Testing it with Ta_2O_5 background showed that there was no difference in the uncertainties.

The final experiment was to investigate if adding a 488 nm laser when imaging with a 640 nm fluorescent dye would deteriorate the localization precision. A short wavelength laser is commonly used in single molecule localization microscopy for tuning of the on and off states during the imaging process. Imaging can take a while in *d*STORM, which results in fluorescent dye molecules stuck in dark states. A short wavelength laser can help relax the dye molecules in dark states back to a fluorescing state. A 488 nm excitation does give a much stronger background compared to 640 in our Si_3N_4 waveguides, so it is of interest to determine whether a 5-10% 488 nm power for reactivating the fluorophores will affect the localization precision. Reconstructions of the same sample with and without 488 nm excitation (in addition to the main 640 nm excitation) showed no detectable difference in the results for both silicon nitride and tantalum pentoxide waveguide materials.

4. Discussion and conclusion

We have studied the background from two commonly used waveguide materials, Si_3N_4 and Ta_2O_5, for applications in super-resolution optical microscopy and Raman spectroscopy in the visible part of the spectrum. Ta_2O_5 has very little background for all the tested excitation wavelengths, which agrees well with previous literature [10]. Si_3N_4, on the other hand, exhibits a relatively strong background at shorter wavelengths (488 nm). Previous literature on Si_3N_4 has reported the comparable performance of Si_3N_4 with respect to the background of Ta_2O_5 when pumped at 785 nm [44]. In agreement with the previous literature, we also observed comparable background between the two materials when excited at 640 nm, however, the background for Si_3N_4 significantly increases at shorter wavelengths. Both platforms are therefore well suited for *d*STORM imaging at 640 nm, whereas Ta_2O_5 is expected to perform better at shorter wavelengths. For shorter wavelengths, such as at 488 nm excitation, the background for Si_3N_4 reduces the localization precision for *d*STORM imaging.

Using fluorescent beads and exciting them with the evanescent field is a simple way to gauge the background of the waveguide for imaging purposes. There was a clear increase in background for Si_3N_4 at shorter wavelengths for both fabrication methods chosen in this study. The fact that the absorption and quantum yield of the beads vary with wavelength makes a direct comparison impossible for one material between different excitation wavelengths, as a change in signal-to-background could be due to a change in e.g. quantum yield of the beads with wavelength. A fall in signal-to-background at shorter wavelengths could also be due to a fall in quantum yield of the beads at shorter wavelengths, rather than an actual increase in the background. However, the beads should exhibit a similar behavior on all platforms over the different excitation wavelengths, although differences in e.g. confinement factor between the platforms may cause some deviations. We are not able to rule out any differences in e.g. confinement factor, but with the results from Figure 3, it is clear that increase in background between the platforms is mostly due to an increase in the background. Since the change is not the same for Si_3N_4 and Ta_2O_5, it means that the background in Si_3N_4 does increase at shorter

wavelengths. This is further proven from the spectral measurements, as the background strength increases significantly at shorter wavelengths for Si_3N_4. From the spectroscopy experiment, it was evident that the background is a very wide fluorescent signal and thus it is not possible to filter it out very efficiently. The background originating in the waveguide, when irradiating at 488 nm, may have different origins (defects, composition, impurities in the silicon nitride core layers), but it seems that the stoichiometry shift could increase the UV absorption showing that films enriched with silicon show higher luminescence in the visible region of the electromagnetic spectrum [45].

The effect of the background signal is important to fluorescence optical microscopy. For diffraction limited imaging the background does reduce the image quality, but is not detrimental, as the signal-to-background ratio in fluorescence microscopy is usually good. For *d*STORM, where signals are observed from single molecules, the background clearly has an adverse effect on the result. The measured increase in e.g. localization uncertainty shown in Figure 4 is not drastic, but it is underestimated in the present experiment, where we have only localized the fluorophores placed directly on top of waveguide surface. According to the calculations on a homogeneous background from Equation 1, a significant loss in localization precision is expected for Si_3N_4 at 488 nm excitation. The reason that the experimental data underestimates the effect is that the reconstruction algorithm disregards localizations outside a given threshold. Thus, several blinks will be disregarded in the experimental data which could necessitate acquisitions of a larger number of images. It could thus be possible to perform *d*STORM at 488 nm, but it will both degrade the result and put restraints on data collection. Additionally, the inhomogeneous background pattern does cause a small bias in the localization precision. The bias has a maximum 4.3 nm in the low intensity case and 3.1 nm in the high intensity case. For Ta_2O_5 no such bias will occur, as there is no detectable background.

When imaging with 640 nm excitation and adding a small percentage (10%) of 488 nm excitation (for *d*STORM), it barely has any detectable difference. This was further investigated by simulations using the same background pattern from Si_3N_4 at 488 nm as above, but increasing the photon count tenfold, showed no discernable difference in vertical and horizontal root mean square error.

In summary, we have investigated Si_3N_4 and Ta_2O_5 for visible wavelength applications, in particular super-resolution optical microscopy and spectroscopic applications. Si_3N_4 has an increase in background at shorter wavelengths, whereas Ta_2O_5 has very weak background, effectively undetectable for imaging purposes. Despite the background of Si_3N_4 it might still be used for diffraction limited imaging. For super-resolution imaging at 488nm with SMLM, due to higher background with Si_3N_4, greater number of single molecule blinks rejected. It is also important to note the possibility of a bias due to the background pattern. With the increasing interest in integrated photonics employing visible light, further investigations into the origin of the background in Si_3N_4 at shorter wavelengths would be interesting to explore in the future, to determine if there are a correlation between the film composition and the background appearing.

Funding. B.S.A acknowledge the funding from UiT Tematiske Satsinger and Research Council of Norway (project #BIOTEK 2021-285571).

Disclosures. B.S.A. has applied for two patents for chip-based optical nanoscopy. The authors declare no conflicts of interest. B.S.A. and Ø.I.H are co-founders of the company Chip NanoImaging AS, which commercializes on-chip super-resolution microscopy systems.

Data availability. Data underlying the results presented in this paper are not publicly available at this time but may be obtained from the authors upon reasonable request.

References

1. G. Lifante, *Integrated Photonics: Fundamentals* (John Wiley & Sons, 2003).
2. L. B. Soldano and E. C. M. Pennings, "Optical multi-mode interference devices based on self-imaging: principles and applications," Journal of Lightwave Technology **13**, 615–627 (1995).
3. A. Aghajani, G. S. Murugan, N. P. Sessions, V. Apostolopoulos, and J. S. Wilkinson, "Waveguide lasers in ytterbium-doped tantalum pentoxide on silicon," Opt. Lett., OL **40**, 2549–2552 (2015).
4. L. Sansoni, F. Sciarrino, G. Vallone, P. Mataloni, A. Crespi, R. Ramponi, and R. Osellame, "Two-Particle Bosonic-Fermionic Quantum Walk via Integrated Photonics," Phys. Rev. Lett. **108**, 010502 (2012).
5. M. Boerkamp, T. van Leest, J. Heldens, A. Leinse, M. Hoekman, R. Heideman, and J. Caro, "On-chip optical trapping and Raman spectroscopy using a TripleX dual-waveguide trap," Opt. Express, OE **22**, 30528–30537 (2014).
6. B. S. Ahluwalia, P. McCourt, T. Huser, and O. G. Hellesø, "Optical trapping and propulsion of red blood cells on waveguide surfaces," Opt. Express, OE **18**, 21053–21061 (2010).
7. X. Fan, I. M. White, S. I. Shopova, H. Zhu, J. D. Suter, and Y. Sun, "Sensitive optical biosensors for unlabeled targets: A review," Analytica Chimica Acta **620**, 8–26 (2008).
8. A. Dhakal, P. C. Wuytens, F. Peyskens, K. Jans, N. Le Thomas, and R. Baets, "Nanophotonic Waveguide Enhanced Raman Spectroscopy of Biological Submonolayers," ACS Photonics **3**, 2141–2149 (2016).
9. C. C. Evans, C. Liu, and J. Suntivich, "TiO2 Nanophotonic Sensors for Efficient Integrated Evanescent Raman Spectroscopy," ACS Photonics **3**, 1662–1669 (2016).
10. D. A. Coucheron, D. N. Wadduwage, G. S. Murugan, P. T. C. So, and B. S. Ahluwalia, "Chip-Based Resonance Raman Spectroscopy Using Tantalum Pentoxide Waveguides," IEEE Photonics Technology Letters 1–1 (2019).
11. Ø. I. Helle, C. I. Øie, P. McCourt, and B. S. Ahluwalia, "Chip-based optical microscopy for imaging membrane sieve plates of liver scavenger cells," in (2015), Vol. 9554, pp. 95540O-95540O–5.
12. N. F. Tyndall, D. A. Kozak, M. W. Pruessner, R. A. McGill, C. A. Roberts, T. H. Stievater, B. L. Miller, E. Luta, M. Z. Yates, E. D. Emmons, P. G. Wilcox, and J. A. Guicheteau, "Backscatter WERS for trace chemical analyte detection using a handheld spectrometer," in *Chemical, Biological, Radiological, Nuclear, and*

Explosives (CBRNE) Sensing XXI (International Society for Optics and Photonics, 2020), Vol. 11416, p. 1141603.
13. R. Baets, A. Z. Subramanian, A. Dhakal, S. K. Selvaraja, K. Komorowska, F. Peyskens, E. Ryckeboer, N. Yebo, G. Roelkens, and N. Le Thomas, "Spectroscopy-on-chip applications of silicon photonics," in (2013), Vol. 8627, pp. 86270I-86270I–10.
14. F. Peyskens, A. Dhakal, P. Van Dorpe, N. Le Thomas, and R. Baets, "Surface Enhanced Raman Spectroscopy Using a Single Mode Nanophotonic-Plasmonic Platform," ACS Photonics **3**, 102–108 (2016).
15. Z. Wang, M. N. Zervas, P. N. Bartlett, and J. S. Wilkinson, "Surface and waveguide collection of Raman emission in waveguide-enhanced Raman spectroscopy," Opt. Lett. **41**, 4146–4149 (2016).
16. H. M. K. Wong, M. K. Dezfouli, L. Sun, S. Hughes, and A. S. Helmy, "Nanoscale plasmonic slot waveguides for enhanced Raman spectroscopy," Phys. Rev. B **98**, 085124 (2018).
17. P. C. Wuytens, A. G. Skirtach, and R. Baets, "On-chip surface-enhanced Raman spectroscopy using nanosphere-lithography patterned antennas on silicon nitride waveguides," Opt. Express, OE **25**, 12926–12934 (2017).
18. H. Zhao, S. Clemmen, A. Raza, and R. Baets, "Stimulated Raman spectroscopy of analytes evanescently probed by a silicon nitride photonic integrated waveguide," Opt. Lett., OL **43**, 1403–1406 (2018).
19. A. Dhakal, "Nanophotonic Waveguide Enhanced Raman Spectroscopy," (2016).
20. Z. Wang, S. J. Pearce, Y.-C. Lin, M. N. Zervas, P. N. Bartlett, and J. S. Wilkinson, "Power Budget Analysis for Waveguide-Enhanced Raman Spectroscopy," Appl. Spectrosc., AS **70**, 1384–1391 (2016).
21. A. Dhakal, A. Raza, P. Wuytens, F. Peyskens, A. Skirtach, N. L. Thomas, and R. Baets, "Lab-on-a-chip Raman sensors outperforming Raman microscopes," in *2016 Conference on Lasers and Electro-Optics (CLEO)* (2016), pp. 1–2.
22. C. C. Evans, C. Liu, and J. Suntivich, "Integrated-Evanescent Raman Sensors Based on Titanium-Dioxide Nanophotonics," Meet. Abstr. **MA2016-01**, 2008–2008 (2016).
23. T. C. Strekas and T. G. Spiro, "Hemoglobin: Resonance Raman spectra," Biochimica et Biophysica Acta (BBA) - Protein Structure **263**, 830–833 (1972).
24. C. G. Atkins, K. Buckley, M. W. Blades, and R. F. B. Turner, "Raman Spectroscopy of Blood and Blood Components," Applied Spectroscopy **71**, 767–793 (2017).
25. R. Diekmann, Ø. I. Helle, C. I. Øie, P. McCourt, T. R. Huser, M. Schüttpelz, and B. S. Ahluwalia, "Chip-based wide field-of-view nanoscopy," Nat Photon **11**, 322–328 (2017).
26. A. Archetti, E. Glushkov, C. Sieben, A. Stroganov, A. Radenovic, and S. Manley, "Waveguide-PAINT offers an open platform for large field-of-view super-resolution imaging," Nat Commun **10**, (2019).

27. Ø. I. Helle, F. T. Dullo, M. Lahrberg, J.-C. Tinguely, O. G. Hellesø, and B. S. Ahluwalia, "Structured illumination microscopy using a photonic chip," Nature Photonics **14**, 431–438 (2020).
28. A. Priyadarshi, F. T. Dullo, D. L. Wolfson, A. Ahmad, N. Jayakumar, V. Dubey, J.-C. Tinguely, B. S. Ahluwalia, and G. S. Murugan, "A transparent waveguide chip for versatile TIRF-based microscopy and nanoscopy," arXiv:2006.07275 [physics] (2020).
29. N. Jayakumar, N. Jayakumar, Ø. I. Helle, K. Agarwal, B. S. Ahluwalia, B. S. Ahluwalia, and B. S. Ahluwalia, "On-chip TIRF nanoscopy by applying Haar wavelet kernel analysis on intensity fluctuations induced by chip illumination," Opt. Express, OE **28**, 35454–35468 (2020).
30. E. Betzig, G. H. Patterson, R. Sougrat, O. W. Lindwasser, S. Olenych, J. S. Bonifacino, M. W. Davidson, J. Lippincott-Schwartz, and H. F. Hess, "Imaging intracellular fluorescent proteins at nanometer resolution," Science **313**, 1642–1645 (2006).
31. M. J. Rust, M. Bates, and X. Zhuang, "Sub-diffraction-limit imaging by stochastic optical reconstruction microscopy (STORM)," Nat Meth **3**, 793–796 (2006).
32. S. T. Hess, T. P. K. Girirajan, and M. D. Mason, "Ultra-high resolution imaging by fluorescence photoactivation localization microscopy," Biophys. J. **91**, 4258–4272 (2006).
33. M. Heilemann, S. van de Linde, M. Schüttpelz, R. Kasper, B. Seefeldt, A. Mukherjee, P. Tinnefeld, and M. Sauer, "Subdiffraction-Resolution Fluorescence Imaging with Conventional Fluorescent Probes," Angewandte Chemie International Edition **47**, 6172–6176 (2008).
34. R. Jungmann, M. S. Avendaño, J. B. Woehrstein, M. Dai, W. M. Shih, and P. Yin, "Multiplexed 3D cellular super-resolution imaging with DNA-PAINT and Exchange-PAINT," Nature Methods **11**, 313–318 (2014).
35. Ø. I. Helle, D. A. Coucheron, J.-C. Tinguely, C. I. Øie, and B. S. Ahluwalia, "Nanoscopy on-a-chip: super-resolution imaging on the millimeter scale," Opt. Express, OE **27**, 6700–6710 (2019).
36. R. E. Thompson, D. R. Larson, and W. W. Webb, "Precise nanometer localization analysis for individual fluorescent probes," Biophys. J. **82**, 2775–2783 (2002).
37. B. S. Ahluwalia, A. Z. Subramanian, O. G. Hellso, N. M. B. Perney, N. P. Sessions, and J. S. Wilkinson, "Fabrication of Submicrometer High Refractive Index Tantalum Pentoxide Waveguides for Optical Propulsion of Microparticles," IEEE Photonics Technology Letters **21**, 1408–1410 (2009).
38. P. Muñoz, P. W. L. van Dijk, D. Geuzebroek, M. Geiselmann, C. Domínguez, A. Stassen, J. D. Doménech, M. Zervas, A. Leinse, C. G. H. Roeloffzen, B. Gargallo, R. Baños, J. Fernández, G. M. Cabanes, L. A. Bru, and D. Pastor, "Foundry Developments Toward Silicon Nitride Photonics From Visible to the Mid-Infrared," IEEE Journal of Selected Topics in Quantum Electronics **25**, 1–13 (2019).

39. M. A. G. Porcel, A. Hinojosa, H. Jans, A. Stassen, J. Goyvaerts, D. Geuzebroek, M. Geiselmann, C. Dominguez, and I. Artundo, "[INVITED] Silicon nitride photonic integration for visible light applications," Optics & Laser Technology **112**, 299–306 (2019).
40. F. Prieto, B. Sepúlveda, A. Calle, A. Llobera, C. Domínguez, A. Abad, A. Montoya, and L. M. Lechuga, "An integrated optical interferometric nanodevice based on silicon technology for biosensor applications," Nanotechnology **14**, 907 (2003).
41. Neerad Phansalkar, Sumit More, Ashish Sabale, and Madhuri Joshi, "Adaptive local thresholding for detection of nuclei in diversity stained cytology images," in *2011 International Conference on Communications and Signal Processing* (2011), pp. 218–220.
42. M. Ovesný, P. Křížek, J. Borkovec, Z. Švindrych, and G. M. Hagen, "ThunderSTORM: a comprehensive ImageJ plug-in for PALM and STORM data analysis and super-resolution imaging," Bioinformatics **30**, 2389–2390 (2014).
43. R. E. Thompson, D. R. Larson, and W. W. Webb, "Precise Nanometer Localization Analysis for Individual Fluorescent Probes," Biophysical Journal **82**, 2775–2783 (2002).
44. A. Raza, S. Clemmen, P. Wuytens, M. de Goede, A. S. K. Tong, N. L. Thomas, C. Liu, J. Suntivich, A. G. Skirtach, S. M. Garcia-Blanco, D. J. Blumenthal, J. S. Wilkinson, and R. Baets, "High index contrast photonic platforms for on-chip Raman spectroscopy," Opt. Express, OE **27**, 23067–23079 (2019).
45. H. T. Nguyen, F. E. Rougieux, D. Yan, Y. Wan, S. Mokkapati, S. M. de Nicolas, J. P. Seif, S. De Wolf, and D. Macdonald, "Characterizing amorphous silicon, silicon nitride, and diffused layers in crystalline siliconsolarcellsusingmicro-photoluminescence spectroscopy," Solar Energy Materials and Solar Cells **145**, 403–411 (2016).

Paper II

Chip-based nanoscopy: towards integration and high-throughput imaging

D. A. Coucheron, Ø. I. Helle, C. I. Øie, F. T. Dullo, B. S. Ahluwalia.

Chip-based nanoscopy: towards integration and high-throughput imaging

Coucheron, David, Helle, Øystein, Øie, Christina, Dullo, Firehun, Ahluwalia, Balpreet

David A. Coucheron, Øystein I. Helle, Christina I. Øie, Firehun T Dullo, Balpreet S. Ahluwalia, "Chip-based nanoscopy: towards integration and high-throughput imaging," Proc. SPIE 10350, Nanoimaging and Nanospectroscopy V, 103500W (14 December 2017); doi: 10.1117/12.2273902

SPIE.

Event: SPIE Nanoscience + Engineering, 2017, San Diego, California, United States

Chip Based Nanoscopy: Towards Integration and High-throughput Imaging

David A. Coucheron*[1], Øystein I. Helle[1], Cristina I. Øie[1], Firehun T. Dullo[1], Balpreet S. Ahluwalia[1]
[1]UiT – The Arctic University of Norway, Department of Physics and Technology, 9037 Tromsø, Norway.
*david.a.coucheron@uit.no

ABSTRACT

Super-resolution optical microscopy, commonly referred to as optical nanoscopy, has enabled imaging of biological samples with a resolution that was only achievable previously using electron microscopy. Optical nanoscopy is a rapidly growing field, with several different techniques and implementations that overcome the diffraction limit of light. However, the common nanoscope continues to be a rather complex, expensive and bulky instrument. Direct stochastic optical reconstruction microscopy (*d*STORM) imaging was recently demonstrated using a waveguide platform for excitation in combination with a simple microscope for imaging. High refractive index waveguide materials have a high intensity evanescent field stretching around 100-200 nm outside the guiding material, which is ideally suited for total internal reflection fluorescence (TIRF) excitation over large areas. We demonstrate *d*STORM imaging of the plasma membrane of liver sinusoidal endothelial cells (LSECs) and trophoblasts (HTR-8 cells) using waveguide excitation, with resolution down to around 70 nm. Additionally, we present TIRF imaging of LSEC micro-tubules over a 500 μm x 500 μm area, laying the foundation for large field of view (f-o-v) nanoscopy.

Keywords: Waveguide, *d*STORM, TIRF, LSEC, HTR-8, super-resolution optical microscopy

INTRODUCTION

The fluorescence microscope is an indispensable tool in biological research, and has contributed to many important discoveries[1]. However, the spatial resolution of the technique has long been limited by the diffraction limit of light. As light from a point emitter is focused by a lens to form an image, it will actually focus into an airy disk of lateral size approximately half the wavelength of the light (ca. 250-300 nm)[2]. The diffraction limit restricts the optical resolution of imaging techniques, as two closely placed overlapping airy disks will be unresolvable, giving rise to the resolution limit. Overcoming the diffraction limit is of great importance, as many biological processes and structures are smaller than the diffraction limit, and are therefore unresolvable by optical microscopy.

Research into super-resolution optical microscopy started a couple of decades ago and has led to several different techniques, each with different advantages and disadvantages. In 1994, Hell et al. proposed a theoretical basis for overcoming the resolution limit in optical microscopy[3]. In the following years, Hell and coworkers demonstrated and advanced the technique called saturated emission depletion microscopy (STED). In 2006, super-resolution optical microscopy emerged as a research field, with three similar fluorescence based techniques introduced almost simultaneously, commonly termed single molecule localization (SLM) microscopy. The techniques are fluorescence photoactivation localization microscopy (FPALM)[4], photoactivated localization microscopy (PALM)[5], and stochastic optical reconstruction microscopy (STORM)[6]. Two years later, a more versatile and general approach to STORM was introduced, termed direct-STORM (*d*STORM) since it does not use activator fluorophores[7]. A third class of super-resolution microscopy techniques based on structured illumination was introduced in 2000[8]. Linear structured illumination microscopy (SIM) is, however, limited to a twofold increase in resolution, unlike STED and SML techniques.

In SLM based microscopy, the super-resolution is achieved by exploiting the fact that diffraction limits resolution, but not necessarily the localization precision of fluorophores. Specialized fluorophores that exhibit both a fluorescing (on) and a non-fluorescing (off) state are used to image only sparse subsets of the fluorophores simultaneously. The key requirement is that the active fluorophores are sparse enough to be identified as single emitters, meaning that they have to be separated by more than the diffraction limit. Having the prior information that the signals

Nanoimaging and Nanospectroscopy V, edited by Prabhat Verma, Alexander Egner, Proc. of SPIE
Vol. 10350, 103500W · © The Authors. Published under a Creative Commons Attribution
CC-BY 3.0 License · doi: 10.1117/12.2273902

(photons) come from the single emitter (single fluorophore molecule), the two-dimensional Gaussian profile can be fitted with high accuracy to determine the center location of the fluorophore. The localization precisions of the center position is influenced by the signal to noise ratio and with an increase of photons number the localization precision of 10 nm or better can be obtained.

Since the discovery of optical nanoscopy, the field has emerged rapidly and optical nanoscopes are slowly making inroads in mainstream biology and life sciences. However, present day optical nanoscopy still possess several challenges, with the most prominent being: costly and complex microscopes, lack of multi-modality, low temporal resolution, need of special fluorophores, and low-throughput.

There is a growing interest for high-throughput imaging in biological research[9]. High-throughput diffraction limited fluorescence microscopy is used in biological research, partly motivated by the pharmaceutical industry. High-throughput can refer to many things: high-speed imaging, parallel imaging, increased field-of-view (f-o-v) or multiplexing. Super-resolution microscopy, however, poses new challenges when moving towards high-throughput imaging. Increased temporal resolution has seen much interest, with SIM performing well, albeit at limited resolution[10]. STED can also achieve very high temporal resolution, when performing imaging over small field-of-views[11]. In 2014, *d*STORM was also performed at video-rate acquisition by employing specialized fitting algorithms for sCMOS cameras in combination with multi-emitter fitting algorithms[12].

Super-resolution optical microscopy has also been moving towards high throughput by imaging an increased f-o-v. STED is a confocal based point scanning technique and therefore inherently slow when imaging large areas. On the other hand, the techniques like SML microscopy and SIM are wide field techniques. In SML microscopy techniques, such as *d*STORM, the sample is commonly illuminated either by the evanescent field generated using a total internal reflection fluorescence (TIRF) objective lens, or a highly inclined thin illumination (HiLo) from the same type of lens. A TIRF lens with high N.A. (e.g 1.4) is required to illuminate the sample with an angle of incidence greater than the critical angle of incidence to generate evanescent field at the interface. The high N.A. TIRF lens also comes with high magnification (typically 60-100X) that limits the f-o-v down to around 100 x 100 μm^2. Despite rather small f-o-v, simultaneous multi-color imaging has been achieved in various ways[13–15], reducing collection time significantly.

In this paper, we show TIRF and super-resolution imaging using a photonic chip waveguide platform that is ideally suited for high-throughput TIRF and super-resolution imaging[16]. Waveguide structures are today commonly employed in e.g. sensing applications[17], Raman spectroscopy[18] and optical trapping[19,20]. Integrated photonic circuit enables easy beam shaping, and is well suited for integration with e.g. microfluidic devices. The key aspect of the waveguide platform is that the guided light will generate an evanescent field at the surface of the waveguide structure. As the evanescent field decays over 100-200 nm, it offers intrinsic optical sectioning. The sample is placed directly on top of the waveguide surface and is illuminated by the evanescent field of the waveguide (Fig. 1a). By using high-refractive index materials for the waveguide structures and by confining the light tightly inside a thin waveguide (100-200 nm thick) the light in the evanescent field can be intensified, enabling fluorophore blinking, which is a key requirement for *d*STORM. Traditionally, super-resolution imaging is performed with advanced microscopes to excite and collect the fluorescence. In the proposed set-up, the photonic circuits are used both to hold and to excite the sample, whereas the signal is collected using a simple microscope. The photonic chip-based system has many important advantages. It decouples the excitation and the collection light paths. As discussed above, in conventional *d*STORM a TIRF objective lens is commonly used both to excite the fluorophores and to collect the emitted fluorescence, therefore limiting the f-o-v. Instead of using the objective lens to both generate evanescent field excitation and to collect fluorescence, the waveguide platform is used to produce evanescent field illumination over the whole structure. The illumination area can therefore be very large, as it is only limited by the waveguide size, unlike TIRF objectives. By using a low magnification lens for collection, large areas can be imaged. The increased depth of field of lower magnification lenses is not a problem, as waveguides give intrinsic optical sectioning. Additionally, the photonic chips allow easy integration with other integrated optical functions such as e.g. optical trapping[19,20] and Raman spectroscopy[21]. Finally, the waveguide chips can be made cost-effective by mass-production.

Our aim was to investigate the potential of the waveguide platform for large f-o-v *d*STORM imaging. Using the photonic chip based TIRF microscope, we image the plasma membrane of liver sinusoidal endothelial cells (LSECs) and trophoblasts (HTR-8 cells) with *d*STORM. We were able to image the LSEC fenestrations, transmembrane holes of 50-150 nm in diameter, morphological characteristic of these cells, demonstrating a resolution of around 70 nm. *d*STORM imaging was performed over modest f-o-v (using 60x/1.2 N.A. WI objective lens), but we also present a TIRF image of LSEC microtubulin over 500 μm x 500 μm (25x/0.8 N.A. WI/OI objective lens). This clearly illustrates that the waveguide platform is ideally suited for large area TIRF excitation, a prerequisite for large f-o-v *d*STORM imaging.

METHODS

1.1 CHIP-BASED NANOSCOPE

The experimental set-up of the chip-based optical nanoscope is shown in Fig. 1b. In this work, we used an Olympus compound microscope for collection. A Cobolt Flamenco 660 nm laser and an Oxxius 488 nm laser were used for the excitation. The laser beams were expanded to slightly overfill the coupling objective, coupling into a single-mode fiber. Light is coupled into to the planar waveguides from the single mode fiber by allowing the cleaved fiber tip to almost touch the end facet of the waveguide. The portion of light that is coupled into the waveguide will be guided in discrete modes along the full stretch of the waveguide. For wide waveguides, a large number of modes will populate the structure in multi-mode interference patterns. The effect is rather devastating on the homogeity of the evanescent field, resulting in a non-uniform excitation of the fluorophores. To compensate for this, we scramble the modes using a piezo scanning translation stage. The input fiber is shifted laterally along the waveguide facet using the piezo stage, resulting in a new subset of modes for every new position of the input fiber. Depending on the speed of the mode scrambling the average of a set frames will give a much more homogenous excitation. Additionally, the piezo stage is also used for optimizing the coupling on to the planar waveguide initializing the experiment. Chips were held using a vacuum stage on top of an xyz-stage. The coupling and sample stages were mounted on a long travel distance stage for sample translation. The emitted fluorescence is collected using a 60x/1.2NA WI objective lens for small f-o-v or a 25x/0.85 NA WI/OI objective lens for large f-o-v. The collected signal is passed through a 664 LP filter and 692/40 emission filter. For 488 nm excitation, a 488 LP filter and a 520/36 emission filter were used. An Olympus tube lens forms the image on an sCMOS camera (Hamamatsu ORCA Flash v2). TIRF imaging was done at 100 mW from the laser, passing through an ND 2.0 filter. The *d*STORM images were captured using 550 mW power from the 660 nm laser. Typical camera exposure times for TIRF imaging is in the range of 100 ms, while dSTORM imaging is acquired around 30 ms, although individual adjustments are required for the blinking ratio of the given fluorophore/experiment.

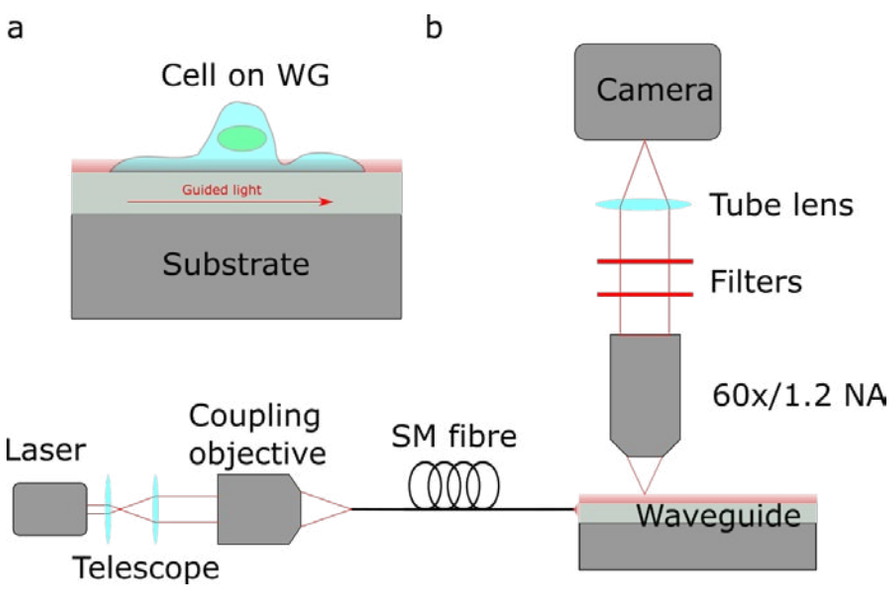

Figure 1: (a) Illustration of how the evanescent field can be used in TIRF imaging. The light is guided inside the waveguide, generating an evanescent field stretching approximately 100-150 nm out of the waveguide. The sample is placed in contact with the waveguide structure. (b) Schematic of the set-up, with fiber coupling into the waveguide and collection through a standard microscope.

1.2 SAMPLE PREPARATION

The waveguides were fabricated using previously designed procedures[22,23] The waveguides were cleaned before experiments for 10 minutes in 1% Hellmanex in deionized (DI) water at a 70°C hotplate. Following soaking, the waveguides were rinsed with DI water, iso-propanol and DI water again. A hollow rectangular PDMS frame was applied to form the sample chamber, containing the aqueous imaging buffer and to limit the cell attachment. The PDMS frames are shaped like small windows forming a sample chamber, open in the center outlining the imaging area. The thickness of the PDMS chambers is kept shallow (130 µm) to not exceed the working distance of the microscope objectives. The waveguides surface was coated with human fibronectin (50 $\mu g ml^{-1}$) for 10 min at RT prior to cell seeding. Isolated rat LSECs in RPMI 1640 were seeded on the waveguide and allowed attachment for 1 h at 37°C in incubator, followed by removal of non-adherent cells, and another 1h for cytoplasm extension. Human placenta epithelial trophoblast cell line (HTR-8) were seeded on waveguides and incubated for 4 hours. Finally, the cells were washed with PBS and fixed with a solution of 4% paraformaldehyde in PBS and 0.02 M sucrose (pH 7.2) for 30 min.

The plasma membranes of both cell types were stained using Cell Mask Deep Red (CMDR), using the following protocol. The fixative was removed and the cell cultures rinsed with PBS 2 times for 5 minutes. A solution of 1% bovine serum albumin (BSA) in PBS was added to the cells for 30 minutes at RT to block unspecific binding sites prior to staining with CMDR. The cells were then permeabilized for 15 minutes at RT using 0.1%Triton-X in 1% BSA in PBS . The permeabilized cells were stained using a 1:1000 CMDR in PBS solution, incubating for 30 minutes and then rinsed with PBS. Microtubules were stained using an anti-tubulin-Alexa Fluor®488 antibody (1:100 dilution in 5% BSA for 60 minutes). Once the samples were labeled, the chamber was sealed with a cover slip. A rectangular piece of black PDMS, with a transparent thin bottom was placed on top of the waveguide to block stray light. The photonic chip was then mounted on the vacuum holder and the laser light coupled into the waveguide structure. The *d*STORM imaging is carried out in a traditional buffer containing an enzymatic oxygen scavenging system (glucose oxidase and catalase in glucose) and a reducing thiol (100 mM MEA) in PBS[24] .

1.3 WAVEGUIDE FABRICATION

Si_3N_4 waveguide were fabricated by standard CMOS fabrications processes. A 2 µm silica layer was grown thermally on the silicon wafers as a substrate. Si_3N_4 layer of 150 nm was then deposited using low-pressure chemical vapor deposition (LPCVD) at 800 °C. Waveguide structuring was done by standard photolithography, followed by reactive ion etching to fabricate strip structures. The masking photoresist was then removed. A 1.5 µm top layer of silica was then grown using PECVD at 300 °C. The top cladding prevents sample interactions with the waveguides outside the desired areas. Imaging areas were then opened up with RIE etching, exposing the waveguide to the sample. The resulting structures were 150 nm thick Si_3N_4 waveguides of different width, with only the imaging areas uncladded. Waveguide widths ranged from 40 µm to 500 µm.

RESULTS AND DISCUSSIONS

The liver sinusoidal endothelial cells (LSECs) form the wall of the hepatic capillary blood vessels, the sinusoids. Their functions are related to trafficking of molecules and cells between the liver parenchyma and the blood, scavenging of potential dangerous macromolecules from the blood, liver immunity, and liver aging[25]. LSECs have a very distinct morphological characteristic represented by nano-size transmembrane pores, or fenestrations, organized in sieve plates. These fenestrations have a diameter of 50-200 nm and allow solutes and colloids to pass through, but blocks larger particles such dietary lipids like chylomicrons. The fenestrated sieve plates are generally found in the extensive, attenuated parts of the cytoplasm, where the thickness of the cell is approximately 150 to 170 nm[26] . Because of the thickness of the cytoplasm and the size of the fenestrations, TIRF *d*STORM is ideal for imaging LSECs. Sufficiently high intensities (0.5-10 KW/cm^2) for fluorophore blinking are achieved in the evanescent field by using high refractive index materials in the waveguides. Using optical waveguides, we performed *d*STORM imaging of the LSECs'. Figure 2 presents diffraction limited and super-resolved images of the plasma membrane of LSECs. We were able to visualize fenestrations in the plasma membrane of around 70 nm size, as seen from the line plot in Figure 3.

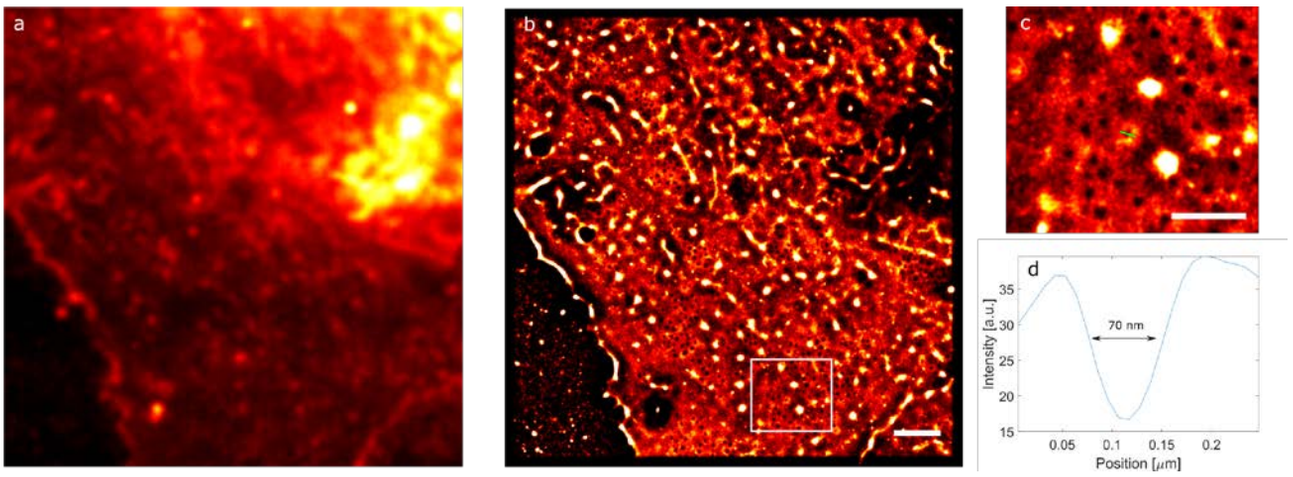

Figure 2: (a) TIRF image of LSEC. (b) *d*STORM image of same region of LSEC. Multiple fenestrations are clearly visible in the super-resolved image (examples are found e.g. inside the white rectangle). The images were captured using a 60x/1.2 NA water immersion objective lens. Scale bar is 2 μm. (c) Enlarged area from figure (b) (marked by the white rectangle). Scale bar is 1 μm. (d) Line plot along the green line in figure (c), demonstrating a resolution of 70 nm for the fenestration diameter.

To further highlight the potential of the technique, we stained the plasma membrane of HTR-8 cells with Cell Mask Deep Red. In Figure 3, we show both the diffraction limited (a) and *d*STORM (b) images of the HTR-8 plasma membrane. HTR-8 cells form the outer layer of the placenta and express filopodia, which are actin-rich plasma membrane protrusions with roles in sensing, migration and cell-cell interaction[27], both imaging methods show the filopodia, but *d*STORM imaging gives a higher contrast and increased resolution (220 nm) as compared to the diffraction limited TIRF image (450 nm) (Figure 3).

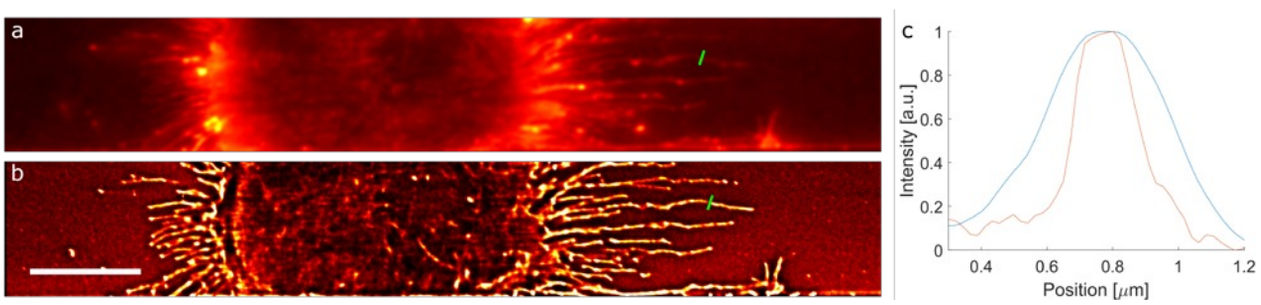

Figure 3: a) TIRF image of the plasma membrane of HDR-8 cells. b) *d*STORM image of HTR-8 cells. The contrast is greatly improved, and the resolution enhancement is best visible in the filopodia. The images were captured using a 60x/1.2 NA water immersion objective lens. Scale bar is 10 μm. (c) Line plot along the filopodium marked with green line in figure (a and b), with FWHM of 450 nm for TIRF and 220 for *d*STORM.

One of the main advantages for chip-based microscopy is the decoupling of the excitation and emission light paths. This enables us to acquire images using both high and low NA objectives, and still keep the benefit of TIRF illumination. Chip based microscopy therefore offers a choice between resolution and field of view, but without compromising the advantages of having a perfect TIRF illumination. In Figure 4, we present a 500 μm x 500 μm TIRF image of LSEC microtubules is presented. The image was taken with a 25x/0.85 NA objective lens and a 500 μm wide waveguide was used for excitation. The extra-ordinary large f-o-v TIRF images enables visualization of over 100 LSECs within a single f-o-v. Achieving large area TIRF excitation is the first step towards large f-o-v *d*STORM imaging. Additionally, the complexity of the chip based optical setup is reduced when compared to traditional TIRF setup, as the need to steer the light precisely in the back focal plane of the TIRF objective lens is gone. Further more, multiplexing of wavelengths is

straightforward. In traditional TIRF microscopy, the critical angle in the TIRF objective must be adjusted for each excitation wavelength, whereas optical waveguide provides pre-aligned geometry for the generation of the evanescent field for any wavelength of the light coupled and guided inside the optical waveguide. The high refractive index material allows tight confinement of the light inside the waveguide and by making thin waveguide (150 nm) a high intensity in the evanescent field can be generated that allows for efficient photoswitching of single molecules, even for relatively wide structures (Fig. 2-3). With optimized waveguide structures, it should be possible to perform *d*STORM over areas equal to that in Figure 2. The system is ideal for imaging thin samples, or samples with defined structures within the reach of the evanescent field such as focal adhesion points, membrane fenestration (see Fig. 2), membrane nuclear pores and membrane trafficking.

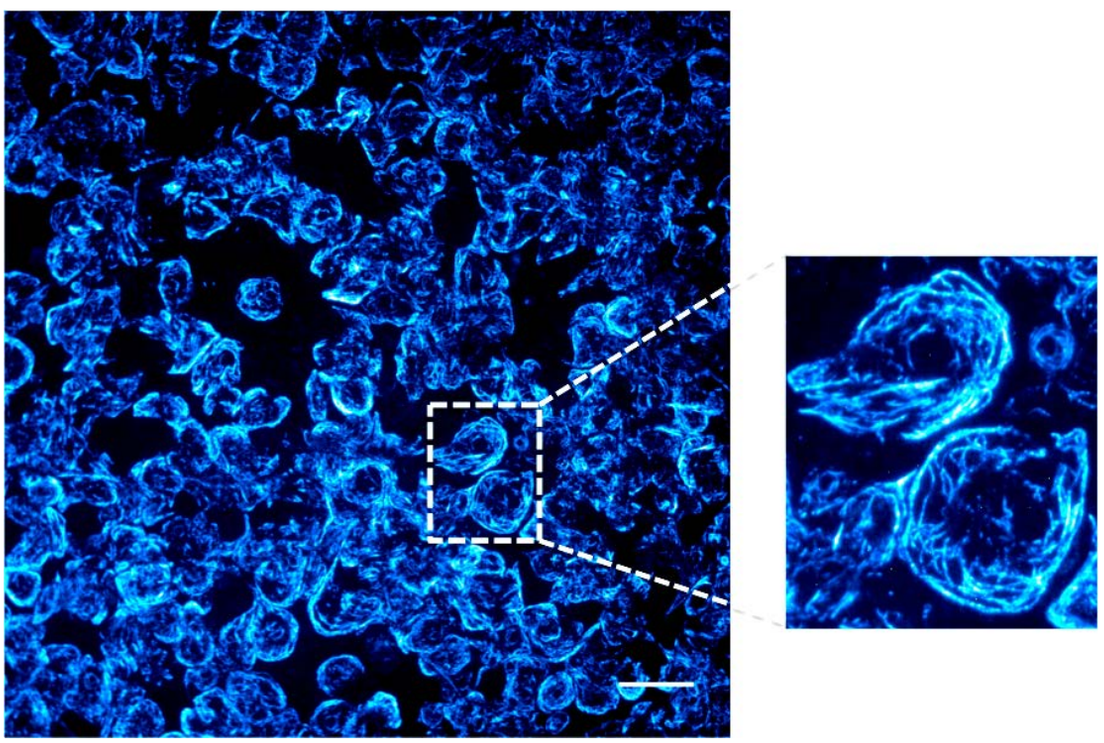

Figure 4: Large field of view TIRF image of LSEC microtubules stained with an anti-tubulin-Alexa Fluor®488 antibody. The image was captured with a 25x/0.85 NA objective lens and with a 500 μm wide waveguide. Scale bar is 50 μm. The white dotted box shows the zoomed image of selected region.

CONCLUSION

We have demonstrated that high refractive index contrast waveguides (Si_3N_4) provide high intensity in the evanescent field, enabling single molecule localization microscopy based on *d*STORM technique. Optical waveguides both hold the cells (LSEC and HTR-8) and excite the through the evanescent field. The separation of excitation and collection light paths provided by the optical waveguide platform opens up opportunities for large area TIRF excitation, a prerequisite for large f-o-v TIRF *d*STORM imaging. The light coupled inside the waveguide is guided in a pre-defined path, generating an evanescent field all along the length of the waveguide. A large f-o-v can be achieved by increasing the width of the waveguide. We have presented very large f-o-v (500 μm x 500 μm) TIRF imaging of microtubulin in LSECs, showing that excitation in wide waveguides works well for imaging. The waveguide platform is thus a promising tool towards high throughput optical nanoscopy.

ACKNOWLEDGEMENTS

Authors acknowledge assistance from Rajwinder Singh and Purusotam Basnet for their help with the preparation and the supply of HTR-8 cells. Authors acknowledge Jean-Claude Tinguely for his assistance with the optical waveguides. This work was supported by the European Research Council (grant no. 336716 to B.S.A.) and UiT, The Arctic University of Norway (Tematiske Satsinger to B.S.A.).

References

1. Ishikawa-Ankerhold, H. C., Ankerhold, R. & Drummen, G. P. C. Advanced Fluorescence Microscopy Techniques-FRAP, FLIP, FLAP, FRET and FLIM. *Molecules* **17,** 4047–4132 (2012).
2. Abbe, E. Beiträge zur Theorie des Mikroskops und der mikroskopischen Wahrnehmung. *Arch. Für Mikrosk. Anat.* **9,** 413–418 (1873).
3. Hell, S. & Wichmann, J. Breaking the Diffraction Resolution Limit by Stimulated-Emission - Stimulated-Emission-Depletion Fluorescence Microscopy. *Opt. Lett.* **19,** 780–782 (1994).
4. Betzig, E. *et al.* Imaging intracellular fluorescent proteins at nanometer resolution. *Science* **313,** 1642–1645 (2006).
5. Hess, S. T., Girirajan, T. P. K. & Mason, M. D. Ultra-high resolution imaging by fluorescence photoactivation localization microscopy. *Biophys. J.* **91,** 4258–4272 (2006).
6. Rust, M. J., Bates, M. & Zhuang, X. Sub-diffraction-limit imaging by stochastic optical reconstruction microscopy (STORM). *Nat. Methods* **3,** 793–796 (2006).
7. Heilemann, M. *et al.* Subdiffraction-Resolution Fluorescence Imaging with Conventional Fluorescent Probes. *Angew. Chem. Int. Ed.* **47,** 6172–6176 (2008).
8. Gustafsson, M. G. L. Surpassing the lateral resolution limit by a factor of two using structured illumination microscopy. *J. Microsc.* **198,** 82–87 (2000).
9. Pepperkok, R. & Ellenberg, J. High-throughput fluorescence microscopy for systems biology. *Nat. Rev. Mol. Cell Biol.* **7,** 690–696 (2006).
10. Kner, P., Chhun, B. B., Griffis, E. R., Winoto, L. & Gustafsson, M. G. L. Super-resolution video microscopy of live cells by structured illumination. *Nat. Methods* **6,** 339–342 (2009).
11. Westphal, V. *et al.* Video-Rate Far-Field Optical Nanoscopy Dissects Synaptic Vesicle Movement. *Science* **320,** 246–249 (2008).
12. Huang, F. *et al.* Video-rate nanoscopy using sCMOS camera-specific single-molecule localization algorithms. *Nat. Methods* **10,** 653–658 (2013).
13. Bates, M., Huang, B., Dempsey, G. T. & Zhuang, X. Multicolor Super-Resolution Imaging with Photo-Switchable Fluorescent Probes. *Science* **317,** 1749–1753 (2007).
14. Lampe, A., Haucke, V., Sigrist, S. J., Heilemann, M. & Schmoranzer, J. Multi-colour direct STORM with red emitting carbocyanines. *Biol. Cell* **104,** 229–237 (2012).
15. Zhang, Z., Kenny, S. J., Hauser, M., Li, W. & Xu, K. Ultrahigh-throughput single-molecule spectroscopy and spectrally resolved super-resolution microscopy. *Nat. Methods* **12,** 935–938 (2015).
16. Diekmann, R. *et al.* Chip-based wide field-of-view nanoscopy. *Nat. Photonics* **11,** 322–328 (2017).
17. Fan, X. *et al.* Sensitive optical biosensors for unlabeled targets: A review. *Anal. Chim. Acta* **620,** 8–26 (2008).
18. Dhakal, A. Nanophotonic Waveguide Enhanced Raman Spectroscopy. (2016).
19. Ahluwalia, B. S., Helle, Ø. I. & Hellesø, O. G. Rib waveguides for trapping and transport of particles. *Opt. Express* **24,** 4477 (2016).
20. Helle, Ø. I., Ahluwalia, B. S. & Hellesø, O. G. Optical transport, lifting and trapping of micro-particles by planar waveguides. *Opt. Express* **23,** 6601 (2015).
21. Dhakal, A. *et al.* Evanescent excitation and collection of spontaneous Raman spectra using silicon nitride nanophotonic waveguides. *Opt. Lett.* **39,** 4025–4028 (2014).
22. Ahluwalia, B. S. *et al.* Fabrication of Submicrometer High Refractive Index Tantalum Pentoxide Waveguides for Optical Propulsion of Microparticles. *IEEE Photonics Technol. Lett.* **21,** 1408–1410 (2009).
23. Prieto, F. *et al.* An integrated optical interferometric nanodevice based on silicon technology for biosensor applications. *Nanotechnology* **14,** 907 (2003).
24. van de Linde, S. *et al.* Direct stochastic optical reconstruction microscopy with standard fluorescent probes. *Nat. Protoc.* **6,** 991–1009 (2011).
25. McLean, A. J. *et al.* Age-related pseudocapillarization of the human liver. *J. Pathol.* **200,** 112–117 (2003).
26. Wisse, E. *et al.* Structure and function of sinusoidal lining cells in the liver. *Toxicol. Pathol.* **24,** 100–111 (1996).
27. Mattila, P. K. & Lappalainen, P. Filopodia: molecular architecture and cellular functions. *Nat. Rev. Mol. Cell Biol.* **9,** 446–454 (2008).

Paper III

Nanoscopy On–a–chip: Super–resolution Imaging on the Millimeter Scale

Ø. I. Helle, D. A. Coucheron, J. C. Tinguely, C. I. Øie, and B. S. Ahluwalia

Research Article | Vol. 27, No. 5 | 4 Mar 2019 | OPTICS EXPRESS 6700
Optics EXPRESS

Nanoscopy on-a-chip: super-resolution imaging on the millimeter scale

ØYSTEIN I. HELLE, DAVID A. COUCHERON, JEAN-CLAUDE TINGUELY, CRISTINA I. ØIE, AND BALPREET S. AHLUWALIA*

UiT-The Arctic University of Norway, Klokkargårdsbakken 35, 9037 Tromsø, Norway

*balpreet.singh.ahluwalia@uit.no

Abstract: Optical nanoscopy techniques can image intracellular structures with high specificity at sub-diffraction limited resolution, bridging the resolution gap between optical microscopy and electron microscopy. So far conventional nanoscopy lacks the ability to generate high throughput data, as the imaged region is small. Photonic chip-based nanoscopy has demonstrated the potential for imaging large areas, but at a lateral resolution of 130 nm. However, all the existing super-resolution methods provide a resolution of 100 nm or better. In this work, chip-based nanoscopy is demonstrated with a resolution of 75 nm over an extraordinarily large area of 0.5 mm x 0.5 mm, using a low magnification and high N.A. objective lens. Furthermore, the performance of chip-based nanoscopy is benchmarked by studying the localization precision and illumination homogeneity for different waveguide widths. The advent of large field-of-view chip-based nanoscopy opens up new routes in diagnostics where high throughput is needed for the detection of non-diffuse disease, or rare events such as the early detection of cancer.

1. Introduction

For a long time, the spatial resolution in optical microscopy was believed to be bound by the diffraction limit. The famous resolution equation [1], shows that the resolving power of the microscope is a simple function of numerical aperture (N.A.) and the wavelength of light, effectively limiting the lateral resolution to around 200-300 nm for visible wavelengths. However, from the early 90s up until now a range of techniques developed that aim to produce images with spatial resolution way beyond that of the diffraction limit. This field is commonly known as super-resolution optical microscopy or optical nanoscopy, and has given biologists tools to observe living intracellular structures with unprecedented high resolution. Lately, improvements in the nanoscopy methods have pushed the spatial resolution towards the ultimate limit i.e. the physical size of the fluorescent labels [2]. For conventional immunolabeling at room temperature using antibody-binding of fluorophores, this typically means a few tens of nanometers.

While nanoscopy has pushed the optical resolution, the improvement does not come for free. One of the major payoffs is the reduced size of the field of view (FOV) with images typically being on the size of 10 μm x 10 μm to 50 μm x 50 μm. This severely limits the throughput of the current super-resolution techniques since only parts of a cell, or up to 1-2 cells can be imaged simultaneously. Most of the nanoscopy methods aim to separate the fluorescence molecules in time by manipulating the photo-physics of the fluorescent dye molecules, achieving a spatial resolution down to around 10-30 nm. These techniques include scanning methods such as stimulated emission depletion (STED) [3], and single-molecule localization microscopy (SMLM) methods such as (direct) stochastic optical reconstruction microscopy (d)STORM) [4, 5] and (fluorescence) photoactivated localization microscopy ((f)PALM) [6,7]. Methods like stochastical optical fluctuation intensity microscopy (SOFI) [8], entropy-based super resolution imaging (ESI) [9] and multiple signal classification algorithm (MUSICAL) [10] lessen the demand on the control of the photophysics of single-molecules by working with signals from multiple fluorophores and using clever reconstruction algorithms to achieve an improved resolution. One

#345909 https://doi.org/10.1364/OE.27.006700
Journal © 2019 Received 25 Sep 2018; revised 9 Dec 2018; accepted 29 Dec 2018; published 22 Feb 2019

Optics EXPRESS

of the most used methods for live cell imaging is structured illumination microscopy (SIM) [11], which use light pattern illumination to encode high frequency content (unresolved) in low frequency signals, yielding around 100 nm lateral resolution. SIM has gained popularity by its live cell compatibility, minimal photo-toxicity, ease of use, and compatibility with most bright fluorophores.

The next breakthrough in optical nanoscopy would represent high throughput imaging. This refers to techniques that can extend the amount of data acquired, by imaging at super-resolution over large areas/volumes fast. The limited throughput of present day nanoscopy methods hinders the collection of sufficient information for drawing statistically relevant conclusions from biological systems. When looking at extending the field of view of optical nanoscopy the easiest would be to employ SIM and create a stitched image consisting of many SIM images side by side. SIM is inherently fast, since it only use 9 /15 images to create one super resolved SIM image in 2D/3D, and a stitched image can be created in a reasonable amount of time, but with spatial resolution limited to around 100 nm. To get the resolution below 100 nm it is thus necessary to increase the FOV of one of the other nanoscopy techniques. The intrinsic scanning nature of STED makes these techniques slow for large areas (such as 500 μm x 500 μm). On the other hand, SMLM being a wide field method, the entire FOV can be acquired simultaneously which is desirable when moving to large area imaging. SMLM methods are typically not very fast (tens of minutes), since thousands of images needs to be acquired to generate a super-resolved image. However, using advanced reconstruction algorithms including compressive sensing [12], SMLM with high-temporal resolution (i.e. in seconds), has been demonstrated.

To increase the FOV for SMLM images it is desirable to use a low magnification objective lens to cover large areas without scanning. For a given optical set-up, the imaged area acquired for a 20X objective lens will be approximately 10X larger than that of a 60X objective lens. In a conventional SMLM setup, excitation light is sent through a high numerical aperture (N.A.) objective lens, and the emitted fluorescence is detected with the same objective. Using a low magnification and low N.A. objective lens in SMLM will create two problems. Firstly, a low magnification/N.A. objective will have a large depth of field, which scales inversely to N.A. squared. This results in the collection of light signals from rather large volumes, giving increased background signal. This will eventually reduce the localization precision and the optical resolution for SMLM, which relies on 2D Gaussian fits over individual blinking events. Presently this problem is solved by using a high magnification/N.A. total internal reflection fluorescence (TIRF) objective lens. A TIRF lens creates an evanescent field illuminating only a thin section of the sample, typically up to 100-150 nm from the surface and thus generating illumination capable of achieving an excellent signal to noise ratio. However, a low magnification/N.A. TIRF objective lens is not commonly available.

Secondly, the illumination for SMLM needs to be uniform. SMLM relies on sparse blinking of the fluorophores, which for the case of *d*STORM is achieved by photo-switching in the presence of a reducing buffer. An uneven illumination will thus provide un-even switching rates generating poor images. The objective lens generates excitation light with a Gaussian profile, where only the most central part of the FOV is useful for SMLM imaging. A few approaches have improved upon this problem [13, 14], but both methods are still collecting with the same high N.A. objective lens, effectively limiting the FOV.

To alleviate the above mentioned problems, it is evident that the separation of the illumination and collection light paths for SMLM will be beneficial. Recently [15], it was shown that by using a photonic chip to illuminate the specimen one could use low magnification objectives to acquire *d*STORM images over an area of 500 μm x 500 μm, 100X larger area than the conventional approach, with lateral resolution of 130 nm.

However, in the previous work the resolution demonstrated by chip-based *d*STORM was limited to around 130 nm and thus could not surpass the diffraction barrier of 100 nm. With a

Optics EXPRESS

resolution of 130 nm chip-based *d*STORM lacked the impact over SIM which can acquire slightly better resolution (100-120 nm) over the same area by scanning and stitching in less time than chip based *d*STORM. In this paper we show that chip-based *d*STORM can be used to acquire images with an optical resolution of 70-75 nm over an extra-ordinary large FOV (500 μm x 500 μm), and thus breaking the diffraction barrier of 100 nm for high throughput optical nanoscopy. Here, we have also investigated crucial parameters to benchmark the performance of chip-based nanoscopy such as localization precision as a function of waveguide width and input power; and the uniformity of the illumination generated by the chip as a function of waveguide width.

2. Principle of chip-based fluorescence imaging

In conventional microscopy/nanoscopy the sample is prepared on a glass-slide/coverslip. Chip-based microscopy replace this arrangement with a photonic integrated circuit (PIC) and the sample is prepared directly on the PICs top surface, as depicted in Fig. 1(a). The PIC chip is made on a Silicon substrate with a buffer layer of Silicon Dioxide (SiO_2) followed by a thin top layer of Silicon Nitride (Si_3N_4). By shaping the geometry, i.e creating side-walls, the layer functions as as an efficient waveguide for propagating excitation light to the specimen. Laser-light is coupled into the waveguide by focusing a beam of light on to the end-facet using an objective lens. The light propagates inside the waveguide by total internal reflection, however a small part the field leaks out in the form of an evanescent wave. The specimen is fluorescently labeled and the fluorophores are excited via the evanescent field stretching around 150 nm in to the sample as shown i Fig. 1(b). This means that only the part of the specimen located within these 150 nm will be illuminated. The evanescent field penetration depth is fully determined by the wavelength, and the local refractive index at the waveguide-sample boundary. The sample can be mounted following the same protocols as for the glass-slide/coverslip arrangement, and the PIC has also shown to be bio-compatible supporting live cells experiments [16].

For efficient photo-switching of the fluorophores, the evanescent field intensity directly at the surface must be strong (ideally 1-10 kW/cm^2), which is achieved by the use of a high refractive index material, in this work Si_3N_4 having n$\approx$ 2.0, for 660 nm excitation laser light. The high-refractive index material together with a shallow cross-section (waveguide thickness of 150 nm) confines the light tightly inside the waveguide, but with up to 5-10% of the guided power available in the evanescent field. The high refractive index contrast also ensure that the penetration depth of the evanescent field is shallow, yielding good optical sectioning.

Using a high-refractive index waveguide such as Si_3N_4 at visible wavelengths, higher order modes are supported by the strip waveguide geometry starting from waveguide widths of 1.5 μm. These modes travel in discrete paths generating non-uniform illumination patterns. As the dimensions increase above a few micrometers, more modes starts to interfere with each other, creating a highly chaotic illumination pattern, referred to as multi-mode interference (MMI) patterns. The resulting evanescent field illumination is thus also contaminated with non-uniform MMI patterns, resulting in images of poor quality, disturbed by stripe patterns. The MMI patterns can be scrambled, and thus create a uniform image by shifting the mode patterns in time, and then take the average of several sub-sets of MMI patterns. There are two possibilities to achieve this, either rapid scanning the input beam using a galvo mirror, or slow scanning the input beam by moving the coupling objective lens using a motorized/piezo stage. The galvo mirror can scan quicker than the camera exposure time so every frame captured will show uniformity. The other approach scans slowly, using the average of a few hundred frames to create a uniform image. In the case of *d*STORM several thousand frames are captured by default so any of the two methods can be used. In this paper we chose to slow-scan the input beam by moving the coupling objective with a piezo stage as discussed in [15].

Unlike the TIRF objective lens, the generation of the evanescent field by an optical waveguide is decoupled from the imaging objective lens. As a consequence, the evanescent field is available

Optics EXPRESS

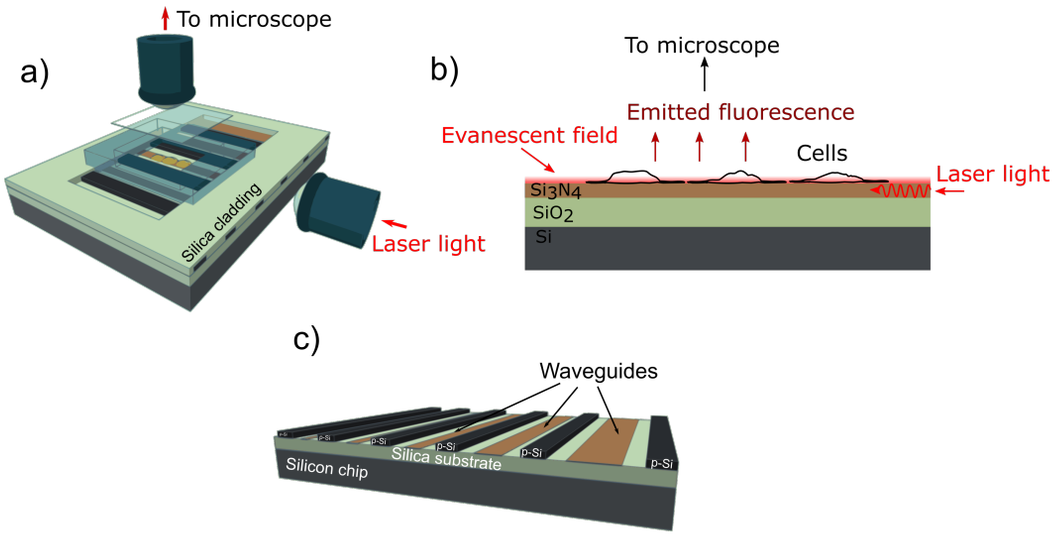

Fig. 1. a) Laser light is coupled into a PIC via an objective lens, and light is guided towards the specimen in optical waveguides. On top of the chip there is a PDMS microchamber to contain the image buffer. b) In the center of the chip there is an opening in the protective cladding where the specimen is mounted to come in contact with the evanescent field. The fluorescent signal is captured by an upright microscope. c) The PIC has lateral dimension of around 3 cm x 3 cm. A layer of SiO_2 give a strong refractive index contrast against the Si_3N_4 waveguide. In between the guiding material are layers of Poly-Silicon that blocks light from passing in to neighboring waveguides.

over large areas, only limited by the waveguide dimension. Furthermore, it allows a free choice of the objective lens used to collect the emitted fluorescence. In this way, a low N.A. objective lens can be used to acquire a large FOV without sacrificing the excellent optical sectioning provided by the chip-based illumination.

3. Materials and methods

3.1. Waveguide fabrication

The waveguides were made by first sputtering a 2 μm thick layer of SiO_2 onto a silicon wafer. The 150 nm thick guiding layer of Si_3N_4 was then added by low-pressure chemical vapor deposition at 800°C, before the waveguide structure was outlined by photo-lithography. The strip waveguide structures were then realized by ion etching all the way down to the silica cladding. Another layer of poly-silicon was realized to function as a light absorbing layer in between neighboring waveguides to stop unguided light from leaking to other waveguides. This can be seen as the black layer in Fig. 1(c). A 1.5 μm thick layer of SiO_2 was used to create a protective top cladding, and reactive ion etching was used to open up the cladding at the imaging area, where cells can be seeded directly on top of the waveguide core accessing the evanescent field. For fluorescence imaging of biological samples, the dimensions typically must be larger than the cells under investigation. Here, waveguide widths between 50 μm and 1 mm were used. A PDMS micro-chamber was used to contain the aqueous image buffer during the measurements. The thickness of the chamber was approximately 130 μm, well below the working distance of the objective lens used for the collection.

Optics EXPRESS

3.2. Experimental setup

The setup was based around an Olympus modular upright microscope fitted with a water cooled sCMOS camera (Hamamatsu ORCA flash). Images were acquired using two different objective lens (Olympus UplanSApo x60/1.2 w and Zeiss LD LCI Plan-Apochromat x25/0.8). The Zeiss multi-immersion objective lens was used to gather the large FOV images. The Zeiss objective lens was used with the olympus tube lens, such that the effective magnification of the setup changed, leaving around 27 x effective magnification. The chip was secured by a vacuum air-lock to further minimize sample drift. Laser was coupled into the chip using a x50/0.8 objective lens. The laser used for *d*STORM is a Cobolt Flamenco 660 nm with up to 500 mW output power. The microscope was mounted on motorized stages enabling lateral movement for observation of different regions on the chip. The data was acquired using a computer and the localization data was analyzed using Fiji open source image processing software and the localization data analysis plugin ThunderStorm [17]. The camera exposure time was set to 25 ms for all *d*STORM experiments.

3.3. Sample preparation

A fluorescently labeled surface was created by incubating a solution of 50nM Alexa647 molecules in 0.05% Poly-L-Lysine for 10 minutes at room temperature (RT). The solution was aspirated and the surface rinsed gently three times with dH20. *d*STORM buffer was prepared following [18]. The buffer contains an enzymatic scavenger system containing Catalase (Sigma #C100) and Glucose Oxidase(Sigma #G2133) together with 100 mM Mercaptoethylamine (MEA, Sigma #M6500). The addition of 2mM Cyclotetraene (COT, Sigma #138924) has shown to help with blinking performance of Alexa647 on waveguides. Cells were harvested from male Sprawgly rat, with body weights between 150-300 g. Liver sinusoidal endothelial scavenger cells were isolated using the method from [19], and kept alive in RPMI 1640. To help with attaching the cells to the waveguides chips, the surface was coated with fibronectin (50 μg/ml) for 10 minutes at RT. The cell suspension was incubated on the surface of the chips for 1 hour at 37°C and 5% O_2. The surface was rinsed with fresh RPMI 1640, to remove debris and the chips were incubated for 2 more hours to allow spreading of the cytoplasm. Fixation of the cells were performed using 4% Paraformaldehyde for 30 min. The tubulin was stained using primary antibody β-tubulin(Sigma Aldrich) at 1:400 in PBS for 1h at RT. The secondary antibody was goat anti-mouse Alexa Fluor 647 at 1:400 in PBS, incubated for 1H at RT. The cells were washed three times with PBS before the image buffer was applied and the chambers sealed with a coverglass.

4. Results

For high throughput chip-based nanoscopy, wide waveguides are essential to illuminate large areas. The dimensions of the waveguides must be made such that the evanescent field intensity is sufficiently strong, enabling photo-switching of fluorophores on top of the waveguide surface. In order to establish the appropriate waveguide dimensions for large FOV imaging we investigate the impact of waveguide width and input power for a *d*STORM on-chip measurement. This was achieved by measuring localizations coming from a single-molecule layer deposited on top of the waveguide surface, as a function of waveguide widths and at different input powers. A *d*STORM experiment was carried out on the surface over a fixed area, and repeated for different waveguide widths. Waveguides of different widths were located next to each other on the same chip as indicated in Fig. 1(a). In Fig. 2 the number of localizations acquired using 1000 frames of data is plotted against the input power for 4 different waveguide widths. The number of localizations detected for each waveguide width follow the same trend for waveguide widths up to 400 μm, while for the 600 μm wide waveguide the curve takes on another shape. This shows that waveguides of widths 200-400 μm generate an evanescent field suitable to efficiently

Optics EXPRESS

photo-switch the fluorophores with an input power of 25 mW. While, for the 600 μm waveguide, 100 mW input power is needed to get the maximum number of localized emitters for a similar imaging area.

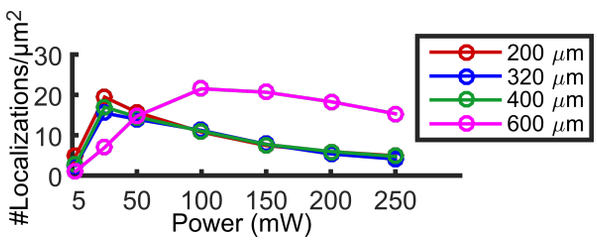

Fig. 2. Localizations as a function of power and width – The average number of localizations over a fixed area for different waveguide widths and input powers. We see that for waveguides 200 - 400 μm wide around 25 mW at the input of the waveguide is enough to get optimum blinking, while for 600 μm waveguide we must increase the power to 100mW.

To systematically investigate the achievable uniformity of chip-based illumination, we measured the intensity profiles acquired by staining the waveguide surface with a dense thin layer of fluorophores (Alexa 647 in Poly-L-Lysine) and diffraction limited imaging by using mode averaging. In Fig. 3(a) the MMI pattern is shown without using mode averaging, while in Fig. 3(b) the same area is imaged after mode averaging. The line-profile in Fig. 3(b) indicate the position from where the modulation depths for different waveguide widths are calculated. The measured modulation depth for waveguide widths stretching between 120 μm up to 1000 μm are shown in Fig. 3(c) using 500 frames of data, with Fig. 3(d) showing the line-profile from Fig. 3(b) as an example. When calculating the modulation depth, the edge artifacts observed in Fig. 3(d) are neglected. Interestingly, it was observed that the modulation depth for these dimensions are rather stable in terms of being viable for *d*STORM imaging, with around 17 % for the 120 μm and up to 27 % for 1000 μm wide waveguides.

We demonstrate the method by imaging liver sinusoidal endothelial cells (LSECs) stained for the micro-tubules network. The *d*STORM localization list was filtered to only keep the localizations with the best statistics, like brightness and shape, ensuring that few overlapping emitters introduce errors for the fitting algorithm. The number of images used to compile the reconstructed image was around 25000 selected from a stack of 65000 images acquired. The image shown in Fig. 4(a) show that by using the 25x 0.8 N.A. objective lens an extremely large area of almost 500 μm x 500 μm with a resolution down to 70-75 nm can be imaged. The large area illuminated by the waveguide allow 200-300 cells to be imaged simultaneously. The zoom in Fig. 4(b) show the comparison to the diffraction limited image visualizing a 6-fold resolution enhancement of the 25x 0.8 N.A objective lens. In Fig. 4(c) the zoom also indicates the position of the lineplot in Fig. 4(d) which show a clear separation of tubulin filaments located 78 nm apart. In Fig. 4(e), this resolution is confirmed using Fourier ring correlation [20], which suggest a lower threshold for the resolution over the entire image to be around 72 nm. Furthermore, we see that the average localization precision in the image, as measured by the reconstruction software is peaking around 23 nm (Fig. 4(f)), indicating a lower limit for the resolution of around 65 nm.

It can be noticed from Fig. 4(a) that a slight decay in the number of localized molecules towards the edges of the image, which is caused by the limited field flatness of the imaging objective lens. To study the influence of field flatness of the imaging objective lens, we investigated the achieved localization precision as a function of position in the field of view. As it can be seen from Fig. 3(c), the waveguides can set up an evanescent field where the intensity modulation depth is around 25 % for large fields of view. However, when producing really large high-resolution images we are still limited by the collection optics. Microscope objectives with high numerical aperture

Optics EXPRESS

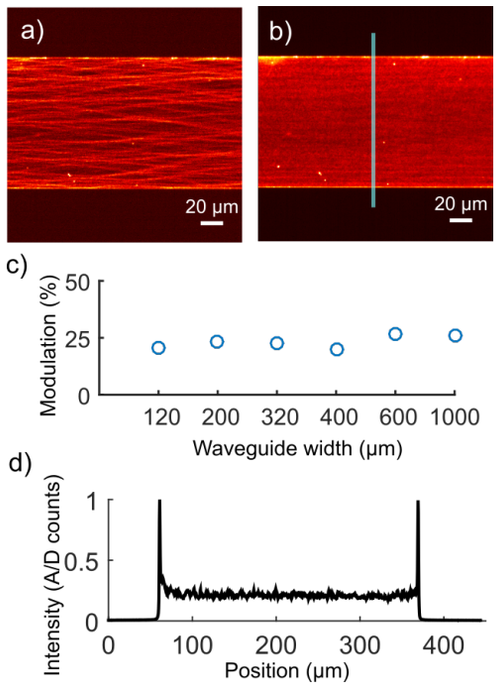

Fig. 3. Modulation depth as function of waveguide width – a) Illumination MMI pattern without mode averaging. b) After mode averaging the resulting illumination is close to uniform. c) The modulation depth is plotted for different waveguide widths, and only small changes is observed when the width increases. d) The line-profile indicated in b). When calculating the modulation depth the edge artifacts are ignored.

and low magnification are not very common, and the ones that do exists typically have to pay the price for these unusual characteristics in terms of field flatness. Most microscope objectives expressing these characteristics give a nice focus only in the middle of the FOV. Fig. 5 shows the localizations from the image in Fig. 4(a) grouped in bins of 10 μm along x (horizontally) but with the full field-of-view along y (vertically). The number of localization detected for each bin is displayed, visualizing how the number of localizations decrease when moving away from the center. The likelihood of acquiring a good localization is decreasing when the emitter is laying in the periphery of the FOV, which means that either we need to accept a decrease in resolution (keeping less good localizations), or we need to increase the acquisition time to allow enough localizations to be captured to fully resolve the structures at acceptable resolution.

5. Discussion and conclusion

Super-resolution microscopy has so far come at the cost of throughput. Currently, commercial setups provide unprecedented resolution but the size of the field of view is small, with images typically covering only parts of a cell. This is a consequence of conventional setups being bound to a high N.A. and high magnification objective lens for both the illumination and the collection. To make use of optical nanoscopy to study statistical biological nanometer sized phenomenon on large length scales, the need to increase the throughput of the methods is apparent. In this study we used planar optical waveguides as a mean to illuminate fluorescently labeled specimen located on top of the waveguide surface via intrinsic evanescent fields. This method of exciting fluorescence via planar waveguides allows for TIRF optical nanoscopy with the additional feature of a free choice of the imaging objective lens, allowing scalable super-resolution microscopy

Optics EXPRESS

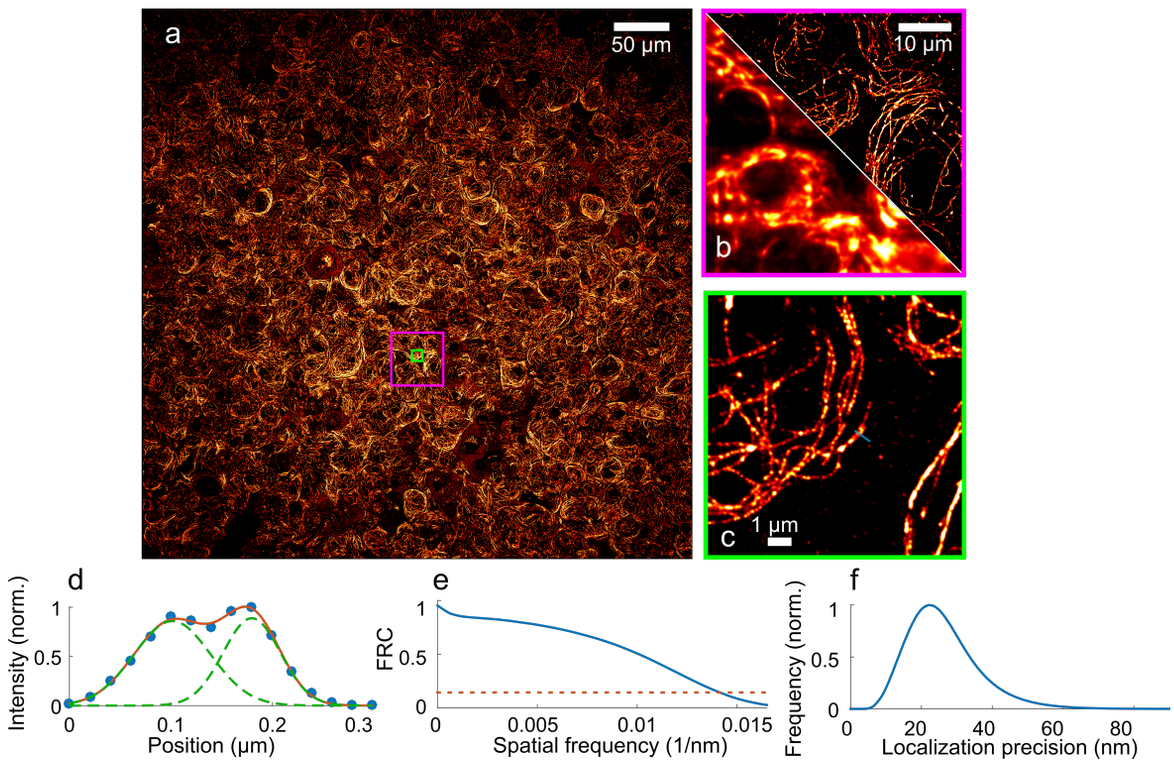

Fig. 4. a) Large field of view *d*STORM image of Alexa 647 stained tubulin in rat L SECs. The image has a resolution of around 70-75 nm with 200-300 cells being imaged simultaneously. b) Zoomed image from a) with comparison to the diffraction limited image. c) Zoomed image marked in green from a) with the position of the lineplot shown in d) marked. d) The lineplot show tubulin filaments clearly separated by a distance of 78 nm. e) Fourier ring correlation indicated a resolution of around 72 nm. f) The localization precision measured by the reconstruction software further backs a resolution between 70-75 nm.

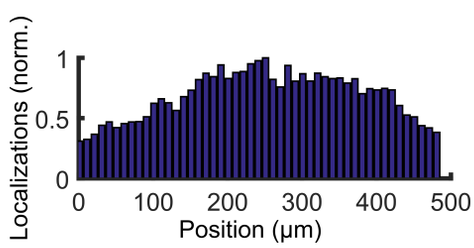

Fig. 5. Localizations from Fig. 4 as function of width across the field of view. Each data point includes all localizations within a bin width of $10\mu m$ horizontally separated . We see that the number of properly localized molecules decrease moving away from the center of the objective lens.

Optics EXPRESS

with a compromise between FOV size and resolution.

Compared to the standard coverglass/glass slide arrangement, the PIC chips are more expensive to make. However, when mass produced using CMOS fabrication processes and in a foundry the price per chip can be reduced significantly. The price range of a few dollars per millimeter square can easily be achieved during industrialized production. As the price for silicon wafers scales with the chip area, hosting a small chip (e.g. 2 x 2 mm^2) inside a plastic holder could be an alternative for easy handling of the chip.

The previously published results [15] using the chip-based approach greatly enhanced the size of the field of view available for nanoscopy imaging, but with the resolution not exceeding more than 130 nm. In this work, we show that the method is capable of generating images with 70-75 nm resolution, by carefully selecting the objective lens used in the image acquisition. The increased resolution surpasses the possible 100 nm resolution achievable using SIM. Other previously reported techniques [13, 14] on increased FOV SMLM have achieved a more uniform excitation light spanning over a larger area, but they are still limited by the high N.A. objective lens for acquiring the emitted fluorescence, effectively limiting the FOV to around 200 μm x 200 μm at best.

Furthermore, we investigated how the blinking of fluorophores on waveguides react to different parameters such as waveguide width and laser intensity. As seen from Fig. 2, the switching rates was at its best at 25 mW input power using a single molecule surface with widths of 200-400 μm but a 4 times increase in power was needed to get equally good blinking from a 600 μm waveguide. The surface intensity scales with the width of the waveguide, justifying the need for more input power at 600 μm width, but other factors like coupling efficiency could also impact the curves of Fig. 2. It has been shown that Alexa 647 exhibits faster switching kinetics at high powers [21]. The drop in the number of localizations found above 25 mW (for 200-400 μm) and 100 mW (for 600 μm) could indicate that the fluorophores are blinking much faster than the exposure time of the camera giving increased background. It might also be that the increased intensity is pushing more fluorophores in to more long lived dark-states or to a permanent off-state by photo-bleaching. In either case, laser powers above 25 mW is too strong for efficient SMLM on waveguides using the *d*STORM method, and that the surface intensity is higher than earlier estimates [15], where it was shown that an input laser power of 500 mW yielded up to 10kW/cm^2 evanescent field i ntensity. From experimental data using cells we have experienced that the intensity needed to efficiently photo-switch Alexa 647 must be scaled up a few times to achieve adequate blinking in cells. This is probably due to fluorophores sitting tens of nanometers or more away from surface in case of cells, while the illumination is exponentially decaying away from the surface.

The modulation depth of the resulting illumination pattern after mode averaging was studied. In *d*STORM imaging the modulation depth plays a role in terms of the pattern being viable for use with the *d*STORM technique. As long as there is sufficient intensity to effectively photo-switch the fluorophores, the modulation has little impact. However if intensity reduces in some regions to such an extent that the photo-switching is affected, this can create a problem. For waveguides of 120 μm a modulation depth of 17% which corresponds well with earlier investigations, and for wider waveguides we see that the number increase to 25-30%. When looking at the *d*STORM image of Fig. 4(a) we see that this plays little role in the end result. However, the temporal resolution might be reduced if the modulation is decreased, in that more fluorophores in general will be in the desired on/off state at each instance. To reduce the modulation index for wide waveguides the scan range could be increased to scan over the entire input width, contrary to 20μm as achieved here. The waveguide could also start at a lower width, and taper out to wide dimension to reduce the need for larger scan range.

The chip-based platform also supports different on-chip optical modalities such as Raman spectroscopy on chip [22], on-chip micro-particle manipulation [23], interferometric microparticle

Optics EXPRESS

sensing [24] and gas sensing [25], where several of these techniques can be combined creating advanced lab-on-a-chip multimodality platforms. In this work, we have investigated the relationship between waveguide widths and some parameters related to extending the FOV in super-resolution microscopy imaging. By using the waveguide-chip we have by-passed the need of a conventional objective lens to generate the excitation light, however we still reply on using an objective lens to collect the fluorescence s ignal. The impact of chip-based nanoscopy will be further enhanced if we can replace the objective lens with a micro-lens array to collect the fluorescence s ignal. Such a system will not only be highly compact [26] but will also benefit from the extra-ordinary large illumination area as the waveguide can excite fluorescence along its entire length. Furthermore, the resolution of chip-based SMLM is determined by the SNR of the detected single-molecule emissions. By using brighter emitters the resolution can be further improved, e.g using DNA-paint probes [27], where a fluorophore in the ideal case emits all of its photons in one localization event, thus improving the localization precision.

Large field of view nanoscopy will be useful in diagnostic pathology [28]. For non-diffusive diseases, large areas need to be scanned looking for rare events like cancer cells. Pathology mainly focus on thin tissue sections either 4 μm paraffin embedded samples or 100-200 nm cryo-preserved tissue samples. Thin tissue sections are perfectly matched for the large area TIRF illumination produced by the chip-based imaging technology and will be explored in future work.

Funding

European Research Council, project number 336716.

Acknowledgments

This work has made use of the Spanish ICTS Network MICRONANOFABS partially supported by MEINCOM.

References

1. J. Goodman, *Introduction to Fourier Optics* (Roberts & Company, 2005), pp. 156–160.
2. S. Weisenburger, D. Boening, B. Schomburg, K. Giller, S. Becker, C. Griesinger, and V. Sandoghdar, "Cryogenic optical localization provides 3d protein structure data with angstrom resolution," Nat. Methods **14**, 141–144 (2017).
3. S. W. Hell and J. Wichmann, "Breaking the diffraction resolution limit by stimulated emission: stimulated-emission-depletion fluorescence microscopy," Opt. Lett. **19**, 780–782 (1994).
4. M. Heilemann, S. van de Linde, M. Schüttpelz, R. Kasper, B. Seefeldt, A. Mukherjee, P. Tinnefeld, and M. Sauer, "Subdiffraction-resolution fluorescence imaging with conventional fluorescent probes," Angew. Chem. Int. **47**, 6172–6176 (2008).
5. M. J. Rust, M. Bates, and X. Zhuang, "Sub-diffraction-limit imaging by stochastic optical reconstruction microscopy (storm)," Nat. Methods **3**, 793–796 (2006).
6. S. T. Hess, T. P. K. Girirajan, and M. D. Mason, "Ultra-high resolution imaging by fluorescence photoactivation localization microscopy," Biophys. J. **91**, 4258–4272 (2006).
7. E. Betzig, G. H. Patterson, R. Sougrat, O. W. Lindwasser, S. Olenych, J. S. Bonifacino, M. W. Davidson, J. Lippincott-Schwartz, and H. F. Hess, "Imaging intracellular fluorescent proteins at nanometer resolution," Science **313**, 1642–1645 (2006).
8. T. Dertinger, R. Colyer, G. Iyer, S. Weiss, and J. Enderlein, "Fast, background-free, 3d super-resolution optical fluctuation imaging (sofi)," Proc. Natl. Acad. Sci. U.S.A **106**, 22287–22292 (2009).
9. I. Yahiatene, S. Hennig, M. Müller, and T. Huser, "Entropy-based super-resolution imaging (esi): From disorder to fine detail," ACS Photonics **2**, 1049–1056 (2015).
10. K. Agarwal and R. Macháň, "Multiple signal classification algorithm for super-resolution fluorescence microscopy," Nat. Commun. **7**, 13752 (2016).
11. M. G. Gustafsson, "Surpassing the lateral resolution limit by a factor of two using structured illumination microscopy," J. Microsc. **198**, 82–87 (2000).
12. L. Zhu, W. Zhang, D. Elnatan, and B. Huang, "Faster storm using compressed sensing," Nat. Methods **9**, 721–723 (2012).
13. J. Deschamps, A. Rowald, and J. Ries, "Efficient homogeneous illumination and optical sectioning for quantitative single-molecule localization microscopy," Opt. Express **24**, 28080–28090 (2016).

Optics EXPRESS

14. A. Beghin, A. Kechkar, C. Butler, F. Levet, M. Cabillic, O. Rossier, G. Giannone, R. Galland, D. Choquet, and J.-B. Sibarita, "Localization-based super-resolution imaging meets high-content screening," Nat. Methods **14**, 1184–1190 (2017).
15. R. Diekmann, Ø. I. Helle, C. I. Øie, P. McCourt, T. R. Huser, M. Schüttpelz, and B. S. Ahluwalia, "Chip-based wide field-of-view nanoscopy," Nat. Photonics **11**, 322–328 (2017).
16. J.-C. Tinguely, Ø. I. Helle, and B. S. Ahluwalia, "Silicon nitride waveguide platform for fluorescence microscopy of living cells," Opt. Express **25**, 27678–27690 (2017).
17. M. Ovesný, P. Křížek, J. Borkovec, Z. Švindrych, and G. M. Hagen, "Thunderstorm: a comprehensive imagej plug-in for palm and storm data analysis and super-resolution imaging," Bioinformatics **30**, 2389–2390 (2014).
18. S. van de Linde, A. Löschberger, T. Klein, M. Heidbreder, S. Wolter, M. Heilemann, and M. Sauer, "Direct stochastic optical reconstruction microscopy with standard fluorescent probes," Nat. Protoc. **6**, 991–1009 (2011).
19. B. Smedsrød and H. Pertoft, "Preparation of pure hepatocytes and reticuloendothelial cells in high yield from a single rat liver by means of percoll centrifugation and selective adherence," J. Leukoc. Biol. **38**, 213–230 (1985).
20. N. Banterle, K. H. Bui, E. A. Lemke, and M. Beck, "Fourier ring correlation as a resolution criterion for super-resolution microscopy," J. Struct. Biol. **183**, 363–367 (2013).
21. Y. Lin, J. J. Long, F. Huang, W. C. Duim, S. Kirschbaum, Y. Zhang, L. K. Schroeder, A. A. Rebane, M. G. M. Velasco, A. Virrueta, D. W. Moonan, J. Jiao, S. Y. Hernandez, Y. Zhang, and J. Bewersdorf, "Quantifying and optimizing single-molecule switching nanoscopy at high speeds," PloS one **10**, e0128135–e0128135 (2015).
22. P. C. Wuytens, A. G. Skirtach, and R. Baets, "On-chip surface-enhanced raman spectroscopy using nanosphere-lithography patterned antennas on silicon nitride waveguides," Opt. Express **25**, 12926–12934 (2017).
23. Ø. I. Helle, B. S. Ahluwalia, and O. G. Hellesø, "Optical transport, lifting and trapping of micro-particles by planar waveguides," Opt. Express **23**, 6601–6612 (2015).
24. F. T. Dullo and O. G. Hellesø, "On-chip phase measurement for microparticles trapped on a waveguide," Lab Chip **15**, 3918–3924 (2015).
25. F. T. Dullo, S. Lindecrantz, J. Jágerská, J. H. Hansen, M. Engqvist, S. A. Solbø, and O. G. Hellesø, "Sensitive on-chip methane detection with a cryptophane-a cladded mach-zehnder interferometer," Opt. Express **23**, 31564–31573 (2015).
26. A. Orth and K. Crozier, "Gigapixel fluorescence microscopy with a water immersion microlens array," Opt. Express **21**, 2361–2368 (2013).
27. J. Schnitzbauer, M. T. Strauss, T. Schlichthaerle, F. Schueder, and R. Jungmann, "Super-resolution microscopy with dna-paint," Nat. Protoc. **12**, 1198–1228 (2017).
28. F. Herrmannsdörfer, B. Flottmann, S. Nanguneri, V. Venkataramani, H. Horstmann, T. Kuner, and M. Heilemann, *3D dSTORM Imaging of Fixed Brain Tissue* (Springer New York, 2017), pp. 169–184.

Paper IV

High-Throughput Total Internal Reflection Fluorescence and Direct Stochastic Optical Reconstruction Microscopy Using a Photonic Chip

D. A. Coucheron, Ø. I. Helle, C. I. Øie, J. C. Tinguely, B. S. Ahluwalia.

Note: This publication is a video article. The manuscript is attached here, but the video is found at jove.com, doi: 10.3791/60378.

Video Article

High-Throughput Total Internal Reflection Fluorescence and Direct Stochastic Optical Reconstruction Microscopy Using a Photonic Chip

David André Coucheron[1], Øystein Ivar Helle[1], Cristina Ionica Øie[2], Jean-Claude Tinguely[1], Balpreet Singh Ahluwalia[1]

[1]Department of Physics and Technology, UiT The Arctic University of Norway

[2]Vascular Biology Research Group, Department of Medical Biology, UiT The Arctic University of Norway

Correspondence to: Jean-Claude Tinguely at jean-claude.tinguely@uit.no

URL: https://www.jove.com/video/60378
DOI: doi:10.3791/60378

Keywords: Biochemistry, Issue 153, Fluorescence, total internal reflection fluorescence, Super-resolution optical microscopy, nanoscopy, waveguides, integrated optics

Date Published: 11/16/2019

Citation: Coucheron, D.A., Helle, Ø.I., Øie, C.I., Tinguely, J.C., Ahluwalia, B.S. High-Throughput Total Internal Reflection Fluorescence and Direct Stochastic Optical Reconstruction Microscopy Using a Photonic Chip. *J. Vis. Exp.* (153), e60378, doi:10.3791/60378 (2019).

Abstract

Total internal reflection fluorescence (TIRF) is commonly used in single molecule localization based super-resolution microscopy as it gives enhanced contrast due to optical sectioning. The conventional approach is to use high numerical aperture microscope TIRF objectives for both excitation and collection, severely limiting the field of view and throughput. We present a novel approach to generating TIRF excitation for imaging with optical waveguides, called chip-based nanoscopy. The aim of this protocol is to demonstrate how chip-based imaging is performed in an already built setup. The main advantage of chip-based nanoscopy is that the excitation and collection pathways are decoupled. Imaging can then be done with a low magnification lens, resulting in large field of view TIRF images, at the price of a small reduction in resolution. Liver sinusoidal endothelial cells (LSECs) were imaged using *direct* stochastic optical reconstruction microscopy (*d*STORM), showing a resolution comparable to traditional super-resolution microscopes. In addition, we demonstrate the high-throughput capabilities by imaging a 500 µm x 500 µm region with a low magnification lens, providing a resolution of 76 nm. Through its compact character, chip-based imaging can be retrofitted into most common microscopes and can be combined with other on-chip optical techniques, such as on-chip sensing, spectroscopy, optical trapping, etc. The technique is thus ideally suited for high throughput 2D super-resolution imaging, but also offers great opportunities for multi-modal analysis.

Video Link

The video component of this article can be found at https://www.jove.com/video/60378/

Introduction

Since the initial demonstration of single molecule localization microscopy, many variations have been developed to solve different challenges[1,2,3]. One challenge that has remained, however, is large field of view dSTORM imaging. Many *d*STORM setups use the same objective lens to both excite the sample and to image it. In order to increase the field of view, a low magnification lens is needed. Low magnification and low numerical aperture (NA) objective lenses typically have a large depth of field, resulting in an increased out-of-plane signal that will reduce the localization precision. TIRF objectives are commonly used to increase the image contrast by reducing out-of-plane fluorescence. Through TIRF, the excitation is limited to an optical thickness of approximately 150 nm from the surface by means of an evanescent field[4]. TIRF objective lenses require a large NA resulting in a small field-of-view (FOV) (e.g., 50 x 50 µm^2), which limits the throughput significantly. There are, however, alternative ways to generate an evanescent field.

An optical waveguide is a structure that will confine and guide light if it is coupled into the structure. Most commonly, waveguides are used in fiber-based telecommunication. Great effort has been made in order to develop 2D integrated waveguides as a main component of photonic integrated circuits. The technology has advanced to a point where fabricating low-loss nano-structured optical waveguides can be routinely done[5]. Today, several foundries around the world can be used to develop photonic integrated circuits. Waveguides guide light through total internal reflectance also exhibiting an evanescent field at the surface. By careful design of the waveguide structure, a high intensity can be achieved in the evanescent field. A sample placed directly on top of the waveguide surface can thus also be illuminated by the evanescent field for imaging applications. The evanescent field will be generated along the entire length and width of the waveguide, and thus it can be made arbitrarily large[6].

We present a novel approach to TIRF *d*STORM that offers an arbitrarily large field of view. Instead of using a TIRF lens for both excitation and collection, we excite using the evanescent field from optical waveguides. This decouples the excitation and collection light pathway, allowing for total freedom along the collection light path without compromising the optical sectioning for a given wavelength provided by the waveguide chip illumination. Low magnification lenses can thus be used to image very large regions in TIRF mode, although a smaller NA will reduce the lateral resolution. Furthermore, multicolor imaging is also greatly simplified using waveguides[7], as several wavelengths can be guided and detected without readjusting the system. This is advantageous for *d*STORM, as low wavelengths can be used to enhance fluorophore blinking and for multicolor imaging. It is worth noting that the penetration depth of the evanescent field will change as a function of wavelength, although

it does not affect how the imaging procedure is performed. The chip is compatible with live cell imaging[8] and is ideal for applications such as the integration of microfluidics. Each chip can contain tens of waveguides, which can allow the user to image under different conditions or apply optical trapping[9] and Raman spectroscopy[10].

The chip-based system works equally well for both diffraction-limited and super-resolution imaging. A similar approach was introduced in 2005 using a prism to generate evanescent field excitation[4]. The photonic chip also excites through the evanescent field, but with modern waveguide fabrication techniques, one can generate exotic light patterns with waveguides. The present chip-based nanoscopy implementation is limited to 2D imaging only, as the excitation field is locked inside the waveguide surface. Future development will aim for 3D applications. Additionally, other super-resolution techniques such as structured illumination microscopy are being developed using the same chip-based microscope[11].

Protocol

1. Preparation of the polydimethylsiloxane (PDMS) layer

1. Prepare a 10:1 mix of Sylgard 184 monomer and curing agent.
2. Place the mixture in a vacuum chamber until air bubbles are gone.
3. Pour 1.7 g of PDMS mixture in the center of a 3.5 inch (diameter) Petri dish.
4. Place the Petri dish on the vacuum chuck of a spin coater.
5. Spin coat the Petri dish for 20 s at 900 rpm, with an acceleration of 75 rpm/s.
6. Cure the dish on a hotplate at 50 °C for at least 2 h.

2. Sample preparation

1. **Waveguide cleaning**
    1. Prepare 100 mL of a 1% dilution of cleaning detergent concentrate (**Table of Materials**) in deionized (DI) water.
    2. Place the chip in a glass Petri dish using a wafer tweezer and cover completely with the detergent solution.
    3. Place the Petri dish on a hot plate at 70 °C for 10 min.
    4. While still on the hot plate, rub the surface with a cleanroom tissue swab.
    5. Remove the chip from the Petri dish. Rinse with at least 100 mL of DI water.
    6. Rinse with at least 100 mL of isopropanol, taking care that solvent does not dry on the surface to prevent evaporation stains.
    7. Rinse with at least 100 mL of DI water. Blow the chip dry with a nitrogen gun.

2. **Chamber preparation**
    1. Prepare a layer of 150 µm polydimethylsiloxane (PDMS) in a Petri dish (section 1).
    2. Use a scalpel to cut a 1.5 cm x 1.5 cm frame from the PDMS layer.
    3. Lift the frame from the Petri dish with a tweezer. Deposit it flat on a clean and polished chip. The sample is now ready for cell seeding.

3. **Fluorescent labeling**
    1. Prepare the following chemicals: phosphate-buffered saline solution, dye solution(s), *d*STORM imaging buffer.
    2. After cell seeding, remove the chip from the media.
    3. Use a pipette to remove any excess fluid from outside the PDMS chamber.
    4. Remove the current fluid from inside the PDMS chamber with a pipette while adding approximately 60 µL of clean PBS at the same time.
       NOTE: The amount added to the chamber will have to be changed according to the chamber size. Be careful not to remove all media from the cell surface.
    5. Replace the PBS with 60 µL of clean PBS and let it incubate for 1 min.
    6. Repeat the previous step, letting it incubate for 5 min this time.
    7. Remove the PBS and replace it with 60 µL of the dye solution. Leave the sample to incubate for around 15 minutes, shielding it from light.
       NOTE: This step might have to change significantly, depending on the fluorescent dye used. We use CellMask Deep Red to label the cell membrane for this experiment
    8. Wash the sample with PBS as in steps 2.3.3-2.3.5.
    9. Remove the PBS and replace it with 40 µL of the imaging buffer at the same time.
       NOTE: There are several different imaging buffers for different fluorescent dyes.
    10. Place a coverslip on top, preventing air bubbles from forming underneath. Gently press the coverslip against the imaging chamber to remove any excess media.
    11. Use a pipette to remove any excess media outside the coverslip. Clean the area outside the coverslip with a water moist swab to avoid crystals formed by dried immersion media residues.

3. Imaging procedure

1. **Component setup**
   NOTE: This version of the setup consists of three main components: the microscope, coupling stage, and sample stage. See the **Table of Materials**.
    1. Use a microscope with a filter holder, white light source, camera, and objective revolver.
    2. Use a 3-axis piezo coupling stage with a fiber-coupled laser and a coupling lens.
    3. Use a one-axis manual sample stage with tip and tilt and a vacuum holder.

4. Mount both the coupling and the sample stage on a 2-axis motorized stage for sample translation.

2. **Waveguide coupling**
   1. Place the chip on the vacuum chuck with the coupling facet towards the coupling objective. Make sure the chip is approximately one focal length away from the coupling objective.
   2. Turn on the vacuum pump.
   3. Turn on the laser to 1 mW. Roughly adjust the chip height so that the beam hits the edge of it. Turn off the laser.
   4. Turn on the white light source. Choose a low magnification objective lens (e.g. 10x). Focus the microscope on a waveguide.
   5. Translate the microscope along the waveguide to see if it is well aligned with the optical path. Move the microscope to the coupling edge.
   6. Turn on the laser at 1 mW or less. Translate the microscope along the coupling edge to find the laser light. Focus the beam on the chip edge.
   7. Adjust the coupling stage along the optical path in the direction that reduces the laser beam spot size until it disappears. The beam is now either above or below the chip surface.
   8. Adjust the coupling stage height until the beam spot reappears and is maximized.
   9. Repeat the two previous steps until the laser forms a focused spot.
   10. Move the focused spot to the waveguide of interest.
   11. Translate the microscope a short distance away from the edge so that the focused beam spot is no longer visible. Turn off the white light.
   12. Adjust the contrast. If the waveguide is guiding, the scattered light along the waveguide should be clearly visible.
   13. Adjust the axes of the coupling stage to maximize the scattered light intensity. Turn off the laser.
   14. Turn on the white light. Adjust the contrast if necessary.
   15. Navigate to the imaging region.

3. **Diffraction limited imaging**
   1. Focus with the desired imaging objective. Turn the white light off.
   2. Insert the fluorescence filter and turn the laser power to 1 mW.
   3. Set the camera exposure time to approximately 100 ms. Adjust the contrast as needed. Ensure that the coupling is still optimized.
   4. Locate a region of interest for imaging. Turn on the piezo stage looping to average out modes.
      NOTE: 20 µm scan range with a step size of 50 nm is suitable for most waveguide structures.
   5. Capture at least 300 images.
   6. Load the captured image stack to Fiji using a virtual stack. From the image menu in Fiji, choose **Stacks** and **z-project**.
   7. Calculate the TIRF image by choosing projection type **average intensity**.

4. ***d*STORM imaging**
   1. Turn on the laser to 1 mW and set the camera exposure time to 30 ms.
   2. Adjust the contrast and focus.
   3. Increase the laser power until blinking is observed.
      NOTE: This might take a while, depending on evanescent field intensity.
   4. Zoom in on a small region of the sample.
   5. Adjust the contrast.
   6. Capture a few images to see if the blinks are well separated.
   7. Adjust the camera exposure time for optimal blinking.
      NOTE: Optimizing blinking is a complex task, but a lot of suitable literature is available[12].
   8. Turn on the piezo stage looping.
   9. Record an image stack of at least 30,000 frames, depending on the blinking density.

5. ***d*STORM image reconstruction**
   1. Open Fiji and load the *d*STORM stack as virtual images.
   2. Adjust the contrast, if necessary.
   3. Use the rectangle tool to select the area to reconstruct.
   4. Open **Run analysis** in the Thunderstorm[13] plugin in Fiji.
   5. Set the basic camera settings in Thunderstorm corresponding to the device. The remaining default parameters are usually satisfactory.
   6. Start the reconstruction.
      NOTE: For the full field of view, the data might need to be divided in substacks, due to the large file size.
   7. Filter the localization list provided by the reconstruction software to remove unspecific localizations. Apple an additional drift-correction if necessary.

Representative Results

TIRF microscopy is a popular technique as it removes out-of-plane fluorescence, increases contrast and thus improves image quality, and is less phototoxic compared to other fluorescence based microscopy techniques. Compared to the traditional objective-based approach, chip-based microscopy offers TIRF excitation without the limited throughput that is usually accompanied with a TIRF lens. An overview of the presented setup can be found in **Figure 1A**. We present diffraction-limited as well as *d*STORM images of liver sinusoidal endothelial cells (LSEC) extracted from mice. A large field of view image of LSECs with labelled microtubulin is also presented, demonstrating the capabilities of high throughput imaging. A conventional *d*STORM setup using an oil immersion TIRF lens (either 60x or 100x magnification) typically images an area of 50 µm x 50 µm, which is 100 times smaller than the chip-based image in **Figure 2**, imaged with a 25x, 0.8 NA objective.

In this method, we use multi-moded Si_3N_4 waveguides for excitation. The utilized chips consist of a strip-etched guiding layer of 150 nm Si_3N_4 deposited over a 2 µm oxidized layer of a silicon chip. A schematic of the chip can be found in **Figure 1B**. Waveguide widths can vary between 200 and 1000 µm. Fabrication details can be found elsewhere[8]. Through interference between the propagating modes the excitation light will not have a homogeneous intensity distribution, but rather a spatially varying pattern. **Figure 2A** presents an image with clearly visible mode patterns. This interference pattern will change with the position of the laser beam at the edge of the waveguide. In order to achieve homogeneous excitation in the final images, we use a piezo stage to oscillate along the coupled facet. Over the course of the imaging procedure, enough variation of the interference patterns exists so that they can be averaged, removing intensity fluctuations in the image. The image stack will consist of several images such as in **Figure 2A**, although with different patterns, but when averaged, the stack will yield an image with homogeneous excitation such as **Figure 2B**. An alternative approach is to use adiabatic tapering to achieve wide, single moded waveguides[8,14], which removes the necessity of mode averaging. However, several millimeters of tapering length are necessary to maintain the single-mode condition to achieve a 100 µm waveguide width. Multi-moded waveguides circumvent this tapering necessity and leave no limitations on the structure width. Beyond the illumination pattern, the highly effective refractive index of the modes allow for unprecedented possibilities towards structured illumination microscopy[11] and fluctuation microscopy methods[7].

The first step in imaging is to collect a diffraction limited image. The experiment results in a stack of around 300 images and the final image is made by taking the average of the stack. In **Figure 2**, we present diffraction limited and *d*STORM imaging of LSECs labelled with CellMask Deep Red using a 60x, 1.2 NA water immersion objective. **Figure 2A** shows inhomogeneous illumination caused by insufficient mode averaging. Successful mode averaging is displayed in **Figure 2B**. **Figure 2C** is a *d*STORM image of the same region, with the marked region shown in **Figure 2D**. Liver sinusoidal endothelial cells have nano-sized pores in the plasma membrane[15], which can be seen here. A Fourier Ring Correlation analysis provided a resolution of 46 nm.

Figure 3 presents a *d*STORM image of a 500 µm x 500 µm region, demonstrating the high throughput capabilities of the technique. A zoomed image of **Figure 3A**, corresponding to a typical *d*STORM field-of-view, is presented together with the diffraction limited image in **Figure 3B**. A Fourier ring correlation to estimate the resolution was performed, yielding a value of 76 nm.

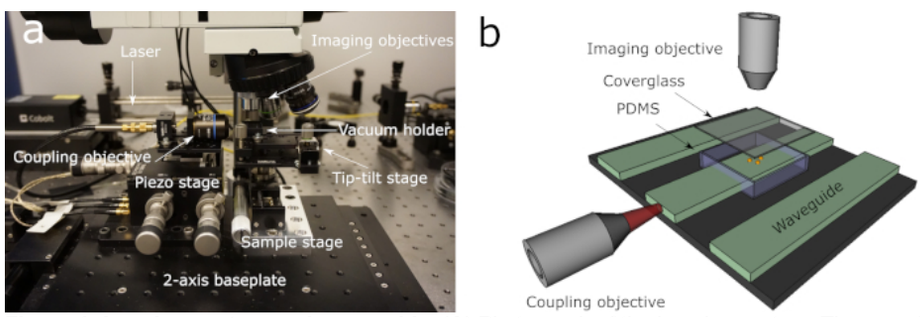

Figure 1: Imaging system and waveguide. (**A**) Photograph of the imaging system. The sample is placed on a vacuum chuck on the sample stage, with the coupling facet of the waveguide towards the coupling objective. A fiber coupled laser and a coupling objective is placed on top of a 3D piezo stage. A lens turret with imaging lenses captures the image from above and relays it to a camera. (**B**) Schematic of the waveguide with coupling and imaging lenses. The coupling lens couples light into the waveguide. The samples (orange beads) are kept inside a sealed PDMS chamber. The evanescent field along the waveguide will excite the sample and the imaging objective will capture the emitted fluorescence. Please click here to view a larger version of this figure.

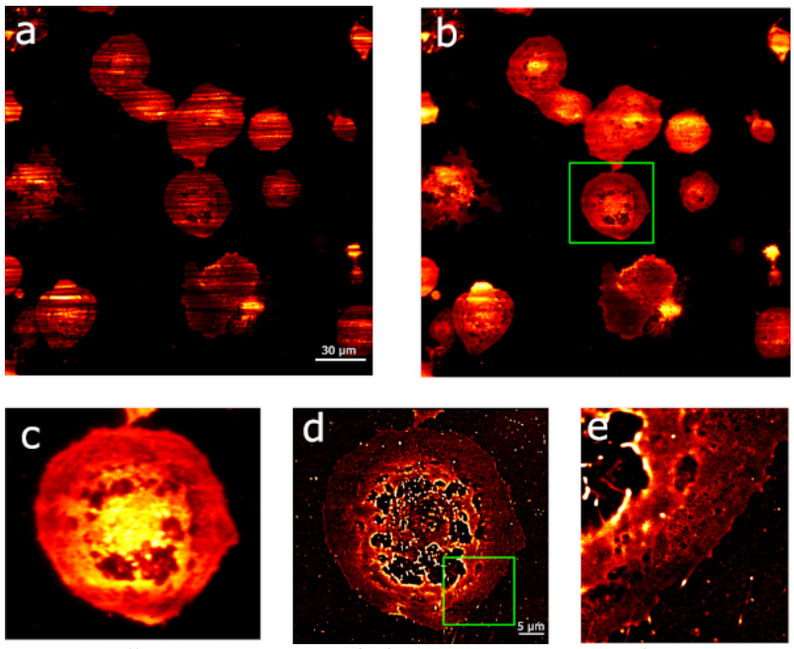

Figure 2: Diffraction-limited and *d*STORM images. (**A**) Image of liver sinusoidal endothelial cells with insufficient mode averaging, resulting in a clearly visible excitation pattern. (**B**) The same region as in (**A**), but with sufficient mode averaging, resulting in homogeneous excitation. (**C**) Diffraction limited image of the inset in (**B**); (**D**) *d*STORM image of the same region. (**E**) Inset of (**D**), clearly showing the fenestrations in the plasma membrane of the cell. Please click here to view a larger version of this figure.

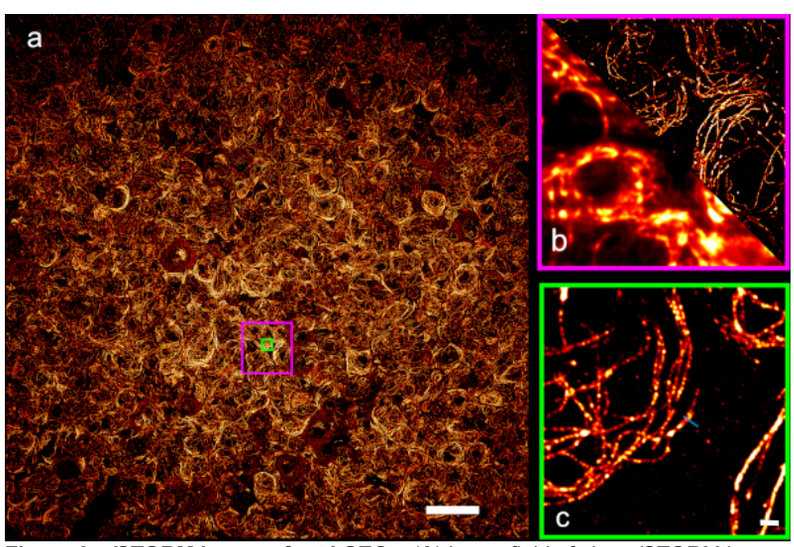

Figure 3: *d*STORM image of rat LSECs. (**A**) Large field of view *d*STORM image of Alexa 647 stained tubulin in rat LSECs. Scale bar = 50 µm. (**B**) Larger marked region from (**A**) comparing diffraction-limited (bottom left) and *d*STORM image (top right). (**C**) Smaller marked region from (**A**). Scale bar = 1 µm. The image has a resolution of 76 nm. Adapted with permission from Helle et al. 2019[6]. Please click here to view a larger version of this figure.

Discussion

Chip-based imaging is similar to conventional *d*STORM imaging. Image quality can thus be gauged using the same approaches as for traditional *d*STORM imaging. The main difference for the user is that the transparent glass slide is exchanged with an opaque Si-wafer. Although they appear very different, the sample handling is practically analogous to a glass slide. The chips are quite sturdy and can easily be handled using wafer tweezers. The imaging procedure and image reconstruction is the same as in a regular *d*STORM experiment. Setting up a functional chip-based microscope requires no special components, except for the photonic chips. Further details of the set-up can be found in previous work[6,7]. The chips used in this work have been fabricated using standard photolithography[8].

Sample preparation encompasses the preparation of the sample chamber. When attaching the PDMS frame to the chip, it is crucial to avoid any small folds or rips where air might enter. If the PDMS folds when attaching it, simply remove it carefully with a tweezer and reattach it. When the sample is ready inside the PDMS chamber, the coverglass must be pressed against it, sealing the region. It is important to avoid any air bubbles

that might form when attaching the coverglass. If an air bubble is formed, gently remove the coverglass and add PBS to the sample chamber to ensure that the sample is covered. The preparation and attachment of the cover slip can then simply be redone.

Coupling light into the waveguide is simplified using the protocol proposed in this paper. There are, however, a few common challenges that can limit coupling. Firstly, if the chip was not cleaned properly and any leftover PBS removed completely, there might be dirt or crystallized PBS on the waveguide. This can introduce major losses, resulting in very little power in the imaging region. Using a moist swab to clean the region outside the cover glass can improve the power significantly. Secondly, if the coupling facet of the waveguide is damaged (e.g., by improper handling), the coupling loss can increase drastically. Optical inspection of the edge will usually reveal any damages easily. The entire coupling facet of the chip can be polished carefully, much like an optical fiber, and will give a smooth coupling facet, which then increases the coupled power.

After the light has been coupled, the imaging procedure is the same as in any conventional *d*STORM setup. If the image has inhomogeneous excitation, as demonstrated in **Figure 2A**, then most likely the mode averaging did not work well. The two most common reasons for this are: 1) too few images captured in order to create an average stack and 2) too short of an oscillation distance/too big of a step size. Collecting too few images can leave out some excitation patterns and the average will thus be inhomogeneous. This can easily be resolved by increasing the number of images in the average stack. Too short of an oscillation distance can also result in an inhomogeneous image, as not enough mode patterns are excited. This can also easily be resolved by increasing the oscillation distance and/or decreasing the step size. In this work we have used a piezo stage to scan the input laser beam over 20 µm and acquire at least 300 images. Another approach could be to use high-speed galvo-mirrors to scan the light across the input waveguide facet within a single acquisition time, such as 10-30 ms. This option is suitable for live cell TIRF imaging, where sub-cellular organelles are in constant motion.

Chip-based *d*STORM offers an unprecedented large area TIRF excitation, which makes it ideally suited for high throughput imaging. The compact character allows for retrofitting to commercial systems, where the chip can be placed upside down for inverted setups or transparent substrates can be developed. The chips are mass fabricated and can be modified to suit many needs. Currently, the main restriction is that it is limited to 2D. The evanescent field is only available approximately 200 nm away from the waveguide surface, so only fluorophores within this region will be excited. Altogether, the field of integrated optics offers many opportunities for chip-based microscopy in the near future, by tackling new imaging questions as well as providing new possibilities to existing ones.

Disclosures

B.S. Ahluwalia has applied for patent GB1606268.9 for chip-based optical nanoscopy. The other authors declare no competing financial interests.

Acknowledgments

The authors would like to acknowledge The European Research Council (grant no. 336716 to B.S.A.). The authors would also like to thank Irati Lagfragua for her invaluable assistance with recording and editing the video.

References

1. Juette, M.F. et al. Three-dimensional sub-100 nm resolution fluorescence microscopy of thick samples. *Nature Methods.* **5** (6), 527-529 (2008).
2. Huang, B., Wang, W., Bates, M., Zhuang, X. Three-Dimensional Super-Resolution Imaging by Stochastic Optical Reconstruction Microscopy. *Science.* **319** (5864), 810-813 (2008).
3. Lampe, A., Haucke, V., Sigrist, S.J., Heilemann, M., Schmoranzer, J. Multi-colour direct STORM with red emitting carbocyanines. *Biology of the Cell.* **104** (4), 229-237 (2012).
4. Wazawa, T., Ueda, M. Total internal reflection fluorescence microscopy in single molecule nanobioscience. *Advances in Biochemical Engineering/Biotechnology.* **95**, 77-106 (2005).
5. Jalali, B., Fathpour, S. Silicon photonics. *Journal of Lightwave Technology.* **24** (12), 4600-4615 (2006).
6. Helle, Ø.I., Coucheron, D.A., Tinguely, J.-C., Øie, C.I., Ahluwalia, B.S. Nanoscopy on-a-chip: super-resolution imaging on the millimeter scale. *Optics Express.* **27** (5), 6700-6710 (2019).
7. Diekmann, R. et al. Chip-based wide field-of-view nanoscopy. *Nature Photonics.* **11** (5), 322-328 (2017).
8. Tinguely, J.-C., Helle, Ø.I., Ahluwalia, B.S. Silicon nitride waveguide platform for fluorescence microscopy of living cells. *Optics Express.* **25** (22), 27678-27690 (2017).
9. Ahluwalia, B.S., McCourt, P., Huser, T., Hellesø, O.G. Optical trapping and propulsion of red blood cells on waveguide surfaces. *Optics Express.* **18** (20), 21053-21061 (2010).
10. Coucheron, D.A., Wadduwage, D.N., Murugan, G.S., So, P.T.C., Ahluwalia, B.S. Chip-Based Resonance Raman Spectroscopy Using Tantalum Pentoxide Waveguides. *IEEE Photonics Technology Letters.* **31** (14), 1127-1130 (2019).
11. Helle, Ø.I., Dullo, F.T., Lahrberg, M., Tinguely, J.-C., Ahluwalia, B.S. Structured illumination microscopy using a photonic chip. *ArXiV.* https://arxiv.org/abs/1903.05512v1 (2019).
12. Metcalf, D.J., Edwards, R., Kumarswami, N., Knight, A.E. Test Samples for Optimizing STORM Super-Resolution Microscopy. *Journal of Visualized Experiments.* (79) (2013).
13. Ovesný, M., Křížek, P., Borkovec, J., Švindrych, Z., Hagen, G.M. ThunderSTORM: a comprehensive ImageJ plug-in for PALM and STORM data analysis and super-resolution imaging. *Bioinformatics.* **30** (16), 2389-2390 (2014).
14. Archetti, A., Glushkov, E., Sieben, C., Stroganov, A., Radenovic, A., Manley, S. Waveguide-PAINT offers an open platform for large field-of-view super-resolution imaging. *Nature Communications.* **10** (2019).

15. Braet, F., Wisse, E. Structural and functional aspects of liver sinusoidal endothelial cell fenestrae: a review. *Comparative Hepatology.* **1**, 1 (2002).

Paper V

Multi-modal On-chip Nanoscopy and Quantitative Phase Imaging Reveals the Nanoscale Morphology of Liver Sinusoidal Endothelial Cells

D. A. Coucheron, A. Butola, K. S., A. Ahmad, J. C. Tinguely, P. McCourt, P. Senthilkumaran, D. S. Mehta and B. S. Ahluwalia.

Multi-modal on-chip nanoscopy and quantitative phase imaging reveals the nanoscale morphology of liver sinusoidal endothelial cells

David A. Coucheron[a,‡], Ankit Butola[a,b,‡], Karolina Szafranska[c], Azeem Ahmad[a,b], Jean-Claude Tinguely[a], Peter McCourt[c], Paramasivam Senthilkumaran[b], Dalip Singh Mehta[b] and Balpreet Singh Ahluwalia[a, d,*]

a: Department of Physics and Technology, UiT The Arctic University of Norway, Norway.
b: Bio-photonics and Green Photonics Laboratory, Department of Physics, Indian Institute of Technology Delhi, Hauz-Khas, New Delhi- 110016, India.
c: Faculty of Health Sciences, Department of Medical Biology, Vascular Biology Research Group, UiT The Arctic University of Norway, 9037 Tromsø, Norway.
d: Department of Clinical Science, Intervention and Technology Karolinska Institutet, Stockholm, Sweden.
‡ These authors contributed equally to this work.
**Corresponding author: balpreet.singh.ahluwalia@uit.no*

Abstract

Visualization of 3D morphological changes in the subcellular structures of a biological specimen is a big challenge in life science. Despite conspicuous refinements in optical nanoscopy, determination of quantitative changes in subcellular structure, i.e., size and thickness, remains elusive. We present an integrated chip-based optical nanoscopy set-up that provides a lateral optical resolution of 61 nm combined with a quantitative phase microscopy (QPM) system with a spatial phase sensitivity of ±20 mrad. We use the system to obtain 3D morphology of liver sinusoidal endothelial cells (LSECs) combined with super-resolved spatial information. LSECs have a unique morphology with small nanopores (30-200 nm in diameter) in the plasma membrane, called fenestrations. The fenestrations are grouped in discrete clusters, which are around 100 nm thick. Thus, imaging and quantification of fenestrations and sieve plate thickness requires resolution and sensitivity of sub-100 nm along both the lateral and the axial directions. In chip-based nanoscopy, the optical waveguides are used both for hosting and illuminating the sample through the evanescent field. The fluorescence signal is captured by an upright microscope, which is converted into a Linnik-type interferometer to sequentially acquire both super-resolved images and quantitative phase information of the sample. The multi-modal microscope provided an estimate of the fenestration diameter of 124±41 nm and average estimated thickness of the sieve plates in the range of 91.2±43.5 nm for two different cells. The combination of these techniques offers nanoscale visualization of both the lateral size and the thickness map of sieve plates.

Significance

We developed a integrated waveguide chip-based optical nanoscopy with a high spatially sensitive quantitative phase microscopy to obtain 3D morphology of liver sinusoidal endothelial cells (LSECs). LSEC which contain large numbers of fenestrations (transcellular nanopores) in the plasma membrane, typically clustered in groups of 10-50 within areas called sieve plates. Determining the diameter and height of fenestrated regions can be important as it can be affected by several drugs, as well as during natural (but detrimental) changes such as aging that result in “pseudocapillarisation”, whereby LSEC simultaneously lose fenestrations and become thicker. Our propsed multi-modal microscope offers the diameter of the fenestrations and optical thickness of the sieve plates.

1: Introduction

Far-field optical nanoscopy techniques are frequently used to visualize subcellular structures in biological specimens by surpassing the diffraction limit. Optical nanoscopy encompasses a plethora of techniques, including stimulated emission depletion (STED) microscopy(1); structured illumination microscopy (SIM)(2); different variants of single molecule localization microscopy (SMLM) such as photo-activated localization microscopy (PALM)(3) and direct stochastic optical reconstruction microscopy (*d*STORM)(4); and intensity fluctuation based techniques such as super-resolution optical fluctuation imaging (SOFI)(5). These techniques can help detect subcellular structures (<200 nm) of biological specimens such as lipids, proteins, membrane structures, microtubules and nucleic acids by specific fluorescence tagging(6). Each technique has respective advantages and

disadvantages, for example, SIM has gained popularity for live-cell imaging due to its fast image acquisition time, but at a limited spatial resolution(7). *d*STORM , on the other hand, is slower, but offers high resolution for e.g. characterization of viral proteins(8) and imaging actin filaments in mammalian cells(9, 10).

To reduce the complexity of the typical SMLM setup using a total internal reflection fluorescence (TIRF) configuration, a photonic chip-based optical nanoscopy system was recently proposed(11-13). In the chip-based system, a photonic integrated circuit is used to replace the usual free space optics for excitation. The collection, however, is done through free space optics. The main advantage of chip-based system is the decoupling of excitation and collection pathways, as well as miniaturization of the excitation light path of the system. In chip-based nanoscopy, the TIRF illumination is generated through the evanescent field of waveguides, rather than using conventional high magnification and high numerical aperture (N.A.) TIRF lens. The evanescent field in waveguides can be generated over extraordinarily large areas, as it is only defined by the waveguide geometry. The waveguide geometry makes it possible to use any imaging objective lens to image arbitrarily large areas as compared to the traditional TIRF-based *d*STORM(12), which is limited by the field of view of the TIRF lens.

On the other hand, quantitative phase microscopy (QPM) is an cutting edge label-free optical technique which facilitates highly sensitive measurements of the refractive index and thickness of both industrial and biological specimens(14). Various QPM methods have been proposed so far for extracting optical phase and dynamics of biological cells(15-17). These techniques offer high phase sensitivity (spatial and temporal), transverse resolution and acquisition rate(15). The spatial and temporal phase sensitivity of the QPM system is highly dependent on the illumination source and the type of interferometric geometry, respectively(17-19). For example, common path QPM techniques offer better temporal phase sensitivity thus can be used to measure membrane fluctuation of the cells(20). In addition, spatial phase sensitivity of the system can be improved by using low coherence light sources (halogen lamps and LED), but requires phase shifting techniques to utilize the whole field of view of the camera(21). A recent advancement in the QPM technique is used to offer three-dimensional information of the samples by measuring the phase across multiple angles of illumination. This technique offers tomography of various biological specimens such as red blood cells (RBC), HT29 cells and bovine embryos(17, 22). Since lateral resolution of the QPM techniques depends on the numerical aperture (NA) of the objective lens, imaging beyond diffraction limit (<200 nm) is still challenging and limits to the study of subcellular structures. Therefore, it is useful to develop multi-modality routes where different microscopy methods can be utilized to provide complementary information about the biological specimen such as liver sinusoidal endothelial cells (LSECs).

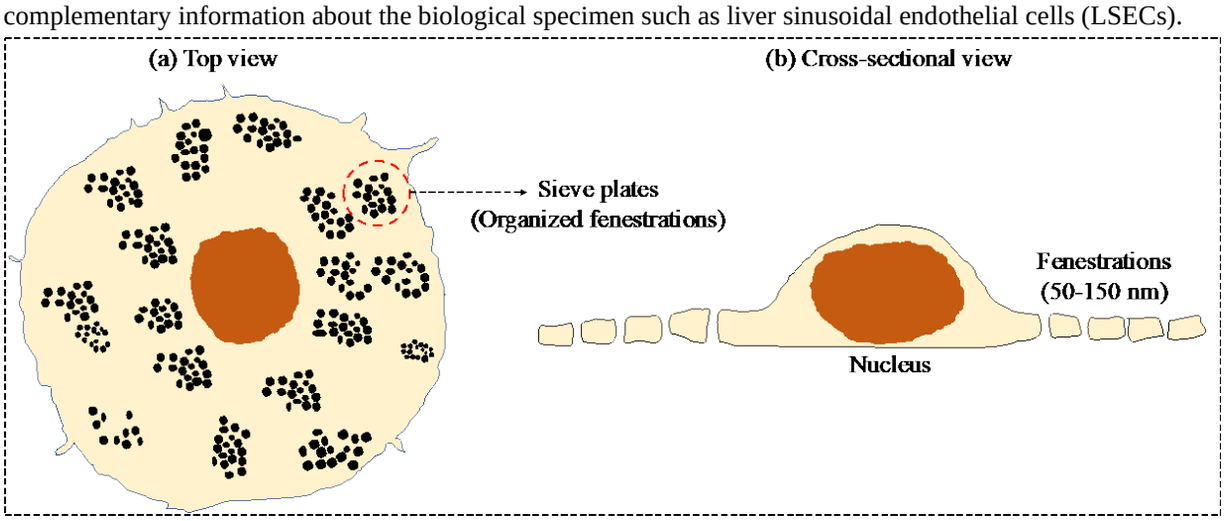

Figure 1: Top view (a) and cross-sectional view (b) of liver sinusoidal endothelial cells. LSECs have unique morphology, where nanoscopic fenestrations are grouped in thin sieve plates. The diameter and the thickness of fenestrations are below the diffraction limit of conventional optical microscopes.

Figure 1 depicts a schematic of a LSEC which contain large numbers of fenestrations (transcellular nanopores) in the plasma membrane, typically clustered in groups of 10-50 within areas called sieve plates(23). The fenestrations act as an ultra-filter between blood and the underlying hepatocytes, facilitating the bi-directional exchange of substrates between hepatocytes and blood. For example, smaller viruses and drugs can pass this barrier while blood cells are retained within the sinusoidal vessel lumen(24, 25). Interestingly, the diameter of the fenestrations (white spots in Fig. 1(a)) varies from 50-200 nm(25-27), smaller than the diffraction limit of optical microscopy. These fenestrations are often clustered in sieve plates and connected by actin fibers to other sieve plates as shown

in Fig. 1(a). The typical thickness of sieve plates is around 100-150 nm(28), and these fenestrations are consequently nanoscale-sized in all the three dimensions. As shown in Fig. 1, the fenestrations and sieve plates are located in the LSEC's plasma membrane and therefore TIRF illumination is ideally suited for imaging these structures. Determining the diameter and height of fenestrated regions can be important as it can be affected by several drugs(29, 30), as well as during natural (but detrimental) changes such as aging that result in "pseudocapillarisation", whereby LSEC simultaneously lose fenestrations and become thicker(31).

Here, we have developed a multi-modal chip-based optical nanoscopy and highly sensitive QPM system to visualize three-dimensional morphological changes in LSECs. The proposed system decouples the light illumination path from the collection path and thus relatively easy integration of *d*STORM and QPM. In addition, the proposed system utilized nanoscale phase sensitivity of the proposed QPM technique is utilized to extract the optical thickness of sieve plates. Moreover, chip-based *d*STORM supports super-resolution imaging down to 50 nm over an extraordinarily large field of view (FOV)(12). Therefore, integration of *d*STORM and QPM allows super resolution imaging in the lateral dimension (with *d*STORM) and nanometric sensitivity in the axial direction (with QPM) giving the complete 3D morphology of the cells. In this work, we demonstrate the capabilities of the system by imaging LSECs with both diffraction limited TIRF microscopy and *d*STORM. The plasma membrane fenestrations and sieve plates are observable with *d*STORM and the average optical thickness of the sieve plate region is obtained using QPM. The system offers a combination of simultaneous functional and quantitative imaging of the cells with large FOV which is otherwise not possible by using TIRF *d*STORM. The integrated system provides a low-cost, field portable and easy-to-use platform with a potential in high-throughput morphological and nanometric imaging for specific biological applications.

2: Experimental details

2.1: Working principle of partially spatially incoherent quantitative phase microscope

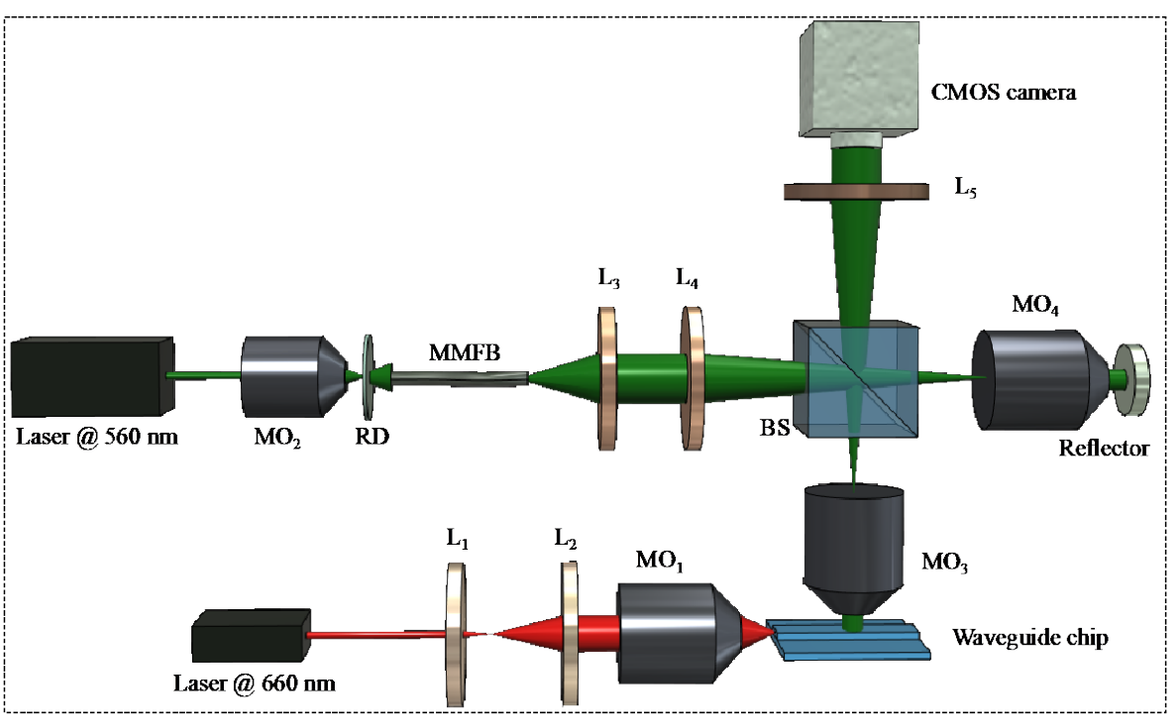

Figure 2: Schematic diagram of integrated partially spatially incoherent quantitative phase microscopy (QPM) and chip-based nanoscopy system for the morphological imaging of liver sinusoidal endothelial cells. MO1-4: Microscopic objective lens, RD: Rotating diffuser, L1-5: Lens, MMFB: Multi-multimode fiber bundle, BS: Beam splitter. High intensity evanescent field is generated on top of the wave-guide chip using 660 nm Cobolt laser for single molecule fluorescence excitation. The fluorescence signal is captured by an upright microscope which is converted into a Linnik type interferometer to perform quantitative phase microscopy (QPM).

The schematic diagram of the system in QPM and *d*STORM mode is shown in Fig. 2. A Cobolt Flamenco laser (@660 nm) is coupled into the waveguide to generate the evanescent field on top of the waveguide to perform the *d*STORM experiment. A highly coherent Cobolt laser (@560 nm) is expanded by a microscopic objective (MO_2)

and passes through the rotating diffuser followed by multi-multimode fiber bundle (MMFB) for the phase imaging. The rotating diffuser and MMFB is used to generate spatial and temporal diversity to convert a highly coherent laser into a partially spatially coherent light source. It has been shown previously that the reduction of spatial coherence results speckle-free images and improves the spatial phase sensitivity of the interferometry system(32). Therefore, partially spatially coherent sources can be utilized to extract the morphological changes of thinnest biological specimens such as LSECs. The partially spatially coherent beam further coupled into the Linnik type QPM system. In the QPM system, light beams reflected from the sample and reference mirror interfere at the beam splitter plane. The 2D interference pattern coded the information of the sample which further captured by the CMOS image sensor (Hamamatsu ORCA-Flash4.0 LT, C11440-42U).
The 2D intensity distribution of the interferogram can be expressed as:

$$I\ (x,y) = a(x,y) + b(x,y)\cos\left[2i\left(f_x x + f_y y + \phi(x,y)\right]\right. \quad (1)$$

where a(x,y) and b(x,y) represent the background and the modulation terms, respectively. $f_x x$ and $f_y y$ are the spatial frequencies of the interference pattern along x and y directions and $\phi\ (x, y)$ is the phase difference between the object and reference beam.
Standard Fourier transform analysis(33) and Goldstein phase unwrapping algorithm(34) is used to extract the phase information of the specimens. The phase information is a combination of refractive index and thickness of the specimens and can be written as:

$$\phi(x,y) = \frac{2\pi}{\lambda} \times 2h(x,y) * \{n_s(x,y) - n_0(x,y)\} \quad (2)$$

where λ is the wavelength of incident light, h is the geometrical thickness of the specimen; n_s and n_o are the refractive indices of the specimen and surrounding medium, respectively and an extra factor of 2 appears because the imaging is performed in the reflection mode. By reformatting the equation an expression for the thickness of the sample can be found:

$$h(x,y) = \frac{\lambda * \phi(x,y)}{4\pi * \{n_s(x,y) - n_0(x,y)\}} \quad (3)$$

2.2: *d*STORM imaging and data analysis:

*d*STORM imaging is performed on waveguide chip based TIRF excitation. Once the sample was stained and the blinking buffer added, the chip was placed on the sample stage and held in place with a vacuum chuck. The excitation light was coupled from free space by end-fire coupling using a 0.5 NA objective lens. The waveguides are multi-moded, giving rise to an inhomogeneous excitation pattern. In order to achieve homogeneous resolution, the coupling objective was scanned along the input facet to average out the modes. Imaging was done with a Hamamatsu Orca sCMOS camera with 30 ms exposure time. For TIRF images, the exposure time was increased to 100 ms and an average of approximately 1000 frames used. Approximately 100 mW power was used for all images, however the power was incrementally increased up to approximately 400 mW towards the end of each imaging procedure to get additional localizations. The data were reconstructed using ThunderSTORM(35), a FIJI plugin.

3: Workflow of the framework: chip preparation, staining protocol, data acquisition and image processing

3.1: Chip preparation:

The workflow of the system to extract the optical thickness of size of fenestrated areas in LSECs is shown in Fig. 3. All imaging in the present work is done using Si_3N_4 strip waveguides with varying widths between 200 and 500 μm. The chips were fabricated using a previously described procedure(36). Before any sample preparation, the chips were thoroughly cleaned using a two-step process. The chips were first cleaned in a 1% Hellmanex in deionized (DI) water at 70^0C for 10 minutes. Following that, the chips were rinsed with DI water, followed by isopropanol and DI water again. Finally, the chips were dried using N_2. A hollow rectangular chamber was created with polydimethylsiloxane (PDMS) and placed on the chip to restrict the area where cells attach.

3.2: Cell isolation and seeding:

Cell have been isolated from C57BL/6 male mouse using modified standard protocol(37). Briefly, perfusion of the liver with Liberase (Roche) was followed by low-speed differential centrifugation and then separated using superferromagnetic beads conjugated with the LSEC-specific antibody CD146 (MACS, Miltenyi Biotec). After isolation the cells were seeded on chips precoated with human fibronectin and incubated in 5% CO_2 at 37°C in RPMI-1640 culture medium for 2 hours. Seeding density was about 100,000 LSECs per 0.5cm^2 PDMS chamber. Samples were fixed by 10 minutes incubation in 4% PFA in PBS and left in 1% PFA at 4°C until imaging.

3.3: Staining protocol and data acquisitions:

The cells were all stained with CellMask Deep Red (CMDR). The chips were rinsed thoroughly with PBS before staining. A 1:1000 dilution of CMDR in PBS water was added inside the PDMS chamber and left to incubate for 10 minutes. The sample was then thoroughly rinsed with PBS again. Prior to imaging, a dSTORM buffer was prepared using 22.5 µL PBS, 22.5 µL H_2O-based oxygen scavenger system solution(38), and 5 µL 1M MEA. The sample was then rinsed thoroughly with PBS before the blinking buffer was applied and the sample area sealed off with a cover slip. Finally, the chip is placed under the microscope to acquire both interferometric and *d*STORM imaging. The extracted phase map and super resolution images are further registered to localize the fenestrated area and to calculate size and optical thickness of the sieve plates.

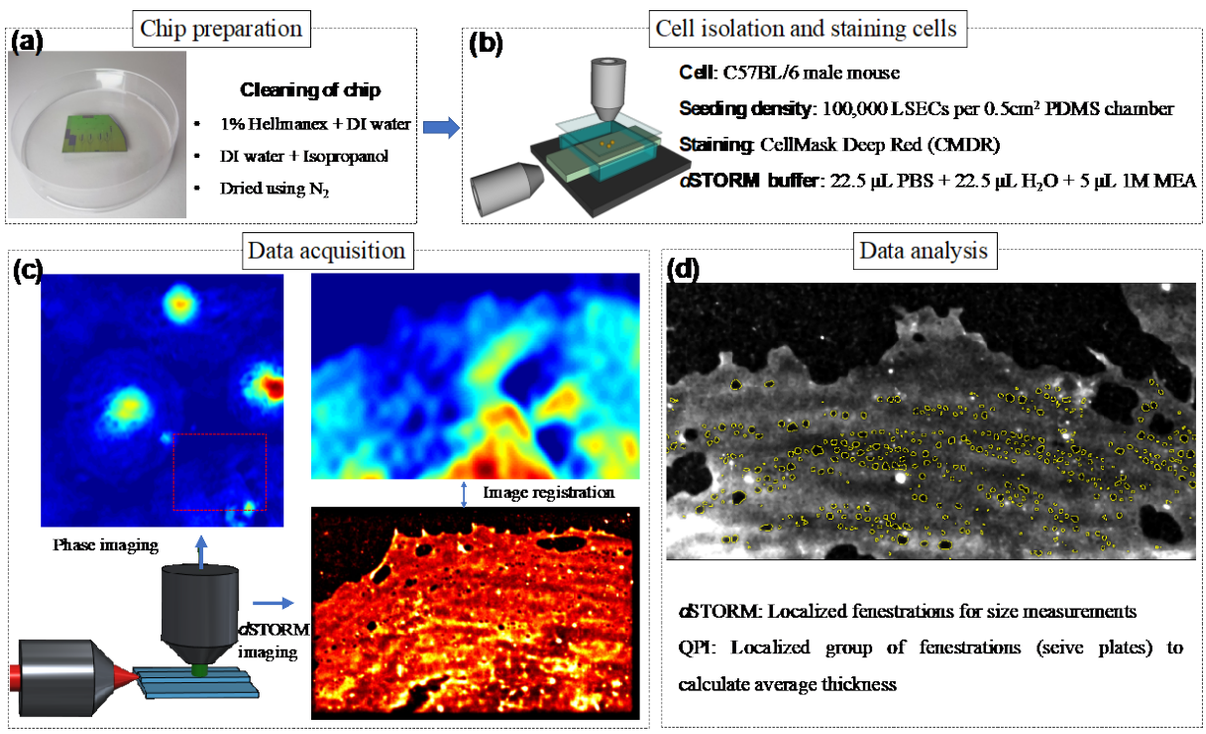

Figure 3: Workflow of the integrated quantitative phase microscopy (QPM) and on-chip nanoscopy system. (a) Si_3N_4 strip waveguides is cleaned thoroughly to perform all imaging experiments. (b) Cells are isolated on top of the chip with a restricted rectangular area created with polydimethylsiloxane (PDMS). (c) and (d) shows the data acquisitions and registration between QPI and super-resolution imaging to calculate the size of the fenestrations and the average thickness of the group of fenestrated areas in liver sinusoidal endothelial cells (LSECs).

4: Results and Discussion:

The proposed platform integrates both on-chip nanoscopy and highly sensitive QPM system. On-chip nanoscopy offers high-throughput imaging by decoupling excitation and emission path whereas partially spatially coherent source in QPM offers nanometric spatial phase sensitivity to identify nanometric morphological changes in the specimens. We first characterize the system by calculating the spatial phase noise i.e., spatial phase sensitivity of the system in QPM mode. To measure the phase noise in the system, a standard flat mirror of surface flatness $\lambda/10$ is used as an object to capture interferometric images. Figure 4(a) shows the recorded interferogram on the mirror surface when operating the system in QPM mode. Ideally, the calculated phase map without any sample on the flat surface should be zero. However, some spatial noise always presents in any QPM system, which can be occurred and difficult to avoid due to experimental imperfections. Figure 4(b) depicts the standard deviation of

the phase variations, i.e., the spatial noise of the system. The average spatial noise of the system is ±20 mrad, which is significantly less than using a direct laser to perform QPM(18, 39).

High spatial and temporal coherence of a direct laser causes speckles and spurious fringes in the final image, reducing the phase sensitivity of the QPM system. This unwanted noise can be avoided by introducing spatial and temporal diversity in the laser beam by passing it through a rotating diffuser and subsequently a MMFB(18). The rotating diffuser and MMFB reduce the spatial coherence of the light source, thus improving the spatial phase sensitivity of the system. A Fourier ring correlation (FRC) test is performed on the *d*STORM data to estimate the resolution of the system in nanoscopy mode, with the result correlation plotted in Fig. 4(c). The resolution at FRC=1/7 is 61 nm. The resolution of our system can, however, be increased by swapping the beam splitter (marked BS in Fig. 2) in the system for a flip mirror, as half of the photons are lost passing through it. We chose to use a beam splitter as it opens up for simultaneous fluorescence and phase imaging, whereas with a flip mirror it would be limited to sequential imaging.

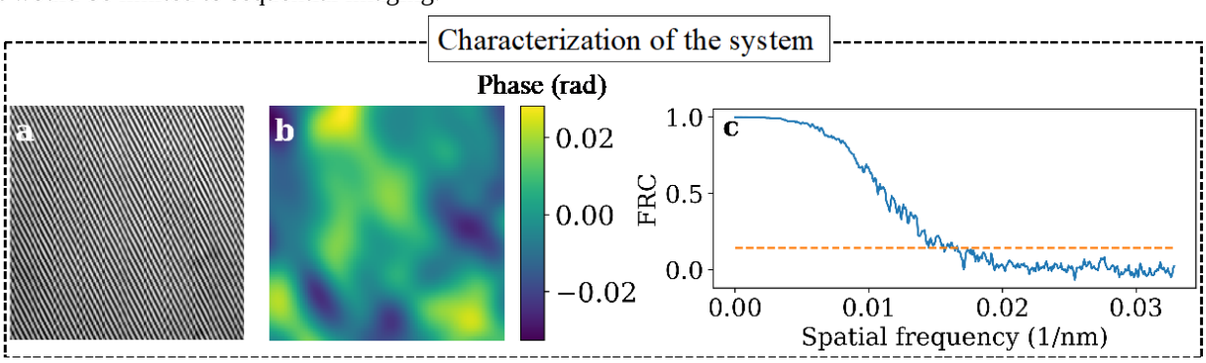

Figure 4: Noise characterization of the QPM system. (a) Interferogram captured by the QPM mode of the proposed setup on a standard mirror of λ/10 surface flatness. (b) Standard deviation of phase in (a) demonstrating the phase noise of the system. The color bar represents the phase map in radians. (c) The 61 nm lateral optical resolution of the chip-based system was obtained on the sample used in Figure 4 using Fourier ring correlation.

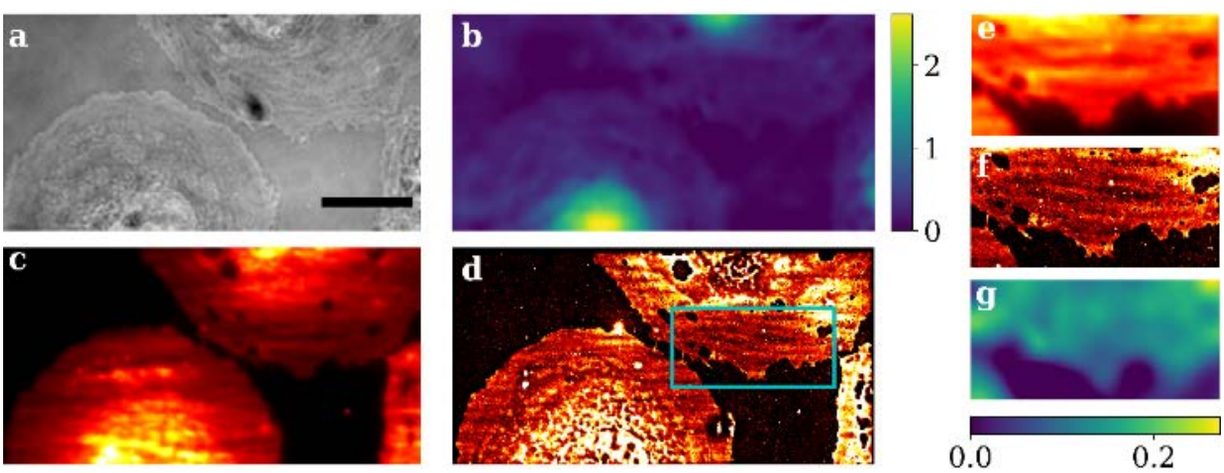

Figure 5: Parts of three cells imaged with brightfield (scalebar is 10 μm) (a), QPM (b), TIRF (c) and *d*STORM (d). The phase map gives morphological information about the cells, with a maximum phase value in the nucleus of the lower left cell of 2.3 rad. The dSTORM image clearly shows plasma membrane fenestrations in the top cell. TIRF, dSTORM and QPM images of the inset in (d) is also presented in (e-g). The colour bars show phase in radians.

Figure 5 shows a complete dataset gathered for one imaged region of LSECs. It consists of: a) a bright field image, b) a phase map of the LSECs, c) a diffraction limited TIRF image and d) a *d*STORM image with visible fenestrations. The bright field image (Fig. 5 (a)) offers clear diffraction limited qualitative imaging of the cell. On the other hand, Fig. 5(b) represents phase map i.e., optical thickness of the LSECs which is without any doubt more quantitative than bright field image. In phase image, higher phase region i.e., deep yellow represents the nucleus, surrounded by mitochondria with the plasma membrane. The maximum phase value is 2.3 rad in the nucleus of the bottom left cell. Figure 5(c) represents diffraction limited TIRF image of the LSECs offers excellent optical sectioning, morphological and functional features of the cells. However, visualization of fine features such as fenestrations presents in the plasma membrane (Fig. 5(d)) can only be noticeable using the super-resolution imaging. Figure 5(e-g) present the inset from Fig. 5 (d) in TIRF, *d*STORM and QPM mode. Comparing Figure 5e and 5f, the fenestrations in the membrane are clearly resolved in the *d*STORM image, not being visible using

diffraction limited TIRF imaging. The phase of the imaged membrane region varies from 0 to approximately 0.25 rad.

LSECs have an interesting morphology with a thick nucleus in the center and an extremely flat cell membrane containing nanoscale fenestrations grouped within sieve plates. We used *d*STORM to locate fenestrated regions in LSECs and QPM to determine the average phase of the fenestrated regions. Figure 6 shows a *d*STORM image and the corresponding phase image. Figure 7 shows the measured phase value for several different fenestrated regions for two different cells in Fig. 6. Although the fenestrations are below the diffraction limit, and thus the spatial resolution limit of the QPM, the average phase of sieve plates can be calculated.

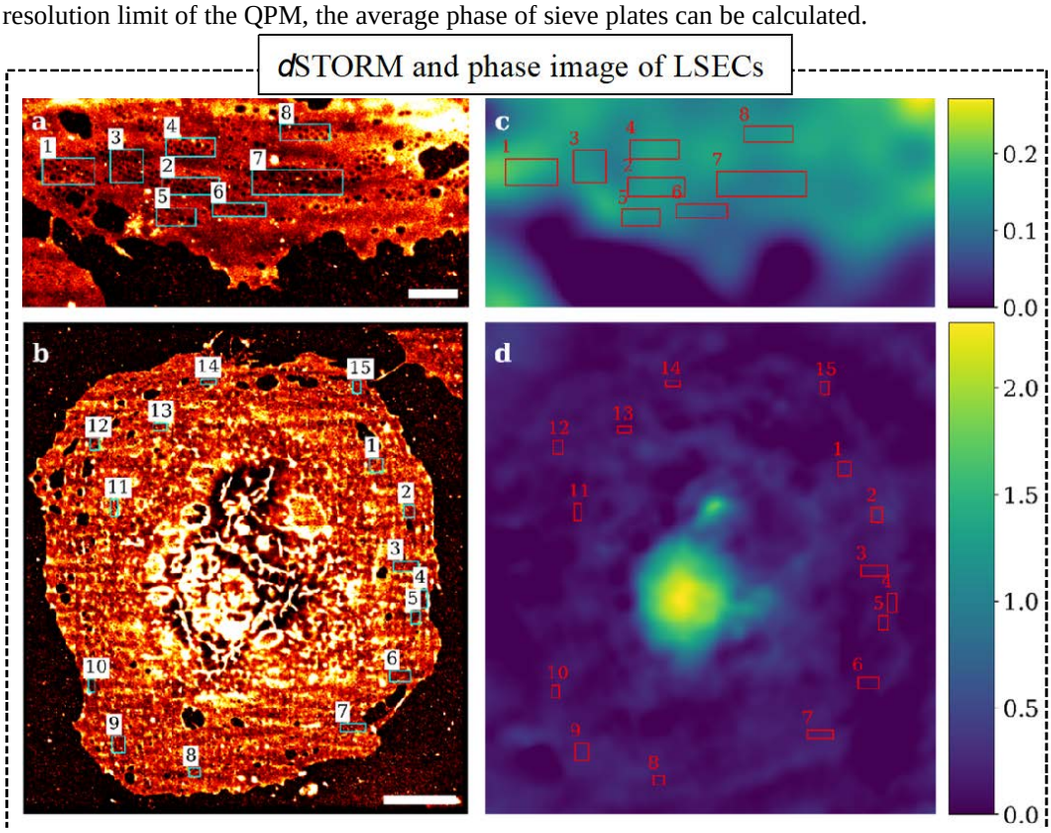

Figure 6: (a,c) *d*STORM and phase image of the inset in Figure 3 of cell 1 The scalebar is 2 µm. (b,d) dSTORM and phase image of cell 2. Fenestrations in the plasma membrane are visible all throughout the cell. The scale bar is 5 µm. The phase shows a maximum phase of 2.3 rad in the nucleus of the cell. The colorbars show phase in radians.

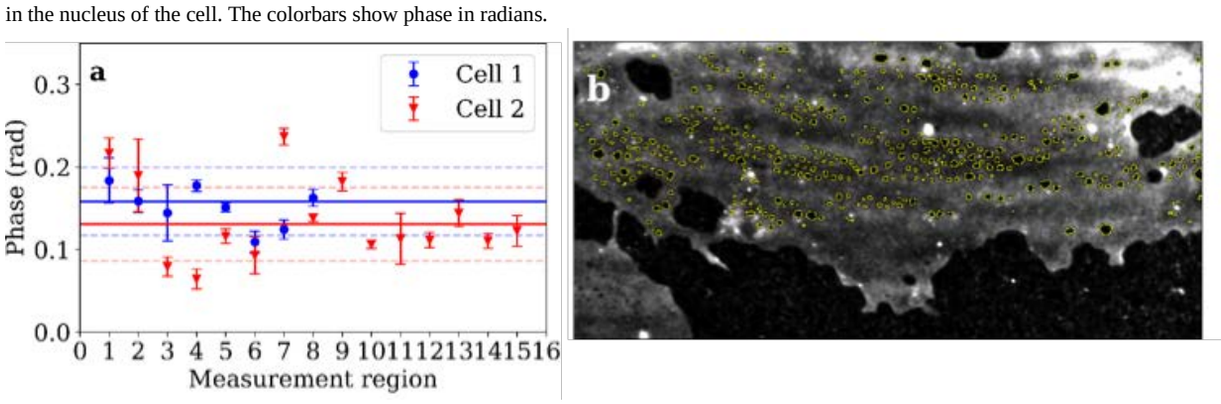

Figure 7: (a) Phase value measured for the marked regions in Fig. 5 (a, b) with standard deviation of each region. The mean values for all regions are presented as a line for both cells, with the standard deviation of the regions presented as dotted lines. (b) Localized fenestrations for diameter measurement.

The measured phase value for all marked regions in Fig. 6 are presented in Fig. 7a, with the standard deviation of the phase in each region. The average optical thickness of the sieve plates can then be calculated based on the phase map. The calculation of the actual thickness does however require an estimate for the effective refractive index. Sample 1 from Fig. 6 has a weighted average phase over all regions of 0.158 rad with a standard deviation of 0.041 rad. Sample 2 has a weighted average phase of 0.131 rad with a standard deviation of 0.045 rad. The values are thus in agreement. If we assume a refractive index range of 1.35 – 1.37(40) using Eq. 3 we get an

average thickness of 92.5±39.1 nm and 76.3±36.4 nm for sample 1 and 2, respectively. Combining the data, the resulting height is 91.2±43.5 nm. We also calculated the diameter of the fenestrations of the sample in Fig. 6 (a) using the Sauvola local thresholding algorithm in FIJI on the image in Fig. 6(a). The identified fenestrations are presented in Fig. 7(b). The mean diameter of the fenestrations is 124 nm with a standard deviation of 41 nm. Both the thickness and the pore diameter agrees well with previous literature(28).

5: Conclusion:

In this work we have developed a muti-modal chip-based optical nanoscopy and highly spatially sensitive quantitative phase microscopy system. To demonstrate the potential of the proposed system, we localized plasma membrane fenestrations in liver sinusoidal endothelial cells (LSECs) using *d*STORM and then measured the thickness of the fenestrated areas using QPM. The system, when operated in the *d*STORM mode, offers nanometric spatial resolution (61 nm) to visualize small fenestrations present in LSECs. Further, precise localization of the group of fenestrations and the improvement in phase sensitivity offers the optical thickness of sieve plates. Assuming an average refractive index of the cell membrane, the measured average thickness of the fenestrated regions is found 92.5±39.1 nm and 76.3±36.4 nm for sample 1 and 2, respectively. Furthermore, the diameter of the fenestration is found to be 124±41 nm.
In the proposed integrated QPM+dSTORM system, same imaging arm is used to capture the phase and super-resolution image without any mechanical displacement in the sample therefore, same location of the cell can be easily identified. On the other hand, the same cell cannot be located easily in two different microscopes as the size of waveguide chip is very large (approximately 25×25 mm). In addition, angular displacement in the final acquired datasets using two different microscopes will certainly create a subpixel mismatch and hard to avoid by image registration mechanics and therefore, affect the measurement accuracy of the study. As in the present study, common optomechanical components are used in the imaging arm for both QPM and dSTORM mode, using two different system will cost almost double which can be considered as another advantage of the proposed system.
In addition, the system enables multi-modal imaging in a simple manner, while still being easy to further customize. For improved resolution in *d*STORM, a simple flip mirror instead of a beam splitter will help. Further enhancement in phase sensitivity is possible by replacing the partial spatial coherent illumination with a perfectly incoherent light source such as white light or a light emitting diode (LED). The white light source offers maximum possible spatial phase sensitivity, but requires multiple frames, i.e., phase shifting interferometry (PSI) to extract the phase information due to poor temporal coherence. Additionally, PSI can also be useful to improve the transverse resolution of the system. Moreover, with minor modifications, different modalities can easily be added with the current system, such as waveguide based optical trapping(40) and spectroscopic techniques(41). The entire system size can also be significantly reduced and automated coupling can be implemented for ease of use (42) Chip-based microscopy has been implemented for live cell imaging of delicate cells(43). In future, we aim to adapt the proposed multi-modality microscopy platform for imaging dynamics of fenestration in living LSECs e.g., when challenged by chemicals or drugs that alter the fenestrations and sieve plates. Being able to get both fenestration diameter and sieve plate thickness makes it possible to track changes in a very detailed manner. This will be a particularly useful tool for the discovery of agents that reverse age-related pseudocapillarisation since the method simultaneously measures two important parameters, LSEC thickness and fenestration, that are increased and reduced (respectively) during the ageing process.

Acknowledgement: B.S.A. acknowledges UiT, The Arctic University of Norway Tematiske Satsinger funding program and Diku - Direktoratet for internasjonalisering og kvalitetsutvikling i høyere utdanning (Project number INCP- 2014/10024). B.S.A. and P.Mc.C. acknowledges the European Union's Horizon 2020 research and innovation program under the Marie Sklodowska-Curie Grant Agreement No. 766181, project "DeLIVER".

Author contributions:

BSA, PMc, DSM and PS discussed the project idea. DAC and AB designed and developed the experimental setup. The samples were provided by KS and PM, who also sought the permission and ethical clearances for this study. KS, BSA and PM provided biological insights for this study. AA and JCT provide the assistance with QPI and dSTORM. QPI and dSTORM datasets are acquired and analyzed by AB and DAC. DAC and AB prepared first

draft of the manuscript and all author contributed towards writing of the manuscript. The work is supervised by BSA.

Competing interests: B.S.A. have applied for patent GB1606268.9 for chip-based optical nanoscopy. B.S.A is a co-founder of the company Chip NanoImaging AS, which commercializes on-chip super-resolution microscopy systems.

References:

1. S. W. Hell, J. Wichmann, Breaking the diffraction resolution limit by stimulated emission: stimulated-emission-depletion fluorescence microscopy. *Optics letters* **19**, 780-782 (1994).
2. M. G. Gustafsson, Surpassing the lateral resolution limit by a factor of two using structured illumination microscopy. *Journal of microscopy* **198**, 82-87 (2000).
3. S. T. Hess, T. P. Girirajan, M. D. Mason, Ultra-high resolution imaging by fluorescence photoactivation localization microscopy. *Biophysical journal* **91**, 4258-4272 (2006).
4. U. Endesfelder, M. Heilemann, "Direct stochastic optical reconstruction microscopy (dSTORM)" in Advanced fluorescence microscopy. (Springer, 2015), pp. 263-276.
5. T. Dertinger, R. Colyer, G. Iyer, S. Weiss, J. Enderlein, Fast, background-free, 3D super-resolution optical fluctuation imaging (SOFI). *Proceedings of the National Academy of Sciences* **106**, 22287-22292 (2009).
6. S. W. Hell *et al.*, The 2015 super-resolution microscopy roadmap. *Journal of Physics D: Applied Physics* **48**, 443001 (2015).
7. L. Shao, P. Kner, E. H. Rego, M. G. Gustafsson, Super-resolution 3D microscopy of live whole cells using structured illumination. *Nature methods* **8**, 1044-1046 (2011).
8. E. Alonas *et al.*, Combining single RNA sensitive probes with subdiffraction-limited and live-cell imaging enables the characterization of virus dynamics in cells. *ACS nano* **8**, 302-315 (2014).
9. M. Heilemann *et al.*, Subdiffraction-resolution fluorescence imaging with conventional fluorescent probes. *Angewandte Chemie International Edition* **47**, 6172-6176 (2008).
10. H. Mao *et al.*, Cost-efficient nanoscopy reveals nanoscale architecture of liver cells and platelets. *Nanophotonics* **8**, 1299-1313 (2019).
11. R. Diekmann *et al.*, Chip-based wide field-of-view nanoscopy. *Nature Photonics* **11**, 322 (2017).
12. Ø. I. Helle, D. A. Coucheron, J.-C. Tinguely, C. I. Øie, B. S. Ahluwalia, Nanoscopy on-a-chip: super-resolution imaging on the millimeter scale. *Optics express* **27**, 6700-6710 (2019).
13. Ø. I. Helle *et al.*, Structured illumination microscopy using a photonic chip. *Nature Photonics*, 1-8 (2020).
14. G. Popescu, *Quantitative phase imaging of cells and tissues* (McGraw-Hill Education, 2011).
15. B. Bhaduri *et al.*, Diffraction phase microscopy: principles and applications in materials and life sciences. *Advances in Optics and Photonics* **6**, 57-119 (2014).
16. P. Girshovitz, N. T. Shaked, Doubling the field of view in off-axis low-coherence interferometric imaging. *Light: Science & Applications* **3**, e151-e151 (2014).
17. T. H. Nguyen, M. E. Kandel, M. Rubessa, M. B. Wheeler, G. Popescu, Gradient light interference microscopy for 3D imaging of unlabeled specimens. *Nature communications* **8**, 1-9 (2017).
18. B. Ankit *et al.*, High spatially sensitive quantitative phase imaging assisted with deep neural network for classification of human spermatozoa under stressed condition. *Scientific Reports (Nature Publisher Group)* **10** (2020).
19. S. Bhatt, A. Butola, S. R. Kanade, A. Kumar, D. S. Mehta, High resolution single shot phase shifting interference microscopy using deep neural network. *arXiv preprint arXiv:2010.07768* (2020).
20. Y. Jang, J. Jang, Y. Park, Dynamic spectroscopic phase microscopy for quantifying hemoglobin concentration and dynamic membrane fluctuation in red blood cells. *Optics express* **20**, 9673-9681 (2012).
21. A. Ahmad *et al.*, Sub-nanometer height sensitivity by phase shifting interference microscopy under environmental fluctuations. *Optics Express* **28**, 9340-9358 (2020).
22. S. R. Kanade, A. Butola, S. Bhatt, A. Kumar, D. S. Mehta (2020) High-resolution quantitative phase imaging using deep neural network. in *3D Image Acquisition and Display: Technology, Perception and Applications* (Optical Society of America), p JW2A. 9.
23. R. Fraser *et al.*, The liver sieve and atherosclerosis. *Pathology* **44**, 181-186 (2012).
24. C. I. Øie *et al.*, New ways of looking at very small holes–using optical nanoscopy to visualize liver sinusoidal endothelial cell fenestrations. *Nanophotonics* **7**, 575-596 (2018).
25. N. J. Hunt, P. A. McCourt, D. G. Le Couteur, V. C. Cogger, Novel targets for delaying aging: the importance of the liver and advances in drug delivery. *Advanced Drug Delivery Reviews* **135**, 39-49 (2018).
26. J. Simon-Santamaria *et al.*, Efficient uptake of blood-borne BK and JC polyomavirus-like particles in endothelial cells of liver sinusoids and renal vasa recta. *PLoS One* **9**, e111762 (2014).
27. B. Zapotoczny *et al.*, Tracking fenestrae dynamics in live murine liver sinusoidal endothelial cells. *Hepatology* **69**, 876-888 (2019).
28. B. Zapotoczny, K. Szafranska, E. Kus, S. Chlopicki, M. Szymonski, Quantification of fenestrations in liver sinusoidal endothelial cells by atomic force microscopy. *Micron* **101**, 48-53 (2017).
29. N. J. Hunt *et al.*, Manipulating fenestrations in young and old liver sinusoidal endothelial cells. *American Journal of Physiology-Gastrointestinal and Liver Physiology* **316**, G144-G154 (2019).
30. B. Zapotoczny, F. Braet, E. Wisse, M. Lekka, M. Szymoński, Biophysical nanocharacterization of liver sinusoidal endothelial cells through atomic force microscopy. *Biophys Rev* **12** (2020).
31. A. J. McLean *et al.*, Age-related pseudocapillarization of the human liver. *The Journal of Pathology: A Journal of the Pathological Society of Great Britain and Ireland* **200**, 112-117 (2003).
32. D. S. Mehta, D. N. Naik, R. K. Singh, M. Takeda, Laser speckle reduction by multimode optical fiber bundle with combined temporal, spatial, and angular diversity. *Applied optics* **51**, 1894-1904 (2012).
33. M. Takeda, H. Ina, S. Kobayashi, Fourier-transform method of fringe-pattern analysis for computer-based topography and interferometry. *JosA* **72**, 156-160 (1982).
34. R. M. Goldstein, H. A. Zebker, C. L. Werner, Satellite radar interferometry: Two-dimensional phase unwrapping. *Radio science* **23**, 713-720 (1988).
35. M. Ovesný, P. Křížek, J. Borkovec, Z. Švindrych, G. M. Hagen, ThunderSTORM: a comprehensive ImageJ plug-in for PALM and STORM data analysis and super-resolution imaging. *Bioinformatics* **30**, 2389-2390 (2014).

36. J.-C. Tinguely, Ø. I. Helle, B. S. Ahluwalia, Silicon nitride waveguide platform for fluorescence microscopy of living cells. *Optics express* **25**, 27678-27690 (2017).
37. B. Hansen, B. Arteta, B. Smedsrød, The physiological scavenger receptor function of hepatic sinusoidal endothelial and Kupffer cells is independent of scavenger receptor class A type I and II. *Molecular and cellular biochemistry* **240**, 1-8 (2002).
38. D. Bar-On *et al.*, Super-resolution imaging reveals the internal architecture of nano-sized syntaxin clusters. *Journal of Biological Chemistry* **287**, 27158-27167 (2012).
39. S. Bhatt, A. Butola, S. R. Kanade, A. Kumar, D. S. Mehta (2020) High-Resolution Full-Field Optical Coherence Microscopy Using Partially Spatially Coherent Monochromatic Light Source. in *Imaging Systems and Applications* (Optical Society of America), p JTh2A. 5.
40. B. S. Ahluwalia, P. McCourt, T. Huser, O. G. Hellesø, Optical trapping and propulsion of red blood cells on waveguide surfaces. *Optics Express* **18**, 21053-21061 (2010).
41. F. Peyskens, A. Dhakal, P. Van Dorpe, N. Le Thomas, R. Baets, Surface enhanced Raman spectroscopy using a single mode nanophotonic-plasmonic platform. *ACS photonics* **3**, 102-108 (2016).
42. B. Diederich *et al.*, Nanoscopy on the Chea (i) p. (2020).
43. I. S. Opstad *et al.*, A waveguide imaging platform for live-cell TIRF imaging of neurons over large fields of view. *bioRxiv* (2019).

Paper VI

Chip-Based Resonance Raman Spectroscopy Using Tantalum Pentoxide Waveguides.

D. A. Coucheron, D. N. Wadduwage, G. S. Murugan, P. T. C. So, B. S. Ahluwalia.

Chip-Based Resonance Raman Spectroscopy Using Tantalum Pentoxide Waveguides

David A. Coucheron, Dushan N. Wadduwage, G. Senthil Murugan, Peter T. C. So, and Balpreet S. Ahluwalia

***Abstract*— Blood analysis is an important diagnostic tool, as it provides a wealth of information about the patient's health. Raman spectroscopy is a promising tool for blood analysis, but widespread clinical application is limited by its low signal strength, as well as complex and costly instrumentation. The growing field of waveguide-based Raman spectroscopy tries to solve these challenges by working toward fully integrated Raman sensors with increased interaction areas. In this letter, we demonstrate resonance Raman measurements of hemoglobin, a crucial component of blood, at 532-nm excitation using a tantalum pentoxide (Ta_2O_5) waveguide platform. We have also characterized the background signal from Ta_2O_5 waveguide material when excited at 532 nm. In addition, we demonstrate spontaneous Raman measurements of isopropanol and methanol using the same platform. Our results suggest that Ta_2O_5 is a promising waveguide platform for resonance Raman spectroscopy at 532 nm and, in particular, for blood analysis.**

***Index Terms*— Optical waveguides, Raman scattering, photonic integrated circuits, biosensors.**

I. Introduction

BLOOD is an essential bodily fluid that consists mainly of red blood cells, white blood cells and platelets in a liquid medium called plasma. The components of blood serve different purposes, ranging from oxygen transport to fighting disease and infection. Analyses of blood can thus give vital insight into a person's health and can identify diseases such as diabetes, malaria and sickle-cell disease [1]. Hemoglobin, the major component of red blood cells, has been of interest in the Raman spectroscopy community since the 1970s [2], as it dominates the Raman spectrum of blood. Spontaneous Raman scattering has a very low scattering cross-section and is thus a weak effect. Hemoglobin, however, experiences resonance Raman at 532 nm excitation, enhancing the signal significantly [2]. The widespread application of Raman spectroscopy in routine clinical analysis is, however, limited by e.g. low throughput, complex and costly instrumentation [3].

On-chip Raman spectroscopy [4] using integrated optical waveguides is an attractive route for delivering compact, simple to operate, affordable and highly sensitive Raman spectrometers. The main reason is that the use of waveguides offers a simple way to increase the Raman scattering, as well as the possibility of a fully integrated sensor on chip, making instrumentation far simpler.

Raman spectroscopy using waveguides made of high-refractive index contrast (HIC) materials is experiencing a renewed interest [5]–[8]. Recent achievements include measurements of biological monolayers [9] and trace gases [10]. When light is guided in an optical waveguide, an evanescent field is generated outside the waveguide core, which can be used to probe a sample close to the waveguide surface. Raman scattering from the sample will either recouple into the waveguide or emit into free space (as illustrated in Fig. 1a by the orange arrows). Detection can therefore be done either from the top of the waveguide or from the end facet of the waveguide-chip, as illustrated in Fig.1b. This technique is commonly called waveguide enhanced Raman spectroscopy (WERS) when detection is done from the end, as the waveguide structure gives rise to intrinsic enhancement effects for thin samples (e.g. monolayers). Waveguides made of HIC materials benefit from two enhancement effects when using edge detection for thin samples: 1) Radiative enhancement due to the high intensity of the evanescent field and 2) interaction area enhancement due to the increased

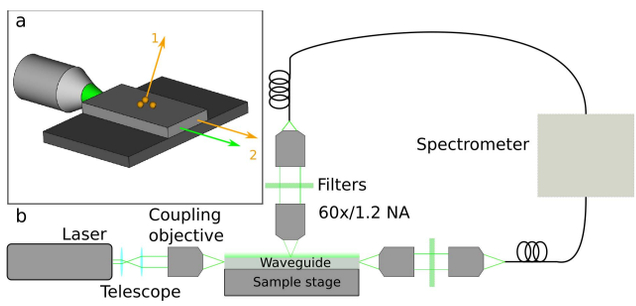

Fig. 1. (a) Illustration of Raman scattering from a sample on a waveguide. The evanescent field can induce Raman scattering in a sample. The scattered photons can either be transmitted into free space (1) or recoupled back into the waveguide (2). (b) Schematic of the system used in the experiments.

Manuscript received February 21, 2019; revised April 6, 2019; accepted April 30, 2019. Date of publication May 8, 2019; date of current version June 25, 2019. This work was supported in part by the European Research Council under Project 336716 and in part by The Arctic University of Norway (UiT) through the Tematiske satsinger. *(Corresponding author: Balpreet S. Ahluwalia.)*

D. A. Coucheron and B. S. Ahluwalia are with the Department of Physics and Technology, The Arctic University of Norway (UiT), 9019 Tromsø, Norway (e-mail: balpreet.singh.ahluwalia@uit.no).

D. N. Wadduwage is with the Laser Biomedical Research Center, Massachusetts Institute of Technology, Cambridge, MA 02139 USA, also with the Department of Biological Engineering, Massachusetts Institute of Technology, Cambridge, MA 02139 USA, and also with the Center for Advanced Imaging, Harvard University, Cambridge, MA 02138 USA.

G. S. Murugan is with the Optoelectronics Research Centre, University of Southampton, Southampton SO17 1BJ, U.K.

P. T. C. So is with the Laser Biomedical Research Center, Massachusetts Institute of Technology, Cambridge, MA 02139 USA, and also with the Department of Biological Engineering, Massachusetts Institute of Technology, Cambridge, MA 02139 USA.

Color versions of one or more of the figures in this letter are available online at http://ieeexplore.ieee.org.

Digital Object Identifier 10.1109/LPT.2019.2915671

interaction area [6]. The HIC material tightly confines the light within the waveguide core, enabling ultra-small footprints of the optical functions. If the propagation loss is low, arbitrarily large interaction areas can be designed through e.g. a spiral geometry [5]. The instrumentation can also be made much simpler, as a waveguide based set-up can have integrated lasers [11], detectors [12] and other components needed for Raman spectroscopy.

Most of the recent result on waveguide based Raman spectroscopy has been performed using silicon nitride (Si_3N_4) nanowires [5] and slot waveguides [13] with 785 nm excitation light. The increased field intensity inside the slot can give a fivefold or more increase in signal strength [14]. Spiral slot waveguides are highly sensitive and have been used to measure biological sub-monolayers [9]. Despite the success of Si_3N_4 spiral waveguides, getting sufficient Raman scattering without cooled detectors, which is relevant for a fully integrated solution, remains challenging. Several approaches have been taken to improve the signal further in combination with the waveguide platform. One interesting approach is to use surface enhanced Raman scattering (SERS), which can give a signal increase of many orders of magnitude. Several approaches have been studied for SERS implementation, including the use of nanoporous gold [15] and gold bow-tie antenna [16]. A challenge with SERS is that it requires surface treatments that can generate hot spots and reduce life-time. Recently, metallic slot waveguides [17] and stimulated Raman scattering [8] approach were proposed. Another promising option for increasing the Raman signal, is by moving to lower wavelengths, as Raman scattering scales with λ^{-4}. Lower wavelengths can, however, also increase any auto-fluorescence background, which is usually much higher than the signals from Raman scattering. If the material background at lower wavelength is mainly from the Raman scattering, and not auto-fluorescence, it should not be a problem though. An additional advantages of lower excitation wavelength is possible resonance effects for selective samples. Resonance Raman occurs for certain samples at low wavelengths and can enhance the signal by several orders of magnitude. Using 532 nm excitation is particularly interesting due to resonance Raman effects in several clinically relevant samples, such as hemoglobin [2] and in cancerous brain [18] and breast tissue [19]. Taking advantage of resonance Raman effects can be key to really bring e.g. Raman based blood analysis to the market.

The development of HIC waveguide platform for resonance Raman spectroscopy using 532 nm excitation is therefore beneficial. Evans et al. have recently demonstrated waveguide based Raman spectroscopy using a TiO_2 platform at 532 nm excitation [7]. Another potential platform for shorter wavelength excitation is Ta_2O_5. Ta_2O_5 is a promising waveguide material for Raman spectroscopy due to its high refractive index contrast with silica cladding, providing strong optical mode confinement and thereby enabling the development of compact photonic circuits with tight bends and spirals. Ta_2O_5 is CMOS compatible and mass-producible, and offers a wide transparency window with UV absorption band edge below 330 nm and has been widely used in sensing applications [20]. Wang et al. have demonstrated both edge and top detection using Ta_2O_5 waveguides with 638 nm excitation [6], however, resonance Raman using 532 nm has yet to be investigated for biological application.

In this work, we present waveguide-based Raman spectroscopy using Ta_2O_5 waveguides using 532 nm excitation. We demonstrate spontaneous Raman spectroscopy of isopropanol and methanol. The background signal from the waveguide platform is investigated by changing the under cladding material between silicon dioxide (SiO_2) and magnesium fluoride (MgF_2). Finally, we measure resonance Raman spectrum of hemoglobin, suggesting the potential of Ta_2O_5 waveguide-based Raman spectroscopy platform for biological applications.

II. Set-Up and Waveguide Fabrication

A 532 nm laser (Verdi V10) was used for all experiments. The laser was coupled into the waveguides using a 0.5 N.A. aspheric lens on a three-axis piezo stage. Collection was done from the top using a 60x/1.2 NA WI objective lens (Olympus), unless otherwise stated. All work was performed with top collection, as we aim to use the spatial information for Raman imaging in future work. The emission light was relayed through two 532 nm edge filters (Semrock RazorEdge) and coupled into a multimode fiber. A spectrograph (Andor Holospec-F/1.8-VIS) was used to analyze the signal coupled out of the fiber. A schematic of the set-up used is presented in Figure 1b. All sample measurements were done using Ta_2O_5 strip waveguides on oxidized silicon (Si) wafers. The optimization of the fabrication process is described in previous work [21].

High-intensity in the evanescent field is desirable for on-chip Raman spectroscopy. This was achieved by fabricating thin, (150 nm) Ta_2O_5 materials in stripe geometry. The waveguide width ranges from 2.5 to 70 μm. The wide waveguides were investigated because our future aim is to use wide waveguides for Raman imaging, and thus requiring excitation of large areas. For the chosen waveguide dimensions up to 10% of the guided power was present in the evanescent field for 532 nm wavelength. The waveguides were originally fabricated for longer wavelengths and we found a relatively high propagation loss at 532 nm excitation of approximately 5 dB/cm and a coupling loss of approximately 11 dB.

Additionally, Ta_2O_5 waveguides were fabricated on MgF_2 substrates to study the background signal from the under-cladding material. Strip waveguides with different widths were defined in the Ta_2O_5 layer using standard photolithography and etched by 150 nm using argon ion beam milling. Finally, the waveguide samples were annealed at 600 °C for 3 hours under an oxygen atmosphere to relieve any stress built up in the films [22] and to replenish the oxygen, which is depleted during the sputtering process. 2.5 μm wide Ta_2O_5 waveguides on SiO_2 and on MgF_2 were used for the measurement. Prior to measurements, the waveguides were cleaned for 10 minutes in 1% Hellmanex in deionized (DI) water at 70 °C. The sample was then added in the hollow rectangular PDMS chamber and a cover slip was used to seal it.

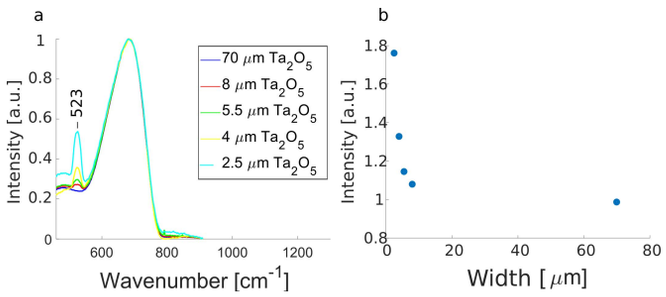

Fig. 2. (a) Normalized spectra measured as a function of waveguide width. (b) The ratio of the emerging peak at 523 cm^{-1} to the largest peak at 680 cm^{-1} as a function of waveguide width. The spectra are normalized to the widest waveguide.

III. Background Measurements

First, we measured the background spectrum of Ta_2O_5 waveguides. The measurements were done with a 70 μm wide Ta_2O_5 strip waveguide. A laser beam (38 mW power) was incident at the input facet of the waveguide. Measurements were taken using a 20 s exposure time. The resulting spectra were normalized with respect to the highest peak at approximately 680 cm^{-1} and is presented in Figure 3a. Ta_2O_5 only exhibits a background signal from wavenumbers shorter than approximately 1000 cm^{-1}. Four peaks can be discerned: a large peak at 680 cm^{-1}; two smaller peaks at 488 cm^{-1} and 196 cm^{-1}; and a shoulder at 899 cm^{-1}. This agrees well with previous literature on amorphous Ta_2O_5 [22]. For peaks above 1000 cm^{-1}, most of the background can thus be filtered out.

We measured the background spectrum for Ta_2O_5 strip waveguides of different widths (2.5-70 μm) as shown in Fig. 2. The signal strength changed significantly for the different waveguide widths, as both coupling and propagation loss depends on the waveguide geometry. The overall spectrum shape, however, remained unchanged as the waveguide width was changed, but a new peak emerged at approximately 523 cm^{-1} for the narrower waveguides, which is typical Si-Si peak, originating from under-cladding. The spectra are thus normalized internally to the 680 cm^{-1} peak for each width. Fig. 2b presents the ratio of the peaks at 523 cm^{-1} to the local background level at 485 cm^{-1}, normalized for the ratio obtained using 70 μm wide waveguide. With decreasing width, the ratio increases rapidly below approximately 5 μm. For thinner waveguides, signals from the under-cladding becomes more prominent. For thin (150 nm) and narrow waveguides (<5 μm), the guided mode stretches further outside the core into the cladding, resulting in small contribution from the cladding. The results suggest that most of the overall spectral signal is from the Ta_2O_5 core and not the under-cladding for wide waveguides.

To further investigate the signal originating from the under-cladding, we compared Ta_2O_5 waveguides fabricated with two different under-claddings: silicon dioxide (SiO_2) and magnesium fluoride (MgF_2). Narrow Ta_2O_5 strip waveguide of 2.5 μm width were measured for two under-claddings, SiO_2 and MgF_2. A laser beam with 110 mW power was incident at the input facet of the waveguides and 10 s exposure time was used. The spectrum was averaged over 10 measurements to

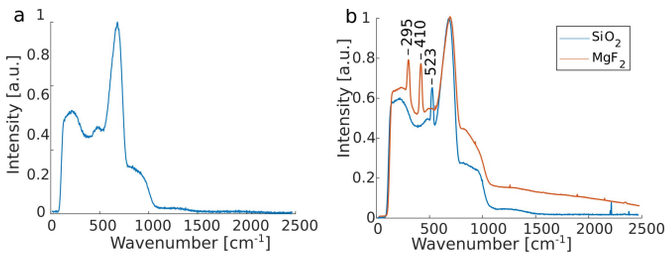

Fig. 3. (a) Background spectrum from a 70 μm wide Ta_2O_5 strip waveguide on a SiO_2 undercladding. (b) Background spectrum from 2.5 μm wide Ta_2O_5 waveguides on a SiO_2 and MgF_2 undercladding.

reduce the noise. The resulting spectra are presented in Fig. 3. The general shape of the spectrum remains unchanged, suggesting that the waveguide material contributes to most of the background signal. There are, however, a few notable changes. The sharp peak at 523 cm^{-1} from the Ta_2O_5 on SiO_2 is replaced with two new peaks at 410 cm^{-1} and 295 cm^{-1} for the Ta_2O_5 on MgF_2. The peaks at 410 cm^{-1} and 295 cm^{-1} are confirmed to be Raman peaks from MgF_2 [23]. The small peak at around 2250 cm^{-1} is a cosmic ray signal. Reducing the background further is thus challenging, since the background signal is dominated by the waveguide material and cannot easily be changed. It might, however, be possible to reduce the background by changing the fabrication process and a more detailed study into the origin of the signal in the Ta_2O_5 structure is needed.

IV. Waveguide Raman Measurements

Spontaneous Raman measurements of methanol and isopropanol with 532 nm excitation were performed using 150 nm thick Ta_2O_5 strip waveguides. The waveguides were 70 μm wide to increase the sensing area. A laser beam of 395 mW power was launched from the coupling objective. Both isopropanol and methanol were measured using a PDMS chamber to hold the sample, sealed with a cover glass. An exposure time of 20 s was used for both the samples. The presented spectrum is the average over three measurements. Spectra for methanol and isopropanol using waveguide excitation are presented in Fig. 4a. The waveguide background has been subtracted and all spectra have been normalized to the 822 cm^{-1} peak for isopropanol and the 890 cm^{-1} peak for methanol. The peaks agree well with literature [24] and the two chemicals are easily distinguishable by e.g. the symmetric C-O-O vibration at 822 and 890 cm^{-1} for isopropanol and methanol, respectively.

A motivation for using 532 nm excitation is to measure resonance Raman signals from hemoglobin, as it is important in lab-on-a-chip blood analysis for point of care diagnosis. Resonance Raman can distinguish different hemoglobin derivatives accurately [2]. For hemoglobin resonance Raman we used human hemoglobin (lyophilized powder from Sigma Aldrich) with 15.5 mM concentration in distilled water, which is similar to the hemoglobin concentration in red blood cells [25]. A drop was placed on the waveguide surface and allowed to dry. Collection was done with a 40x/0.75 NA air objective lens for this experiment, with 2 s exposure time.

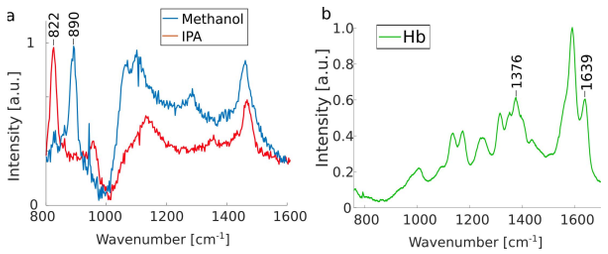

Fig. 4. (a) Spontaneous Raman spectra of methanol and isopropanol (IPA). (b) Resonance Raman spectrum of dried hemoglobin (Hb).

Fig. 4b shows the resonant Raman spectrum of dried hemoglobin. The presence of peaks at 1639 cm^{-1} and 1376 cm^{-1} demonstrates that the sample is oxygenated [1]. The Raman peaks are mostly above 1000 cm^{-1}, therefore, they are not overlapping with the waveguide background. This makes Ta_2O_5 ideally suited for resonance Raman spectroscopy for hemoglobin and blood analysis for point of care diagnostics. Here, we have employed only straight strip waveguides and top detection. The sensitivity can be further increased by changing to a spiral loop geometry and by doing edge detection, which will be explored in future work. The long-term goal is, however, to make use of spatial information of individual red blood cells either by performing optical imaging and/or Raman imaging using waveguide excitation. As such, optimizing wide waveguides for Raman spectroscopy are of interest.

V. Conclusion

Photonic integrated circuits provide a promising approach to Raman spectroscopy. Ta_2O_5 waveguides with its low background signal and high refractive index contrast has been demonstrated as a suitable platform for resonance Raman spectroscopy at 532 nm. By investigating waveguides of different under-claddings it was found that most of the background comes from the Ta_2O_5 core and only a small background from the surrounding media is visible for narrow waveguides. We have tested and validated the waveguide platform by measuring spontaneous Raman spectra of isopropanol and methanol. We have performed resonance Raman measurements of dried hemoglobin at concentration usually found in the red blood cells using the Ta_2O_5 waveguides. The resonance Raman spectroscopy can also be combined with other complementary optical functions developed using Ta_2O_5 material, such as optical nanoscopy [26], [27].

References

[1] C. G. Atkins, K. Buckley, M. W. Blades, and R. F. B. Turner, "Raman spectroscopy of blood and blood components," *Appl. Spectrosc.*, vol. 71, no. 5, pp. 767–793, 2017.

[2] T. C. Strekas and T. G. Spiro, "Hemoglobin: Resonance Raman spectra," *Biochim. Et Biophys. Acta (BBA) Protein Struct.*, vol. 263, no. 3, pp. 830–833, May 1972.

[3] I. Pence and A. Mahadevan-Jansen, "Clinical instrumentation and applications of Raman spectroscopy," *Chem. Soc. Rev.*, vol. 45, no. 7, pp. 1958–1979, Mar. 2016.

[4] A. Dhakal *et al.*, "Single mode waveguide platform for spontaneous and surface-enhanced on-chip Raman spectroscopy," *Interface Focus*, vol. 6, no. 4, Aug. 2016, Art. no. 20160015.

[5] A. Dhakal, A. Z. Subramanian, P. Wuytens, F. Peyskens, N. L. Thomas, and R. Baets, "Evanescent excitation and collection of spontaneous Raman spectra using silicon nitride nanophotonic waveguides," *Opt. Lett.*, vol. 39, no. 13, pp. 4025–4028, Jul. 2014.

[6] Z. Wang, M. N. Zervas, P. N. Bartlett, and J. S. Wilkinson, "Surface and waveguide collection of Raman emission in waveguide-enhanced Raman spectroscopy," *Opt. Lett.*, vol. 41, no. 17, pp. 4146–4149, Sep. 2016.

[7] C. C. Evans, C. Liu, and J. Suntivich, "TiO_2 nanophotonic sensors for efficient integrated evanescent Raman spectroscopy," *ACS Photon.*, vol. 3, no. 9, pp. 1662–1669, Sep. 2016.

[8] C. Zhang *et al.*, "Stimulated Raman scattering flow cytometry for label-free single-particle analysis," *Optica*, vol. 4, no. 1, pp. 103–109, Jan. 2017.

[9] A. Dhakal, P. C. Wuytens, F. Peyskens, K. Jans, N. L. Thomas, and R. Baets, "Nanophotonic waveguide enhanced Raman spectroscopy of biological submonolayers," *ACS Photon.*, vol. 3, no. 11, pp. 2141–2149, Nov. 2016.

[10] S. A. Holmstrom *et al.*, "Trace gas Raman spectroscopy using functionalized waveguides," *Optica*, vol. 3, no. 8, pp. 891–896, Aug. 2016.

[11] A. Aghajani, G. S. Murugan, N. P. Sessions, V. Apostolopoulos, and J. S. Wilkinson, "Waveguide lasers in ytterbium-doped tantalum pentoxide on silicon," *Opt. Lett.*, vol. 40, no. 11, pp. 2549–2552, Jun. 2015.

[12] H. Park *et al.*, "A hybrid AlGaInAs-silicon evanescent waveguide photodetector," *Opt. Express*, vol. 15, no. 10, pp. 6044–6052, 2007.

[13] A. Dhakal, F. Peyskens, A. Z. Subramanian, N. Le Thomas, and R. Baets, "Enhanced spontaneous Raman signal collected evanescently by silicon nitride slot waveguides," in *Proc. CLEO, Sci. Innov.*, May 2015, pp. 1–2, Paper. STh4H.3.

[14] D. M. Kita, J. Michon, S. G. Johnson, and J. Hu, "Are slot and sub-wavelength grating waveguides better than strip waveguides for sensing?" *Optica*, vol. 5, no. 9, pp. 1046–1054, 2018.

[15] Q. Cao, J. Feng, H. Lu, H. Zhang, F. Zhang, and H. Zeng, "Surface-enhanced Raman scattering using nanoporous gold on suspended silicon nitride waveguides," *Opt. Exp.*, vol. 26, no. 19, pp. 24614–24620, Sep. 2018.

[16] P. C. Wuytens, A. G. Skirtach, and R. Baets, "On-chip surface-enhanced Raman spectroscopy using nanosphere-lithography patterned antennas on silicon nitride waveguides," *Opt. Express*, vol. 25, no. 11, pp. 12926–12934, May 2017.

[17] A. Raza *et al.*, "ALD assisted nanoplasmonic slot waveguide for on-chip enhanced Raman spectroscopy," *APL Photon.*, vol. 3, no. 11, Oct. 2018, Art. no. 116105.

[18] Y. Zhou *et al.*, "Human brain cancer studied by resonance Raman spectroscopy," *J. Biomed. Opt.*, vol. 17, no. 11, Nov. 2012, Art. no. 116021.

[19] C.-H. Liu *et al.*, "Resonance Raman and Raman spectroscopy for breast cancer detection," *Technol. Cancer Res. Treat.*, vol. 12, no. 4, pp. 371–382, Aug. 2013.

[20] K. Schmitt, K. Oehse, G. Sulz, and C. Hoffmann, "Evanescent field sensors based on tantalum pentoxide waveguides—A review," *Sensors*, vol. 8, no. 2, pp. 711–738, 2008.

[21] B. S. Ahluwalia, A. Z. Subramanian, O. G. Hellso, N. M. B. Perney, N. P. Sessions, and J. S. Wilkinson, "Fabrication of submicrometer high refractive index tantalum pentoxide waveguides for optical propulsion of microparticles," *IEEE Photon. Technol. Lett.*, vol. 21, no. 19, pp. 1408–1410, Oct. 12, 2009.

[22] C. Joseph, P. Bourson, and M. D. Fontana, "Amorphous to crystalline transformation in Ta_2O_5 studied by Raman spectroscopy," *J. Raman Spectrosc.*, vol. 43, no. 8, pp. 1146–1150, Aug. 2012.

[23] S. P. S. Porto, P. A. Fleury, and T. C. Damen, "Raman spectra of TiO_2, MgF_2, ZnF_2, FeF_2, and MnF_2," *Phys. Rev. J. Arch.*, vol. 154, no. 2, pp. 522–526, Feb. 1967.

[24] D. Lin-Vien, N. B. Colthup, W. G. Fateley, and J. G. Grasselli, *The Handbook of Infrared and Raman Characteristic Frequencies of Organic Molecules*. Amsterdam, The Netherlands: Elsevier, 1991.

[25] J. B. Wallach, *Interpretation of Diagnostic Tests*. Philadelphia, PA, USA: Lippincott Williams & Wilkins, 2007.

[26] R. Diekmann *et al.*, "Chip-based wide field-of-view nanoscopy," *Nature Photon.*, vol. 11, no. 5, pp. 322–328, May 2017.

[27] Ø. I. Helle, D. A. Coucheron, J.-C. Tinguely, C. I. Øie, and B. S. Ahluwalia, "Nanoscopy on-a-chip: super-resolution imaging on the millimeter scale," *Opt. Express*, vol. 27, no. 5, pp. 6700–6710, Mar. 2019.

Bibliography

[1] R. Hooke. *Micrographia: Or Some Physiological Descriptions of Minute Bodies Made by Magnifying Glasses, with Observations and Inquiries Thereupon*. Courier Corporation, 2003.

[2] E. Abbe. "Beiträge zur Theorie des Mikroskops und der mikroskopischen Wahrnehmung." *Archiv für mikroskopische Anatomie* 9.1 (1873).

[3] S. Hell and E. H. K. Stelzer. "Fundamental improvement of resolution with a 4Pi-confocal fluorescence microscope using two-photon excitation." *Optics Communications* 93.5 (1992).

[4] T. A. Klar and S. W. Hell. "Subdiffraction resolution in far-field fluorescence microscopy." *Optics Letters* 24.14 (1999).

[5] M. Dyba and S. W. Hell. "Focal Spots of Size $\ensuremath{\lambda}/23$ Open Up Far-Field Florescence Microscopy at 33 nm Axial Resolution." *Physical Review Letters* 88.16 (2002).

[6] V. Westphal and S. W. Hell. "Nanoscale Resolution in the Focal Plane of an Optical Microscope." *Physical Review Letters* 94.14 (2005).

[7] M. J. Rust, M. Bates, and X. Zhuang. "Sub-diffraction-limit imaging by stochastic optical reconstruction microscopy (STORM)." *Nature Methods* 3.10 (2006).

[8] E. Betzig, G. H. Patterson, R. Sougrat, O. W. Lindwasser, S. Olenych, et al. "Imaging Intracellular Fluorescent Proteins at Nanometer Resolution." *Science* 313.5793 (2006).

[9] S. T. Hess, T. P. K. Girirajan, and M. D. Mason. "Ultra-High Resolution Imaging by Fluorescence Photoactivation Localization Microscopy." *Biophysical Journal* 91.11 (2006).

[10] R. Diekmann, Ø. I. Helle, C. I. Øie, P. McCourt, T. R. Huser, et al. "Chip-based wide field-of-view nanoscopy." *Nature Photonics* 11.5 (2017).

[11] D. Long. *The Raman Effect: A Unified Treatment of the Theory of Raman Scattering by Molecules | Wiley*. 2002.

[12] F. G. Prendergast and K. G. Mann. "Chemical and physical properties of aequorin and the green fluorescent protein isolated from Aequorea forskalea." *Biochemistry* 17.17 (1978).

[13] W. P. Ambrose, P. M. Goodwin, and J. P. Nolan. "Single-molecule detection with total internal reflection excitation: Comparing signal-to-

background and total signals in different geometries." *Cytometry* 36.3 (1999).

[14] C. W, H. Bd, L. Ja, A. Eh, and A. Dt. "Soft X-ray microscopy at a spatial resolution better than 15 nm." *Nature* (2005).

[15] I. J. Cox, C. J. R. Sheppard, and T. Wilson. "Improvement in resolution by nearly confocal microscopy." *Applied Optics* 21.5 (1982).

[16] S. Roth, C. J. Sheppard, K. Wicker, and R. Heintzmann. "Optical photon reassignment microscopy (OPRA)." *Optical Nanoscopy* 2.1 (2013).

[17] J. Huff. "The Airyscan detector from ZEISS: confocal imaging with improved signal-to-noise ratio and super-resolution." *Nature Methods* 12.12 (2015).

[18] S. Hell and J. Wichmann. "Breaking the Diffraction Resolution Limit by Stimulated-Emission - Stimulated-Emission-Depletion Fluorescence Microscopy." *Optics Letters* 19.11 (1994).

[19] M. G. L. Gustafsson. "Surpassing the lateral resolution limit by a factor of two using structured illumination microscopy." *Journal of Microscopy* 198.2 (2000).

[20] T. Dertinger, R. Colyer, G. Iyer, S. Weiss, and J. Enderlein. "Fast, background-free, 3D super-resolution optical fluctuation imaging (SOFI)." *Proceedings of the National Academy of Sciences* 106.52 (2009).

[21] I. Yahiatene, S. Hennig, M. Müller, and T. Huser. "Entropy-Based Super-Resolution Imaging (ESI): From Disorder to Fine Detail." *ACS Photonics* 2.8 (2015).

[22] M. Heilemann, S. van de Linde, M. Schüttpelz, R. Kasper, B. Seefeldt, et al. "Subdiffraction-Resolution Fluorescence Imaging with Conventional Fluorescent Probes." *Angewandte Chemie International Edition* 47.33 (2008).

[23] R. Jungmann, C. Steinhauer, M. Scheible, A. Kuzyk, P. Tinnefeld, and F. C. Simmel. "Single-Molecule Kinetics and Super-Resolution Microscopy by Fluorescence Imaging of Transient Binding on DNA Origami." *Nano Letters* 10.11 (2010).

[24] T. Klein, S. Proppert, and M. Sauer. "Eight years of single-molecule localization microscopy." *Histochemistry and Cell Biology* 141.6 (2014).

[25] F. Huang, T. M. P. Hartwich, F. E. Rivera-Molina, Y. Lin, W. C. Duim, et al. "Video-rate nanoscopy using sCMOS camera-specific single-molecule localization algorithms." *Nature Methods* 10.7 (2013).

[26] T. Klein, A. Löschberger, S. Proppert, S. Wolter, S. van de Linde, and M. Sauer. "Live-cell dSTORM with SNAP-tag fusion proteins." *Nature Methods* 8.1 (2011).

[27] W. E. Moerner and L. Kador. "Optical detection and spectroscopy of single molecules in a solid." *Physical Review Letters* 62.21 (1989).

[28] J. R. Allen, S. T. Ross, and M. W. Davidson. "Single molecule localization microscopy for superresolution." *Journal of Optics* 15.9 (2013).

[29] R. E. Thompson, D. R. Larson, and W. W. Webb. "Precise Nanometer Localization Analysis for Individual Fluorescent Probes." *Biophysical Journal* 82.5 (2002).

[30] D. Baddeley, I. Jayasinghe, C. Cremer, M. Cannell, and C. Soeller. "Light-Induced Dark States of Organic Fluochromes Enable 30 nm Resolution Imaging in Standard Media." *Biophysical journal* 96 (2009).

[31] U. Endesfelder and M. Heilemann. "Direct stochastic optical reconstruction microscopy (dSTORM)." *Methods in Molecular Biology (Clifton, N.J.)* 1251 (2015).

[32] S. van de Linde, A. Löschberger, T. Klein, M. Heidbreder, S. Wolter, et al. "Direct stochastic optical reconstruction microscopy with standard fluorescent probes." *Nature Protocols* 6.7 (2011).

[33] J. Xu, H. Ma, and Y. Liu. "Stochastic optical reconstruction microscopy (STORM)." *Current protocols in cytometry* 81 (2017).

[34] M. Heilemann, S. van de Linde, A. Mukherjee, and M. Sauer. "Super-Resolution Imaging with Small Organic Fluorophores." *Angewandte Chemie International Edition* 48.37 (2009).

[35] G. Lifante. *Integrated Photonics: Fundamentals*. John Wiley & Sons, 2003.

[36] T. H. Maiman. "Stimulated Optical Radiation in Ruby." *Nature* 187.4736 (1960).

[37] B. S. Ahluwalia, P. McCourt, T. Huser, and O. G. Hellesø. "Optical trapping and propulsion of red blood cells on waveguide surfaces." *Optics Express* 18.20 (2010).

[38] K. Schmitt, K. Oehse, G. Sulz, and C. Hoffmann. "Evanescent field Sensors Based on Tantalum Pentoxide Waveguides – A Review." *Sensors* 8.2 (2008).

[39] R. Baets, A. Z. Subramanian, A. Dhakal, S. K. Selvaraja, K. Komorowska, et al. "Spectroscopy-on-chip applications of silicon photonics." Vol. 8627. 2013.

[40] N. Fabricius, G. Gauglitz, and J. Ingenhoff. "A gas sensor based on an integrated optical Mach-Zehnder interferometer." *Sensors and Actuators B: Chemical* 7.1 (1992).

[41] A. Dhakal. "Nanophotonic Waveguide Enhanced Raman Spectroscopy." PhD thesis. 2016.

[42] C. A. Barrios. "Optical Slot-Waveguide Based Biochemical Sensors." *Sensors* 9.6 (2009).

[43] E. Ryckeboer, R. Bockstaele, M. Vanslembrouck, and R. Baets. "Glucose sensing by waveguide-based absorption spectroscopy on a silicon chip." *Biomedical Optics Express* 5.5 (2014).

[44] A. Z. Subramanian, E. Ryckeboer, A. Dhakal, F. Peyskens, A. Malik, et al. "Silicon and silicon nitride photonic circuits for spectroscopic sensing on-a-chip [Invited]." *Photonics Research* 3.5 (2015).

[45] M. Muneeb, X. Chen, P. Verheyen, G. Lepage, S. Pathak, et al. "Demonstration of Silicon-on-insulator mid-infrared spectrometers operating at 3.8m." *Optics Express* 21.10 (2013).

[46] J. Jágerská, M. Vlk, V. Mittal, and G. S. Murugan. "Trace Gas Spectroscopy on a Chip with Mid-Infrared Photonic Waveguides." *Light, Energy and the Environment 2018 (E2, FTS, HISE, SOLAR, SSL)*. Optical Society of America, 2018.

[47] R. Shankar, I. Bulu, and M. Lončar. "Integrated high-quality factor silicon-on-sapphire ring resonators for the mid-infrared." *Applied Physics Letters* 102.5 (2013).

[48] J. F. Bauters, M. J. R. Heck, D. John, D. Dai, M.-C. Tien, et al. "Ultra-low-loss high-aspect-ratio Si_3N_4 waveguides." *Optics Express* 19.4 (2011).

[49] C. G. H. Roeloffzen, M. Hoekman, E. J. Klein, L. S. Wevers, R. B. Timens, et al. "Low-Loss Si3N4 TriPleX Optical Waveguides: Technology and Applications Overview." *IEEE Journal of Selected Topics in Quantum Electronics* 24.4 (2018).

[50] F. Morichetti, A. Melloni, M. Martinelli, R. G. Heideman, A. Leinse, et al. "Box-Shaped Dielectric Waveguides: A New Concept in Integrated Optics?" *Journal of Lightwave Technology* 25.9 (2007).

[51] M. H. P. Pfeiffer, A. Kordts, V. Brasch, M. Zervas, M. Geiselmann, et al. "Photonic Damascene process for integrated high-Q microresonator based nonlinear photonics." *Optica* 3.1 (2016).

[52] A. Raza, S. Clemmen, P. Wuytens, M. Muneeb, M. Van Daele, et al. "ALD assisted nanoplasmonic slot waveguide for on-chip enhanced Raman spectroscopy." *APL Photonics* 3.11 (2018).

[53] D. J. Blumenthal, R. Heideman, D. Geuzebroek, A. Leinse, and C. Roeloffzen. "Silicon Nitride in Silicon Photonics." *Proceedings of the IEEE* 106.12 (2018).

[54] R. Halir, Y. Okawachi, J. S. Levy, M. A. Foster, M. Lipson, and A. L. Gaeta. "Ultrabroadband supercontinuum generation in a CMOS-compatible platform." *Optics Letters* 37.10 (2012).

[55] J. Yue, F. H. Falke, J. C. Schouten, and T. A. Nijhuis. "Microreactors with integrated UV/Vis spectroscopic detection for online process analysis under segmented flow." *Lab on a Chip* 13.24 (2013).

[56] M. Boerkamp, T. v. Leest, J. Heldens, A. Leinse, M. Hoekman, et al. "On-chip optical trapping and Raman spectroscopy using a TripleX dual-waveguide trap." *Optics Express* 22.25 (2014).

[57] L. Liu, D. Shan, X. Zhou, H. Shi, B. Song, et al. "TriPleX™ waveguide-based fluorescence biosensor for multichannel environmental contaminants detection." *Biosensors and Bioelectronics* 106 (2018).

[58] B. S. Ahluwalia, A. Z. Subramanian, O. G. Hellso, N. M. B. Perney, N. P. Sessions, and J. S. Wilkinson. "Fabrication of Submicrometer High Refractive Index Tantalum Pentoxide Waveguides for Optical

Propulsion of Microparticles." *IEEE Photonics Technology Letters* 21.19 (2009).

[59] Z. Wang, M. N. Zervas, P. N. Bartlett, and J. S. Wilkinson. "Surface and waveguide collection of Raman emission in waveguide-enhanced Raman spectroscopy." *Optics Letters* 41.17 (2016).

[60] B. S. Ahluwalia, Ø. I. Helle, and O. G. Hellesø. "Rib waveguides for trapping and transport of particles." *Optics Express* 24.5 (2016).

[61] Ø. I. Helle, B. S. Ahluwalia, and O. G. Hellesø. "Optical transport, lifting and trapping of micro-particles by planar waveguides." *Optics Express* 23.5 (2015).

[62] A. Dhakal, P. Wuytens, A. Raza, N. Le Thomas, and R. Baets. "Silicon Nitride Background in Nanophotonic Waveguide Enhanced Raman Spectroscopy." *Materials* 10.2 (2017).

[63] A. Raza, S. Clemmen, P. Wuytens, M. d. Goede, A. S. K. Tong, et al. "High index contrast photonic platforms for on-chip Raman spectroscopy." *Optics Express* 27.16 (2019).

[64] T. Lipiäinen, J. Pessi, P. Movahedi, J. Koivistoinen, L. Kurki, et al. "Time-Gated Raman Spectroscopy for Quantitative Determination of Solid-State Forms of Fluorescent Pharmaceuticals." *Analytical Chemistry* 90.7 (2018).

[65] R. M. Stöckle, Y. D. Suh, V. Deckert, and R. Zenobi. "Nanoscale chemical analysis by tip-enhanced Raman spectroscopy." *Chemical Physics Letters* 318.1 (2000).

[66] Q. Cao, J. Feng, H. Lu, H. Zhang, F. Zhang, and H. Zeng. "Surface-enhanced Raman scattering using nanoporous gold on suspended silicon nitride waveguides." *Optics Express* 26.19 (2018).

[67] S.-J. Baek, A. Park, J. Kim, A. Shen, and J. Hu. "A simple background elimination method for Raman spectra." *Chemometrics and Intelligent Laboratory Systems* 98.1 (2009).

[68] N. L. Thomas, A. Dhakal, A. Raza, F. Peyskens, and R. Baets. "Impact of fundamental thermodynamic fluctuations on light propagating in photonic waveguides made of amorphous materials." *Optica* 5.4 (2018).

[69] C. Joseph, P. Bourson, and M. D. Fontana. "Amorphous to crystalline transformation in Ta_2O_5 studied by Raman spectroscopy." *Journal of Raman Spectroscopy* 43.8 (2012).

[70] W. Lee, W. Lee, P. Muñoz-Galindo, P. Muñoz-Galindo, I. Hegeman, et al. "Study on multiple waveguide platforms for waveguide integrated Raman spectroscopy." *OSA Continuum* 3.5 (2020).

[71] A. Dhakal, F. Peyskens, S. Clemmen, A. Raza, P. Wuytens, et al. "Single mode waveguide platform for spontaneous and surface-enhanced on-chip Raman spectroscopy." *Interface Focus* 6.4 (2016).

[72] C. C. Evans, C. Liu, and J. Suntivich. "Low-loss titanium dioxide waveguides and resonators using a dielectric lift-off fabrication process." *Optics Express* 23.9 (2015).

[73] C. C. Evans, J. Burton, J. Suntivich, and D. Schlom. "Single-crystal Titanium Dioxide Strip-Loaded Waveguides." *Conference on Lasers and Electro-Optics (2016), paper SF1P.7*. Optical Society of America, 2016.

[74] C. C. Evans, C. Liu, and J. Suntivich. "Integrated-Evanescent Raman Sensors Based on Titanium-Dioxide Nanophotonics." *Meeting Abstracts* MA2016-01.39 (2016).

[75] F. Mirabella. *Internal Reflection Spectroscopy: Theory and Applications*. 1992.

[76] H. M. Grandin, B. Städler, M. Textor, and J. Vörös. "Waveguide excitation fluorescence microscopy: A new tool for sensing and imaging the biointerface." *Biosensors and Bioelectronics* 21.8 (2006).

[77] A. Hassanzadeh, M. Nitsche, S. Mittler, S. Armstrong, J. Dixon, and U. Langbein. "Waveguide evanescent field fluorescence microscopy: Thin film fluorescence intensities and its application in cell biology." *Applied Physics Letters* 92.23 (2008).

[78] A. Hassanzadeh, S. Armstrong, S. J. Dixon, and S. Mittler. "Multimode waveguide evanescent field fluorescence microscopy: Measurement of cell-substratum separation distance." *Applied Physics Letters* 94.3 (2009).

[79] R. Horváth, H. C. Pedersen, and N. B. Larsen. "Demonstration of reverse symmetry waveguide sensing in aqueous solutions." *Applied Physics Letters* 81.12 (2002).

[80] R. Horvath, H. C. Pedersen, N. Skivesen, D. Selmeczi, and N. B. Larsen. "Monitoring of living cell attachment and spreading using reverse symmetry waveguide sensing." *Applied Physics Letters* 86.7 (2005).

[81] R. Horvath, K. Cottier, H. C. Pedersen, and J. J. Ramsden. "Multidepth screening of living cells using optical waveguides." *Biosensors and Bioelectronics* 24.4 (2008).

[82] B. Agnarsson, S. Ingthorsson, T. Gudjonsson, and K. Leosson. "Evanescent-wave fluorescence microscopy using symmetric planar waveguides." *Optics Express* 17.7 (2009).

[83] B. Agnarsson, A. B. Jonsdottir, N. B. Arnfinnsdottir, and K. Leosson. "On-chip modulation of evanescent illumination and live-cell imaging with polymer waveguides." *Optics Express* 19.23 (2011).

[84] S. Ramachandran, D. A. Cohen, A. P. Quist, and R. Lal. "High performance, LED powered, waveguide based total internal reflection microscopy." *Scientific Reports* 3 (2013).

[85] Ø. I. Helle, C. I. Øie, P. McCourt, and B. S. Ahluwalia. "Chip-based optical microscopy for imaging membrane sieve plates of liver scavenger cells." Vol. 9554. 2015.

[86] F. Braet and E. Wisse. "Structural and functional aspects of liver sinusoidal endothelial cell fenestrae: a review." *Comparative Hepatology* 1.1 (2002).

[87] Zhou Wang, A. C. Bovik, H. R. Sheikh, and E. P. Simoncelli. "Image quality assessment: from error visibility to structural similarity." *IEEE Transactions on Image Processing* 13.4 (2004).

[88] N. J. Hunt, G. P. Lockwood, A. Warren, H. Mao, P. A. G. McCourt, et al. "Manipulating fenestrations in young and old liver sinusoidal endothelial cells." *American Journal of Physiology-Gastrointestinal and Liver Physiology* 316.1 (2018).

[89] B. Diederich, Ø. Helle, P. Then, P. Carravilla, K. O. Schink, et al. "Nanoscopy on the Chea(i)p." *bioRxiv* (2020).

[90] M. Lahrberg, F. T. Dullo, and B. S. Ahluwalia. "Photonic-chip based free space beam shaping and steering for advanced optical microscopy application." *OSA Continuum* 3.2 (2020).

[91] J. Sun, E. Timurdogan, A. Yaacobi, E. S. Hosseini, and M. R. Watts. "Large-scale nanophotonic phased array." *Nature* 493.7431 (2013).

[92] A. Priyadarshi, F. T. Dullo, D. L. Wolfson, A. Ahmad, N. Jayakumar, et al. "A transparent waveguide chip for versatile TIRF-based microscopy and nanoscopy." *arXiv:2006.07275 [physics]* (2020).

[93] R. Diekmann, K. Till, M. Müller, M. Simonis, M. Schüttpelz, and T. Huser. "Characterization of an industry-grade CMOS camera well suited for single molecule localization microscopy – high performance super-resolution at low cost." *Scientific Reports* 7.1 (2017).

[94] D. N. Wadduwage, V. R. Singh, H. Choi, Z. Yaqoob, H. Heemskerk, et al. "Near-common-path interferometer for imaging Fourier-transform spectroscopy in wide-field microscopy." *Optica* 4.5 (2017).

[95] P. L. Stiles, J. A. Dieringer, N. C. Shah, and R. P. V. Duyne. "Surface-Enhanced Raman Spectroscopy." *Annual Review of Analytical Chemistry* 1.1 (2008).

[96] E. Bailo and V. Deckert. "Tip-enhanced Raman scattering." *Chemical Society Reviews* 37.5 (2008).

[97] G. Eckhardt, R. W. Hellwarth, F. J. McClung, S. E. Schwarz, D. Weiner, and E. J. Woodbury. "Stimulated Raman Scattering From Organic Liquids." *Physical Review Letters* 9.11 (1962).

[98] E. M. Purcell. "Spontaneous Emission Probabilities at Radio Frequencies." *Confined Electrons and Photons*. Ed. by E. Burstein and C. Weisbuch. NATO ASI Series 340. Springer US, 1995.

[99] A. Dhakal. *The role of index contrast in the efficiency of absorption and emission of a luminescent particle near a slab waveguide*. 2012.

[100] A. Dhakal, P. Wuytens, F. Peyskens, A. Z. Subramanian, N. Le Thomas, and R. Baets. "Silicon-nitride waveguides for on-chip Raman spectroscopy." *SPIE Photonics Europe*. International Society for Optics and Photonics, 2014.

[101] A. Dhakala, A. Z. Subramaniana, N. Le Thomasa, and R. Baetsa. "Raman spectroscopy using photonic waveguides." *XXIV International Conference on Raman Spectroscopy (ICORS 2014)*. Citeseer, 2014.

[102] A. Dhakal, A. Raza, F. Peyskens, A. Z. Subramanian, S. Clemmen, et al. "Efficiency of evanescent excitation and collection of spontaneous Raman scattering near high index contrast channel waveguides." *Optics Express* 23.21 (2015).

[103] A. Dhakal, F. Peyskens, A. Subramanian, N. Le Thomas, and R. Baets. "Enhanced spontaneous Raman signal collected evanescently by silicon nitride slot waveguides." *CLEO: Science and Innovations*. Optical Society of America, 2015.

[104] Z. Wang, S. J. Pearce, Y.-C. Lin, M. N. Zervas, P. N. Bartlett, and J. S. Wilkinson. "Power Budget Analysis for Waveguide-Enhanced Raman Spectroscopy." *Applied Spectroscopy* 70.8 (2016).

[105] A. Dhakal, A. Z. Subramanian, P. Wuytens, F. Peyskens, N. L. Thomas, and R. Baets. "Evanescent excitation and collection of spontaneous Raman spectra using silicon nitride nanophotonic waveguides." *Optics Letters* 39.13 (2014).

[106] A. Dhakal, P. Wuytens, F. Peyskens, A. Subramanian, A. Skirtach, et al. "Nanophotonic lab-on-chip raman sensors: a sensitivity comparison with confocal Raman microscope." *2015 INTERNATIONAL CONFERENCE ON BIOPHOTONICS (BIOPHOTONICS)*. IEEE, 2015.

[107] F. Peyskens, A. Z. Subramanian, P. Neutens, A. Dhakal, P. V. Dorpe, et al. "Bright and dark plasmon resonances of nanoplasmonic antennas evanescently coupled with a silicon nitride waveguide." *Optics Express* 23.3 (2015).

[108] F. Peyskens, A. Subramanian, A. Dhakal, N. L. Thomas, and R. Baets. "Enhancement of Raman Scattering Efficiency by a Metallic Nano-antenna on Top of a High Index Contrast Waveguide." *CLEO: 2013 (2013), paper CM2F.5*. Optical Society of America, 2013.

[109] C. Atkins, K. Buckley, M. Blades, and R. Turner. "Raman Spectroscopy of Blood and Blood Components." *Applied Spectroscopy* 71.5 (2017).

[110] L. Lu, L. Shi, J. Secor, and R. Alfano. "Resonance Raman scattering of -carotene solution excited by visible laser beams into second singlet state." *Journal of Photochemistry and Photobiology. B, Biology* 179 (2018).

[111] Y. Zhou, C.-H. Liu, Y. Sun, Y. Pu, S. Boydston-White, et al. "Human brain cancer studied by resonance Raman spectroscopy." *Journal of Biomedical Optics* 17.11 (2012).

[112] C.-L. Wu, B.-T. Chen, Y.-Y. Lin, W.-C. Tien, G.-R. Lin, et al. "Low-loss and high-Q Ta_2O_5 based micro-ring resonator with inverse taper structure." *Optics Express* 23.20 (2015).

[113] Q. Fang, J. Song, X. Luo, X. Tu, L. Jia, et al. "Low Loss Fiber-to-Waveguide Converter With a 3-D Functional Taper for Silicon Photonics." *IEEE Photonics Technology Letters* 28.22 (2016).

[114] D. N. Wadduwage, J. K. Park, J. R. Boivin, Y. Xue, and P. T. C. So. "Descattering with Excitation Patterning (DEEP) Enables Rapid Wide-field Imaging Through Scattering Media." *arXiv:1902.10737 [physics]* (2019).

[115] L. B. Soldano and E. C. M. Pennings. “Optical multi-mode interference devices based on self-imaging: principles and applications.” *Journal of Lightwave Technology* 13.4 (1995).

[116] N. Jayakumar, N. Jayakumar, Ø. I. Helle, K. Agarwal, B. S. Ahluwalia, et al. “On-chip TIRF nanoscopy by applying Haar wavelet kernel analysis on intensity fluctuations induced by chip illumination.” *Optics Express* 28.24 (2020).

[117] Ø. I. Helle, F. T. Dullo, M. Lahrberg, J.-C. Tinguely, O. G. Hellesø, and B. S. Ahluwalia. “Structured illumination microscopy using a photonic chip.” *Nature Photonics* 14.7 (2020).

[118] M. P. Edgar, G. M. Gibson, and M. J. Padgett. “Principles and prospects for single-pixel imaging.” *Nature Photonics* 13.1 (2019).

[119] X. Li, H. Xu, X. Xiao, Z. Li, J. Yu, and Y. Yu. “Demonstration of a highly efficient multimode interference based silicon waveguide crossing.” *Optics Communications* 312 (2014).